Metal-silicate differentiation in early-accreted small bodies of the Solar System : a multidisciplinary approach

Adrien Néri

THÈSE

En vue de l'obtention du

DOCTORAT DE L'UNIVERSITÉ DE TOULOUSE

Délivré par : *l'Université Toulouse 3 Paul Sabatier (UT3 Paul Sabatier)*

Présentée et soutenue le *26/11/2019* **par :**

Adrien Néri

Étude de la différenciation métal-silicates dans les petits corps du Système Solaire : une approche pluridisciplinaire

---

JURY

Renaud Deguen	ISTerre-UJF, Grenoble	Président du Jury
Valérie Malavergne	LGE-UPEM, Paris	Rapporteure
Daniel J. Frost	BGI, Bayreuth	Rapporteur
Brigitte Zanda	MNHN-IMPMC, Paris	Examinateure
Denis Andrault	LMV-UCA, Clermont-Fd	Examinateur
Michael J. Toplis	IRAP, Toulouse	Directeur de thèse
Ghylaine Quitté	IRAP, Toulouse	Co-Directrice de thèse

École doctorale et spécialité :
SDU2E : Sciences de la Terre et des Planètes Solides
Unité de Recherche :
Institut de Recherche en Astrophysique et Planétologie (IRAP - UMR 5277)
Directeur(s) de Thèse :
Michael J. Toplis et *Ghylaine* Quitté
Rapporteurs :
Valérie Malavergne et *Daniel J.* Frost

Remerciements

Ces trois années sont passées très vite, je m'y suis lancé sans trop savoir à quoi m'attendre, mais je me suis pris au jeu. À l'aide de mes quatres directeurs, nous avons réussi à pousser l'aspect multidisciplinaire assez loin, je suis assez fier du résultat final. Tout ce travail n'aurait pas été ce qu'il est maintenant sans le soutien de beaucoup de personnes, que ce soit sur le plan professionel ou amical, je tiens à remercier sincèrement toutes ces personnes.

Tout d'abord, un grand merci à tout mes directeurs, Ghylaine Quitté, Mike Toplis, Jérémy Guignard et Marc Monnereau. Je tiens à souligner l'implication des deux derniers, bien que n'ayant pas de reconnaissance officielle, je les considère comme mes directeurs et les remercie de m'avoir donné de leur temps, ma thèse n'aurait pas été la même sans eux. Je voudrais en profiter pour faire une mention spéciale à Jérémy, qui m'a toujours donné de son temps, même s'il avait d'autres choses à faire. Merci à toi Jérémy.

Merci à Denis Andrault et à Micha Bystricky pour leur implication dans mon comité de suivi de thèse et leurs conseils. Je voudrais dire merci à tout les membres de l'équipe DIP, vous aviez toujours le sourire ça a été très agréable. Je souhaites également remercier toutes les personnes qui m'ont aidé expérimentalement, sur la plateforme de planétologie toulousaine : Jérémy, Frédéric Béjina, Micha et Alain Pagès ; lors des expériences piston-cylindre au LMV à Clermont-Ferrand : Ken Koga et Didier Laporte ; lors des expériences en presse Paris-Edimbourg lors de notre session à SOLEIL : Denis, Jean-Philippe Perrillat, Micha, Ghylaine, Marc, Jérémy, Andrew King et Nicolas Guignot. Merci à tout ceux m'ont aidé à réaliser les analyses sur mes échantillons, surtout à l'équipe du centre de microcaractérisation Raimond Castaing : Stéphane Leblond du Plouy pour le MEB, Sophie Gouy et Philippe de Parseval pour la microsonde électronique, ainsi que Claudie Josse et Arnaud Proietti pour l'EBSD ; mais aussi à Christophe Tenailleau et Benjamin Duployer du CIRIMAT pour les analyses de microtomographie 3D.

Je tiens à remercier tout les membres d'UniverSCiel avec lesquels j'ai pu animer le festival Astro-Jeunes à Fleurance, ou d'autres interventions, ça aura été un réel plaisir de travailler avec vous. Merci également à tout les thésards de l'IRAP avec qui j'ai pu passer de très bons moments. Un grand merci à l'équipe des "Bras Cassés" : Mathilde, Louise, Pauline, Edoardo et Geoffroy pour toutes les escape game que nous avons fait à Toulouse. Merci aux copains Lyonnais, que ce soit du Parc : Jean et Valentin, ou de l'ENSL : Alexandre, Antonin, Thomas et Valentin. Je voudrais finir ce paragraphe par dire merci à mes amis proches arlésiens : Jérémy et Vincent, mes bros, "The Wolf Pack", avec qui je suis resté en contact pendant toutes ces années malgré la distance.

Pour finir, je voudrais remercier ma famille, qui m'a toujours soutenu dans ce que je voulais faire. Merci tout particulièrement à mes parents et à mon frère. Merci à toi Mathilde ma chérie d'avoir partagé ces années avec moi, merci pour tout ce que tu m'apportes et merci de me rendre meilleur.

Adrien

Contents

List of Figures

List of Tables

Avant-propos

Les météorites sont les objets les plus anciens que l'on puisse tenir dans les mains, plus anciens que les plus anciennes roches terrestres, plus anciens que la Terre elle-même, la Lune, Mars, ou toute autre planète tellurique, puisque les météorites sont des fragments des tous premiers corps formés dans et par le système solaire, des corps dont sont nées les planètes. Ces pierres tombées du ciel ne sont pas uniques que par leur âge, mais surtout par le témoignage qu'elles renferment sur les processus de différenciation à l'œuvre dès les premiers stades de l'accrétion des embryons planétaires. Mais ce message est difficile à déchiffrer, car il en dit tout autant sur la diversité des natures de ces corps que sur la complexité de leur structure interne. Une des caractéristiques communes à toutes les météorites est que leur état est resté figé pendant des milliards d'années, c'est-à-dire qu'elles ont gardé toutes les traces de leur évolution, elles n'ont pas été effacées contrairement à la Terre dont la surface est constamment renouvelée par la tectonique des plaques. Cette thèse porte un regard sur certains de ces objets pour tenter de dépasser la simple classification qu'il en est fait classiquement en revélant des liens génétiques entre eux.

La ceinture d'astéroïdes est vraisemblablement le résultat des migrations précoces des planètes géantes gazeuses (Walsh et al., 2011, 2012), qui ont permis de mélanger des matériaux formés à différentes distances héliocentriques et à les piéger à cet endroit précis. Parmi les petits corps, "archives" des stades précoces du Système Solaire, se trouvent les astéroïdes ainsi que les comètes. Des missions spatiales récentes ont été lancées dans le but d'étudier la surface des astéroïdes à l'aide de deux techniques différentes : soit à l'aide d'analyses par télédétection, soit le retour des échantillons. La mission Dawn est un exemple récent d'analyse par télédétection de la surface de (1) Ceres et (4) Vesta. Les analyses spectroscopiques permettent de déterminer la composition de la croûte de ces astéroïdes, en terme de proportions de phases et d'éléments majeurs. D'autres capteurs basés sur les mesures des champs de gravité de ces corps permettent de déterminer les structures internes possibles. Sur la base de simulations thermodynamiques et de processus à l'équilibre ou fractionnés, il est alors possible de comprendre comment ces corps ont acquis leur structure interne. Cependant, au vu de la faible précision des analyses de composition par télédétection, d'autres missions sont dédiées au retour sur Terre d'échantillons collectés à la surface d'astéroïdes. Peu d'échantillons ont été ramenés sur Terre jusqu'à présent, par exemple, quelques grains de poussière de la queue de la comète 81P/Wild par la mission Stardust en 2006, ou encore de la surface de l'astéroïde (25143) Itokawa par la mission Hayabusa en 2010. D'autres missions ont été lancées ces dernières années pour augmenter la masse d'échantillons ramenée sur terre : Hayabusa 2 lancée en 2014 s'intéresse à l'astéroïde (162173) Ryugu et devrait revenir sur Terre en 2023 ; OSIRIS-REx, quand à elle lancée en 2016 , s'intéresse à la surface de l'astéroïde Bénou et devrait également être de retour sur Terre en 2023. Les échantillons retournés par ces missions représentent une extrême minorité du matériel disponible parmi les collections. Les météorites de nos collections sont des objets qui ont été éjectés de la ceinture d'astéroïdes et sont tombés sur Terre. Il y a un énorme biais sur le type d'objets retrouvé pour différentes raisons : la

dynamique de collision des astéroïdes, la trajectoire des météorites éjectées, leur préservation pendant leur voyage dans l'espace qui peut provoquer une érosion mécanique, le lieu de chute (d'avantage d'objets sont retrouvés dans les zones inhabitées, e.g. déserts chauds ou froids) et enfin, le renouvellement constant de la surface terrestre dû à la tectonique des plaques. Il est important de garder à l'esprit que les objets qui sont retrouvés ont voyagé dans l'espace pendant des temps très différents avant d'atteindre la Terre. Ensuite, la traversée de l'atmosphère nécessite qu'ils aient une certaine taille, ni trop petite, auquel cas is seraient vaporisés par la friction de l'air, ni trop grosse, car ils pourraient alors éclater en plusieurs morceaux. Enfin, les objets doivent tomber dans des régions inhabitées où, de préférence, il n'y a pas de végétation, et être retrouvés dans des laps de temps assez courts, sinon ils pourraient ne pas résister à l'altération terrestre. Les météorites sont récupérées et étudiées par l'homme depuis plus de 3000 ans (déjà au cours de l'Égypte antique), ce qui reste un clin d'œil en comparaison au flux reçu par la Terre sur des échelles de temps géologiques.

Les météorites sont classées en trois grandes catégories selon leur degré de différenciation, c'est-à-dire leur degré de séparation métal-silicate. Les objets les plus primitifs et les plus indifférenciés sont représentés par les chondrites, alors que les plus évolués sont incarnés par les météorites de fer et achondrites qui sont entièrement composées de métal ou de silicate. Le stade intermédiaire est typiquement illustré par les achondrites primitives qui ont subi une extraction partielle des produits de fusion des sous-systèmes silicatés et métalliques. Il est important de noter que ces familles de météorites sont composées de multiples clans, groupes et sous-groupes avec chacun leurs propres caractéristiques ; l'image globale est donc bien plus compliquée que le schéma simple décrit ici. Cependant, cette séquence globale d'objets indique qu'à partir d'un matériau chondritique primitif, le métal et les silicates ont pu se séparer à des degrés plus ou moins importants. Les grandes questions sont donc : **dans quelles conditions se produit la différenciation métal-silicate ? Quels sont les processus physiques à l'œuvre et sont-ils efficaces ? Quand la différenciation s'est-elle produite et sur quelles échelles de temps ?**

Deux processus majeurs peuvent conduire à la différenciation métal-silicate : la sédimentation de particules métalliques dans un liquide silicaté ou la percolation d'un réseau métallique interconnecté (par exemple Rubie, 2015). Ces deux processus nécessitent que le matériel précurseur soit à haute température et partiellement ou totalement fondu. La source de chaleur principale des petits corps du Système Solaire est la désintégration de l'^{26}Al, à courte demi-vie. Le sédimentation des gouttelettes métalliques a vraisemblablement lieu en présence de grandes quantitées de liquide silicaté, et peut constituer le mécanisme principal de la différenciation des météorites de fer et achondrites, caractérisées par un fort taux de fusion. À l'inverse, la ségrégation d'un réseau interconnecté de métal a plutôt lieu pour les échantillons présentant de faibles taux de fusion, et peut constituer le mécanisme principal de différenciation des achondrites primitives. Ces deux mécanismes dépendent de la fraction de cristaux silicatés, c'est-à-dire de leur température maximal, et des énergies d'interfaces. Les systèmes naturels tendent à favoriser les contacts de faible coût énergétique afin de minimiser le budget énergétique global. Il y a un équilibre entre énergies d'interfaces, qui peuvent forcer les phases à rester en contact (dans le cas de faibles coûts énergétiques), et l'attraction gravitationnelle du planétésimal, qui pousse les phases à se séparer en fonction de leurs densités relatives. Les petits corps accrétés tôt dans l'histoire du Système Solaire n'excèdent pas 300 km de rayon, ce qui implique un champ de gravité relativement faible. Dans ces conditions, les

énergies d'interfaces peuvent jouer un rôle important et contrer l'attraction gravitaire. Cette thèse s'intéresse plus particulièrement aux processus de différenciation métal-silicates par la formation de réseaux interconnectés, d'un point de vue microscopique et macroscopique.

La plupart des études s'appuient sur un système à deux phases solide-liquide où il y a deux énergies d'interfaces : entre deux grains de solide et entre le solide et le liquide. Cependant, un raisonnement simple basé sur des systèmes binaires est mis à défaut car les échantillons naturels montrent des signes de fusion partielle des deux sous-systèmes métalliques et silicatés. Il existe donc une troisième phase, le liquide silicaté, qui a sa propre énergie d'interface et peut affecter le bilan énergétique global et changer les seuils d'interconnectivité des phases métalliques. Le travail de cette thèse vise à caractériser expérimentalement les géométries d'équilibre d'un tel système à trois phases et à étudier les paramètres qui peuvent les modifier et affecter leur évolution. J'ai cherché à caractériser les deux échelles, microscopiques et macroscopiques, en déterminant les énergies d'interfaces à partir de mesures d'angles dièdres, et avec l'acquisition d'images de microtomographie 3D à rayons-X. Ces résultats ont ensuite été appliqués au contexte de la différenciation métal-silicate à l'aide de bilans de masse et de modélisation thermodynamique, mais aussi à travers l'étude d'échantillons naturels (acapulcoites, lodranites et winonaites). Le premier chapitre de ce manuscrit rappelle les premières étapes de la formation et de l'évolution de notre Système Solaire, puis il détaille l'approche générale de l'interconnectivité du point de vue des angles dièdres. Enfin, il tire des conclusions concernant la mobilité des différentes phases et discute des conséquences sur la différenciation métal-silicate. Les méthodes expérimentales sont ensuite décrites dans un second chapitre. Trois types d'assemblages ont été utilisés dans le cadre de cette thèse (four haute température à atmosphère contrôlée, piston-cylindre et presse Paris-Édimbourg). Les techniques analytiques utilisées pour la caractérisation des échantillons ainsi que les façons d'exploiter les données associées sont aussi présentées. Le troisième chapitre, correspondant à un article scientifique publié (Néri et al., 2019), présente la caractérisation microscopique du système à trois phases et propose un modèle pour expliquer la formation des acapulcoites et des lodraintes. Plus précisément, Il aborde la question de l'interconnectivité du liquide métallique en fonction de sa teneur en soufre et de la façon dont cela affecte la différenciation. Le quatrième chapitre est ensuite dédié à l'étude des textures macroscopiques du métal au cours des expériences, en fonction les proportions relatives de chacune des phases. Ce chapitre souligne l'effet des différents taux de maturation texturales, ainsi que de la coalescence des métaux qui peut avoir lieu dans les océans de magma en convection. Le cinquième chapitre décrit les paramètres à l'équilibre des océans magma dans les petits corps, en tenant compte de la dépendance de la viscosité en fonction de la fraction de cristaux, affectant la vigueur de la convection et l'efficacité de la dissipation de chaleur. Les résultats sont ensuite utilisés pour construire un modèle thermodynamique en faveur d'une origine magmatique pour les pallasites. Enfin, le sixième chapitre est consacré à l'analyse texturale de neuf sections d'achondrites primitives : cinq acapulcoites, deux lodranites et deux winonaites. Les résultats sont analysés sur des arguments pétrologiques avant de les utiliser dans les équations de compaction afin de comprendre les échelles de temps nécessaires à la différenciation. Des simulations thermodynamiques sont finalement menées pour contraindre le matériel précurseur de ces achondrites primitives.

Foreword

Meteorites are the oldest objects that can be held in your hands, older than the oldest Earth's rocks, older than the Earth itself, the Moon, Mars or any terrestrial planet, since meteorites are fragments of the very first bodies formed in and by the Solar System, bodies from which the planets were built. These stones fallen from the sky are not only unique in their age, but also in the testimony they contain about the differentiation processes at work from the first stages of the accretion of planetary embryos. However the message is difficult to decipher, it says as much about the diversity of natures of these first bodies as about the complexity of their internal structure. One of the common characteristic of meteorites is that they did not evolve further for billions of years, meaning that they kept all tracks of their evolution, they were not erased unlike for Earth which surface is constantly renewed due to plate tectonics. This thesis looks at some of these objects in an attempt to go beyond the simple classification that is made by disclosing genetic links between them.

The asteroid belt is thought to be the result of early migrations of the giant gas planets (Walsh et al., 2011, 2012) that led to mixing of materials formed at varying heliocentric distances and to trap them at this specific location. Among the small bodies, "archives" of the Solar System, are asteroids as well as comets. Recent space-based missions have been launched with the aim of studying the surface of these asteroids based on two different techniques: either remote sensing analyses or samples return missions. The Dawn mission is a recent example of remote sensing analysis of the surface of (1) Ceres and (4) Vesta. The spectroscopic analysis allows to determine the composition in terms of phases and bulk chemistry of major elements of the outer crust. Other sensors based on the measurements of the gravity fields of these bodies allow to determine possible inner structures. Based on thermodynamic simulations and equilibrium or fractionated processes it is then possible to understand how their inner structure was shaped. However, due to low precision of composition analyses using remote sensing data, other missions are dedicated to bring samples collected on planetary or asteroidal surfaces back to Earth. There are small amounts of samples that were brought back to Earth until now. For instance, some dust grains from the tail of comet 81P/Wild by the Stardust mission in 2006, or from the surface of asteroid (25143) Itokawa by the Hayabusa mission in 2010. Other space-based missions were launched in the past few years in order to increase the mass of the samples brought back to Earth: Hayabusa 2 launched in 2014 will take interest to asteroid (162173) Ryugu and should be back to Earth in 2023; as for OSIRIS-REx, this mission was launched in 2016 and will study the surface of asteroid (101955) Bennu, it should also be back to Earth in 2023. Samples returned by these missions represent an extreme minority of the material available for study. The meteorites of our collections are objects that were ejected from the asteroid belt and fell to Earth. There is a huge bias on the objects sampled for different reasons: the collisional dynamics of the asteroids, the trajectory of the ejected meteorites, their preservation during their travel in space which may cause mechanical erosion, the location where they fall (more are found in unmanned zones, e.g. cold or hot deserts) and last but not least, the constant renewal of Earth's surface due to plate tectonics. It is important to keep in mind that the objects we find traveled for different times in space

before reaching Earth. Then, crossing the atmosphere requires that their size is small enough to not create major impacts, but not too small, such that friction with air did not cause them to explode or to be vaporized. Finally, objects have to fall in unmanned regions with preferably no vegetation and they have to be found within a short time frame, otherwise terrestrial weathering will alter them and turn them into sand. Meteorites are recovered and studied by mankind since more than 3000 years (already during ancient Egypt), which is a blink of an eye for Earth's and geological timescales.

Their classification in three main categories follows their degree of differentiation, i.e. the degree of metal-silicate separation. The most pristine and undifferentiated objects are thought to be chondrites, in which no metal or silicate has been extracted, while the most evolved of them is represented by achondrites that are entirely composed of either metal or silicate. The intermediate stage is typically illustrated by primitive achondrites that experienced partial melting and partial extraction of both silicate and metallic subsystems. It is to note that each of these meteorite families are composed of multiple clans, groups and subgroups with their own specific properties, hence the global picture is far more complicated than the simple scheme drawn here. However, this overall sequence of objects indicates that starting from a pristine chondritic material, metal and silicate were able to separate to different extents. The main questions are then: **under which conditions does metal-silicate differentiation occur? What are the physical processes driving differentiation and are they efficient? When does differentiation occur and what are the timescales?**

Two main processes may drive metal-silicate differentiation: the settling of metallic particles in molten silicates or the percolation of an interconnected metallic network (e.g. Rubie, 2015). Both processes require that the precursor material is at high temperature and partially or fully molten. The main heat source of these bodies is thought to be the decay of short-lived ^{26}Al. Metallic droplet settling most likely occurs in the presence of large silicate melt contents and may be the driving mechanism for the differentiation of achondrites which show evidence for large silicate melting degrees. On the other hand, the segregation of an interconnected iron-sulfide melt network most likely occurs for samples with low silicate melting degree and may be the driving mechanism for the partial differentiation of primitive achondrites. Both mechanisms then depend on the silicate crystal content of the material, i.e. their peak temperature, and on the interfacial energies. Natural systems tend to favor contacts of low energetic cost to minimize the bulk interfacial energy budget. There is a balance between interfacial energies, that may force the phases to stick together (in the case of low interfacial energies), and the gravitational forces of the planetesimal, that drive the phases to separate as a function their densities. Early-accreted small bodies have radii no greater than 300 km, implying a weak gravity field. In these conditions, interfacial energies most likely play an important role as they may counteract gravity. In the present PhD, interest is focused on metal-silicate differentiation through the formation of an interconnected iron-sulfur network, from micro- to macro-scale.

Most studies rely on a two-phase solid-liquid system, where there are two interfacial energies: between two solid grains and between the solid and the liquid. However, simple reasoning based on binary systems is flawed by the fact that natural samples show evidence for partial melting of both metallic and silicate subsystems. Hence, there is a third phase, the silicate melt, with its own interfacial energy that may affect the interfacial energy balance

and change the interconnection threshold of the metallic phases. The work of this PhD aimed at the experimental characterization of the equilibrium geometry of such three-phase systems and to investigate the parameters affecting it or its time-scale. Interests were taken to both the micro- and macro-scales, with the determination of interfacial energies from the measurement of dihedral angles, and the acquisition of 3D X-ray microtomography images to determine the organization and interconnection of the metallic phases. These results were then applied in the framework of the metal-silicate differentiation using mass balance and thermodynamic modeling, but also with the study of sections of natural samples (acapulcoites, lodranites and winonaites). The first Chapter of this manuscript recalls the first steps of the formation and evolution of our solar system, then details the general approach on the question of interconnectivity considering a dihedral angle point of view and finally draws conclusions concerning the mobility of different phases and the consequences for metal-silicate differentiation. Then, experimental methods are described in the second Chapter. Three different set-ups have been used in the framework of this PhD (atmosphere controlled furnace, piston-cylinder and Paris-Edinbugh press) and are presented. Analytical techniques used for sample characterization as well as the associated data processing are also depicted. The third Chapter, corresponding to a published paper (Néri et al., 2019), presents the microscopic characterization of the three-phase system used and proposes a model to explain the formation of acapulcoites and lodraintes. In detail, it addresses the question of the interconnection of an iron-sulfur melt as a function of its sulfur content and how it affects differentiation. A fourth Chapter is then dedicated to the study of the large-scale textures of the metal during experiments, following the relative proportions of the solid and molten silicates. This Chapter highlights the effect of different textural maturation rates and the coalescence that may occur during convection in a magma ocean. The fifth Chapter considers the equilibrium parameters of magma oceans in small bodies, taking into account the dependence of viscosity on crystal fraction that most likely affects the vigor of convection and the efficiency of heat dissipation. Results are then used to derive thermodynamic models that argue in favor of a magmatic origin for pallasites. Last but not least, the sixth Chapter is dedicated to the textural analysis of nine sections of primitive achondrites: five acapulcoites, two lodranites and two winonaites. Results are analyzed from a petrological point of view, before comparing them with compaction equations to understand the timescales of metal-silicate differentiation. Finally, thermodynamic simulations were conducted to investigate the precursor material of these primitive achondrites.

Chapter 1

State of the art

Contents

1.1 From the nebula to the Asteroid Belt

Remnants of the early accreted small bodies of the Solar System are stored in the Asteroid Belt. The presence of such reservoir of primitive objects is not observed in other exoplanetary systems. Either the Solar System is an exception or there are observational biases due to a resolution that is not sufficient. In any cases, the Asteroid Belt provides a unique laboratory to study the time-line of the evolution of planetesimals that accreted early. The present part aims at describing briefly the different steps of formation of our Solar System, from the gaseous nebula to the present planetary system with its anomalous Asteroid Belt.

1.1.1 Gravitational collapse of the protosolar nebula

The Universe is composed of a massive super structure made up of filaments surrounded by voids. These filaments are in turn composed of galaxy clusters and subsequently, galaxies. At a smaller scale, galaxies host planetary systems, i.e. stars and planets, and nebulae, i.e. gas clouds. A genetic link between planetary systems and nebulae has been proposed by Swedenborg (1734) who imagined that planetary systems could form from the gravitational collapse of a dense gas cloud. Observations of protoplanetary disks around young stellar objects indicate that most disks have a short lifetime of ≈ 6 Myr (Haisch, Jr. et al., 2001). Planetary accretion is likely to be main disk clearing process. However, the short timescale is likely to match only the formation of the giant planets (Boss and Goswami, 2006).

The protosun and protonebula formed from the gravitational collapse a dense cold molecular cloud Boss and Goswami (for a detailed review, see 2006, and references therein). Diffuse objects are stable and need to undergo a shock of some sort to collapse on themselves, e.g. the supernova of a neighboring star which may also bring short-lived radionuclides that will be incorporated in the first solids to condensate. Once the collapse initiated, the cloud is contracting on itself, starts to rotate, forms a disk perpendicular to the rotation axis and temperature rises. Due to a differential stress between the inner and outer regions of this disk, gas particles are slowed down, making them drift toward the center of the disk and forming the Sun. As the mass of the disk is reduced, the differential stress is less vigorous and the disk is able to cool. Density and temperature of a specific location will determine the chemical species that will be able to form. For a detailed review on the physics of nebular evolution, see Ciesla and Charnley (2006).

1.1.2 Primary accretion - Shaping the planetary embryos

Primary accretion defines the step in which meteorites parent bodies are formed, i.e. planetesimals. From a dynamical point of view, primary accretion of planetesimals can be subdivided into four steps (Nichols Jr, 2006): (1) gravitational collapse of gas and dusts, (2) formation of millimeter to centimeter sized grains from aggregation of small particles, (3) gravitational accretion of meter to kilometer sized objects and (4) collisions and impacts leading to planetary formation and evolution (e.g. differentiation, alteration). It is of note that the different steps do not have sharp limits and are likely to overlap between each other.

As the protosolar disk cools down, elements are able to go from the gaseous state to the solid state, forming the first condensates with sizes on the order of the micrometer. These particles are subject to the dynamics of the gas causing them to collide and to coagulate thanks to Van der Waals forces. These first aggregates are porous and can easily dissipate the collisional energy, allowing them to reach centimeter to meter sizes (Cuzzi and Weidenschilling, 2006; Russell et al., 2006). Then, these particles are large enough to escape the inward radial gas drag and will settle toward the midplane. Collision velocities between centimeter sized objects are too high to allow them to form aggregates and gravity forces are too low to bond them. Although counterintuitive, turbulence fosters accretion as it does not only have a global dispersing effect, but also concentrates the centimeter sized ones in some areas (Cuzzi and Weidenschilling, 2006). If particles density exceeds that of the gas, there can be local gravitational collapses that form small bodies with sizes larger than a meter and up to 10-100 km. Planetary embryos then form rapidly through runaway growth: the largest bodies have collisional cross sections increased due to their gravitational attraction, the largest one of a given region gains mass more rapidly than the next largest and dominates that region (Weidenschilling and Cuzzi, 2006). This process is repeated at different distances from the Sun, forming several embryos of the size of the Moon or Mars. Bodies of this size can no longer be shattered by collisions and will continue to evolve to form the terrestrial planets. In this context the presence of the Asteroid Belt of our Solar system can be questioned, it should have disappeared and be a part of the terrestrial planets.

1.1.3 The Asteroid Belt and gas giants migrations

At this point, four features of the actual Solar System remain puzzling

1. At its position, Mars should have a size greater than a planetary embryo (i.e. similar to that of the Earth).
2. The asteroid belt lost most of its mass, but is still present. The processes that fostered its partial emptying remains uncertain.
3. Spectral signatures of asteroids show that dry (S-type asteroids) and hydrous (C-type asteroids) material were mixed, i.e. materials that formed at different places (above and beyond the snowline respectively).
4. The surface of the Moon exhibits a peak of cratering $\approx$ 700 Myr after planets accreted. This cataclysmic event is called the Late Heavy Bombardment (LHB) and remains misunderstood in the theory of planets formation.

Migrations of the gas giants provide a model that fits all these features (Tsiganis et al., 2005; Gomes et al., 2005; Morbidelli et al., 2005; Walsh et al., 2011, 2012). The idea that the gas giants may be able to migrate arose from the the observation of hot Jupiters (Mayor and Queloz, 1995), i.e. gaseous planets close to their star, while these bodies are likely to have formed beyond the snowline. The model of gas giants migration is based on two steps. (1) A first stage called the "Grand Tack model" in which Jupiter migrates inward due to gas-drag in the protonebula, and then outward due to a resonant motion with Saturn (Walsh et al., 2011, 2012). This inward-then-outward migration results in two important features: the scatter of material that accreted both inside and outside the snow-line, mixing dry and hydrous objects, and the truncation of the inner disk at 1 AU (Astronomical Unit), i.e. the Sun to

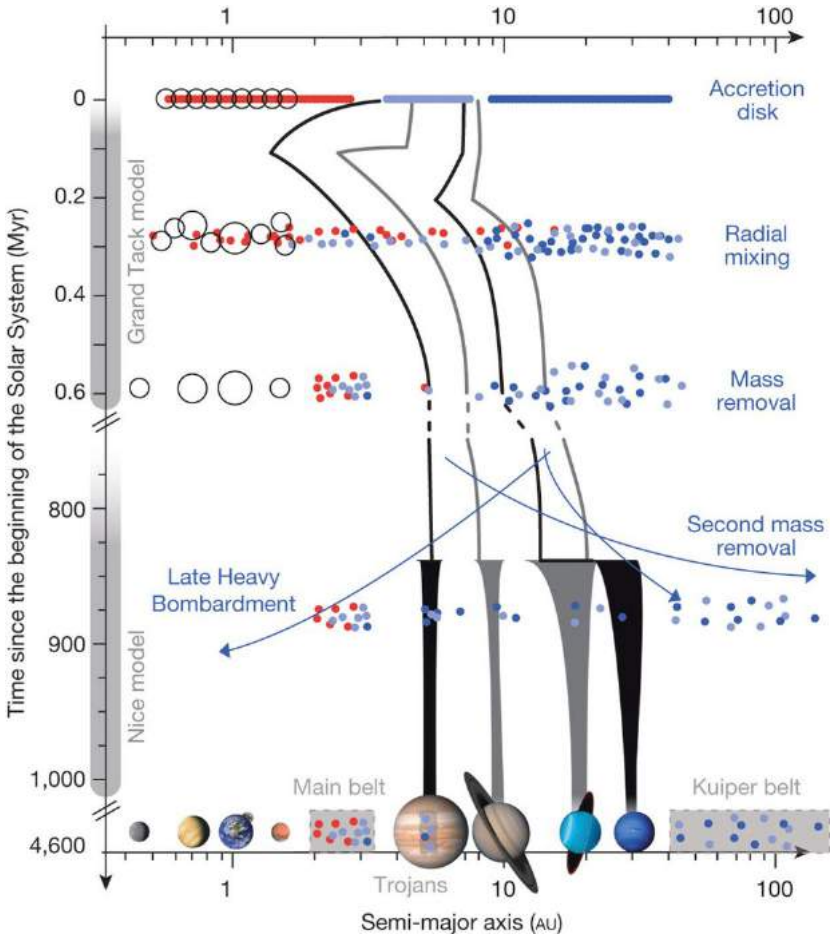

Figure 1.1 – Cartoon illustrating planetary migrations and the effect on the asteroid belt (Demeo and Carry, 2014). The orbit of the gas giants are represented in black and gray lines. Planetesimals are represented as dots which color depends on their accretion region: red for the disk, light blue for the gas giants region and dark blue the region beyond the gas giants. There are two main events of planetary migration: the Grand Tack model that occurred early in the Solar System history and the Nice model that took place much later, around 700 Myr. During the Grand Tack, Jupiter migrated inward due to gas-drag, until Saturn catches it back and enters into a resonant motion, driving both giants back to their original region. Uranus and are also pushed back. During this inward then outward migration, planetesimals that accreted near the Sun and in the gas giants region are mixed together. Terrestrial planets are formed from a truncated disk, except for Mars that formed from embryos that were scattered out of the disk. After a long quiescent period of $\approx$ 700 Myr, Jupiter and Saturn entered in a new resonant motion, driving their orbit and that of Uranus and Neptune into chaotic motions with close encounters between the giants (Nice model). This destabilized the outer planetesimal disk and the asteroid belt, scattering objects all over the Solar System, shaping the asteroid and the Kuiper belts and inducing the Late Heavy Bombardment. This event is the last major event that reshaped the Solar System into what is observed today.

Earth distance. Terrestrial planets formed in that truncated disk to reach their final sizes, except for Mars which formed out of this disk from the scarce planetary embryos that were ejected (Figure 1.1). Following the "Grand Tack model", these gas giants migration occurred early in the Solar System history, within its first million year (Figure 1.1). (2) Then, in a second step called the "Nice model", after a long quiescent period ($\approx$ 700 Myr) an inward migration of Jupiter is caused by resonant motion with Saturn, while the latter, along with Uranus and Neptune, migrate outward (Figure 1.1), conducting to chaotic motions (Tsiganis

et al., 2005; Gomes et al., 2005; Morbidelli et al., 2005). Uranus and Neptune are sent in the massive Kuiper belt, scattering it in all directions, included toward the inner regions. This event resulted in the delivery of the Late Heavy Bombardment (LHB) (Gomes et al., 2005) recorded on the surface of the Moon. Resonant motions between Jupiter and Saturn also ejected objects from the asteroid belt, reducing its mass by a factor of 10. This gas giants migration event is thought to be the last that reshaped the Solar System. It remains mainly unchanged for the 4 billion years to follow. Here the first stage, the "Grand Tack" is of prior interest as it shaped the Asteroid Belt and is responsible for the mixing of dry and hydrous materials.

1.2 Meteorites, messengers from the early Solar System

What remains from the early Solar System, besides the orbital data of the different objects are small bodies stored in the Asteroid Belt. These objects are early-formed rocks that recorded the different events that shaped the Solar System as it is today. Most of these objects were not subject to complex geological history, they remained pristine, meaning that the primitive information they host was not erased. Meteorites thus provide complementary constraints on the early formation and evolution of the Solar System. Due some collision dynamics within the asteroid belt, small chunks of asteroids may be sent in all directions. Some of them may arrive on Earth. What falls on Earth is likely to be biased and not representative of the whole population of asteroids. Nonetheless, this biased sample of rocks is extremely diverse and complicated, and has not delivered all of its secrets yet.

Meteorites bring information about chemistry, timescales and timing of different processes. These data are used as constraints on the numerical simulations, and in turn the latters shed light on the history of some of these meteorites. Back and forth reasonings coupling data from natural samples, numerical models and laboratory experiments to reproduce the formation conditions of natural samples are needed to improve our understanding of the premises of the Solar System.

One of the basics of classification is to try to find characteristics that outline the differences between different members of a population. In meteorites, this characteristic is the differentiation degree, i.e. how well silicate and metallic phases are separated. Differentiation is the process during which metal and silicates are separated to form a metallic core and a rocky mantle. Following this criteria of differentiation degree, three main families of meteorites arise (Figure 1.2), from the least differentiated and most primitive: chondrites in which metal and silicates are mixed together, to the most differentiated: achondrites which are constituted only of metal (iron meteorites) or of silicates (stony meteorites), indicating an efficient separation of both phases. The stony-iron meteorites are also considered as achondrites, however the mixture of silicate and metal in these meteorites is considered to be the result of brecciation, except for pallasites; these objects will not be discussed in the following. The third family is embodied by the primitive achondrites, which constitute an intermediate between chondrites and achondrites, meaning that the differentiation process initiated but stopped before completion. These three families of meteorites are presented in the following, outlining the highlights they provide on the Solar System formation and differentiation.

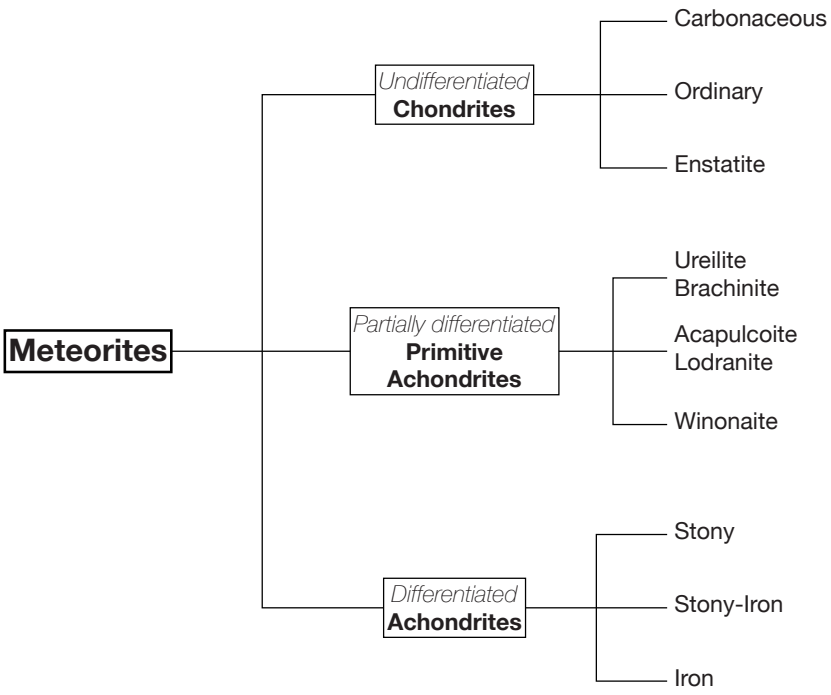

Figure 1.2 – Simplified meteorites classification with emphasis on the differentiation degree of the different objects.

1.2.1 Chondrites, primitive meteorites

Chondrites are among the most primitive objects of the Solar System. They have a particular texture with three main components: Calcium-Aluminum rich Inclusions (CAIs), chondrules and a fine-grained matrix. These components are likely to have formed independently in the protoplanetary disk and recorded the physico-chemical properties of the disk at the location and time of their formation. Hence, they represent the almighty truth for nebular evolution models. Depending on the proportion of each component, bulk chemistry and oxygen isotope signature, different categories of chondrites are defined: carbonaceous, ordinary and enstatite. In a first time, information hosted in each component of chondrites are investigates, then interest is taken to the whole rock to understand why these components that formed in different conditions are aggregated together.

1.2.1.1 Chondritic components and condensation sequences

To understand the formation of meteorites during the cooling of the protoplanetary disk, the condensation sequences can be addressed (Davis and Richter, 2013). This sequence shows that the first condensates, over the range 1800 to 1400 K, are refractory minerals hosting mainly calcium, aluminum and some magnesium (Figure 1.3, inset). These phases correspond to the CAIs, which are refractory inclusions composed of calcium and aluminum rich minerals, such as hibonite ($CaAl_{12}O_{19}$), perovskite ($CaTiO_3$), spinel ($MgAl_2O_4$) and anorthite ($CaMgSi_2O_6$). The high temperature required to form these inclusions along with the

absence of volatile elements suggest that CAIs are likely to be the first condensates that formed in the early Solar System. Dating of these refractory inclusion with lead isotopic system makes these objects the oldest of the Solar System with absolute ages of 4567.18 ± 0.5 Myr (Amelin et al., 2002) or 4568.2 ± 0.3 Myr (Bouvier and Wadhwa, 2010). CAIs formation age is considered as the event dating the beginning of the solid Solar System.

Upon decreasing temperature, condensation sequences show the condensation of metallic phases and less refractory silicates (olivine $(Mg,Fe)_2SiO_4$, pyroxene $(Ca,Mg,Fe)_2Si_2O_6$ and feldspar $(K,Na)AlSi_3O_8$ or $CaAl_2Si_2O_8$, Figure 1.3), forming chondrules (spherical objects with millimeter to centimeter sizes) and the fine-grained matrix. Metallic phases mostly occur under the form of Fe-Ni alloy and / or troilite FeS. Their presence can be easily explained with the condensation sequences (Figure 1.3), although sulfur condensates later and at lower temperature than iron due to its volatility. The presence of troilite in chondrules can then be understood in the framework of the different models that often assume the recycling and mixing of different materials (Zanda, 2004; Connolly and Jones, 2016). Secondary alteration processes may have changed the oxidation degree of the metallic phases, allowing the formation of iron oxides (e.g. magnetite in CI chondrites, King et al., 2015).

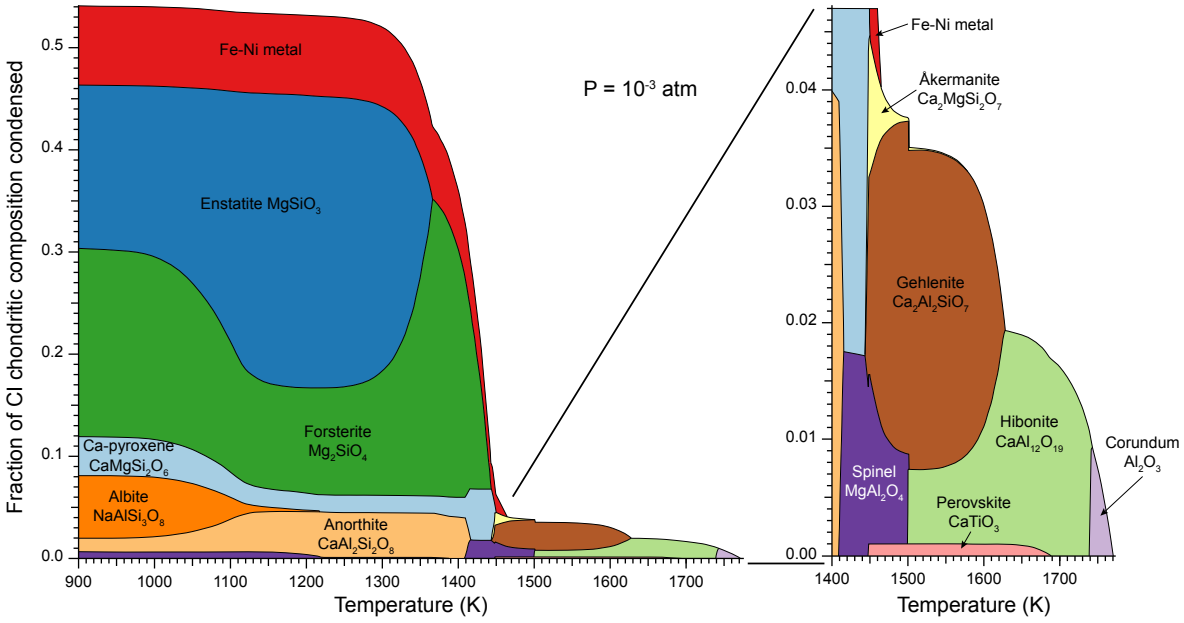

Figure 1.3 – Condensation sequence of a CI chondrite material from Davis and Richter (2013).

The exact formation process of chondrules is still unresolved, many different models exist which will not be developed here (for more information, see Zanda, 2004; Connolly and Jones, 2016, and references therein). Some characteristics are common between the different models: the spherical shape of chondrules indicate that they formed partially or entirely molten and the presence of silicate glass indicate that they were cooled on extremely short timescales. Due to the presence of relict chondrules included in others, multiple formation episodes must have taken place, recycling the previously formed material. The fine-grained matrix of chondrites is volatile-rich. The presence of interstellar organic compounds argues that temperature did not exceed 700 K since their formation (Chambers, 2006). These materials must have been formed in a cold region. Chondrites correspond then to a mixture of materials accreted at

different heliocentric distance. The successive migrations of the gas giant planets are most likely responsible for mixing such different materials.

1.2.1.2 Chondrites as whole rocks

The different compounds building chondrites formed in different regions, at different times and different temperatures. However, they ended together up forming the same material. Relative dating (Pb-Pb and Al-Mg isotopic systems) of chondrules indicate formation ages ranging from 0 to 4 Myr after CAIs (Amelin and Krot, 2007; Villeneuve et al., 2009), with a peak between 1.5 and 3 Myr (Villeneuve et al., 2009). A continuum formation between CAIs and chondrules most likely exist, but CAIs must have survived during all the chondrule formation time before being accreted along with them (detailed information on these processes can be found in Weidenschilling and Cuzzi, 2006; Chambers, 2006). An extended accretion process over time best explains the different compositions and textures of the different chondrite classes. Absolute ages of chondrites parent bodies accretion range from 1.8 Myr to 3.6 Myr after CAIs (Sugiura and Fujiya, 2014).

Mixing CAIs, chondrules and matrix in different proportions and in different conditions gives a whole zoology of chondrites which can be distributed into three classes: carbonaceous, ordinary and enstatite. Carbonaceous chondrites have relatively high matrix abundances, from 35 up to >99 vol% (Weisberg et al., 2006), and host a significant amount of carbonaceous matter. Ordinary chondrites are mainly composed of millimeter sized chondrules, from 60 to 80 vol%, low matrix amount (up to 15 vol%) and scarce CAIs (<1 vol%) (Weisberg et al., 2006). They are classified following their metallicity into H chondrites (high metallicity), L chondrites (low metallicity) and LL chondrites (very low metallicity). Finally, enstatite chondrites have similar volume proportions of CAIs, chondrules and matrix than ordinary chondrites but are defined by a very low oxygen fugacity. Indeed, silicates are mostly magnesian and iron is almost entirely in the metallic state and is found forming alloys with silicon (Weisberg et al., 2006). Enstatite chondrite chondrules are mainly formed by enstatite ($MgSiO_3$). Due to the extreme reducing conditions, sulfide phases are composed of unusual species (e.g. calcium sulfides, magnesium sulfides or even chromium sulfides).

1.2.2 Achondrites

Achondrites are the result of differentiation processes. It depicts a family of meteorites that lost their chondritic texture and have different compositions than chondrites. As a result, most achondrites are either composed of silicates without metal (stony meteorites), or metal without silicates (iron meteorites). However, some of them are still a mixture of metal and silicates (stony-iron meteorites such as pallasites and mesosiderites), but with a refractory mineralogy and a different distribution of metal: it seems gathered and forming a network in opposition to chondrites in which it is finely spread. All these meteorites sample different regions of a differentiated planetesimal. Stony meteorites are representative of the crust or mantle of the body, while iron meteorites sample the core. Pallasites are thought to be representative of the core-mantle boundary, explaining the mixture of iron with refractory minerals. Starting from a chondritic material, differentiation requires heating and melting

of the body to allow metal-silicate separation. Achondrites are representative of the final state differentiation. Igneous processes that occurred erased all information about incipient differentiation and nebular processes. Instead, these meteorites recorded the last event before they were ejected from their parent body, i.e. cooling and core or mantle/crust crystallization.

Slow cooling of iron-nickel alloys at low temperature (1073 to 473 K) allows the exsolution of Ni-poor (kamacite) and Ni-rich (taenite) crystals, forming an alternation of bands known as the Widmanstätten pattern. This exsolution is driven by a diffusion process, making it highly dependent on cooling rate (Goldstein et al., 2009). Hence, determining the properties of Widmanstätten pattern gives information on the cooling rate of iron meteorites. Core cooling rates are on the order of 50 K per million year for most iron meteorites (IIIAB), but can go as high as 4300 K per million year for the IVB group (Chabot and Haack, 2006). From these rates and knowing silicate thermal diffusion, a parent body radius can be calculated, giving relatively small bodies with radii lower than 100 km. Radio-isotopes allow dating of different events that affected these meteorites. An isotopic system of interest to date differentiation is the Hafnium-Tungsten one. Indeed, Hafnium is a lithophile element that will have a tendency to remain in the silicates, while Tungsten has a moderately siderophile behavior and partitions into the forming core. Hafnium has a short-lived isotope, the ^{182}Hf that decays into ^{182}W with a half-life of 8.9 Myr. Once differentiation is complete, all the ^{182}Hf hosted in the silicate mantle decays into ^{182}W, and the metal has a deficit of ^{182}W relative to an undifferentiated material. This isotopic system thus allows the dating of the last metal-silicate equilibrium. All iron meteorites exhibit a deficit of ^{182}W relative to chondrites, indicating accretion and differentiation within 2 Myr after CAIs (Markowski et al., 2006; Kruijer et al., 2014).

Another class of achondrites is only composed of silicates. For instance, the HED (Howardite - Eucrite - Diogenite) clan is thought the be the result of igneous processes that affected asteroid (4) Vesta (e.g. McSween et al., 2011, and references therein). These objects sample the crust of this body, which is composed of basalts, gabbro and ultramafic cumulates, implying large degrees of melting and efficient metal-silicate separation. The HED parent body is thought to have accreted within the first million year after CAIs (based on geochemical evidence (^{53}Mn-^{53}Cr system), Sugiura and Fujiya, 2014) and to have had an extended magmatic activity from 3 Myr to $\approx$ 10 Myr after CAIs (McSween et al., 2011). The homogeneous oxygen isotope signature of the HED clan argues in favor of a large-scale melting of the body (Greenwood et al., 2014).

Achondrites parent bodies accreted before chondrites parent bodies, making the most primitive material younger than the evolved one. This feature is explained by the nature of the heat source at work in the differentiation of these bodies: the decay of short-lived ^{26}Al with a half-life of 0.73 Myr. Early accreted bodies can thus reach high temperatures that allow them to melt to a large extent and makes differentiation complete. Bodies that accreted later do not have enough energy to melt to a large extent or to simply melt, differentiation does not reach advanced states, forming primitive achondrites, or differentiation does not occur at all, forming chondritic materials. The question of the heat source is tackled in more details in section 1.2.4.

1.2.3 Primitive Achondrites

Primitive achondrites are thought to be partial melt residues of a chondritic parent body. As a consequence, these meteorites lost their chondritic texture but kept a primitive composition, close to chondritic values. This family of meteorites is representative of early differentiation stages. It offers images of the incipient metal-silicate separation processes. This is quite valuable to understand the dynamics of the process. Among these meteorites, the winonaite and the acapulcoite-lodranite clan is of particular interest here as shows no secondary processes, i.e. no brecciation, no deformation and low shock degree (Weisberg et al., 2006). Winonaites correspond to a poorly evolved material, with a chondritic mineralogy, some relict chondrules and recrystallized textures. This clan will be discussed in more details in Chapter 6. The acapulcoite-lodranite clan is subdivided into two groups: the acapulcoite and the lodranites. The main difference between both is their differentiation degree, offering images of the differentiation at different stages.

1.2.3.1 The acapulcoite group

The acapulcoites are named after their reference specimen Acapulco, which fell in 1976. This meteorite is composed of feldspar, orhtopyroxene, olivine and Fe-Ni alloy, with minor diopside, chromite, phosphate and troilite (Palme et al., 1981). Looking closely at textures and composition of phases give additional information about the evolution of the rock. Frequent minerals triple junctions at 120° indicate textural equilibrium. Mean grain sizes of 100 up to 500 µm show that this sample is highly recrystallized (Palme et al., 1981). Each mineral phase can be found included in one another, indicating simultaneous growth. Crystals do not show any sign of shock and bubbles are still present, meaning that no extensive deformation applied to the parent body (Palme et al., 1981). In term of composition, Acapulco is very similar to H-type chondrites (Palme et al., 1981). Thermometry based on Fe-Mg partitioning in pyroxene crystals give closure temperatures of 1388 ± 75 K. At such temperatures, silicate should have melted to some extent. Based on the composition of metallic inclusions in orhtopyroxene and olivine, Zipfel et al. (1995) estimated that Acapulco should have reached a peak temperature of 1473 K, corresponding to a silicate melting degree of ≈20%. The melt cooled and crystallized in situ, without moving. However, McCoy et al. (1996) argued that due to the heterogeneity in iron-sulfide blobs composition, this estimate is likely to be overestimated. In addition, the presence of iron-sulfide veins that cross-cut the plagioclase crystals indicate that this silicated phase was solid during the formation of these veins. Hence, on the basis of textural arguments, temperature is not likely to have reached that required for partial melting of the silicates. Rather than no melting at all, other data showed that acapulcoites underwent low melting degree (< 5 vol%). Indeed, Mittlefehldt et al. (1996) showed that a loss of 2-3% partial melt could explain some K and La depletion in Acapulco-like meteorites. An upper bound for acapulcoites can then be set by Monument Draw in which the formation on metallic veins is likely to have required about 4-5 vol% of partial melting (McCoy et al., 1997). Cooling rates measured in metals indicate that Acapulco and Acapulco-like meteorites parent bodies are smaller than H chondrite parent body. Chemical evidences based on oxygen isotopes (Greenwood et al., 2017) show that acapulcoites and H chondrites do not share a similar origin. However the precursor material to acapulcoites seems to have a composition close

to that of H chondrites. Determination of oxygen fugacity yields conditions of 2.3 log units below the iron-wustite (IW) buffer, which is more reducing than H chondrites (1 log unit below the IW buffer, Brett and Sato, 1984).

1.2.3.2 The lodranite group

Lodranites are named after the reference specimen Lodran, which fell on 1868. This meteorite is composed of orthopyroxene, olivine and Fe-Ni alloy with minor diopside, chromite, phosphate and troilite (Bild and Wasson, 1976). Lodranites are depleted in feldspar and troilite in comparison with acapulcoite. Textures show frequent triple junctions at 120°, indicative of textural equilibrium. These meteorites do no seem to have experienced extensive deformation. Mean grain sizes are on the order of 540-700 µm, which is larger than in Acapulco. This feature shows that Lodran experienced a higher temperature peak than Acapulco, or that the parent body remained at its peak temperature longer. Thermometry in Lodran indicates peak temperatures on the order of 1473 K. At such temperatures, a melting degree of $\approx$ 20% is reached. The absence of feldspar in the latter specimen points out an efficient melt extraction that did not occur in the acapulcoite parent bodies. Troilite also seems to be a depleted component in lodranites in comparison to acapulcoite, indicating that silicate melt was extracted along with an iron-sulphide melt. Measured oxygen fugacities in minerals give conditions of 2 log units below the IW buffer, which is quite similar to acapulcoites. However, there is a reverse zoning rim in olivine grains, with the border of crystals depleted in iron with respect to the core. This seems to indicate that a reductive event occurred, causing the exsolution of iron from the rim (Bild and Wasson, 1976).

1.2.3.3 Acapulcoite-Lodranite relation

Acapulcoites and lodranites are representative of partially differentiated meteorites, but indicate different differentiation degrees. Acapulco-like meteorites may have initiated silicate melting, but experienced poor silicate melt extraction. Lodranites melted to a larger extent and are likely to have experienced important melt extraction due to the lack of feldspar. Simultaneously, these meteorites seem to have also lost a sulphide melt. Both groups have similar oxygen isotopes signatures, indicating a close relation between them (Greenwood et al., 2017). Hence, they may have a genetic link, with Lodran-like meteorites being more evolved than the Acapulco-like. Acapulcoite have a composition close to that of H chondrites. However, due to different isotopic signatures (e.g. oxygen isotopes Greenwood et al., 2017, and references therein), this type of chondrite does not seem to be the precursor material.

It is not clear yet whether acapulcoites and lodranites originate from the same parent body (Mittlefehldt et al., 1996). However, if so, the specimens indicate that they underwent different processes at a more localized scale. It seems that their parent bodies accreted 1.3 Myr after CAIs (Sugiura and Fujiya, 2014), which is after the iron meteorites, but before chondrites. Hence, these planetesimals had a lower heating potential, explaining why they did not achieve differentiation. Some studies tried to refine the classification instead of a simple dichotomy. Indeed, there is a whole zoology of intermediates between both endmembers (Acapulco and Lodran) that do not perfectly fit into any categories.

Floss (2000) was one of the first authors who tried to refine the classification, on the basis of trace elements. The partitioning between different samples can be understood in terms of formation and removal of silicate partial melts. Although different degrees of silicate partial melting and melt extraction can explain most samples, some still do not fit in, they appear to be enriched in siderophile and chalcophile elements, requiring also an injection of metal-sulfide melt. The work of Patzer et al. (2004) added an even more refined classification taking into account this chalcophile and siderophile enrichment. It is based on five subtypes including primitive, typical, transitional and enriched acapulcoites on one hand and lodranites on the other hand. Primitive acapulcoites basically correspond to a highly metamophized chondritic material that kept the pristine chondritic composition but lost the texture. Typical acapulcoites differ from the latter due to a lower chalcophile/siderophile ratio, indicative of a partial melting at the Fe-Ni-S eutectic and subsequent loss of the sulfur-rich melt. The transitional acapulcoites represent a more advanced stage that experienced extensive melting and melt extraction to the point that plagioclase are entirely depleted. Metallic phases appear to be enriched at this point. The final step of this sequence correspond to lodranites, residues of partial melting. The strong depletion in potassium, sodium and aluminum along with siderophile and chalcophile elements clearly indicate the loss of two components, a first one of silicate melt mainly composed of feldspar and a second one of sulfur-rich melt. The last subgroup are the enriched acapulcoites. This category is a bit off the classical evolution sequence as it represents a state that trapped silicate melt instead of losing it. Amounts of sulphide and metallic phases are highly heterogeneous from a sample to another.

Assuming that acapulcoites and lodranites originate from the same parent body, its thermal and physical evolution can be modeled. Such study allows to find regions in a body that have similar properties to that of meteorites and hence gives a depth for these meteorites. Depending on studies, different burial depths are found. For instance, based on a simple heat conduction model, Golabek et al. (2014) found a best fit for a parent body with a radius of 25-65 km, an acapulcoite burial depth of 9-19 km and lodranite burial depth of 14-25 km. Considering silicate and metallic melts mobility, Neumann et al. (2018) found a best fit for a larger body with a radius of roughly 260 km and burial depths of 7 km for the acapulcoites and 13 km for the lodranites (these models are more detailed in section 1.4.3). In any cases, acapulcoites and lodranites originate from relatively shallow regions. A single impact could have excavated both acapulcoites and lodranites.

1.2.4 Heat sources for primitive bodies

Meteorites show evidence that their parent bodies heated to a certain extent. Chondrites underwent inefficient heating and did not melt, primitive achondrites suffered partial meting and achondrites experienced very efficient heating that lead them to melt to a large extent. Hence, the early accreted material was subject to heating process that was more efficient than the late-accreted one. This requires a phenomenon that decreases with time. In this aim, two main heating processes may fit: accretional heating due to impacts and decay of radionuclides.

1.2.4.1 Accretional heat

The process of planetary accretion is constituted of the agglomeration of small objects to form a larger one. At the beginning of the Solar System, collisions were widespread. If this process constitutes an efficient heat source, it could explain that achondrites formed before chondrites. From a physical point of view, each agglomeration of small objects can be considered as a collision between them. Each impact brings more energy into the large body and may be a heat source. The energy of such collision depends on the size of the newly formed body and corresponds to the potential energy lost to form the larger body. This energy E_{acc} is given by the following:

$$E_{acc} = \frac{3}{5}\frac{GM^2}{R}\,, \tag{1.1}$$

with G the universal gravitational constant (in $m^3.kg^{-1}.s^{-2}$), M the mass of the body (in kg) and R its radius (in m). With the approximation that all this energy is transformed into heat, Joule's law allows to write the accretional energy as a function of thermodynamic parameters:

$$E_{acc} = MC_p\Delta T\,, \tag{1.2}$$

with C_p the mean calorific capacity of the body (in $J.kg^{-1}.K^{-1}$) and ΔT the increase in temperature (in K) resulting from the collision. A limitation to this calculation is that considering the perfect conservation of the accretional energy, the temperature increases are overestimated, a part of the energy is radiated during the impact. The increase in temperature resulting from the collision ΔT is thus equal to:

$$\Delta T = \frac{3}{5}\frac{GM}{RC_p} = \frac{4\pi}{5}\frac{G\rho R^2}{C_p} \tag{1.3}$$

with ρ the mean density of the body.

The result of such calculation is shown in Figure 1.4. It shows that this process is efficient for large bodies only. The formation of relatively small bodies on the order of a hundred kilometers (like the asteroid 6-Hébé) results only in an increase of a few kelvin degrees, while the formation of bodies larger than 1-Ceres, i.e. with radii greater than 1000 km, causes a temperature increase of $\approx$ 1000 K. Such increment would be necessary to melt silicates and metal, promoting differentiation of these bodies. Hence, small bodies require another heat source to initiate their differentiation.

1.2.4.2 Radionuclides decay

The interior of planetesimals is also heated by the decay of radionuclides. Four of them still contribute to the heat production in Earth: ^{40}K, ^{232}Th, ^{235}U and ^{238}U. However, at the early stages of the protosolar nebula, radionuclides with very short half-lives also contributed to the heating of planetesimals. These extinct radionuclides are ^{26}Al (that decays into ^{26}Mg with a half-life of 0.73 Myr) and ^{60}Fe (that decays into ^{60}Ni with a half-life of 2.62 Myr). As their half-lives are extremely short, they must have been freshly nucleosynthesized when they

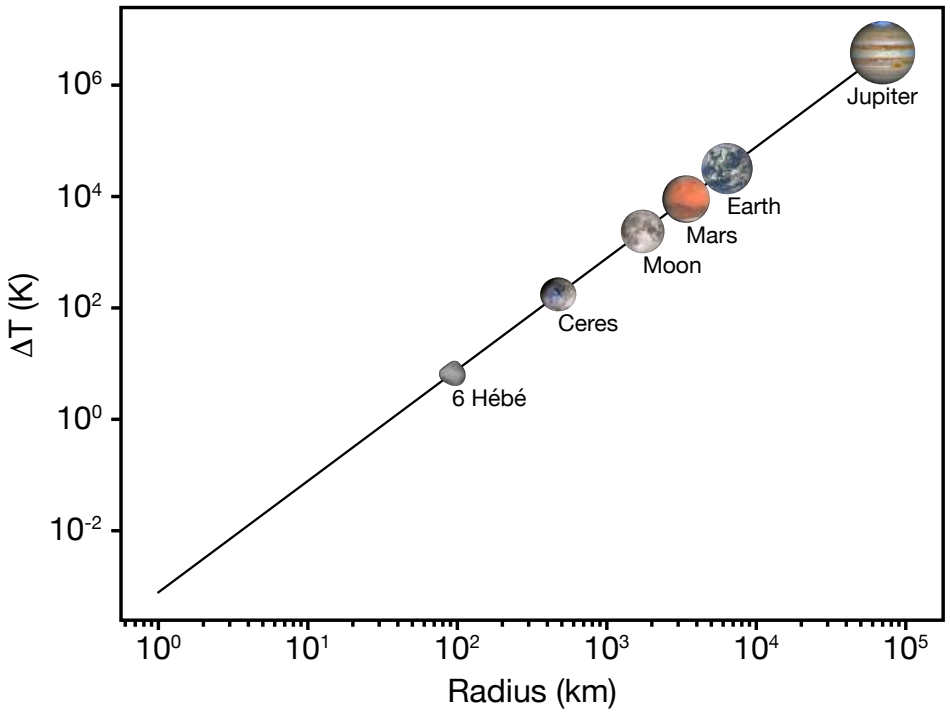

Figure 1.4 – Temperature increase (in K) due to the accretion as a function of the radius of the newly formed body (in km). For this calculation, the mean calorific capacity is taken as 750 $J.kg^{-1}.K^{-1}$ and the mean density as 3500 $kg.m^{-3}$.

were injected into the protosolar disk. Their nucleosynthesis is likely to have occurred into the neighboring stars. The decay of a radionuclide as a function of time follows the law:

$$^{n}\mathrm{X}(t) = {}^{n}\mathrm{X}_0\, 2^{\frac{-t}{t_{1/2}}}\,, \tag{1.4}$$

with $^{n}\mathrm{X}(t)$ the quantity of radionuclide at t time, $^{n}\mathrm{X}_0$ the initial quantity of radionuclide, $t_{1/2}$ the half-life of the radionuclide and t the time.

The quantity of energy produced by the decay of radionuclides at a given time t and per mass unit, noted as $Q_r(t)$ is then:

$$Q_r(t) = \sum_{i=1} Q_{r_i}(0) \exp\left(-\frac{t}{\tau_i}\right)\,. \tag{1.5}$$

With:

$$Q_{r_i}(0) = {}^{n}\mathrm{X}_i/\mathrm{X}_i \omega_i \frac{\mathcal{N}_A}{M_i} E_i\,, \tag{1.6}$$

where $^{n}\mathrm{X}_i/\mathrm{X}_i$ is the fraction of isotope $^{n}X_i$ of element X_i, ω_i is the mass fraction of element X_i in the considered material and M_i its molar mass, $\mathcal{N}_A$ is Avogadro's constant, E_i the energy produced by radioactive decay and τ_i the inverse to the decay constant, which is also equal to $t_{1/2}/\ln(2)$.

Then the heat power per mass unit $\dot{Q}_r(t)$ is given derivating the previous equation, yielding:

Table 1.1 – Physical parameters of radioisotopes that contribute to heating the interior of planetesimals. ^{n}X is the isotope n of element X and ω is its mass fraction in CI type chondrites.

^{n}X	$t_{1/2}$ (year)	E (MeV *)	^{n}X/X initial	ω initial
^{26}Al	7.17×10^5	3.16	5×10^{-5}	8.6×10^{-3}
^{40}K	1.277×10^9	1.33	1.53×10^{-3}	5.6×10^{-4}
^{60}Fe	2.620×10^6	2.71	1×10^{-8}	1.82×10^{-1}
^{232}Th	1.405×10^{10}	42.7	1	3.63×10^{-8}
^{235}U	7.038×10^8	46.0	0.243	2.18×10^{-8}
^{238}U	4.468×10^9	51.7	0.757	2.18×10^{-8}

* 1 MeV $= 1.602 \times 10^{-13}$ J

$$\dot{Q}_r(t) = \sum_{i=1} \frac{Q_{r_i}(0)}{\tau_i} \exp\left(-\frac{t}{\tau_i}\right) . \tag{1.7}$$

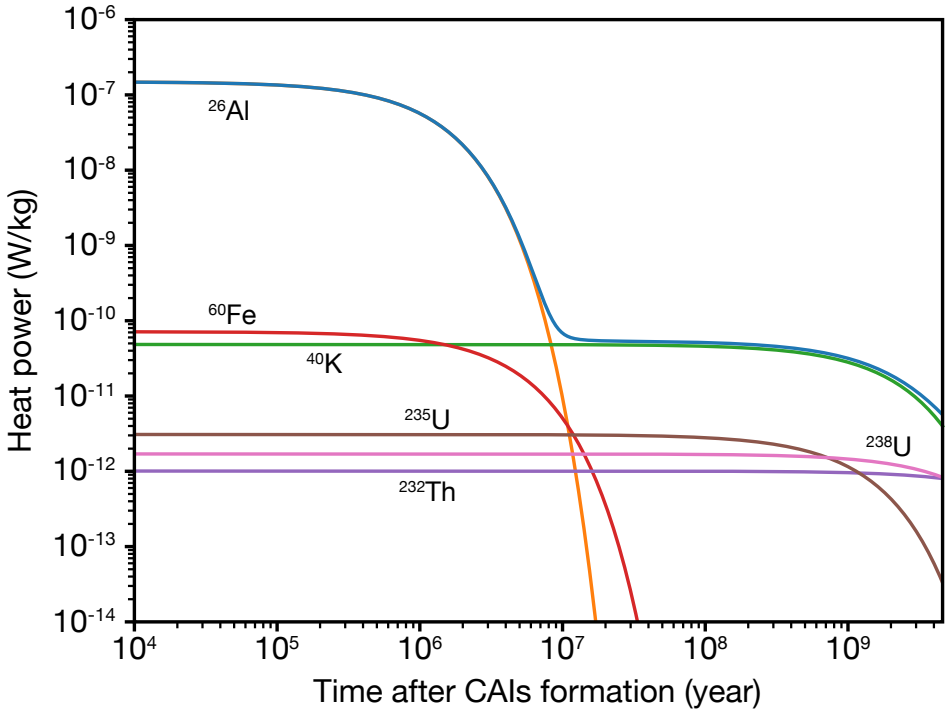

Figure 1.5 – Heat power per mass unit generated from the decay of radionuclides in a CI chondritic material as a function of time after the formation of CAIs. The blue curve represents the total power.

Plotting the heat power per mass unit as a function of time after CAIs formation (Figure 1.5) indicates that the main heat source at the very beginning of the Solar System is ^{26}Al. However as this element has an extremely short half-life (0.73 Myr), only the early formed planetesimals (within the first million years) are heated efficiently by this element. The other most efficient heating radionuclides, have a heat power that is at least three orders of magnitude lower than that of ^{26}Al. Soon after ^{26}Al has become negligible, ^{40}K takes over and dominates the heat production, which is still the case today. Assuming a simple conductive regime for heat extraction, the core temperature, i.e. the maximum temperature, of a body

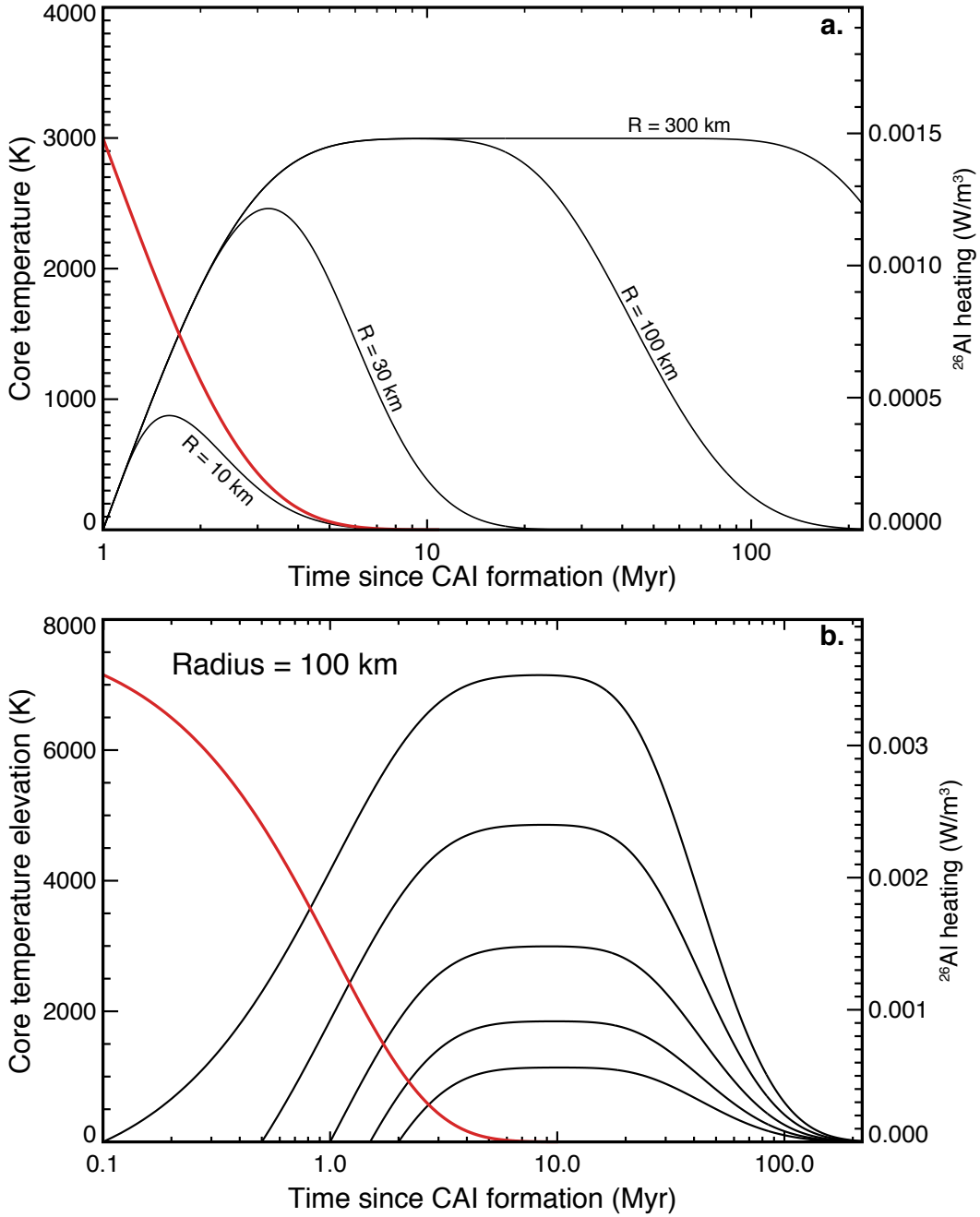

Figure 1.6 – Core temperature as a function of time since CAIs formation for (a) different radii and an accretion date of 1 Myr after CAIS and (b) different accretion time for a body with a radius of 100 km. Red curves represent the heat power per volume unit due to ^{26}Al decay. (Marc Monnereau, personal communication)

can be calculated solving the heat equation. The results of such calculation are shown on figure 1.6 for different radii (1.6a.) and different accretion dates (1.6b.). Increasing the radius of a body increases its core temperature as there is more total heat power available. However, for large radii, there is a maximum temperature that cannot be exceeded at a given accretion date, radius only affects the cooling time, (Figure 1.6a). The effect of the accretion date is

quite straightforward: the earliest the accretion, the more radionuclides are available to decay and more heat power per mass unit is available, increasing the core temperature (Figure 1.6 b.). It is to note that these calculation only consider conductive heat dissipation and no convective processes. Hence the obtained temperature can be overestimated, especially in the case of extremely high values from 3000 to 7000 K at which the silicates are entirely molten (melting temperature of pure forsterite $\approx$ 2160 K) and may also be vaporized. What should be emphasized from these calculations are the effects of varying the radii, the larger the hotter, and accretion dates, the earlier the hotter, and that the bodies that accreted later than $\approx$ 2 Myr after CAIs should not have heated enough to allow extensive melting.

Natural samples formed at times that allowed them to reach different differentiation degree. Iron meteorites and achondrites formed early (accretion within 1 Myr after CAIs), at this time the quantity of ^{26}Al is still high and the planetesimals can reach high temperatures. Hence, most of the bodies were molten and metal-silicate segregation could occur easily. On the contrary, chondrites accreted later ($\approx$ 3 Myr after CAIs), their heating power is a few order of magnitude lower than that of achondrites, explaining why they experienced almost no melting of the silicates. Primitive achondrites accreted in between these two endmembers, initiating partial melting of both silicates and metallic phases, but there was not enough heat power to reach large melting degrees. However, the question remains: is this melting degree enough to initiate differentiation? In other words, is it enough to make the silicate and metallic phases mobile?

1.3 General approach on interconnection thresholds and dihedral angles in two-phases systems

Differentiation mechanisms require that both silicate and iron-sulfide melts are mobile to be able to segregate. Both molten phases must then form interconnected networks to be able to segregate.

1.3.1 General concept

Conceptually, a phase forms an interconnected network as soon as its volume fraction exceeds a critical value called the interconnection threshold. This threshold is the reflect of a process of interfacial energy minimization. In a system composed of different phases, each phase has an interfacial energy with respect to another. As in all natural systems, it will tend to have the lowest energy budget possible, minimizing the contact surface between phases of high energetic cost and increasing the contact surface between those of low energetic cost. At the small-scale, this minimization process is reflected by dihedral angles, which is the angle of a phase at a triple junction.

In a polyphased system, a triple junction can be represented as in Figure 1.7 (a). Dihedral angles are noted as θ with the phase in underscore, e.g. θ_1 for phase 1 dihedral angle. Interfacial energies are noted as γ with the two phases forming the interface in underscore, e.g. γ_{12} for the phase 1 - phase 2 interfacial energy.

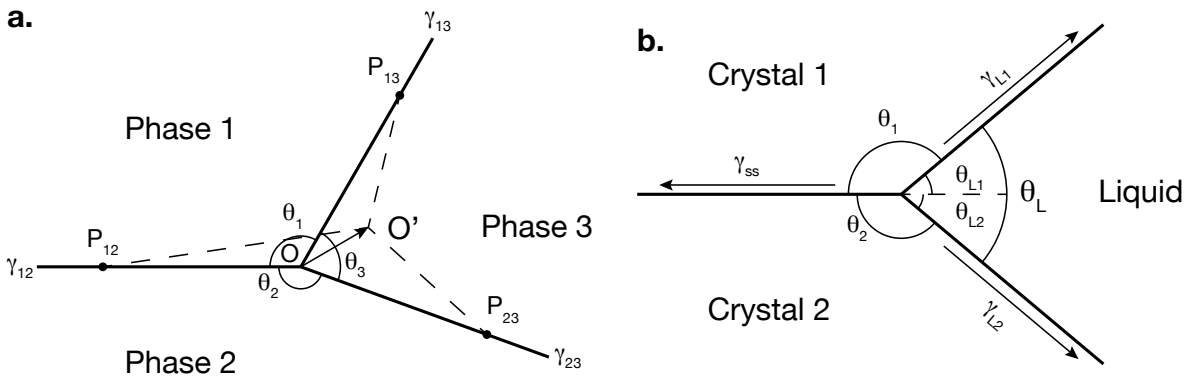

Figure 1.7 – Sketch showing the 2D organisation of a triple junction in a three-phase system (a) and in a two-phase system (b), between two solid crystals and a liquid. θ are dihedral angles and γ are interfacial energies. γ_{SS} stands for the solid-solid interfacial energy and θ_L for the liquid dihedral angle.

For a given triple junction, the minimum energy budget can be calculated looking at the effect of an infinitesimal displacement of the junction line in any direction (O $\rightarrow$ O') (Laporte and Provost, 2000). A small variation of interfacial energy δE would then result from replacing the interfaces OP_{12}, OP_{13} and OP_{23} by $O'P_{12}$, $O'P_{13}$ and $O'P_{23}$. In the case of isotropic interfaces, this would give:

$$\delta E = \sum \gamma_{ij} \left(O'P_{ij} - OP_{ij} \right) , \tag{1.8}$$

Indices $_{ij}$ cover the three interfacial energies $_{12}$, $_{13}$ and $_{23}$. A first order approximation for $O'P_{ij}$ would be $O'P_{ij} \approx OP_{ij} - \overrightarrow{u_{ij}} \cdot \overrightarrow{OO'}$, giving :

$$\delta E = - \left(\sum \gamma_{ij} \overrightarrow{u_{ij}} \right) \cdot \overrightarrow{OO'} , \tag{1.9}$$

with $\overrightarrow{u_{ij}}$ the unit vector along ij interface.

The condition for textural equilibrium is $\delta E = 0$, then giving:

$$\gamma_{12} \overrightarrow{u_{12}} + \gamma_{13} \overrightarrow{u_{13}} + \gamma_{23} \overrightarrow{u_{23}} = \overrightarrow{0} , \tag{1.10}$$

Projecting each unitary vector in a direct orthonormed xy system gives:

$$\begin{cases} \overrightarrow{u_{12}} = \begin{pmatrix} -1 \\ 0 \end{pmatrix} \\ \overrightarrow{u_{13}} = \begin{pmatrix} -\cos(\theta_1) \\ \sin(\theta_1) \end{pmatrix} \\ \overrightarrow{u_{23}} = \begin{pmatrix} -\cos(\theta_2) \\ -\sin(\theta_2) \end{pmatrix} \end{cases} \tag{1.11}$$

Which yields the following set of equations:

$$\begin{cases} \gamma_{13} \cos(\theta_1) + \gamma_{23} \cos(\theta_2) = -\gamma_{12} \\ \gamma_{13} \sin(\theta_1) - \gamma_{23} \sin(\theta_2) = 0 \end{cases} \tag{1.12}$$

Producing the equation that dictates the geometry at a triple junction:

$$\frac{\gamma_{12}}{\sin(\theta_3)} = \frac{\gamma_{13}}{\sin(\theta_2)} = \frac{\gamma_{23}}{\sin(\theta_1)}\,. \tag{1.13}$$

In a two phase system with a triple junction between a melt and two crystals of the same mineral species, as in Figure 1.7 (b), equation 1.13 can be simplified assuming that due to crystalline isotropy $\gamma_{L1} = \gamma_{L2} = \gamma_{SL}$, $\theta_1 = \theta_2$ and $\theta_{L1} = \theta_{L2} = \frac{\theta_L}{2}$. This gives the following:

$$2\cos\left(\frac{\theta_L}{2}\right) = \frac{\gamma_{SS}}{\gamma_{SL}}\,. \tag{1.14}$$

Equation 1.14 links dihedral angle to interfacial energies in a two-phase system. This equation only applies in the case of a perfect isotropic crystal at textural equilibrium. If these conditions are validated, equation 1.14 allows the prediction of small-scale geometry from the konwledge of interfacial energies or dihedral angle. The consideration of anisotropic system is more complicated as equations require a parameter called the anisotropic factor, varying between 0 and 1 (Laporte and Provost, 2000). This factor is poorly constrained, thus for the sake of simplicity, the assumption of an isotropic system is often made.

The total wetting of grain boundaries requires the replacement of all crystal-crystal interfaces by melt-crystal interfaces. In other term, a single crystal-crystal interface is replaced by two melt-crystal interfaces. In order for this change to be energetically favorable, the condition is:

$$2\gamma_{SL} \leq \gamma_{SS}\,. \tag{1.15}$$

Looking at equation 1.14 shows that this condition is only reached for a dihedral angle of 0°, allowing to reach equality between the two terms. For dihedral angle $0° < \theta \leq 60°$, solid-solid interfaces exist and represent a stable configuration; the melt forms an interconnected network but does not wet entirely the grain boundaries. However, for $\theta > 60°$ a minimum melt fraction is required to achieve interconnection, the interconnection threshold.

One can already guess that the knowledge of dihedral angle allows the prediction of the interconnection threshold in a two-phase systems. The study of Wray (1976) was the first one to derive an analytic equation to predict the interconnection threshold as a function of dihedral angle. The equation is the following:

$$\phi_c = \frac{\sqrt{3}}{24}\left(\frac{\sqrt{3\mu+1}+1}{\mu}\right)^3\left[f(\mu) + g(\mu) + \frac{\sqrt{2}}{3}\left(\sqrt{3\mu+1}-1\right)\right], \tag{1.16}$$

With:

$$\begin{cases} \mu = \frac{1-3\cos(\theta)}{1+\cos(\theta)} \\ f(\mu) = \sqrt{2}\,(\mu+3)^{3/2}\left(\arctan\left(\sqrt{\frac{3\mu+1}{\mu+3}} - \frac{\pi}{6}\right)\right) \\ g(\mu) = (3\mu+7)\left(\arctan\frac{\sqrt{2}}{2} - \arctan\sqrt{\frac{3\mu+1}{2}}\right) \end{cases} \tag{1.17}$$

If the dihedral angle is $\leq 60°$, the melt theoretically forms an interconnected network, even for an infinitesimal volume. Then, for dihedral angles greater than 60°, if the melt

fraction is below the interconnection threshold, the melt occurs as isolated pockets at grain corners, while if the melt fraction exceeds the threshold, then the melt forms an interconnected network. Figure 1.8 red curve illustrates this behavior following equation 1.16. It is to note that equation 1.16 is an approximation for values of interconnection threshold as it assumes crystals with a tetrakaidecahedral shape and the tetrahedral symmetry. However, Figure 1.8 (red curve) still shows that the interconnection threshold increases rapidly with increasing dihedral angle, from 0.6 vol.% at $\theta = 60°$ to 27.8 vol.% at $\theta = 180°$.

1.3.2 Distribution of apparent dihedral angles

Numerical models of dihedral angles to address the sectionning effects during measurement allow a better understanding of the statistics requirement to have accurate values. In turn, the modeling of percolative networks gave insights into the dynamics of melt extraction and the role of interfacial energies. Both approach are reported in the following.

Dihedral angles are measured on a polished 2D section of a sample. Measurements should be repeated on a succession of at least a hundred different junctions to have a relevant statistical population. These measured angle distributions are called the apparent distributions, while the value of the dihedral angle in the 3D volume is called the true dihedral angle. Jurewicz and Jurewicz (1986) conducted a study to model apparent dihedral angle populations and compare them with true dihedral angle ones. It appeared that the true dihedral angle can be determined from the median of the apparent distribution. True dihedral angle distribution can be fitted using a Gaussian distribution centered on the median value of the apparent distribution. Even though this Gaussian fit seems an extremely simple solution, this simple function provides a really good approximation.

The Gaussian approximation is only valid for a single true dihedral angle. If the system is anisotropic, it is likely that different true dihedral angles exist, depending on crystal orientation at triple junctions. Jurewicz and Jurewicz (1986) explored the case of two true dihedral angles and showed that the resulting differential distributions become asymmetric. The two true dihedral angles can be determined as long as they are sufficiently different in size, i.e. greater than 10°. If the difference is lower than 10°, the angle distribution is likely to appear unimodal and the theoretical Gaussian fit may provide a good approximation with a large standard deviation, but the two angles would be indistinguishable; although it might be a question of the resolution at which dihedral angles are measured.

1.3.3 Interconnection threshold and hysteresis effects

Wray (1976) assumed truncated octahedra shaped crystals and tetrahedra shaped melt pockets at grain corners. A recent study (Ghanbarzadeh et al., 2017) reestimated the interconnection threshold as a function of crystal shape from numerical simulations. They explored the case of truncated octahedra (i.e. tetrakaidecahedra) and irregular grains, the shape of the melt pocket is not constrained (Figure 1.8). In natural samples minerals are more likely to have irregular shapes, hence this shape is taken as the most representative of Nature. Wray's analytical formula is shown to overestimate the interconnection threshold for $\theta < 70°$. Unfor-

tunately, simulations of Ghanbarzadeh et al. (2017) go only up to 120°, and the comparison with high values of dihedral angles is unavailable. However, in the range $70° < \theta < 120°$, Wray's analytical formula and simulation with regular truncated octahedra have extremely close behaviors. These two trends underestimates the interconnection threshold up to almost a factor of 2 at $\theta = 120°$ in comparison to irregular grains (Figure 1.8).

Ghanbarzadeh et al. (2017) also investigated the dynamics of melt removal once it forms a network. They showed that upon extracting, not only the melt fraction exceeding the interconnection threshold is removed, but almost all of it at the exception of a small fraction that remains trapped in the percolative network irregularities. This small fraction, called the trapping threshold, depends poorly on dihedral angles (green curve in Figure 1.8) and is about a few percent ($\approx$ 1-2 %). This indicates a hysteresis in connectivity that allows an efficient extraction of a melt once an interconnected network is formed.

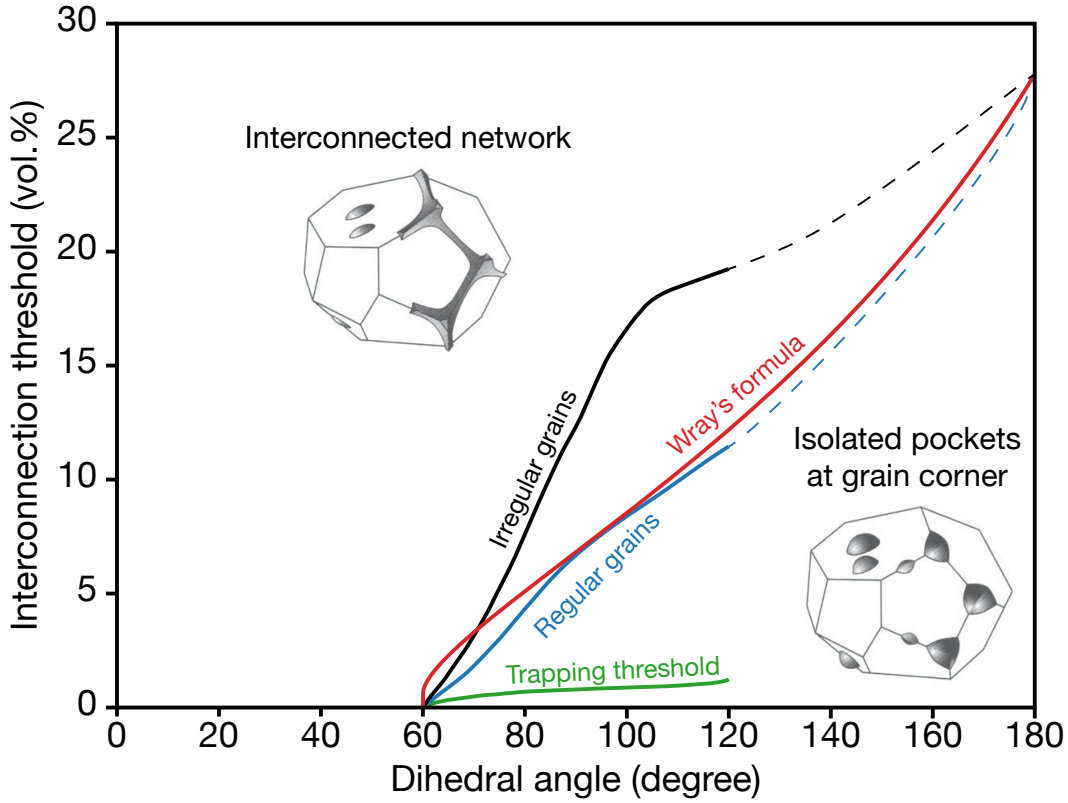

Figure 1.8 – Interconnection threshold as a function of dihedral angle for tetrakaidecahedra or irregular shaped crystals. The analytical solution of Wray (1976) is represented in red. The trapping threshold corresponds to the green curve. Dashed lines represent extrapolation of the numerical simulations to higher dihedral angles. This plot is adapted from Laporte and Provost (2000); Ghanbarzadeh et al. (2017).

At the scale of a planetesimal, percolative core formation is possible given that the planetesimal has a metal content high enough to allow the formation of an interconnected network. Once percolation onsets, all the metal but the trapped fraction is extracted. Hence, it is likely that differentiation can occur on partially molten planetesimals and may explain the formation of Primitive Achondrites.

1.3.4 Dihedral angle measurement and crystalline anisotropy

Studies on the microstructure of two-phase samples, e.g. silicate melt in an olivine matrix, gave a better understanding on the important parameters that govern the equilibrium geometries in samples, how to properly measure dihedral angles or even on setting interconnection threshold values. Cmíral et al. (1998) studied the equilibrium geometries of olivine-basalt samples with high resolution Transmission Electron Microscopy (TEM). Authors report extremely low values of the melt dihedral angle, ranging from 0° to 10°, while previous study typically gave values of $\approx 50°$ (see Laporte and Provost, 2000, for a complete review). Cmíral et al. (1998) argued that this gap is likely to be due to the different magnifications at which dihedral angles were measured, as their high-resolution TEM study allowed the imaging a thin melt channels of a few tenth of nanometers. Hence, accurate measurements of dihedral angles require high magnification. Unfortunately, in most dihedral angle studies, magnification is not specified, thus it is difficult to assess the reliability of the data.

The TEM study of Cmíral et al. (1998) also reports for a high anisotropy behavior of olivine. Indeed, olivine crystals exhibit planar faces called F-faces. Dihedral angles of the basalt measured at F-faces bearing triple junctions are higher from 10° to 30° than the rest of the population. Even though F-faces bearing triple junctions are scarce, it clearly indicates that the classic equation between dihedral angle and interfacial energies (equation 1.14) cannot be applied on the whole set of measurements. Olivine exhibits different crystal planes with different interfacial energies. This behavior is thus reflected in different dihedral angle populations. Wanamaker and Kohlstedt (1991) and Jung and Waff (1998) also reported different interfacial energies among the different crystal planes.

Olivine crystals are widely known as anisotropic. However to the best of my knowledge, no study quantified the effect of such anisotropy on interfacial energies, only sorting of these energies are reported (Wanamaker and Kohlstedt, 1991; Jung and Waff, 1998). Most dihedral angle studies chose to consider olivine crystals as isotropic for the sake of simplicity, and $\gamma_{Ol-Melt}$ is often set to 0.5 ± 0.2 J.m^{-2} (Cooper and Kohlstedt, 1982).

1.3.5 Parameters controlling interconnection threshold

Interconnection threshold varies from a phase to another but also with composition. Pure iron is a phase that has a relatively high dihedral angle with olivine (Ballhaus and Ellis, 1996; Shannon and Agee, 1996), on the order of 130°, corresponding to an interconnection threshold of ≈ 15 vol.% (estimated with Wray's equation 1.16). Such a high value precludes an efficient percolation of the metal. One way to reduce the dihedral angle of a phase is to change its composition. Indeed, experimental studies (Ballhaus and Ellis, 1996; Shannon and Agee, 1996; Gaetani and Grove, 1999; Holzheid et al., 2000; Rose and Brenan, 2001) proved that forming iron alloys with light elements, such as sulfur or oxygen, reduces its dihedral angles. A general trend indicates that dihedral angle decreases with increasing the total anions to total cations ratio: Holzheid et al. (2000) proposed a compilation of all data available and a linear relation seems to appear between the anion to cation ratio and dihedral angle, from $\theta = 110°$ at $\frac{\text{anion}}{\text{cation}} = 0.3$ to $\theta = 80°$ at $\frac{\text{anion}}{\text{cation}} = 1$. An updated version of such compilation is shown in Figure 1.9. Although the broad trend proposed by Holzheid et al. (2000) seems

to fit with most data, some are way out of the range. Different effects may result in such dispersion. Temperature and pressure may have an impact, as suggested by Guignard et al. (2016); Terasaki et al. (2008). However, no clear trend seems to come out over the broad range of temperature and pressure illustrated in Figure 1.9. Another important parameter to take into account is the magnification at which dihedral angles are measured. Indeed, as showed by Cmíral et al. (1998), high magnification images allow imaging thin melt films or channels between grain that change the value of the measured dihedral angle. Although, very oxidized or sulfur-enriched compositions (high anions to cations ratio) allow reaching dihedral angles lower than 60°, such extreme composition are not realistic with respect to the composition of chondrites (7 wt% of sulfur content in the metallic subsystem for H chondrites Wasson and Kallemeyn, 1988).

In comparison with the trend proposed by Holzheid et al. (2000), Rose and Brenan (2001) studied the wetting properties of iron alloys with oxygen and proposed an exponential decrease of the dihedral angle as a function of the oxygen content. The largest change occurs from 0 to 5 mol.% of oxygen, with the angle shifting from 90 to 60°. then for larger contents of oxygen, the decrease is much smoother, with a loss of only 10° up to 35 mol% of oxygen. Results of Terasaki et al. (2005, 2007) on Fe-O-S liquids within a perovskite, olivine or ringwoodite matrix seem to support this idea.

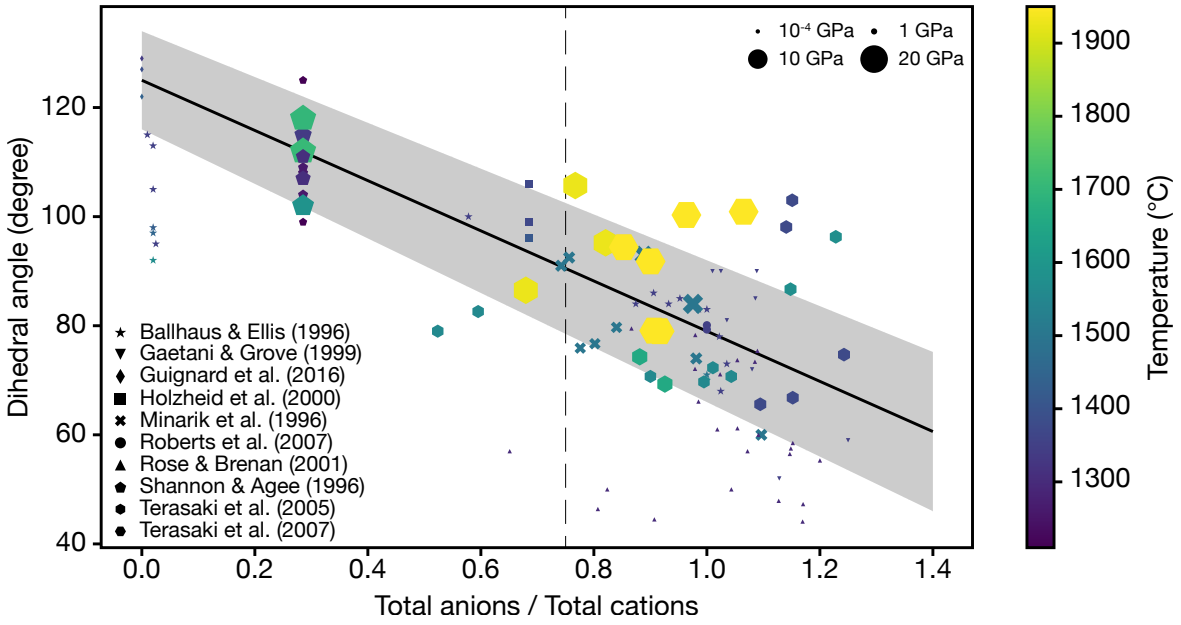

Figure 1.9 – Dihedral angle as a function of the total anions to total cations ratio. This data compilation has been updated since Holzheid et al. (2000). Data were taken from Ballhaus and Ellis (1996); Gaetani and Grove (1999); Guignard et al. (2016); Holzheid et al. (2000); Minarik et al. (1996); Roberts et al. (2007); Rose and Brenan (2001); Shannon and Agee (1996); Terasaki et al. (2005, 2007). The thin dashed line represent the Fe-FeS eutectic composition at 1 bar. With increasing pressure, the eutectic is likely to be depleted in sulfur, shifting this dashed line toward lower anions to cations ratios, e.g. 0.56 at 10 GPa (Buono and Walker, 2011).

Interconnection thresholds can be determined with two different techniques. The first one is from dihedral angle measurements, assuming that the considered ϕ_c vs θ trend considered is correct. The second one is from electrical conductivity measurements during experiments.

The idea is quite simple: when metal forms a network, the electrical conductivity of the sample is much greater than if the metal forms isolated beads. Using the first method with data on a Fe-FeS eutectic composition (Holzheid et al., 2000) gives $\phi_c = 5$ vol.% (Wray's formula equation 1.16) or $\phi_c = 7$ vol.% (Ghanbarzadeh et al., 2017) for $\theta = 80°$, and $\phi_c = 10$ vol.% (Wray's formula equation 1.16) or $\phi_c = 20$ vol.% (Ghanbarzadeh et al., 2017) for $\theta = 110°$. Pure iron dihedral angles were measured by Guignard et al. (2016) who proposed values of $\theta = 120 - 130°$. This would correspond to an interconnection threshold varying between 12 vol.% using Wray's formula (equation 1.16) and ≈ 20 vol.% using Ghanbarzadeh et al. (2017) simulations. The second method using electrical conductivity measurements does not require any $\phi_c - \theta$ dependence. Yoshino et al. (2003) determined interconnection thresholds for the Fe-S eutectic in the range 3-6 vol.%, Watson and Roberts (2011) estimated higher values on the order of 10 vol.%, while Bagdassarov et al. (2009a) proposed a much higher value of 17.5 vol.%. Interconnection threshold determined by Yoshino et al. (2003); Watson and Roberts (2011) are in agreement with dihedral angle values determined for Fe-FeS eutectic compositions, in opposition with the high value of Bagdassarov et al. (2009a). Literature data show huge discrepancies, without finding any agreement to explain the spread; a different approach may be necessary to reconcile these datasets. Hence, interconnection thresholds remain poorly constrained; this question will be addressed as a part of this PhD study.

1.4 Metal-silicate differentiation and small bodies evolution

Once the interconnection threshold exceeded, the metallic phases form a network and are able to migrate. However, whether that network can be mobile or not depends on physical parameters of the planetesimal. At the first order, its mobility depends on the accretion date of the body and thus its heating potential: a formed network is likely to be more mobile when molten. However heating potential also goes with silicate melting degree, the more silicate melt, the less viscous is silicate matrix, facilitating the extraction of the metallic network. As the silicate melt has an interconnection threshold which is almost null, whether this melt may in turn be mobile or not must be determined; its mobility changes drastically the fate of the metal, switching from a scenario with relatively high melt contents to depleted one. Besides, as the silicate melt hosts most of the heat source (^{26}Al), its extraction would "freeze" the inner regions. This part aims at conceptualizing the metal-silicate segregation problem, first with a determination of some physical parameters of a planetesimal, such as pressure and gravity, then the silicate melt mobility is addressed along with the consequences on metal mobility, finally a review of metal-silicate differentiation models of small bodies will be drawn.

1.4.1 Gravity and pressure of early accreted bodies

Two important parameters to conceptualize these bodies are their gravity field and pressure profile. For a spherical body, the gravity profile along the radius is:

$$g(r) = \frac{4\pi G}{r^2} \int_{r=0}^{r} \rho(r) r^2 \mathrm{d}r \,, \tag{1.18}$$

with G the universal gravitational constant and ρ the density (in kg.m^{-3}). In the case of small planetesimal, density can be considered constant along the radius, yielding $g(r)$ for $r \leq R$:

$$g(r) = 4\pi G\rho r\,. \tag{1.19}$$

Then, pressure is:

$$P(r) = \frac{2}{3}\pi G\rho^2 \left(R^2 - r^2\right)\,. \tag{1.20}$$

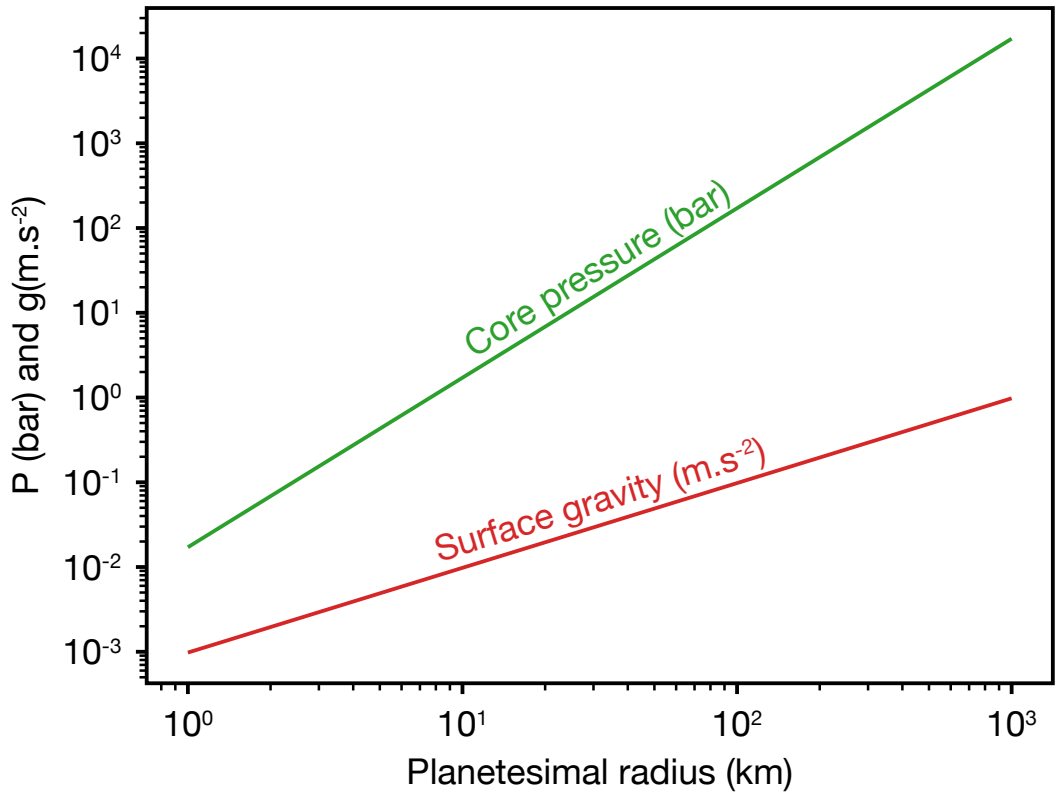

Figure 1.10 – Core pressure (green curve) and surface gravity (red curve) as a function of the planetesimal radius. Density is taken to be 3500 kg.m^{-3}.

Results of this calculation are shown on Figure 1.10 for a density of ordinary chondrites $\rho = 3500$ kg.m^{-3} (e.g. Britt and Consolmagno, 2003). Surface gravity range from 10^{-3} to ≈ 1 m.s^{-2} for a body with a radius ranging from 1 to 1000 km. This huge variation causes also a great shift in pressure, from 10^{-1} bar for a 1 km plantesimal to a few GPa for a large body of 1000 km. A planetesimal with a radius of at least 300 km is necessary to reach pressures greater than 1 GPa. Parent bodies of primitive achondrites are not thought to have radii greater than 300 km, thus density should not affected by pressure effects, and the assumption of a constant value in an undifferentiated body is valid. Equation 1.19 is used in the following to calculate surface gravity.

1.4.2 The question of silicate melt mobility

1.4.2.1 Modeling the silicate melt migration

Through different models, the parameters controlling the efficiency of silicate melt migration were determined to be the accretion date, grain size, size of the body and viscosities of both the silicate melt and the solid silicate matrix (Moskovitz and Gaidos, 2011; Mizzon, 2015; Lichtenberg et al., 2019).

The study of Moskovitz and Gaidos (2011) shows that for bodies with radii on the order of 100 km and low silicate melt viscosities (< 1 Pa.s), migration occurs on a time-scale similar to the half-life of ^{26}Al. The relocation of the heat source then reduces the internal peak temperature of the body and, as a consequence, the maximum silicate melting degree. Depending on the viscosity of the melt and the grain size of the matrix, a silicate melting degree of ≈ 27 % can be reached. Upon removal of the melt, the inner regions of the body are composed of a refractory silicate residue (depleted in feldspar) and of the metallic phases. The upward melt migration makes the crust enriched in ^{26}Al and allows further melting if the body accreted within 2 Myr after CAIs. However, the inner regions of the body are depleted in ^{26}Al, freezing its thermal evolution, unless the decay of short-lived ^{60}Fe is in turn powerful enough to allow further melting. Although this solution may seem a good alternative to reach larger melting degrees, Quitté et al. (2010) showed that there are large heterogeneities in the distribution of ^{60}Fe in the early solar system, making its contribution to internal heating largely uncertain. In addition, recent measurements of the initial abundance of ^{60}Fe/^{56}Fe in the early solar system (Trappitsch et al., 2018) indicate that this ratio was extremely low, making the contribution ^{60}Fe as a heat more than ambiguous.

Lichtenberg et al. (2019) argued that, for fixed radius (60 km), grain-size of the silicate matrix is the main parameter controlling the migration of silicate melt. This study calculated that at relatively low melt fraction, e.g. ≈ 15 vol.%, grain sizes have to reach at least 1 mm so that the melt can effectively extracted. For lower grain-sizes, they found that only melts with a high density contrast with respect to the solid matrix are able to migrate (e.g. reduced melts with composition close to the enstatite chondrite compositions). However, natural samples hardly exhibit millimeter sized grains. Besides, following the study of Moskovitz and Gaidos (2011), it would appear that for larger radii, the grain size required to allow efficient melt migration decreases drastically. Based on a simplified chemical model (idealized binary model for each mineral species, i.e. olivine, feldspar and pyroxene), Lichtenberg et al. (2019) shows that an efficient melt segregation leads to a chemical stratification of the body, with a crust enriched in low melting temperature phases, while the mantle concentrated the refractory phases.

A similar conclusion was reached by Mizzon (2015) who used a much more elegant modelization of the silicate melting, based on a ternary diagram (Olivine-Anorthite-Silica). The author showed that upon successive fractionate melting (due to efficient melt migration) and crystallization, a vertical chemical stratification settles with the refractory materials that remained buried in the inner parts of the planetesimal while the fusible migrated toward the shallow regions. For a sufficiently large body (≈ 200 km), the resulting structure corresponds to an onion-shell with an outer crust of eucrites, an inner crust of diogenites and an olivine-

rich mantle which is extremely close to the structure of (4) Vesta. The effects of grain-sizes of the matrix and viscosity of both the silicate melt and matrix are also found to have a great influence on the time-scale of silicate melt migration. Indeed, at a given grain-size and planetesimal radius, low melt and matrix viscosities reduce the migration time.

These different models highlight successively the importance of each parameter but no clear systematics seem to come out. In this aim, Marc Monnereau derived compaction equations to calculate the migration time as a function of different sets of parameters: radius, grain size and viscosities. This formalism is described in the following.

1.4.2.2 Theoretical considerations

Planetesimals that accreted within the first million years after CAIs are likely to have reached temperatures high enough to allow substantial melting of the silicates (figure 1.6b.). Whether the silicate melt is mobile or not depends on two competing processes. On one hand the motion of the fluid in a porous matrix due to Darcy flow and on the other the compaction of the matrix. Comparison of the characteristic timescales of both processes gives a better idea of how the system behaves. The characteristic time of Darcy flow, noted as τ_D can be expressed as the ratio of the body radius R to the filtration velocity:

$$\tau_D = \frac{R\mu_f}{\Delta\rho g_s k_0} \propto \frac{\mu_f}{a^2}\,. \tag{1.21}$$

Here, μ_f is the fluid viscosity, $\Delta\rho = \rho_m - \rho_f$ the density contrast between the matrix and the fluid, g_s the surface gravity, $k_0 = k(\phi_0)$ the permeability of a matrix with a porosity ϕ_0 and a the grain size of the matrix. Then, the time for matrix deformation, noted as τ_C, is the ratio of the matrix viscosity μ_m to the pressure scale as follows:

$$\tau_C = \frac{\mu_m}{\Delta\rho g_s R} \propto \frac{\mu_m}{R^2}\,. \tag{1.22}$$

Note that the first time scale is independent of the size of the body while the second has a quadratic dependence.

These two characteristic times indicate that the segregation of a fluid from the matrix depends on the viscosities of the two phases, grain size of the matrix (dictating porosity) and radius of the body. It is possible to derive the equations to express the draining time τ (defined as the time necessary to reach 90% of segregation between the fluid and the solid) as a function of the two characteristic times and porosity (Marc Monnereau, personal communication), yielding the following equation:

$$\phi_0\tau \approx 4.3\times10^4\frac{\mu_m}{R^2} + 6.3\times10^5\frac{\mu_f}{a^2} \tag{1.23}$$

Plotting the draining time as a function of τ_D and τ_C gives figure 1.11. At first sight, two regimes can be defined. A first one controlled by matrix compaction, in which τ depends mainly on the radius of the planetesimal and the viscosity of the matrix (white region in figure 1.11), and a second one controlled by Darcy flow, where τ depends both to the grain size of

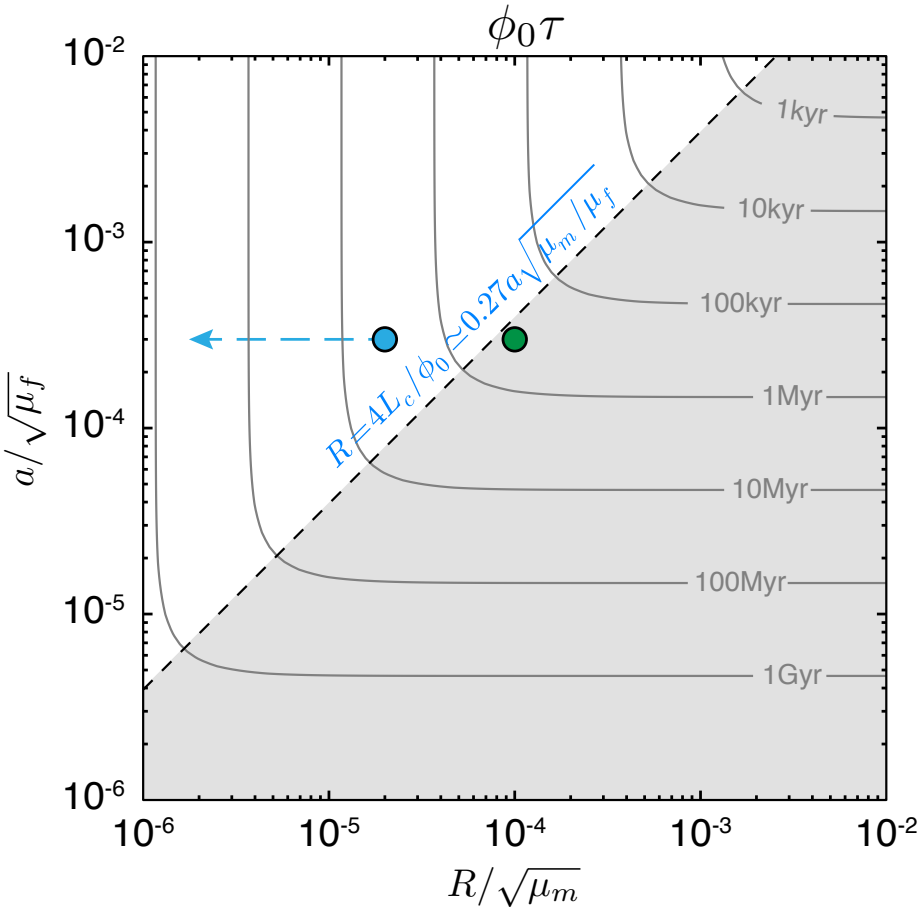

Figure 1.11 – Darcy time as a function of compaction time for different fixed draining times (gray lines). The dashed line, which equation is $\phi_0 R/L_c = 4$, separates regimes controlled by the compaction of the matrix (white) from regimes controlled by the Darcy flow time scale (grey region). The green dot indicates the draining time for a body with a radius of 100 km, while the blue one that of a planetesimal with a radius of 20 km. The dashed blue arrow shows the trend for bodies with radii lower than 20 km.

the matrix and the viscosity of the fluid (grey region in figure 1.11). These two regimes are separated by the dashed line on figure 1.11 which equation is:

$$\frac{\phi_0 R}{\sqrt{\frac{\mu_m k_0}{\mu_f}}} = 4 \tag{1.24}$$

From these two domains and equation 1.23, the draining time has to be compared to the cooling time in order to infer if a phase can move on a reasonable time-scale. Indeed, if the draining time is lower than the cooling time, then drainage of a melt is realistic, while if the draining time is greater than the cooling time, drainage will be partial or null. Cooling time τ_T expresses as follow:

$$\tau_T = \frac{R^2 \rho C_p}{k_T} \tag{1.25}$$

With ρ the mean density of the body, C_p its mean massic heat capacity and k_T the thermal conductivity.

For a given set of parameters (e.g. $\eta_f = 10$ Pa.s, $a = 1$ mm and $\mu_m = 10^{18}$ Pa.s), the draining time can be estimated for different planetesimals. For bodies with a radius lower than 20 km (blue dot and blue dashed curve on Figure 1.11), drainage of the silicate melt is driven by matrix compaction. In this case, the draining time of the silicate melt is greater than 5 Myr while the cooling time of the planetesimal is lower than 5 Myr. In these conditions, magma extraction would remain partial. For larger radii bodies, e.g. larger than 100 km (green dot on Figure 1.11), silicate melt migration is now mostly driven by Darcy flow. The cooling time has increased by almost two orders of magnitude (≈ 100 Myr) while the draining time is drastically lowered, less than a million year. In these conditions, silicate melt is able to segregate away. The grain size of the matrix is great importance here, in the Darcy flow regime, a shift in one order of magnitude in the grain size changes the draining time by one order of magnitude. This feature emphasize the need for grain sizes larger than ≈ 100 µm to allow an efficient silicate melt migration.

With varying parameters (grain-size, radius, and viscosities of the phases of a body), two planetesimal evolution patterns can be determined following the draining and cooling times comparison. A first one in which silicate melt is efficiently extracted, producing a region in which metal grains are trapped at silicate grain corners and cannot segregate. The second pattern constitutes a body in which silicate melt is not or poorly extracted, allowing an extensive melting.

1.4.3 Metal-silicate differentiation models

There are only a few literature studies that took interest to the differentiation of small bodies. Most of the metal-silicate differentiation models have applications to the Earth, i.e. a significantly larger body with different physical processes occurring. The work Taylor (1992) is pioneer in this domain. Two main processes, that match the evolutionary schemed mentioned above (following the mobility of silicate melt), are highlighted: (1) porous flow of a metallic network and (2) settling of metallic globules.

(1) Porous flow is only possible if the metal is forming an interconnected network. In a body of 10 km and with a matrix grain size of 1 mm, a metallic network segregates to the center of the planetesimal within 30 yr for silicate melting degrees ranging from 10 to 50 vol% (Taylor, 1992). At lower silicate melt content, the effect of interfacial energy may be of great importance, hindering drastically the percolation velocities. However, the formation of an interconnected network is not a simple question. Metals have high interfacial energies with solid silicates (e.g. Laporte and Provost, 2000), rising their interconnection threshold to high values. Taylor (1992) estimated this threshold to 50 vol%, which is extremely high. In these conditions, the initial content of metal in meteorites is much lower than the interconnection threshold (≤ 10 vol%). Some silicate melt has to be extracted to locally increase the metallic content and allow its interconnection. With an interconnection threshold of 50 vol% and an initial metallic content of 10 vol% (Guignard and Toplis, 2015), the formation of an interconnected network requires almost 90 vol% of silicate removal (following data from Taylor, 1992). More recent estimates of the interconnection threshold of pure iron points toward a lower interconnection threshold of ≈ 15 vol% (see section 1.3.5), which would require the extraction of 30-40 vol% of silicate melt to form a network (following data from Taylor, 1992).

Such model does not fit the formation of lodranites in which the extraction of 20-25 vol% of silicate melt was sufficient to allow a partial extraction of the metallic phases. Neglecting the effect of sulfur on the interconnection threshold of metallic melts most likely drove to this misfit. Also, relocation of the heat source is not considered in the porous flow model of Taylor (1992), due to the depletion of the refractory mantle, large silicate melt contents are not likely to be reached.

(2) The settling of metallic globules requires that interfacial energies are overcome. Indeed, melting experiments of chondritic material show that metallic beads remain suspended with silicate melt contents as high as 50 % (Takahashi, 1983). Walker and Agee (1988) suggested that suspension exists due to interfacial energies that make the metallic spheres stick to the solid silicate matrix. In this aim, Taylor (1992) estimated the minimum radius of a metallic globule that allows is to sink in a silicate mush for different crystal fractions and planetesimal radii. For low silicate melt fraction (< 30 %), large bodies (radius of 250 km) must host globules of a few meters to allow efficient metal settling, while small bodies (radius of 10 km) must host globules of a few tens of meters. For high silicate melt contents (> 70 %), these grain sizes are lowered by two orders of magnitude, requiring centimeter to meter sizes. Taylor (1992) thus argued that the settling of metallic spherules requires a relatively high melting degree, greater or equal than 50 %. This scenario can then occur only on early-accreted bodies in which the silicate melt is not mobile. Besides, the metal sizes mentioned here are much larger than grain sizes typically found in natural samples, which are about 10^{-6} to 10^{-3} m (e.g. Guignard and Toplis, 2015, for H-chondrites). To have such large metallic pools, a mechanism much more efficient than normal grain-growth has to be invoked. Taylor (1992) then proposed that coalescence in a convective magma ocean could allow to reach such sizes. However, coalescence goes along with fragmentation. Modeling of both processes by Ichikawa et al. (2010) suggests that metallic blobs can only reach a maximum stable grain size on the order of the centimeter, precluding the settling of metallic particles for small bodies with low silicate melt contents.

Overall, the models of Taylor (1992) clearly suggest that the presence of silicate melt is necessary for the differentiation of early-accreted bodies. In the case of magma oceans, differentiation is classically assumed to be complete. However in the case of bodies that accreted slightly later, e.g. the parent body of primitive achondrites, differentiation by porous flow does not seem to be completed as easily, giving rise to compaction models.

Šrámek et al. (2012) was one of the first study who derived such models in 1D with a spherical geometry. For simplicity and to emphasize the mobility of metallic melts, the silicate melt is considered to have the same density as the silicate matrix, rendering these two phases immobile with respect to each other. Assuming a low interconnection threshold of the metallic phases and no dependence with the sulfur content, a vertical stratification settles upon progressive heating and melting of the body (radius of ≈ 500 km). The model suggests an outer layer of undifferentiated material, overlying a partially differentiated one and then at the core, a differentiated material. Compaction waves developed, yielding thin layers that are particularly enriched in metal. Such waves develop when the extraction of the liquid becomes difficult due to a very low silicate melt content. This study then indicates that differentiated, partially differentiated and undifferentiated materials can all come from the same parent body.

A similar outcome was reached by Neumann et al. (2012) who modeled the migration of both metallic and silicate melts, but along different grain boundaries, meaning that their percolation do not disturb that of the other phase. The interconnection of iron-sulfide melts is set to 3 vol% and does not depend on its sulfur content. The removal of the silicate melt makes the inner depleted region subject to a lower peak temperature while the part that stored it is allowed to reach a much greater peak temperature. In order to investigate the effect of varying sulfur content of the material, several liquidus temperatures were investigated. Results show that the migration of iron-sulfide melts in the case of a high-temperature liquidus is driven by the melting of the silicate melt: the presence of silicate melt increases the permeability of the matrix, allowing an efficient and simultaneous extraction of both melts. In this case, the metal is extracted before its complete melting, but as the heat source is removed, the metallic residue is likely to remain trapped, leading to a partial differentiation. On the opposite, the migration of iron-sulfide melts with a low-temperature liquidus occurs before the onset of silicate melting. Indeed, due to a larger proportion of metallic melt at low temperature, the permeability of the matrix is greater for lower temperatures, allowing an efficient extraction of iron-sulfide melts. Such features can lead to different differentiation degrees, adding a degree of complexity with varying accretion date. Nevertheless, in almost all models, the outcome is a planetesimal with different different degrees along its radius.

Such models are used to determine the formation conditions of primitive achondrites. The main idea is to investigate the conditions (peak temperature and melt fraction) at different depths of a parent in order to find the best match to the formation conditions of natural samples. In this aim, Golabek et al. (2014) built a thermal evolution model that takes only takes into account conduction, not convection. Here, the silicate melt is assumed to be immobile, meaning that ^{26}Al is not redistributed within the planetesimal. Then varying the accretion time and size of the parent body, a range of radius comes out: between 25 and 65 km, with an accretion time of 1.3 Myr after CAIs. Models with diapirs are rejected here as there are no signs of deformation in the acapulcoites-lodranites. More recently, Neumann et al. (2018) derived a more realistic model that takes into account the migration of silicate and iron-sulfide melts, with similar assumptions than Neumann et al. (2012). In this case, the best fit model indicates a parent body of $\approx$ 260 km, significantly larger than in Golabek et al. (2014), with an accretion time of 1.7 Myr after CAIs. The discrepancy between these two studies most likely lies in the different assumptions of the models, more specifically, the consideration of melts mobility.

Overall, metal-silicate segregation most likely occurred by percolation processes. The metal-silicate differentiation can then have been partial or complete. Timescales indicate that differentiation on small-bodies took place within 10 Myr after CAIs (e.g. Neumann et al., 2012). Results also tend to indicate that materials with different differentiation degrees, e.g. iron meteorites, primitive achondrites and chondrites, may come from the same parent body (e.g. Moskovitz and Gaidos, 2011; Šrámek et al., 2012; Neumann et al., 2012, 2018).

1.4.4 Metal-silicate segregation: the big picture so far

High precision isotopic measurements on the Hf-W system showed that metal segregation of primitive achondrites must have occurred within 3 Myr after CAIs (Touboul et al., 2009;

Budde et al., 2015). For metal to be separated with low amounts of silicate melt (at most 20 vol%), it has to form an interconnected network, i.e. to have a volume fraction greater than the interconnection threshold. The first iron-sulfide melt formed is sulfur-rich (Fe-FeS eutectic, Figure 1.12) and is likely to have a low interconnection threshold ($\approx$ 3-6 vol.%). However temperature will rise with the decay of ^{26}Al and the metallic melt is likely to become more and more iron-rich (Figure 1.12), increasing its interconnection threshold (up to $\approx$ 20 vol.% for pure iron). If the interconnection threshold is reached before all the iron is molten, the solid residue will be left mixed with silicates, while if interconnection occurred when all the iron is molten, then the extraction is efficient and leaves only a small trapped fraction in the irregularities of the percolative network (Ghanbarzadeh et al., 2017). The latter would require temperatures on the order of 1673 - 1773 K for a H-chondrite precursor. At this temperature, the metallic melt coexists with a significant amount of silicate melt. In fact, the Fe-FeS eutectic melting temperature (1261 K) is very close to that of silicate ($\approx$ 1273 K, from MELTS simulation assuming an H-type chondrite precursor). The presence of this third phase changes the energetic budget with the appearance of two additional interfacial energies. The question is then: how are these new interfacial energies in comparison to the other ones? Are they lower or greater? This is what will dictate the small-scale geometry. Holzheid et al. (2000) studied the behavior of a Fe-FeS eutectic melt in contact with a molten basalt and San Carlos olivine. This study reports similar values of interfacial energies for the basalt - Fe-FeS eutectic melt interface and the basalt-olivine interface, which are ≈ 0.5 J.m^{-2}. This indicates that the basalt wets almost equally the two other phases and that the metallic melt prefers to be in contact with the latter than with olivine. As no simple equation can be derived to obtain the interconnection threshold from the knowledge of dihedral angle or interfacial energies in a three-phase system, this parameter should be measured experimentally. To my best knowledge, no experimental constraints report values of this threshold in such systems.

Some experimental studies report the effect of the silicate melt on the interconnection of a sulphide melt. Bagdassarov et al. (2009b) conducted centrifuge assisted experiments with a piston-cylinder which seem to indicate that metal segregation velocities are much higher in a presence of a silicate melt. Hence, the presence of this melt seems to be necessary to have an efficient metal-silicate separation. However it remains unclear if the interconnection threshold of the metallic melt is increased or lowered by the presence of a silicate melt or even if it varies with the silicate melt fraction. Primitive achondrites are partial melting residues, indicating that sulfide melt, iron, silicate melt and crystalline silicates coexisted. Thus a three-phase system seems to be better representative of natural samples than just a two-phase one, even though a system bearing four phases would be the perfect match for Nature.

Cerantola et al. (2015) conducted deformation experiments on a similar three-phase system and showed that the silicate melt is the phase that accommodates deformation and segregates away, while the metallic melt remains trapped along grain corners. Authors also argue that the presence of silicate melt hinders the interconnection of metallic phases. In the context of a planetesimal, the silicate melt would take away the ^{26}Al as it is extracted (e.g. Moskovitz and Gaidos, 2011), leaving a silicate - Fe-FeS mixture that would remain trapped into its partially differentiated state. In order for deformation to play a role in metal-silicate segregation, it should affect the body quite early, just after overstepping the Fe-FeS solidus, while the silicate melt fraction is still low. However, as no evidence of deformation are found in acapulcoites and lodranites, it is likely that the migration of silicate melt is dictated by grain sizes, radius of

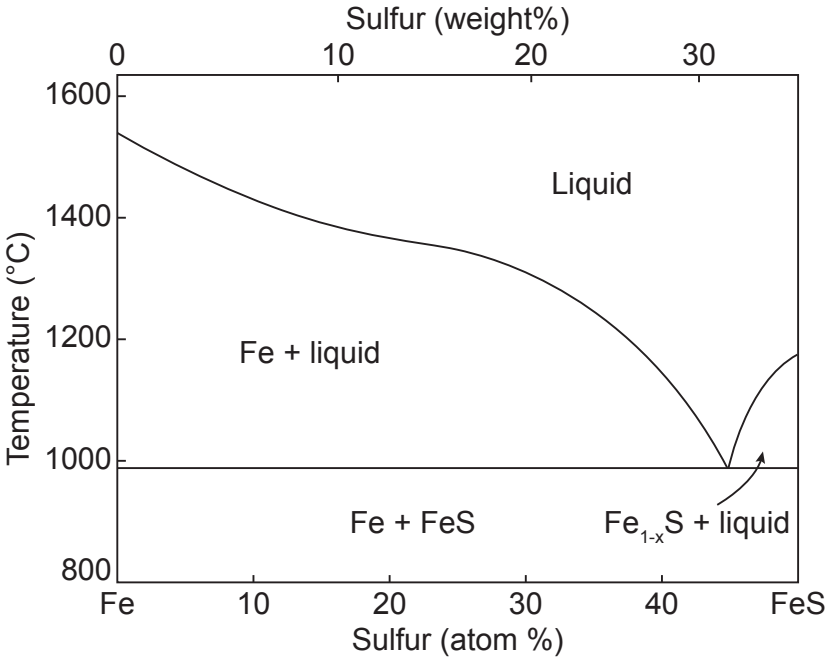

Figure 1.12 – Iron-sulfur phase diagram at 1 bar.

the parent body, and viscosities of both the silicate melt and the matrix. For the appropriate set of parameters that allow an efficient extraction, both silicate and iron-sulfide melts must have been extracted simultaneously.

The work of Chung and Mungall (2009) aimed at bringing physical constraints on the migration of immiscible fluids through partially molten silicates. Using the equations linking the internal variation of pressure within an iron-sulfide droplet as a function of interfacial energies and dimensions of the droplet. Following the relative sizes of the metallic melt droplets and crystals of the silicate matrix, three main regimes were found. If microdroplets of metallic melt are ≈ 10 times smaller than the grains of the crystal mush, they are able to travel large distances, as they can travel through narrow necks. Droplets with sizes similar to that of the crystalline matrix are trapped in the pores along grain corners: due to their surface tension, they cannot deform and go through pore throats narrower than themselves. These droplets are only able to move if they are fed with a microdroplet rain, allowing to form interconnected networks with neighboring droplets trapped. If the metallic melt forms an interconnected network, then it is able to migrate downward through vertically oriented channels, provided that its height is sufficiently high to overcome the surface tensions. This critical height ζ depends on interfacial energies γ, gravity g (and hence radius of the planetesimal), grain size a, crystal fraction ϕ and density contrast between metal and silicates $\Delta\rho$ with the following equation (Sweeney and Martin, 2003; Chung and Mungall, 2009):

$$\zeta = \frac{1}{2(1-\phi)} \frac{2\gamma}{\Delta\rho g a} \,. \tag{1.26}$$

There are two possibilities for a metallic melt to be extracted in a partially molten silicate: either the melt forms droplets smaller than the grain size of the silicate matrix, either it

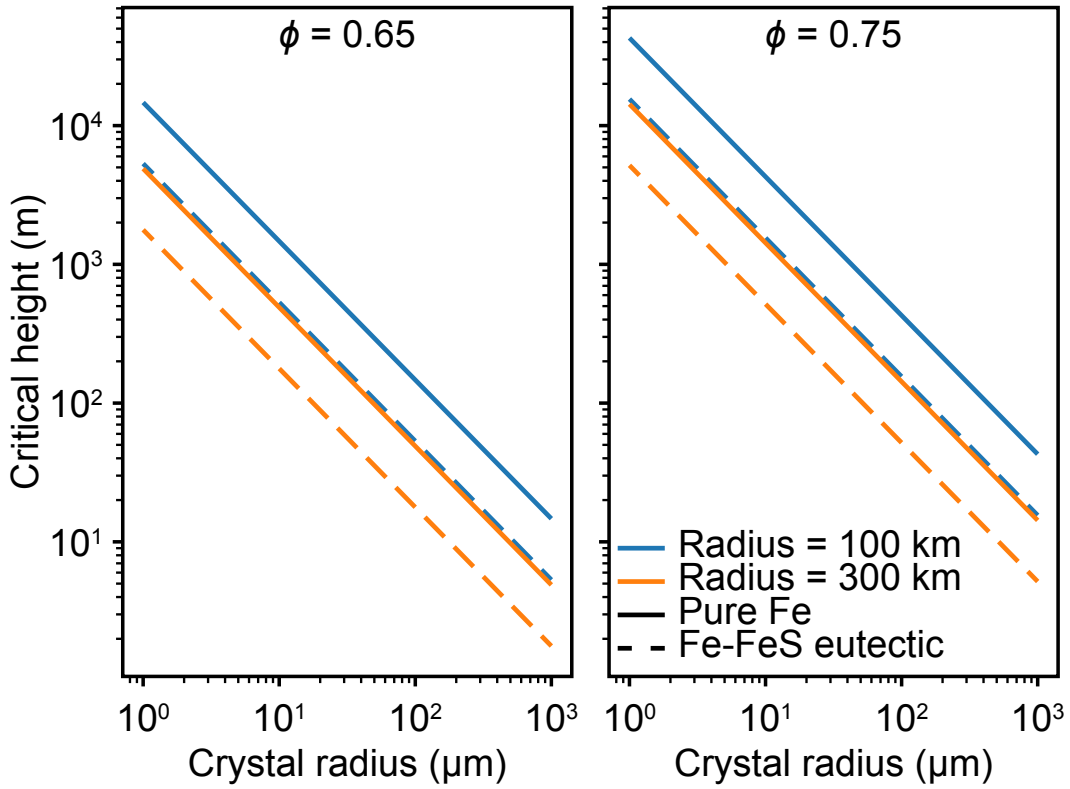

Figure 1.13 – Critical height for a network to sink as a function of the silicate matrix crystal radius. Left panel is drawn for a crystal fraction of 0.65 and right panel for a crystal fraction of 0.75. Dashed line represents a eutectic composition of the iron-sulfide network while full line represents a pure iron composition. Blue is for a planetesimal with a radius of 100 km and orange for a radius of 300 km. Values of interfacial energies were taken from Holzheid et al. (2000) and Néri et al. (2019).

forms a vertically widespread network. Grain sizes in natural samples indicate that silicates and metals (iron and troilite) have similar grain sizes. Hence, the metal has to form an interconnected network to be extracted. The critical height as a function of crystal radius is plotted in Figure 1.13. Here, the critical height decreases with increasing matrix grain size as the porosity of the matrix is increased, making the segregation of the interconnected network more efficient. However, this effect is countered by increasing the crystal fraction, which decreases the permeability. The parameters gravity and density decrease the critical height as these are forces that act against the surface tension of the network. In the case of primitive achondrites, grain sizes of the silicate are on the order of a few hundred microns, the critical height of network to allow its extraction ranges then from a few tens of meters to a few hundreds of meter depending on the composition of the iron-sulfide network and radius of the planetesimal (for a crystal fraction between 0.65 and 0.75, Figure 1.13).

To sum up, here is a non-exhaustive list of all the main conclusions drawn from this overview of literature on metal-silicate segregation in early-accreted small bodies:

— Metal-silicate differentiation in planetesimals is more a three-phase problem than a two-phase one
— Three-phase systems are poorly understood and constraints are scarce
— Variations of dihedral angles and interconnection thresholds from a two-phase system

to a three-phase one are not known
— The effect of the sulfur content on the interconnection threshold of the iron-sulfide melt is poorly known

From this state of the art, many questions arise and remain unanswered. The main one is: could a precursor material of acapulcoites and lodranites go through differentiation? Reducing this complex natural material to a simplified three-phase system, the subsequent questions appear: what are the small scale geometries in a three-phase system representative of natural samples? Is it possible to predict these geometries from the dihedral angles or interfacial energies? How does the interconnection threshold evolves in that case? What can learn us the primitive achondrites on the early history of planetesimal differentiation? The present thesis aims at shedding light on these questions with multidisciplinary approach, using experimental petrology, petrology on natural samples and modeling.

1.5 Thesis outline

This PhD thesis largely relies on experimental work. Hence, methods, techniques and experimental setups are presented in detail in Chapter 2. Using a three-phase system, theoretical predictions of interfacial energy ratios and equilibrium geometries were conducted. Then, different type of experiments were performed to determine the micro and macro-scale equilibrium of such system. In a first time, high temperature experiments in an atmospheric furnace were conducted to determine the micro-scale equilibrium geometries of experimental charges, with special interest on dihedral angles and interfacial energies. This study is presented as a paper in Chapter 3 with emphasis on the formation of primitive achondrites. Then in a second time, piston-cylinder experiments were conducted to determine the interconnection threshold of the metallic phase and the effect of varying amounts of silicate melt on this parameter. In a same time, Paris-Edinburgh experiments coupled with fast 3D microtomography imaging were lead to study the textural changes due to varying composition of the metallic phase and varying amounts of silicate melt. These data sets are discussed as a paper in Chapter 4. A model was then derived to study the differentiation processes in the context of large melting degrees, i.e. magma oceans, and is presented in Chapter 5. Besides, thick sections of primitive achondrites were obtained from the *Muséum d'Histoire Naturelle* (MNHN, Paris), NIPR (Tokyo, Japan) and NASA NASA (Antarctic Meteorite Collection; JSC Houston) to analyze their microstructure, composition and determine the thermal history of the parent body. All these samples were analyzed using high resolution Scanning Electron Microscopy (SEM), Electron MicroProbe Analysis (EMPA), Electron Back-Scattered Diffraction. The details and interpretation of these analyses with comparison to the models described in the former Chapters are depicted in Chapter 6.

Chapter 2

Methods

Contents

The goal of this PhD project is to have a better understanding of metal-silicate segregation processes. In order to do so, different approaches have been chosen. A first one consists in performing experiments to have a clear understanding of the conditions in which metal-silicate segregation occurs. To do so, a three-phase experimental system was designed based on literature data on the composition of partially differentiated primitive achondrites. Controlled-atmospheric high temperature furnace experiments were lead to constrain the equilibrium geometries of the studied system. Piston-cylinder experiments were conducted to have constraints on the interconnection threshold of the metal. Paris-Edinburgh experiments coupled with *in-situ* 3D X-Ray microtomography were performed to study the behavior of system when composition or proportions of the phases vary. The second approach is the petrologic study of relevant natural samples, i.e. primitive achondrites (winonaites, acapulcoites and lodranites). SEM and EDS maps were collected to image the features of the samples and to have a good understanding of their mineralogy, then EMPA and EBSD measurements were conducted. Data on the composition of each mineral are then used to calculate closure temperatures and oxygen fugacities. These data are to be used as inputs for MELTS models to have better constraints on the precursor material and its thermal evolution.

2.1 Description of the experimental system

2.1.1 Design of the three-phase system

The experimental system is chosen to mimic natural samples of primitive achondrites. Some simplifications are made with regard to their mineralogy, as the result of a will to control the composition of each phase during the experiments. Metal and crystalline silicates are simplified to pure phases, progressive melting is mimicked by a silicate glass that is in equilibrium with the crystalline mineral.

The metal phase in Primitive Achondrites is composed of two species: an iron-nickel alloy (kamacite and taenite) that hosts ∼10 wt. % of nickel in average and a sulfide composed of troilite (FeS). Most studies on core formation focused on a sulfide metallic melt, hence the choice is made here to focus on the other end-member, the pure metal. Iron is the most abundant element in the metallic phase, but it is quite difficult to control perfectly its oxidation state as it is partitioned in silicates, making the control of the mineralogy more complicated. Hence, nickel is used here as its lower melting temperature (1728 K) and stability field at higher fO_2 allow a better control on the chemistry (figure 2.5 a.). Also, for some experiments (detailed in the following), nickel sulfide is used to provide complementary experiments. This sulfide is made mixing pure Ni and Ni_3S_2 powders to obtain the desired composition.

Regarding silicates, several mineral species coexist in Primitive Achondrites: feldspar, clinopyroxene, orthopyroxene and olivine. The two first species have melting temperatures that are lower than that of pure nickel, preventing them to be good choices. Due to the incongruent melting of pyroxenes, magnesian olivine (forsterite Mg_2SiO_4) is selected as the crystalline silicate for the experimental system. Besides, its high melting temperature (2163 K) allow the sampling of a large range of experimental conditions.

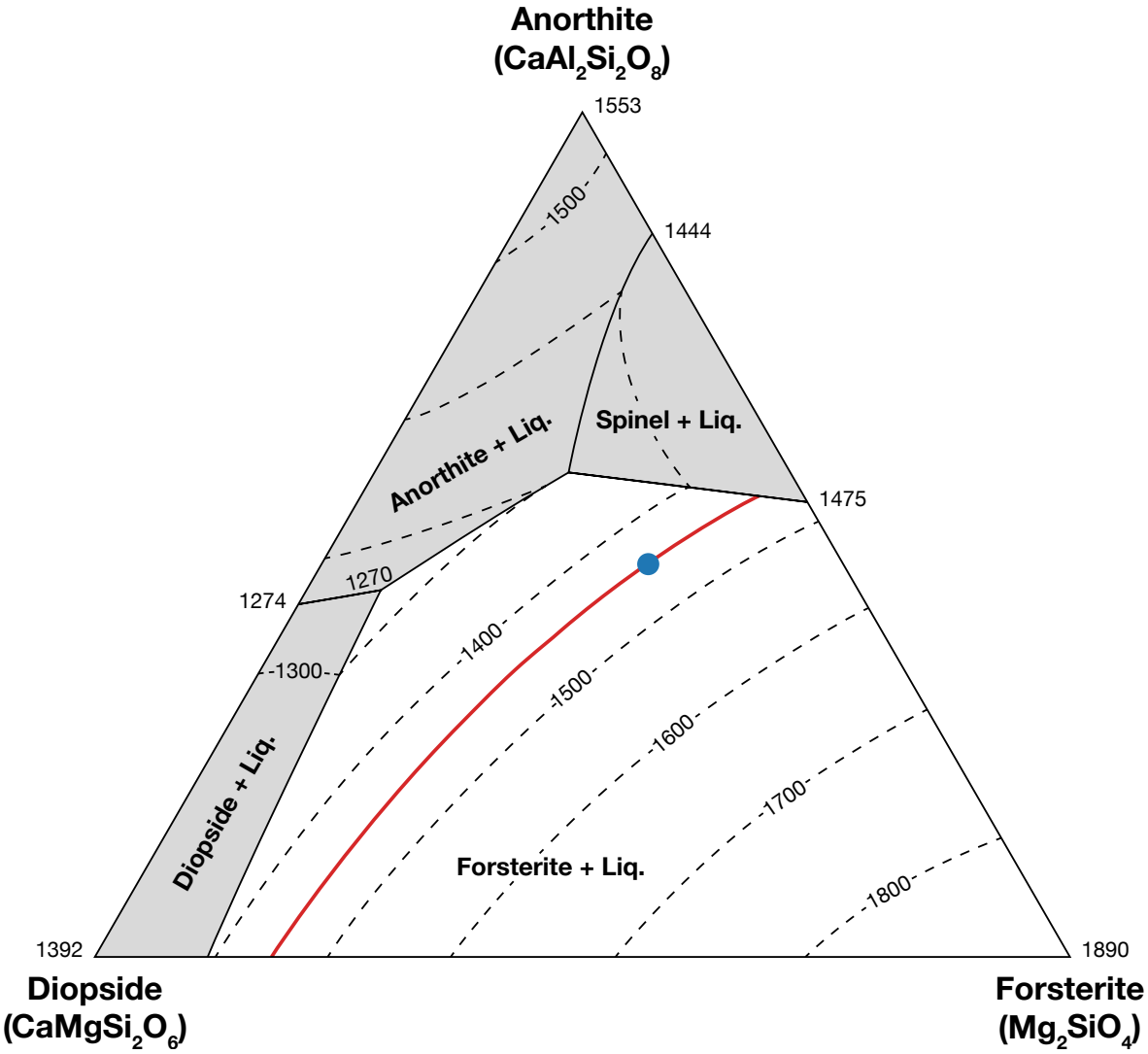

Figure 2.1 – Anorthite - Diopside - Forsterite ternary diagram at 1 bar (adapted from Presnall et al., 1978). The white region corresponds to the domain of composition in which the silicate melt is in equilibrium with forsterite, black lines correspond to limits between each equilibrium region and dashed lines correspond to the isotherm curves. Temperatures are written in degrees Celsius. The red curve corresponds to the 1723 K isotherm and the blue dot to the aimed silicate melt composition.

Composition of the silicate melt is taken from the Diopside - Forsterite - Anorthite ternary diagram (Figure 2.1) as it is a good analogue of iron-free basaltic melts. Composition of the silicate melt is chosen to be in equilibrium with forsterite (white region in figures 2.1 and 2.2). For experiments in the 1-atmosphere controlled high temperature furnace, composition of the melt is set along the 1723 K isotherm (red curve figure 2.1) so that the behavior of both solid and molten nickel can be studied without changing the composition of the silicate melt. The composition is arbitrarily set to the blue dot in figure 2.1; the oxide composition is specified in table 2.1. These choices also allow to vary the proportion of silicate melt at a fixed temperature without changing its composition. The exact same silicate melt composition is used for piston cylinder experiments, however the equilibrium temperature is shifted to about

Table 2.1 – Mineral and oxide composition of the silicate melt in equilibrium with forsterite in weight percent. These values correspond to the blue dot in figure 2.1.

	Mineral composition (wt%)			
	Diopside $CaMgSi_2O_6$	Anorthite $CaAl_2Si_2O_6$	Forsterite Mg_2SiO_4	
Silicate melt (1723 K isotherm)	20.0	46.5	33.5	
Silicate melt (1 GPa eutectic)	30	52	18	
	Oxide composition (wt%)			
	Al_2O_3	SiO_2	CaO	MgO
Silicate melt (1723 K isotherm)	17.04	45.49	14.55	22.92
Silicate melt (1 GPa eutectic)	19.06	46.80	18.25	15.90

1773 K (Figure 2.2) due to pressure. Paris-Edinburgh press experiments are performed to study the effect of increasing silicate melt on the geometry of the nickel grains. To do so, a silicate melt with a composition of the eutectic at 1 GPa is prepared and mixed with forsterite. The composition of the silicate melt evolves along a given path (figure 2.2 green line) that allows to determine the melting degree at any temperature. The composition of such eutectic glass is specified in table 2.1.

2.1.2 Synthesis of silicate glass

To synthesize the silicate glass, oxide powders (SiO_2 99.8% - Alfa Aesar, Al_2O_3 99.999% extra pure - Acros) and carbonates ($CaCO_3$ 99+% - Acros, $4(MgCO_3).Mg(OH)_{2.5}(H_2O)$ - Acros) were mixed in the appropriate proportions. Carbonate powders are chosen here instead of CaO and MgO for stability purposes. Indeed, these oxides have important hygroscopic properties that would prevent accurate weighting of the powders and induce a bias on the composition. These powders are kept in a drying oven at 373 K. Precise MgO content of the $4(MgCO_3).Mg(OH)_{2.5}(H_2O)$ powder was measured by mass spectrometry and is found to be 40.39 wt.% (J. Guignard, personal communication). Each batch is prepared to obtain 20 g of silicate glass in order to lessen the effect of weighting uncertainties on the composition. Powders are mixed mechanically shaking the vial and then placed in a platinum crucible which is in turn held for two hours at 1373 K in a muffle furnace to allow complete dehydration and decarbonation. Temperature is then set to 1773 K for two more hours to ensure complete melting and chemical mixing by diffusion processes. The crucible is quenched in water and the recovered material is finely ground in an agate mortar under ethanol and put back in the furnace at 1773 K for two additional hours to ensure chemical homogeneity. After quenching, a small chunk of glass is recovered to check chemical composition with Electron Probe Micro-Analysis (EPMA), the rest being finely crushed in an agate mortar under ethanol.

2.1.3 Sample preparation

The synthetic silicate glass powder is mixed with forsterite (Neyco CERAC, Inc., 325 mesh, 99% pure, grain size 0-40 µm) and nickel (Goodfellow, 99.8% pure, grain size 1-70 µm) powders in the desired proportions. As the interconnection thresholds are usually expressed in volume percent, the proportion of each phase, silicate glass, forsterite and nickel is also expressed in

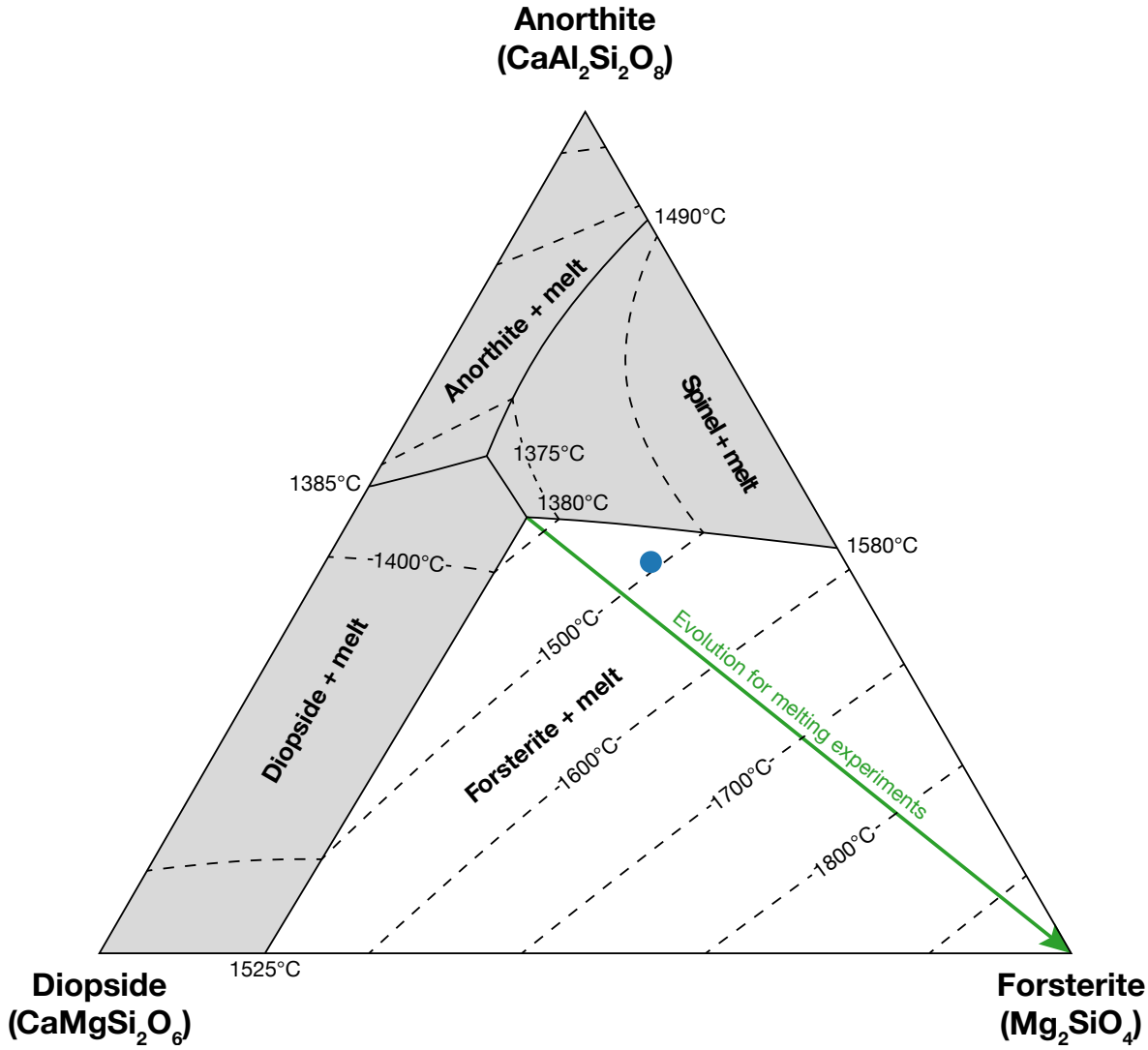

Figure 2.2 – Anorthite - Diopside - Forsterite ternary diagram at 1 GPa (adapter from Presnall et al., 1978). The white region corresponds to the domain of composition in which the silicate melt is in equilibrium with forsterite, black lines correspond to limits between each equilibrium region and dashed lines correspond to the isotherm curves. Temperatures are written in degrees Celsius. The blue dot corresponds to the aimed composition which is the same that at 1 bar. The green line represents the evolution path of a glass of the 1 GPa eutectic composition that reacts with forsterite upon temperature increase.

volume percent, unless specified. However, as the system will equilibrate at high temperature ($\approx$ 1723 K), efforts are made to prepare mixtures that will have the right volume proportions at high temperature, taking into account thermal expansion of the different phases. Density of forsterite and nickel at high temperature (1723 K) are taken to be $\rho_{Fo} = 3110\,\mathrm{kg.m^{-3}}$ (Bouhifd et al., 1996) and $\rho_{Ni} = 8210\,\mathrm{kg.m^{-3}}$ (Abdullaev et al., 2015), respectively. The calculation of the silicate melt density is a bit more complicated as it requires the knowledge of the molar volume of each oxide. These are taken to be 26.9 $\mathrm{cm^3.mol^{-1}}$ for SiO_2, 37.11 $\mathrm{cm^3.mol^{-1}}$ for Al_2O_3, 16.57 $\mathrm{cm^3.mol^{-1}}$ for CaO and 11.45 $\mathrm{cm^3.mol^{-1}}$ for MgO (M. Toplis, personal communication). Then, knowing the molar mass and the mass proportion of each oxide into

the glass, the density can be calculated and is found to be $\rho_{Melt} = 2680$ kg.m^{-3}. From the knowledge of the desired volume proportion $x_{i_{vol}}$ for each phase $_i$, the mass proportion ω_i can be calculated following:

$$\omega_i = \frac{\rho_i}{\rho_{tot}} \times x_{i_{vol}} \,, \tag{2.1}$$

With ρ_{tot} the density of the mixture:

$$\rho_{tot} = \sum_i x_{i_{vol}} \rho_i \qquad \text{or} \qquad \rho_{tot} = \frac{\prod_i \rho_i}{\sum\limits_{\substack{i,j \\ i \neq j}} \rho_i \omega_j} \,. \tag{2.2}$$

The mass proportion of each phase does not depend on temperature, thus mixtures are prepared at room temperature. Powders are put in an agate mortar and mixed under ethanol. Due to the density gradient between the silicates and nickel, nickel grains have a tendency to settle during the mixing. Hence, care is taken to mix to powders until the mixture with the ethanol becomes viscous enough so that nickel cannot separate from the silicates. When mixtures are dry, they are recovered and put in glass vials.

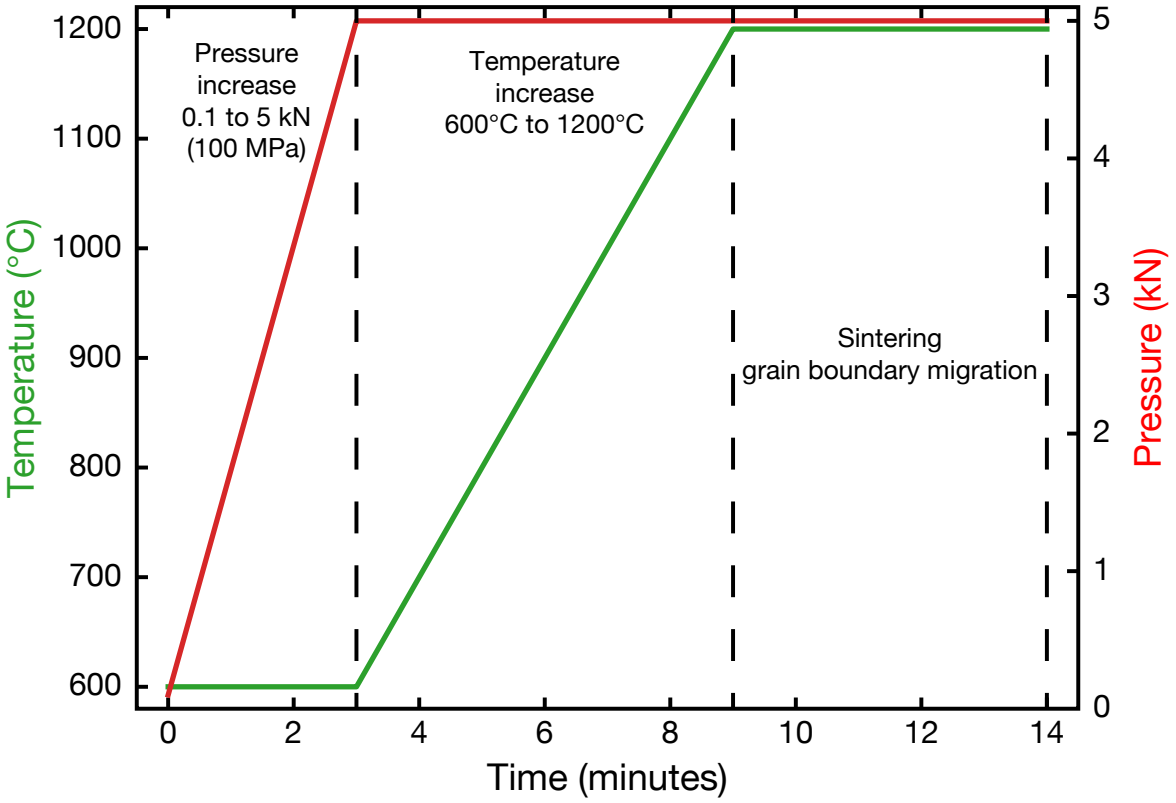

Figure 2.3 – Sintering pressure - temperature path. The green curve shows the evolution of temperature with time and the red curve the evolution of pressure with time. Pressure is first increased up to 100 MPa, then temperature rises to 1473 K, favoring sintering and grain boundary migration without melting of the silicate glass.

Samples dedicated to piston-cylinder and Paris-Edinburgh press experiments are kept in the form of powders. The one dedicated to atmospheric furnace experiments are either

prepared with the wire loop technique or sintered with the Spark Plasma Sintering (SPS) technique, at the PNF^2 platform (CIRIMAT, Toulouse). The wire loop technique consists in making a loop with a platinum wire ($\varnothing = 0.2$ mm, 99.9% pure - Johnson Matthey), on which is placed a droplet of water. The sample, in the form of a powder, is then put on the loop, holding due to water surface tension. This set up is finally put for 30 seconds at 1723 K to allow the melting of the silicate melt, forming a new droplet that holds to the platinum wire due to surface tension again. This droplet is then quenched in air and recovered. This set up is well suited for samples containing high amounts of silicate melt ($\geq$ 50 vol%). The sintering technique consists in putting the samples in a graphite mold that is sealed with two graphites piston. This set up is then placed in an argon vacuum for heating and compression. The argon vacuum allows to avoid significant reaction of nickel with air at high temperature. One sintering cycle lasts for 14 minutes and follows the procedure described by Guignard et al. (2011), which is shown on figure 2.3. It can be roughly subdivided into three parts, first, pressure is increased up to 100 MPa in 3 minutes, then, temperature rises up to 1473 K in 6 minutes, in the last part, these conditions are held for 5 minutes, allowing grain boundary migration without melting the silicate. However, the glass undergoes recrystallization during heating, causing a volume change that may break the graphite mold if there is too much glass, the upper limit being $\approx$ 50 vol%. Hence, this technique is more suitable for low silicate melt content, less than 50 vol%. Recovered sintered samples are cut into small pieces using a low speed saw (IsoMet 11-1180 low speed saw - Buehler Ltd.) with a thin (150 µm thick) diamond coated disk.

2.2 Experimental setups

Different experiments using different apparatus are used to study different aspects of the three-phase system. First experiments in a 1-atmosphere controlled high temperature furnace are used to determine the equilibrium geometries at triple junction. Then, piston-cylinder experiments are carried out to determine the interconnection threshold of pure nickel with varying silicate melt content. Finally, time-resolved in-situ Paris-Edinburgh using synchrotron radiation is used to study the effect of the evolution of the sulphide composition and progressive melting of the silicate.

2.2.1 Annealing experiments in 1-atmosphere controlled high temperature furnace setup

Annealing experiments in a 1-atmosphere controlled high temperature furnace (AF) are used to determine the equilibrium geometries. Indeed, air bubbles expand due to thermal expansion, preventing accurate interconnection threshold determination. However, porosity does not disturb equilibrium triple junction geometries between forsterite, silicate melt and nickel. Air bubbles are also present in sintered samples, a part of the porosity must remain under pressure and heating allows it to re-open. The interest for such furnace is that gas inputs can be used to control the oxygen fugacity f_{O_2}, setting it oxidizing or reducing. The f_{O_2} is expressed in comparison to a buffer, i.e. a chemical equilibrium. In the present case, CO / CO_2 gas inputs are used to set a reducing atmosphere, three log units below the Ni

- NiO buffer (simplified as NNO buffer in the remainder of the text), in order to limit the diffusion of nickel into the silicate phases and to keep it in the metallic state. Experiments were performed on the experimental petrology platform at IRAP, OMP in Toulouse.

2.2.1.1 Experimental setups

Different experimental setups are used depending on the temperature conditions, mostly below or above the nickel melting temperature, or if it is an equilibrium or a time-series experiment. However, above all the choice of materials to suspend the samples in the furnace is of prime importance and can be tricky as there are no inert phases with all components of the three-phase system used here. The high temperature conditions (> 1673 K) require refractory materials with a greater melting temperature. The presence of nickel in samples precludes the use of most metals as they are expected to form alloys. No contact with oxides should exist as they would react with the silicate melt and change its composition. For instance, contact with alumina and melt would form spinels. Hence choices are made to put samples in contact with either nickel, for relatively low temperatures (< 1728 K), or platinum, for higher temperatures. Here platinum is the least worst alternative as even though nickel and platinum are expected to form alloys, this effect can be negligible at the scale of the sample, as demonstrated later on.

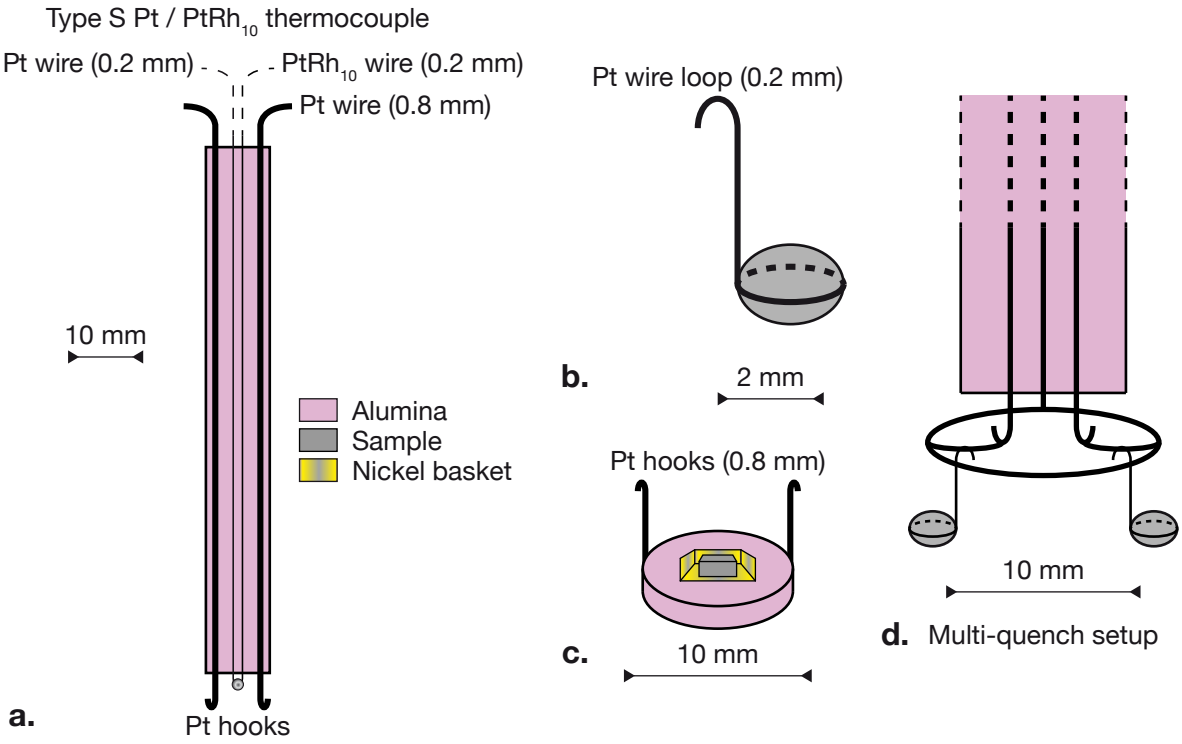

Figure 2.4 – Atmosphere controlled high temperature furnace setups. (a.) Scheme of the alumina rod with fours holes that allow suspending the samples and temperature measurement with a type S thermocouple. (b.) Sketch of the wire loop technique. (c.) Sketch of a piece of a sintered sample put in a nickel basket and on an alumina disk. This last setup is only valid for temperatures lower than that of nickel melting, i.e. lower than 1728 K.

For the equilibrium experiments, samples are placed into the furnace using a long ($\approx$ 1 m) alumina rod (sintered pure alumina 99.7 % Al_2O_3, type C 799 - AMTS) bearing four holes (figure 2.4 a). Two of them are used to suspend the samples using thick platinum wires (0.8 mm, 99.9 % - Johnson Matthey) twisted to form hooks, the two remaining are used to monitor temperature using a type S thermocouple Pt - $PtRh_{10}$ (figure 2.4 a.). Samples prepared with the wire loop technique are directly suspended on the thick platinum wires (figure 2.4 b.). Sintered samples are suspended using two different setups, depending on the temperature. If temperature is lower than that of nickel melting (1728 K), they are put in a nickel basket attached to an alumina disk that is suspended to the alumina rod using a thick platinum wire (figure 2.4 c.). However, if temperature is higher than that of nickel melting, samples are tied in thin platinum wire (0.2 mm) and suspended to the alumina rod, to form something similar to the wire loop technique (figure 2.4 b.). These samples are quenched in the air using the length of the alumina rod to place them in the cold zone at the bottom of the furnace.

Interest is also taken to do time-series experiment to follow the textural evolution of samples. To do so, an alumina bearing eight holes is used and like in the previous setups, two of them are used for thermocouple wires (figure 2.4 d.). The idea of this setup is to suspend five samples with the wire loop technique, which will undergo the exact same condition but will be quenched at different times without having to change any temperature or f_{O_2} conditions. To do so, a short circuit is used to break the platinum wire at a given fragility point. A platinum wire ring surrounds the five platinum hooks and a thinner platinum wire is tied between the ring and each hook. On each of these thin wires, wire loop samples are suspended. In order to quench a given sample, one simply has to connect the wires of an electric generator to the ring and the desired hook, the short circuit breaks the thin platinum wire and the samples drops to the cold region, quenching it. This setup allows to produce samples that undergo the exact same conditions but for different times.

2.2.1.2 Control of experimental conditions

The two main parameters that are controlled in these experiments are temperature and oxygen fugacity f_{O_2}. Temperature is monitored using a type S thermocouple Pt - $PtRh_{10}$, with a precision of $\pm$1 K. Caution is taken to place the samples in the "hot zone", i.e. a zone of $\approx$ 3 cm in which no temperature gradient is measured with the thermocouple, and to put them close to the thermocouple to have the most accurate temperature control possible.

The f_{O_2} along the NNO buffer at varying temperature can be determined from the knowledge of the chemical potential of oxygen μ_{O_2} along the following chemical equilibrium:

$$2Ni + O_2 \rightarrow 2NiO \tag{2.3}$$

From a general point of view, the chemical potential of a species correspond to its molar free enthalpy and can thus be expressed as follows:

$$\mu_{O_2}(T) = \mu^0_{O_2} + RT \ln(a_{O_2}) \ , \tag{2.4}$$

with μ_{O_2} the oxygen chemical potential in J.mol^{-1}, $\mu^0_{O_2}$ the standard state chemical potential of oxygen, R the perfect gas constant (8.314 J.mol^{-1}.K^{-1}), T the temperature (in K) and a_{O_2} the activity of oxygen.

The standard state chemical potential of oxygen is null by definition in the present case: the chemical potential of pure species in their reference state is defined as zero. The activity of a gas corresponds to the ratio of its partial pressure to the reference pressure P_0, which is set to 10^5 Pa. Hence, expressing the log of the oxygen fugacity gives:

$$\log\left(\frac{f_{O_2}}{P_0}\right) = \frac{\ln\left(\frac{f_{O_2}}{P_0}\right)}{\ln(10)} = \frac{\mu_{O_2}(T)}{RT\ln(10)}\,. \tag{2.5}$$

The expression of the oxygen chemical potential as a function of temperature for different buffer have been determined by O'Neill and Pownceby (1993). For the NNO buffer, between 700 and 1700 K, the equations is:

$$\mu_{O_2}(T) = -478967 + 248.514T - 9.7961T \times \ln(T)\,. \tag{2.6}$$

The evolution of the oxygen fugacity along the NNO and IW buffers, and three log units below the NNO buffer (experimental conditions) as a function of temperature are represented in figure 2.5 a. Experiments are performed either with solid nickel at 1713 K or with liquid nickel at 1743 K, and three log units below the NNO buffer, giving $\log\left(\frac{f_{O_2}}{P_0}\right)$ of -8.43 and -8.19 respectively. Knowing the desired oxygen fugacities is only half-way of the problem, the CO / CO_2 gas fluxes have also to be predicted. The reaction governing the partial pressure of oxygen into the furnace is the CO - CO_2 equilibrium:

$$CO + \frac{1}{2}O_2 \rightarrow CO_2 \tag{2.7}$$

The free enthalpy of reaction $\Delta_r G$ can be written as follows:

$$\Delta_r G = \Delta_r G^0 + RT\ln(K)\ , \tag{2.8}$$

with $\Delta_r G^0$ the free enthalpy of reaction in the reference state, R the perfect gas constant (8.314 J.mol^{-1}.K^{-1}), T the temperature (in K) and K the reaction constant. At equilibrium, the free enthalpy of reaction is null; using the expression of free enthalpy as a function of the enthalpy of reaction $\Delta_r H^0$ and entropy or reaction $\Delta_r S^0$, both in the reference state, gives:

$$\Delta_r G^0 = \Delta_r H^0 - T\Delta_r S^0 = -RT\ln(K_{eq})\ . \tag{2.9}$$

with K_{eq} the equilibrium constant of the reaction, which can be expressed as follows:

$$K_{eq} = \frac{P_{CO_2}}{P_{CO}}\sqrt{\frac{P_0}{f_{O_2}}}\,, \tag{2.10}$$

with P_{CO_2} the partial pressure of CO_2, P_{CO} the partial pressure of CO, f_{O_2} the oxygen fugacity and P_0 the reference pressure (10^5 Pa).

Hence the ratio of the two partial pressures of CO_2 and CO can be expressed as a function of temperature, enthalpy and entropy in the reference state and oxygen fugacity:

$$\frac{P_{CO_2}}{P_{CO}} = \sqrt{\frac{f_{O_2}}{P_0}} \times \exp\left(-\frac{\Delta_r H^0 - T\Delta_r S^0}{RT}\right)\,. \tag{2.11}$$

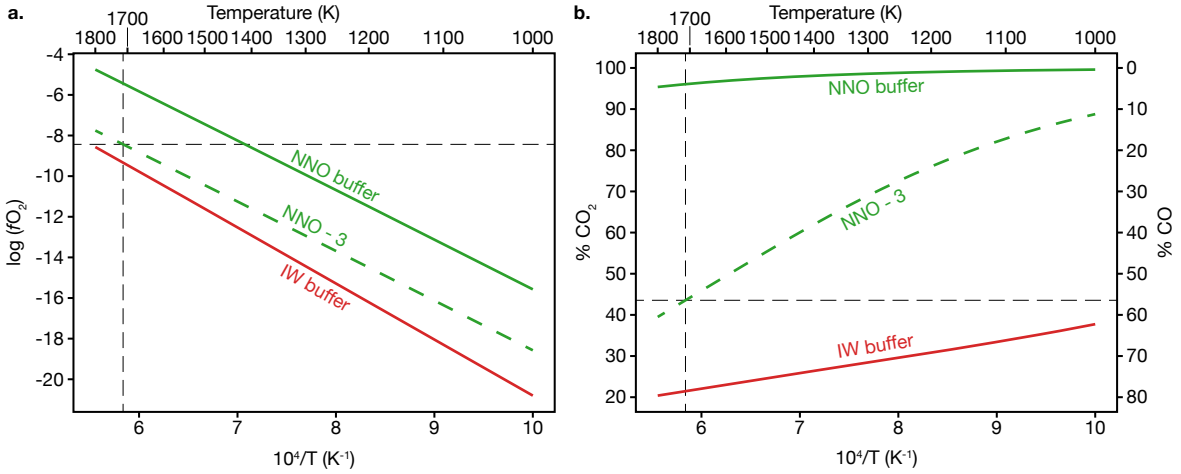

Figure 2.5 – (a.) Evolution of the oxygen fugacity as a function of temperature along the NNO and IW buffers, and the experimental conditions, i.e. three log units below the NNO buffer. (b.) Evolution of the gas fluxes (CO_2 and CO) along the different trends (IW, NNO and NNO - 3) as a function of temperature. Thin black dashed lines illustrate the experimental conditions: 1713 K and $\Delta_{\mathrm{NNO}} = -3$

The gas fluxes are controlled by two valves with a maximum flux of 500 cm^3 per minutes. The valves were calibrated at lower temperature using zircon probes. The user only sets a percentage of the maximum flux on each valve. Hence, assuming that the total pressure of the furnace is controlled by the gas inputs that already mix the carbon monoxide and dioxide in the high temperature equilibrium proportions, the percentage of each gas to be injected can be calculated as follows:

$$\%P_{\mathrm{CO_2}} = \frac{\frac{P_{\mathrm{CO_2}}}{P_{\mathrm{CO}}}}{1 + \frac{P_{\mathrm{CO_2}}}{P_{\mathrm{CO}}}}\,. \tag{2.12}$$

And:

$$\%P_{\mathrm{CO}} = \frac{1}{1 + \frac{P_{\mathrm{CO_2}}}{P_{\mathrm{CO}}}}\,. \tag{2.13}$$

Figure 2.5 b represents the variation of the gas fluxes as a function of temperature along the NNO and IW buffers and the aimed oxygen fugacity for experiments (NNO - 3). At experimental conditions, this corresponds to CO_2 contents of 43.66 % at 1713 K and 42.66 % at 1743 K, using $\Delta_r H^0 = -279674.7$ J.mol^{-1} and $\Delta_r S^0 = -84.703032$ J.mol^{-1}.K^{-1} (M. Toplis, personal communication). As important contents of CO are used, caution is taken to flush the furnace with CO_2 before injecting CO as it could react with air and cause an explosion. The same goes before opening the furnace.

2.2.2 Piston-cylinder apparatus setup

Recovered samples from atmosphere furnace show a tendency to have air bubbles trapped, even if the samples were sintered before experiment. It is likely that a part of porosity is under pressure and can expand at high temperature. Determination of the nickel interconnection threshold seems to be precluded as gas bubbles trying to escape agitated the sample, clustering

nickel grains (see Chapter 4). Hence, piston-cylinder (PC) experiments were conducted to ensure that the phases equilibrated without any disturbance from porosity. These experiments were performed at the *Laboratoire Magmas et Volcans* (Clermont-Ferrand, France) in a 3/4 inch PC assembly, with the help of K. Koga and D. Laporte and D. Andrault. The series of experiments were conducted either at 1753 K with solid nickel or at 1773 K with molten nickel and varying proportions of nickel, silicate melt and forsterite. As a will to compare these experiments with the one performed in the atmosphere controlled furnace, pressure must be as low as possible and was set to 0.8 GPa in the present case.

2.2.2.1 Experimental assembly

Such high temperature and relatively low pressure experiments may give rise to instability problems in the setup. Hence, the choice of materials is of prime importance, but compromises must be made. The chosen setup is represented in figure 2.6. Two pistons composed of steel with an inner cylinder of tungsten carbide will compress the sample inside a steel vessel that is constantly cooled. Plastic foils are placed between the lower piston and the vessel to avoid short circuits, as electricity is delivered through the pistons. The pyrophyllite ring surrounding the steel spacer has the same role between the spacer and the vessel. The outer NaCl cell of the sample ensures hydrostatic pressure throughout the whole volume of the sample. A graphite furnace is used for its stability in such experimental conditions, heat being produced by Joule effect. Two pyrex cylinders surround the graphite furnace to ensure that the furnace does not undergo any shear due to differential shortening of materials. The brass ring ensures the conduction of electricity from the steel pieces to the graphite furnace. Inside the furnace, MgO spacers maintain the capsule containing the sample at the right place and provide an efficient electric isolation between the capsule and the furnace. The thermocouple wires pass through an alumina rod to be as close as possible to the sample. A thin alumina disk is placed between the capsule and the sample to avoid that the alumina rod pierces through the cap of the capsule and intrudes into the sample. The capsule is made of graphite here as this material is the most inert one with regard to the three phases. Although nickel and graphite may be expected to form carbides, recovered samples show few graphite crystals in the nickel grains, less than 1 wt.%. Results also show that micro-scale geometry is identical to that obtained in AF experiments. The graphite capsule acts as a buffer, ensuring reducing conditions. An argon flux is put on the thermocouple wires to avoid their oxidation at high temperature that would degrade the accuracy of temperature measurement.

2.2.2.2 Control of experimental conditions

Temperature is monitored using a type C thermocouple WRe_5 - WRe_26 and controlled with a Eurotherm PID (Proportional Integrative Derivative) controller. The oil pressure of the piston is controlled using a hydraulic hand pump. Oil pressure is measured with an electric detector and pressure inside the vessel is equal to the product of oil pressure to the ratio of the surface of the jack to that of the piston. The oxygen fugacity is not controlled as precisely as in the case of the atmosphere controlled furnace, the graphite capsule acts as a buffer, ensuring that nickel remains in the metallic state.

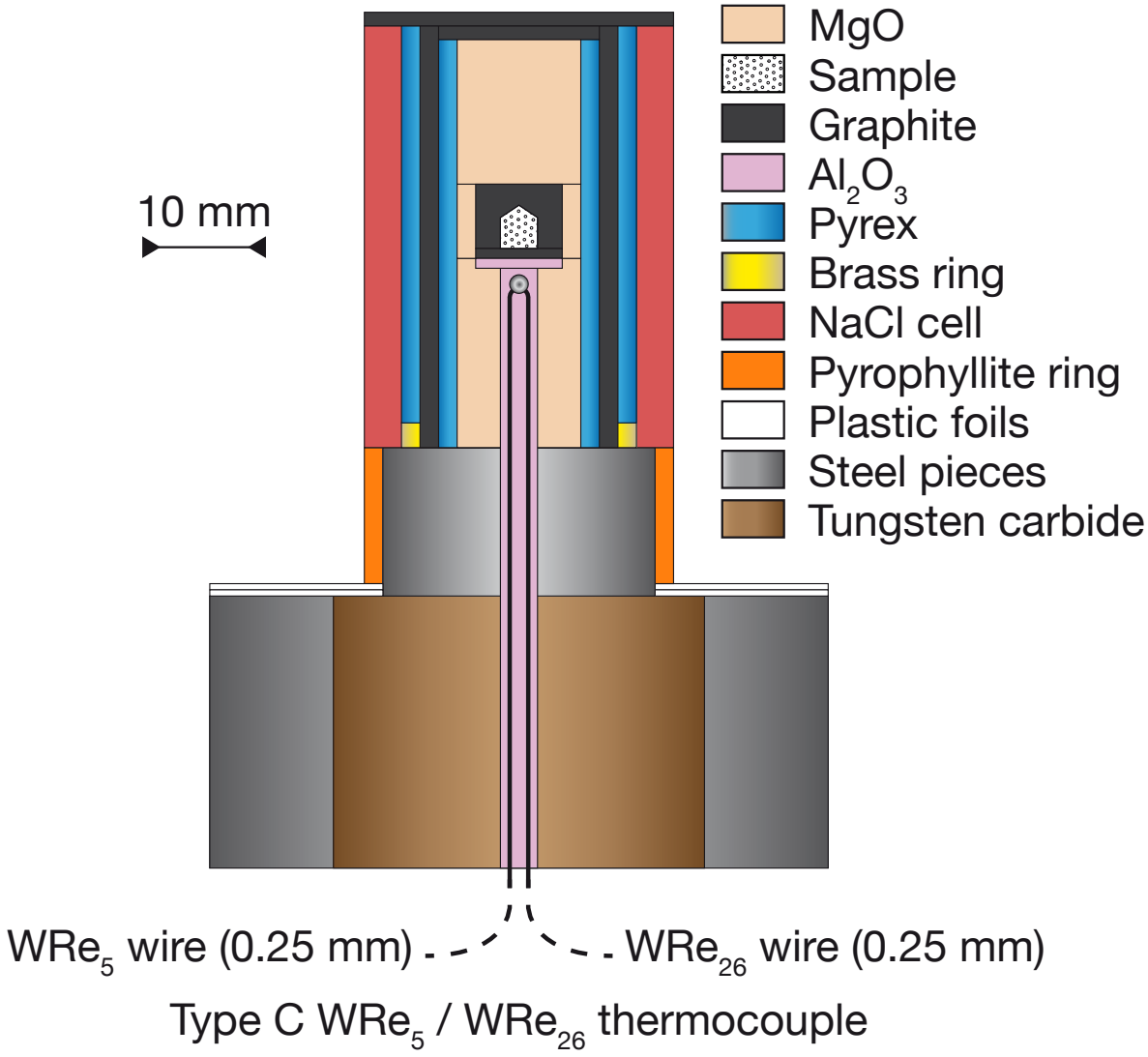

Figure 2.6 – Piston-Cylinder experimental setup.

Pressure is first increased slowly to 0.3 GPa, then temperature increases up to 923 K and remains steady for five minutes. During this time pressure is slowly increased to 0.8 GPa at a rate of 0.1 GPa per minutes. This hot compression avoid cracking of the different materials and helps to stabilize the assembly. Temperature is finally increased to 1773 K.

There are temperature gradients inside the assembly, even though the use of a long graphite furnace should lower them. One can expect that there is a difference between the temperature measured by the thermocouple and the true temperature inside the sample. Hence there is a need to accurately quantify the gradients. In the present case and at the desired conditions, there is a difference of 12 K between the thermocouple and the sample (K. Koga and D. Laporte, personal communication). There is also a temperature gradient of 5 K within the sample. The PID is thus set to maintain temperature at 1756 K, corresponding to a maximum temperature of 1773 K in the sample.

At the end of the experiment, the electrical power is turned-off to quench the sample and pressure is smoothly decreased to avoid cracking of the assembly. As the pressure decrease is done manually, samples may have experienced different decompression, it was difficult to follow the exact same decompression rate for each of them.

2.2.3 Paris-Edinburg press setup

We had our Synchrotron project accepted at beamline PSICHE at SOLEIL (in collaboration with N. Guignot and A. King - proposal 20180672) to do time-resolved 3D X-ray microtomography to study the evolution of the spatial distribution of metallic phases upon progressive melting of either the metallic subsystem (i.e. increasing dihedral angle with the sulfur content of the melt that is diluted) or the silicate one (i.e. varying the forsterite to silicate melt ratio). These experiments were conducted on a Paris-Edinburgh press as this apparatus allows to have a wide opening with respect to X-rays. The series of experiments ran at $\approx$ 1 GPa with increasing temperature, from room temperature ($\approx$ 20 K) to $\approx$ 2023 K. Samples were composed either of fixed metal or sulfide (Ni-Ni_3S_2 eutectic) fraction and progressive melting of silicate or fixed content of silicate and progressive melting of the Ni-S subsystem. Detailed information on the set up are given in the following.

2.2.3.1 Experimental assembly

Here also, to ensure that these high temperature and relatively low pressure experiments are stable and to avoid reactions of the assembly with the sample, the choice of materials is of prime importance. Synchrotron radiation experiments also require that the materials used are transparent to X-rays. These experiments were conducted in collaboration with D. Andrault and J.-P. Perrillat. This latter has a great knowledge of Paris-Edinburgh press experiments and helped a lot with the design of experimental assemblies (Figure 2.7). Our choice was to do double capsule experiments, with the most inner one (in contact with the sample) in graphite for the same reasons as in piston-cylinder (see section 2.2.2.1), and a second one encapsulating this first in hot-pressed boron nitride (hBN). This latter material electrically insulating, thus avoiding any conduction from the surrounding graphite furnace to the inner capsule. Here, as in piston-cylinder heating of the furnace is done with Joule effect. On both extremities of the furnace (top and bottom), pieces are added to ensure electrical conduction, from the closest to the furnace: a graphite disk, a molybdenum disk and a steel ring. Inside of this latter ring is put MgO powder. This cylindrical assembly is then put into a boron epoxy gasket shaped like an olive, which ensures hydrostatic pressure media. A peek ring is placed around the boron epoxy piece in order to hold the assembly during compression and ensure hydrostatic conditions as well. As for the piston-cylinder assembly, the inner graphite capsule is likely to buffer the sample, maintaining reducing conditions.

2.2.3.2 Control of experimental conditions

In Paris-Edinburgh press experiments, control of pressure and temperature is less accurate than in piston-cylinder. As these experiments are for 3D X-ray microtomography, the use of a thermocouple is precluded. Hence, the cross-calibration method is used to determine experimental conditions (Crichton and Mezouar, 2002). The idea of this technique is to use materials with different properties: one that is sensitive to temperature (usually a metal) and another one that is sensitive to pressure (usually a ceramic). In this aim, calibrant materials of Pt and hBN powders were placed at half-height in the hBN capsule. Their equation of state were taken from Zha et al. (2008); Le Godec et al. (2000).

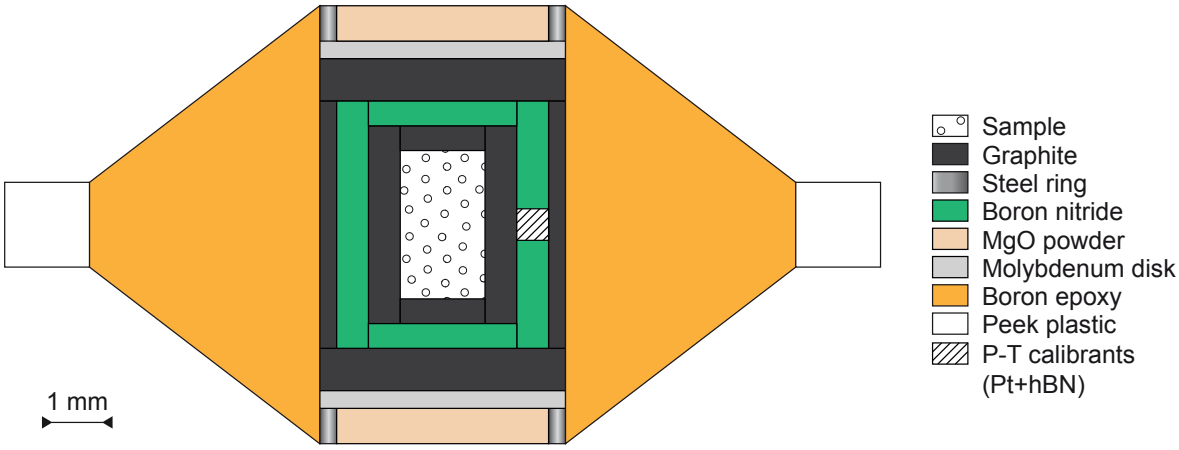

Figure 2.7 – Paris-Edinburgh press experimental assembly.

Pressure is increased by hand with a Enerpac hydraulic hand pump. After successive tries, pressure was increased to 200 bar of oil pressure, which corresponded to ≈ 1 GPa prior to heating. During the time of experiment, pressure decreased to ≈ 0.7 GPa upon heating and could then increase due to thermal pressure. Here, temperature control is much more simple than in piston-cylinder as there is no retroactive loop. Here, the electrical generator has a fixed tension, intensity is increased to reach user determined values of power. Steps of 25 or 50 W were typically used. Maximum temperature reached is on the order of 2023 K.

At the end of the experiment, electrical power is decreased "slowly" to avoid a brutal blow-out of the assembly. Once the sample is cooled, pressure is then smoothly decreased to avoid cracking. As in piston-cylinder, as the pressure decrease is done manually, samples may have experienced different decompression rates.

2.2.4 Detail of all experiments

Different compositions and conditions (mostly temperature) for each kind of experiments are detailed in the following ternary diagrams (Figures 2.8, 2.9 and 2.10). In these diagrams, proportions of each phase is represented in volume percent. The dashed light gray line are placed each 10 vol%.

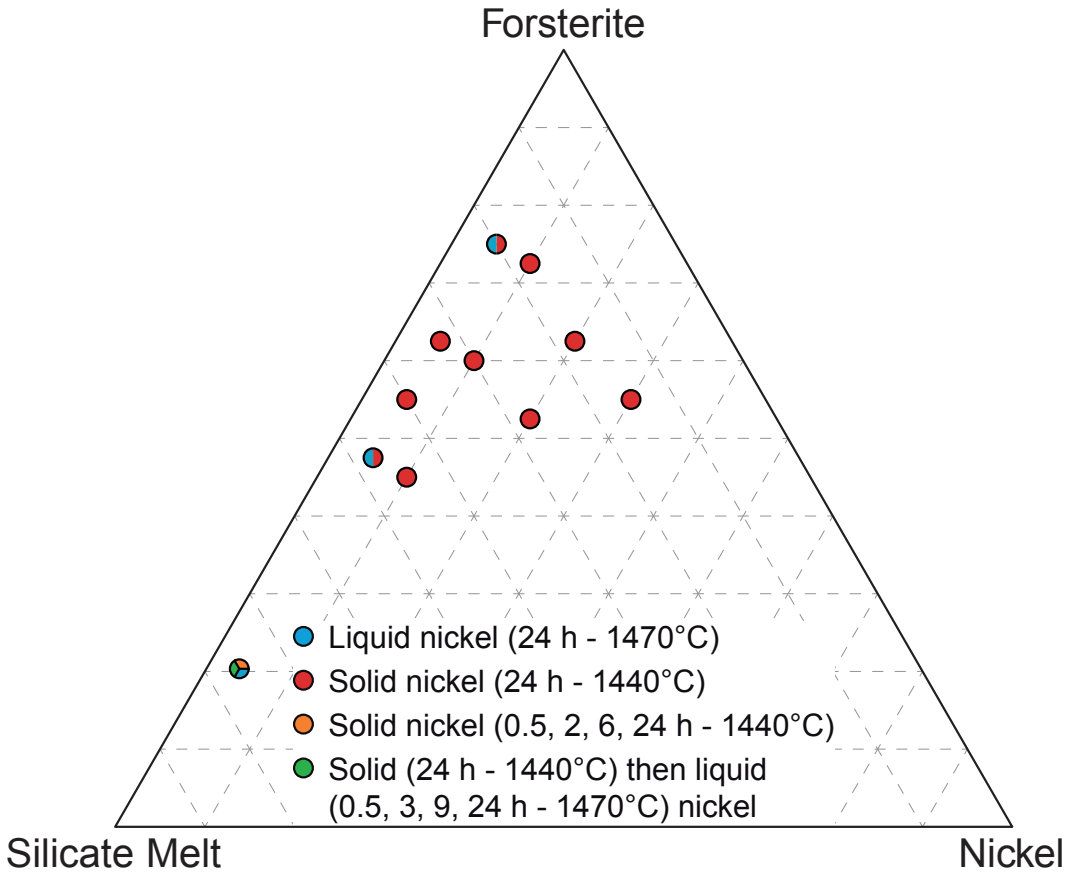

Figure 2.8 – Composition of atmosphere controlled 1-bar high temperature furnace experiments. Oxygen fugacity is set to $10^{-8.46}$ and temperature to 1713 K for experiments with solid nickel (red dots) or 1743 K for experiments with molten nickel (blue dots). Experiment duration is typically 24h. Orange dots correspond to a time-serie experiment with solid nickel. Green dots represent a time-serie experiment of samples that experienced 24 h at 1713 K and then different duration at 1743 K.

Figure 2.8 shows the composition for the AF experiments. Different colors indicate the state of nickel: solid (red dots at 1713 K) or molten (blue dots at 1743 K). Time-series experiments were also performed with the multi-quench setup to study textural evolution with time (orange dots for solid nickel) and with increasing temperature (green dot, from solid to molten nickel). f_{O_2} was set to $10^{-8.46}$ atm, i.e. $\Delta_{NNO} = -3$.

Figure 2.9 represents the composition of the different samples for the PC experiments. Here again, different colors represent different nickel states: red dots for solid (1723 K) and blue dots for molten (1773 K). One analogous experiment to AF with varying nickel state during the experiment was conducted and is represented in green. Green straight lines represent constant forsterite to forsterite plus melt ratios.

Figure 2.10 represents the starting composition of the different samples for the PE experiments. Colors represent the different compositions of the metallic subsystem: black for pure nickel, gray for the Ni-S eutectic ($Ni_{0.67}S_{0.33}$) and white for a composition of $Ni_{0.9}S_{0.1}$. The green dot indicates an experiment without metallic phases. Orange arrows show the path followed during the experiment upon increasing temperature.

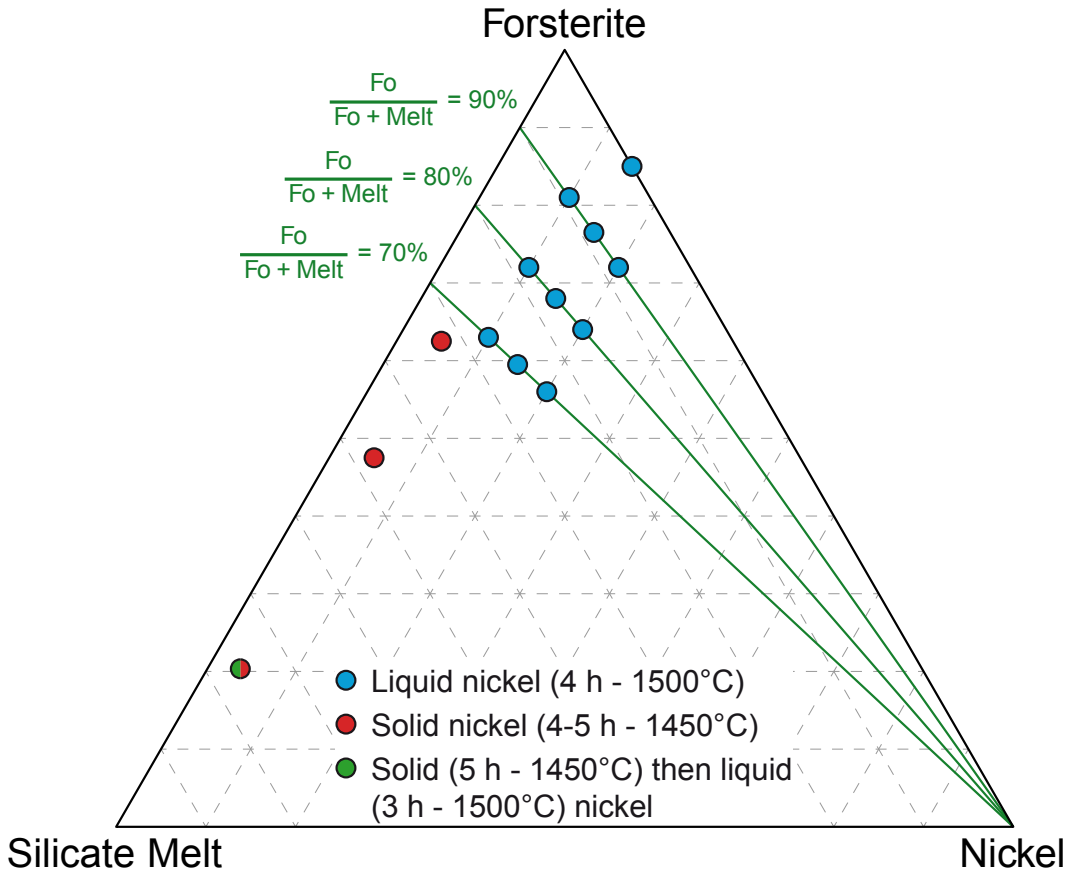

Figure 2.9 – Composition of piston-cylinder experiments. Pressure is set to 1 GPa and temperature to 1723 K for experiments with solid nickel and to 1773 K for experiments with molten nickel. A two-step experiment that underwent a first equilibration for 5 h at 1723 K and then 3 h at 1773 K was also prepared for comparison with the time-serie experiment in atmospheric furnace.

2.3 Analytical techniques

Samples were analyzed with 3D X-ray microtomography, Field Emission Gun Scanning Electron Microscopy (FEG-SEM) imaging, Electron BackScattered Diffusion (EBSD) or Electron Micro Probe Analyzer (EMPA). All these analysis are based on the interaction between matter and radiation, which is either made of X-rays or of an electron beam. 3D X-ray microtomography was applied as much as possible on whole samples (i.e. no slices or polished sections), while the other ones, implying the use of an electron beam, require polished sections for the sake of data quality.

2.3.1 Sample polishing

Recovered samples from experiments are trapped in epoxy resin and polished in a time first with silicon carbide sheets, using successive grain sizes of 25, 15, 8 and 5 µm. Between each grain size, samples are put in an ultrasound bath for $\approx$ 3 minutes to clean them of

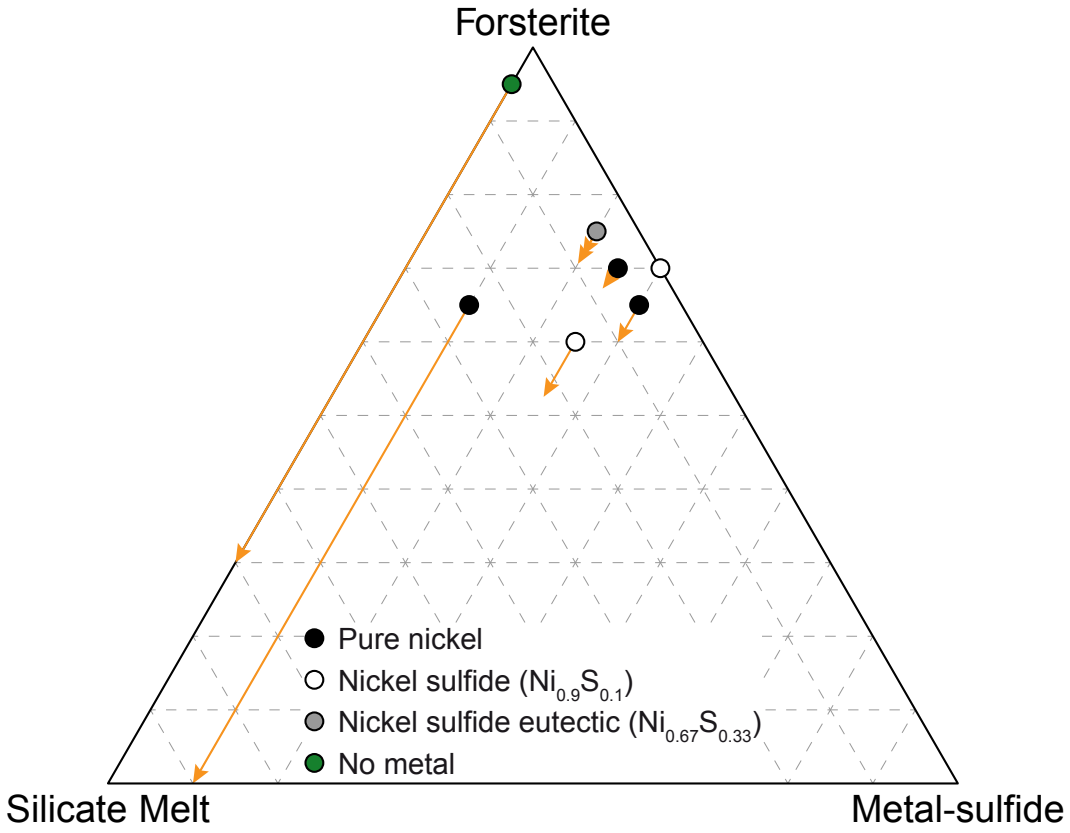

Figure 2.10 – Composition of Paris-Edinburgh press experiments. Pressure is set to 1 GPa and temperature varied up to ≈ 2123 K.Experiments were conducted either with pure nickel (black dots), no metal (green dot), nickel sulfide with a eutectic composition (gray dots) or an intermediate composition giving $Ni_{0.9}S_{0.1}$ in stoichiometry (white dots).

dust that was abraded. Then samples are polished with alumina (Al_2O_3) powder, from grain sizes of 1 (for 1 hour) down to 0.3 µm (for 2 hours). Finally, the surface of the sample was chemically attacked with colloidal silica for 2 additional hours.

Sections of primitive achondrites were re-polished using Al_2O_3 1 µm for one hour and Al_2O_3 0.3 µm for two hours. A881902 was first polished using silicon carbide abrasive paper down to 2.5 µm before using the alumina powders as described above. This fine-grain polishing is a necessary step to have good quality electronic analyses (Scanning Electron Microscopy, Electron BackScattered Diffusion and Electron MicroProbe Analysis). Coloïdal silica was not used to avoid any contamination on the surface of the thick sections.

2.3.2 FEG-SEM imaging

Scanning Electron Microscopy imaging is based on the detection of electrons that result from the interaction between the surface of the sample and an incident electron beam. When a primary electron arrives to the electronic cloud of an atom, it can collide with an electron of the outer regions of the cloud, ejecting it away (Figure 2.11a.). Such electrons are called

secondary electrons. They received a small amount of energy from the primary ones which allow them to travel through small distances of materials, as their energy is quickly dissipated. Hence, such secondary electrons come from the shallowest part of the surface of the sample and are mainly sensitive to topography between phases.

Interactions between incident electron beam and matter can also result in another type of electrons that is of interest: backscattered ones. Indeed, a primary electron that passes through the electronic cloud of an atom can be deviated and be re-emitted toward its incident direction (i.e. backscattered, Figure 2.11b.). Such electrons have properties that depend on the atomic number of the atom with which they interacted: statistically, heavy atoms deviate more electrons than light ones do. Hence, heavy phases will appear brighter than light ones. In the present case, metal will appear the brightest and silicate melt the darkest.

FEG-SEM images were acquired on a JEOL JSM-7800F Prime FEG-SEM at the Raimond Castaing center (Toulouse, France), with the help of Stéphane Leblond du Plouy. Images formed of either of the two type of detections or stacking both were acquired, providing information on the limit between phases and their organization at triple junctions. Magnification was varied to study the effect on the apparent shape of triple junctions and thus apparent dihedral angles of the different phases. Operating conditions are typically a 10 keV accelerating voltage and a 10 nA beam current.

2.3.3 Electron MicroProbe Analysis

EMPA analyses determine the composition of a phase. This technique is based on a different electron - matter interaction. Incident primary electrons can pass through the innermost layers of the electronic cloud of an atom and rip off a core electron, creating a gap. Other electrons from the outer layers will fall to fill this gap, this collapse is accompanied by the emission of X-rays with wavelength and energy that are characteristic of the atomic number of the element (Figure 2.11c.). Composition of a phases is calculated from the relative intensities of characteristic X-rays of different elements. Detection of these characteristics can be done following two main techniques. The first is the Energy Dispersive Spectroscopy (EDS) which sorts X-rays following their energy. This method allows to detect all elements at the same time, at the expense of accuracy of the analyses. EDS is often coupled with SEM in order to give a qualitative information on the composition of a phase. SEM-EDS was used to build mineral maps of the whole surface of the thick sections loaned by the MNHN, NIPR and NASA. The second technique is the Wavelength Dispersive Spectroscopy (WDS) which diffracts X-rays following their wavelength. Diffraction of a given wavelength requires the use of a monocristal. Although the number of elements to be measured is limited by the number of monocristals, accuracy of the measurement is much better.

Quantitative analyses of the composition of the phases were performed on a Cameca SXFive EPMA at the Raimond Castaing center (Toulouse, France), with the help of Philippe de Parseval and Sophie Gouy. Operating conditions are typically a 15 keV accelerating voltage, a 20 nA beam current and an analyzed surface of ≈ 2 µm^2. Periclase, corundum, wollastonite, platinum and nickel oxide were used as standards for Mg, Al, Ca and Si, Pt and Ni respectively.

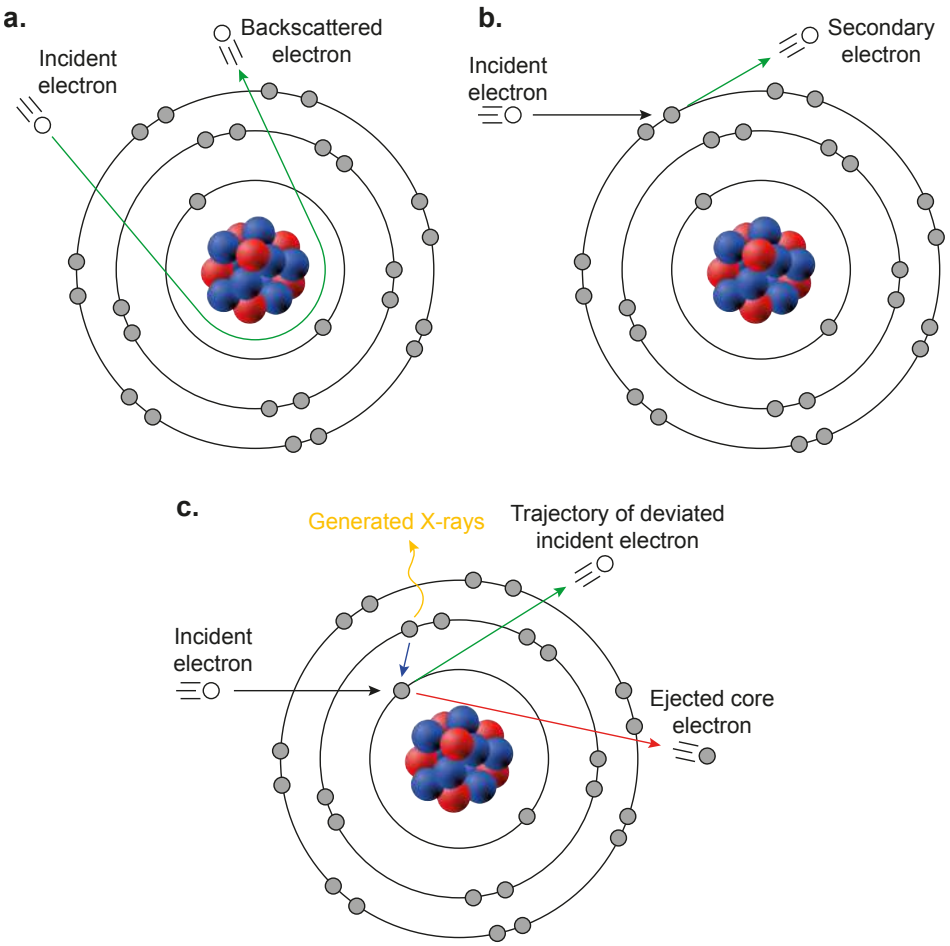

Figure 2.11 – Schemes showing the different incident electron - matter interactions used for the analytical techniques. (a.) Generation of backscattered electrons. (b.) Generation of secondary electrons. (c.) Generation of X-rays.

2.3.4 EBSD

The Electron BackScattered Diffusion is a technique that is coupled with a FEG-SEM to obtain information on crystalline orientations. This method uses another radiation - matter interaction, which is diffraction. The idea is that electrons from the incident beam are backscattered during a first interaction with the surface of the sample, then in a second interaction, they are diffracted on interreticular planes (hkl) following Bragg's law. Constructive interferences between diffracted electrons form two symetrical cones on both side of the hkl plane. When these cones intersect the plane of the detector, slightly curved and symmetric (with respect the hkl plane) bands appear, called Kikuchi lines. The width of a Kikuchi line depends on the distance between the sample and the detector but also on the interreticular space between two crystalline planes. As the distance between the sample and the detector is fixed and known, width of the Kikuchi lines only depend on the interreticular space. Assigning all the Kikuchi lines of a mineral to its hkl planes allows to identify the mineral and to determine its space parameters and orientation. Repeated analysis can be used to make a large-scale orientation map, giving information on the textures and deformation processes

that may have affected the sample. This technique is extremely sensitive to surface state of the sample, thus they were polished carefully following the method described in 2.3.1.

EBSD analyses were conducted on a FEG-SEM JEOL JSM 7100F TTLS LV at the Raimond Castaing center (Toulouse, France), with the help of Arnaud Proietti and Claudie Josse. Operating conditions were typically an accelerating voltage of 20 keV and a beam current of 18 to 20 nA. Large-scale orientation maps were done on natural samples loaned by the MNHN. In this case, as grains are large (100 µm or larger), step between analysis points was set to 8-9 µm.

2.3.5 3D X-ray microtomography

3D X-ray microtomography is an imaging technique based on the absorption contrast of the different phases. The absorption coefficient of a phase is linked to its density, with the heavier phases having larger absorption coefficients. The identification of the different phases is then better for large density differences, e.g. a silicate and a metal or a silicate and porosity. An incident X-ray beam passes through a sample to obtain an image similar to medical radiographies. Then the sample is rotated by a small angle (e.g. 0.25°) and another absorption is acquired (Figure 2.12). When the sample is rotated by 360°, all the images are loaded by a reconstruction algorithm that allows the generation of a 3D reconstructed volume. A three-dimensional data volume is composed of voxels, just as any image is composed of pixels. A voxel is then a cube of unitary length that corresponds to the resolution.

This method oversamples the region close to the rotation axis, as all 2D images intersect here. Resolution of the reconstructed volume depends on the distance between the sample and the X-ray source but also on the distance between the sample and the detector. The closest the sample to the source and the further the detector give the best resolution. With millimeter-sized experimental charges, resolution could go down to 1.5 µm per voxel for *ex-situ* analyses and down to 1.3 µm per voxel for *in-situ* analyses.

2.3.5.1 *Ex-situ* 3D X-ray microtomography

Ex-situ 3D X-ray microtomography was conducted on a Phoenix/GE Nanotom 180 at *CIRIMAT* (Toulouse, France), with the help of Benjamin Duployer and Christophe Tenailleau. Samples were stuck to a thin alumina rod with two holes, one of which bore a nickel wire with a measured diameter of 253 ± 3 µm. This wire is used as a standard to ensure proper thresholding of the nickel (see section 2.3.5.3). Samples were put as close as possible to the X-ray source and the detector as far as possible, in order to have a better resolution. A series of 1441 images was taken, giving a step of 0.25° in angle between two successive slices. For each slice, 5 images (750 ms per image) are acquired, out of which the first one is skipped to avoid remanence effects on the detector and the four other are stacked to improve the signal to noise ratio. The 1441th image acquired allow to check, and correct if necessary, the small motion of the sample that may have occurred during the acquisition. Indeed, the X-ray beam causes the samples to slightly heat, which may result in micrometric displacements. Data were then processed with Datosx reconstruction software to obtain the 3D volume.

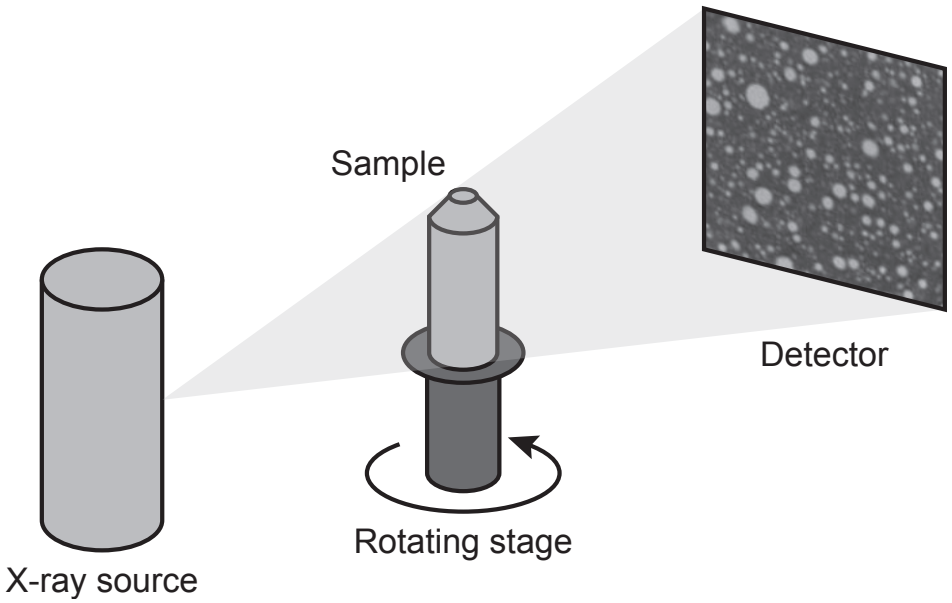

Figure 2.12 – Scheme showing the principle of 3D X-ray microtomography analysis.

2.3.5.2 *In-situ* 3D X-ray microtomography

In-situ 3D X-ray microtomography was conducted at the SOLEIL Synchrotron (Saclay, France), with the help of Nicolas Guignot and Andrew King. Here distances between the samples and the X-ray source or the detector cannot be varied and are fixed. The geometry of the beamline and beam parameters allow to have a resolution of 1.3 µm per voxel. A serie of 1500 images were taken, corresponding to a step of 0.24° in angle between each slice. As the beam is very energetic, exposure time is of 0.035 seconds per slice, which is way faster than for an *ex-situ* microtomography, allowing the acquisition of the 1500 slices in less than 1 minute. Data were then processed with an algorithm developped by Andrew King at SOLEIL to obtain the 3D volume. A Paganin filter (Paganin et al., 2002) was finally applied to enhance phase contrast. The Synchrotron beam is sufficiently coherent and the bandwidth is sufficiently low to apply this filter which uses the propagation phase contrast to increase contrast where attenuation contrast is limited. In other words, this filter attenuates the edge-enhancement effect, allowing to have better defined limits between phases and thus a better quantification of the blobs characteristics. However, the application of this filter induces a blurring effect, decreasing slightly the resolution.

2.3.5.3 3D data analysis

The analysis of 3D X-ray microtomography data consists in three steps: segmentation, separation and extraction; the order of these steps cannot be changed. In the segmentation step, a given 3D volume is analyzed to affect a set of contiguous voxels (corresponding to a specified range of grayscales) to a given phase. Then, separation allows the detection of individual and disconnected objects or blobs. Then, once all the blobs are identified, all their characteristics can be measured and extracted during the final step.

In the present case, the 3D reconstructed volumes were first visualized using VGStudio (at CIRIMAT, Toulouse, France), and then quantitative analyses were conducted with Blob3D (Ketcham, 2005). Whole volumes of atmospheric furnace experiments were loaded, but smaller Regions of Interest (RoIs) were defined for the piston-cylinder and Paris-Edinburgh experiments - typically $500 \times 500 \times 500$ voxels was defined. Besides the Paganin filter for Paris-Edinburgh press experiments, no additional procedures were applied (no dilation / erosion algorithms). Segmentation is the most critical step of the data analysis. In order to conduct a quantitative analysis, the right grayscale level has to be assigned to the right phase. To do so, simple thresholding was used. Due to the high precision of the weighting during sample preparation, the volume fraction of a phase was determined by its initial composition. For instance, in a mixture of forsterite, silicate melt and nickel with a given volume phase proportion of 72:8:20 (Fo:Liq:Ni), segmentation of the nickel was done so that the nickel volume fraction within the sample is equal to 20 vol%. In the case of *ex-situ* analyses, the Ni wire was used to check the consistency of this threshold with the size of the wire (250 ± 3 µm). No distinction could be done between forsterite and silicate melt, both phases have similar absorption coefficients with respect to the X-rays. Finally, the following parameters were extracted for each separated blob: volume, surface, sphere-normalized surface to volume ratio (SNSVR) and whether or not the blob is in contact with the border of the RoI. Images of blobs or rotating movies were also extracted using both Blob3D and ParaView (Ahrens et al., 2005; Ayachit, 2019).

2.4 MELTS thermodynamic modeling

MELTS simulation are needed to incorporate the experimental results into a larger-scale model and to highlight igneous processes. As primitive achondrites are partial melt residue, it is important to model the partial melting of a precursor material, invoking equilibrium of fractional processes, to understand their formation. In addition, from the data obtained on natural samples, MELTS simulation allow to track back the precursor material and to determine its formation condition in terms of oxygen fugacity.

Table 2.2 – H chondrite composition (in wt%) used for the MELTS thermodynamic simulations (from Wasson and Kallemeyn, 1988); the FeO content is calculated from the FeO/(FeO + MgO) ratio.

H chondrite composition Wasson and Kallemeyn (1988)										
Na_2O	K_2O	CaO	MgO	MnO	FeO	Al_2O_3	Cr_2O_3	SiO_2	TiO_2	P_2O_5
1.17	0.13	2.37	31.43	0.41	11.47	2.89	0.72	48.94	0.14	0.34

Rhyolite-MELTS thermodynamic software (Ghiorso and Sack, 1995; Asimow and Ghiorso, 1998; Gualda et al., 2012; Ghiorso and Gualda, 2015) allows to simulate melting or crystallization path for a given composition, for both equilibrium or fractionate processes. The algorithm is based on the minimization of Gibbs free energy and is calibrated on both natural and experimental samples. In the case of interest, silicate melting curves of H chondrites were calculated for both equilibrium and fractionate melting. Composition of H-type meteorites was taken from Wasson and Kallemeyn (1988); iron content of the silicates was calculated from the FeO/(FeO+MgO) ratio. The bulk silicate composition is detailed in Table 2.2. Oxy-

gen fugacity was set along the Iron-Wustite (IW - Fe-FeO) buffer. As pressure is low in early accreted small bodies, pressure was set to 1 bar and temperature ranged from 1223 to 2273 K. From these simulations, many information can be extracted. Mass and volume proportion were of particular interest, as well as the composition and density of the different phases and also the viscosity of the silicate melt.

Chapter 3

Metal segregation in planetesimals: Constraints from experimentally determined interfacial energies

Contents

Three-phase systems received little interest, it is yet unclear what are the geometry relations between the components. A first necessary step is to characterize phase relations. As the micro-scale geometry is dictated by an interfacial energy balance and that interfacial energies are reflected by the contact angles (dihedral angle), measuring these angles seem to be a key step to have a better apprehension of the organization of the system. In the literature, systems with olivine, basalt and sulfide melt (Fe-FeS eutectic composition) were studied by Holzheid et al. (2000). However, during the evolution of a planetesimal, the composition of the sulfide melt is likely to change due to progressive melting of the iron metallic residue. Hence, composition of the iron-sulfide melt ranges between two end-members: from that of the eutectic to that of pure metal. Choice was made here to focus on the pure metal end-member. In this aim, experiments were conducted in a 1-bar atmosphere controlled high temperature furnace with a mixture of forsterite, silicate melt and pure nickel. Samples are made of the following compositions (in Fo:Liq:Ni vol%): 20:75:5, 47.5:47.5:5, 62.5:32.5:5 and 75:20:5. Experimental conditions were a temperature of 1440 °C and an oxygen fugacity $\log(f_{O_2}) = -8.46$ atm (i.e. $\Delta_{Ni-NiO} = -3$) for 24 hours, except for the 75:20:5 experiment which lasted 10 days to check the attainment of textural equilibrium. For detailed information of sample synthesis and atmosphere furnace experiments, reader is referred to sections 2.1.3 and 2.2.1 respectively.

Chemical composition of the samples was checked using EMPA (following the description in section 2.3.3) and dihedral angles were measured using FEG-SEM (following the description in section 2.3.2). There was a will to do dihedral angle measurements at different magnification (i.e. resolution) of the FEG-SEM images to determine if there are different behaviors following the resolution of the imaged structures. Hence, images were acquired at $\times 250$ (376 nm/pixel), $\times 1,000$ (94 nm/ pixel), $\times 3,000$ (30 nm/pixel) and $\times 10,000$ (9.4 nm/pixel). Results show that there is an evolution of the measured dihedral angles of the different phases, until steady values are reached for resolutions of at least 30 nm/pixel. With this level of details, small-angle wedges of silicate melt at crystal interfaces are revealed, changing locally the dihedral angles and the shape of the triple junction. Besides, such resolutions also reveal an asymmetry in the dihedral angle distributions of silicate melt and olivine, an observation interpreted in terms of crystalline anisotropy of forsterite. Based upon the theoretical relation between dihedral angles and interfacial energies in a three-phase system, the relative magnitudes of interfacial energies have been determined to be: $\gamma_{Melt-Ol} < \gamma_{Melt-Ni} < \gamma_{Ol-Ni}$. This order differs from that obtained with experiments using an iron sulfide liquid close to the Fe-FeS eutectic (Holzheid et al., 2000) for which $\gamma_{Melt-Sulfide} < \gamma_{Melt-Ol} < \gamma_{Ol-Sulfide}$, implying a lower interconnection threshold for sulfur-rich melts than for pure metallic phases. This interconnection threshold - sulfur content dependence will affect the percolation of metallic phases during partial melting of small bodies. Assuming fractionate melting of the silicates, evolution of the metal volume fraction has been modeled following different sulfur content - wettability relations. Results of these calculations show that several sulfur-rich melts extraction events are possible over a range of temperatures relevant with thermometric data obtained on primitive achondrites (1200 - 1400 °C and 25 vol% of silicate melt extracted). These successive events provide novel insight into the variability of sulfur content in primitive achondrites, which are either representative of a region that experienced sulfide extraction or from a region that accumulated sulfide melt from overlying parts of the parent body. This work has been published in Néri et al. (2019).

3.1 Introduction

Metal-silicate differentiation in early-accreted bodies of the solar system involves processes that are still poorly understood. Metal connectivity is a key factor because efficient phase separation requires an interconnected network of the metal-rich phase. In other words, the interconnection threshold (i.e. the volumetric phase fraction at which the phase forms a continuous network) has to be reached. This threshold is often assumed to have a very low value (3 to 6 vol%, e.g. Šrámek et al., 2012). However, the meteoritic record shows evidence of incomplete metal segregation. For example, primitive achondrites (e.g. Acapulcoites and Lodranites) are partially differentiated natural samples that exhibit signs of silicate partial melting, up to 25 vol% (e.g. Bild and Wasson, 1976; McCoy et al., 1997, 1996; Palme et al., 1981; Papike et al., 1995; Zipfel et al., 1995) and have FeNi alloy contents up to $\approx$ 20 vol% and troilite contents of $\approx$ 3 vol% (Bild and Wasson, 1976; Palme et al., 1981). Under these conditions, the metal content is larger than commonly assumed interconnection thresholds and these bodies should be fully differentiated, which they are clearly not. To rationalize this observation, either metal-rich phases did not readily form a connected network and/or the kinetics of metal segregation were slow compared to cooling time-scales. While this latter possibility cannot be excluded for the case of primitive achondrites - because the parent bodies were planetesimals of modest radius (Neumann et al., 2018), the gravitational driving force for segregation was low - the question of relevant values of segregation threshold must be treated first. In general terms, the interconnection threshold is a function of interfacial energies that drive the geometry of local phase boundaries to minimize the energy of the system (Bulau et al., 1979; Jurewicz and Watson, 1985; Smith, 1964). Thus, the system will evolve to shorten high-energy interfaces at the expense of lower energy geometries. Physical expression of these effects corresponds to the set of dihedral angles that form at phase triple junctions (i.e. where three phases meet). In a two-phase system (e.g. melt - mineral), the dihedral angle θ, corresponding to the angle of the melt between two solid grains, is described by equation 3.1 (Smith, 1964).

$$2\cos\left(\frac{\theta}{2}\right) = \frac{\gamma_{SS}}{\gamma_{SL}}\,, \tag{3.1}$$

where γ_{SS} is the solid-solid interfacial energy and γ_{SL} the solid-liquid interfacial energy (in J.m^{-2}).

Measuring dihedral angles is thus a way to quantify the ratios of interfacial energies and to constrain variations in interconnection threshold. Two methods are commonly used to measure dihedral angles: the first one is the sessile drop technique using in-situ X-Ray imaging a droplet on a solid substrate (e.g. Humenik Jr. and Kingery, 1954; Jung et al., 2010). The second one consists in a more statistical approach with repeated measurements on 2D scanning electron images. In this work the second method was preferred as it allows more accurate imaging of the triple junctions. In the case of a two-phase system, such as a metallic melt in an olivine matrix, the relation between interconnection threshold and dihedral angle is well established (e.g. Laporte and Provost, 2000). For instance, an iron-dominated metallic liquid typically has a high dihedral angle of 110 - 130° in an olivine matrix (Gaetani and Grove, 1999; Shannon and Agee, 1996), corresponding to an interconnection threshold of roughly 10 to 15 vol% (Laporte and Provost, 2000). Adding light elements (C, O, S) to this metallic melt decreases its dihedral angle, and therefore its interconnection threshold

(Ballhaus and Ellis, 1996; Gaetani and Grove, 1999; Holzheid et al., 2000; Minarik et al., 1996). For compositions in the vicinity of the Fe–FeS eutectic, dihedral angles span a range from 60° up to 90°, yielding a broad range of interconnection thresholds from 0 to 7 vol% (as estimated from Laporte and Provost, 2000). However, as mentioned above, segregation is not efficient in such systems, core formation being too slow to match with the meteoritic record (Bagdassarov et al., 2009b). Adding a silicate melt makes the experimental system more realistic and tends to promote more efficient segregation (Bagdassarov et al., 2009b). However, equilibrium geometries of such three-phase systems (crystalline silicate + silicate melt + pure metal or sulfide) have received little attention. To our knowledge, data are only available for a Fe-FeS eutectic composition (Holzheid et al., 2000) in a partially molten system of San Carlos olivine and basalt.

During the evolution of a planetesimal, composition of the metallo-sulfide phase ranges from the eutectic composition, representing the first metal-rich liquids produced, to pure metal (FeNi). The present study focuses on the measurement of dihedral angles and equilibrium geometries in that latter end-member. Constraints are obtained using high temperature experiments in a one-atmosphere furnace, a pressure relevant given the low-pressure environment in early-accreted planetesimals. Equilibrium textures in the experimentally produced samples containing partially molten silicate and pure metal are then used to construct a global metal-silicate differentiation model that can help to rationalize the observed mineralogy of primitive achondrites.

3.2 Experimental setup

Experiments were performed in a controlled-atmosphere vertical high-temperature furnace, using a three-phase system. Experiments allow to determine the equilibrium geometries between forsterite, silicate melt and nickel with accurate quantification of the dihedral angles and associated interfacial energies.

3.2.1 Synthesis of starting material

Samples are mixtures of crystalline forsterite (Fo), silicate melt (Liq) and nickel metal (Ni). The starting material was prepared in two steps. First, a silicate glass was synthesized, with a composition in equilibrium with forsterite at 1430 °C as determined from the Anorthite – Diopside – Forsterite ternary phase diagram in the CMAS (CaO – MgO – Al_2O_3 – SiO_2) system (Morse, 1980), a good analogue of iron-free silicate melts in meteorites. Thus, the proportion of silicate melt (of fixed composition) can be varied at a single temperature. Oxide powders (SiO_2 99.8% - Alfa Aesar, Al_2O_3 99.999% extra pure - Acros) and carbonates ($CaCO_3$ 99+% - Acros, $4(MgCO_3).Mg(OH)_{2.5}(H_2O)$ - Acros) were mixed in appropriate proportions to produce the desired composition of silicate melt (Table 3.1). This mixture was finely ground, placed in a platinum crucible and held for two hours at 1100 °C to allow complete dehydration and decarbonation, then heated to 1500 °C for two hours for melting. The material was quenched, ground and put back in the furnace at 1500 °C for two additional hours to ensure chemical homogeneity. After quenching, glass composition was checked using

Electron Micro Probe Analysis (EMPA, Table 3.1). Finally, the glass was finely crushed before mixing with the other components.

Although metal is dominated by iron in natural samples, nickel has been chosen in light of its lower melting point and its stability at higher oxygen fugacity (fO_2). This choice allowed performing experiments (at conditions of temperature and fO_2 that are easily obtained and controlled) in which the metallic subsystem does not interact significantly with the silicates, i.e. the diffusion of Ni in forsterite and silicate melt is low (see section 3.3.1).

In the second stage of sample synthesis, the glass was mixed with commercial powders of forsterite (Neyco CERAC, Inc., 325 mesh, 99% pure; grain size 0-40 µm) and nickel (Goodfellow, 99.8% pure, grain size 1-70 µm), with fixed metal content but varying forsterite/glass ratios to investigate the effect of the relative abundance of these two phases (Fo:Liq:Ni expressed in vol%): 20:75:5, 47.5:47.5:5, 62.5:32.5:5, 75:20:5. The obtained mixtures were sintered to reduce porosity as the gas trapped between grains may act as a fourth phase with its own interfacial energy. Spark Plasma Sintering (SPS) was used at the PNF^2 platform (CIRIMAT, Toulouse, France), in an argon vacuum, at 100 MPa and 1200 °C for 5 min, as described by Guignard et al. (2011). The 20:75:5 mixture could not be sintered by SPS due to devitrification around 900 °C that caused the graphite mold to break due to the large change in volume of the sample. In this case, the wire loop technique was employed using a platinum wire ($\varnothing$ = 0.2 mm, 99.9% pure - Johnson Matthey) on which $\approx$ 30 mg of sample was placed and put for 30 s at 1500 °C to form a droplet held on the loop by surface tension.

3.2.2 Annealing experiments

Experiments were performed in the vertical furnace at a fixed temperature of 1440 °C, $\approx$ 15 °C below the melting point of nickel. Temperature was measured ($\pm$1 °C) using an S-type thermocouple ($PtRh_{10\%}/Pt$). The oxygen fugacity was fixed by mixing appropriate proportions of CO/CO_2 yielding a $\log(fO_2)$ of -8.46 atm. (i.e. Ni-NiO = -3). Such reducing conditions allow nickel grains to remain in their metallic state and limit diffusion and dissolution into silicates. Annealing experiments were run for 24 h for all samples and an additional experiment of 10 days was performed on the 75:20:5 mixture to check attainment of textural equilibrium.

3.2.3 Analytical techniques

After experiments, samples were mounted in epoxy resin and polished down to 0.3 micron using Al2O3 grit for 2 h. FEG-SEM (Field Emission Gun Scanning Electron Microscope) and EPMA were then performed.

Textures and dihedral angles were analyzed with the image processing software Fiji (Eliceiri et al., 2012; Schindelin et al., 2012) from digital images acquired by backscattered electron detection, secondary electron detection, or stacking both kinds of images, on a JEOL JSM-7800F Prime FEG-SEM at the Raimond Castaing center in Toulouse (France). Images were acquired using a 10 keV accelerating voltage and a 10 nA beam current. There are two levels

of organization of triple junctions depending on the scale of observation. At macroscale, the minimization of interfacial energies has a weak effect on the geometry that is principally controlled by crystallographic orientation. On the other hand, at microscale, at the apex of the triple junctions, geometry is dictated by the minimization of interfacial energies between the three phases. To quantify a potential shift from a macroscopic to a microscopic behavior, various magnifications and thus resolutions were investigated: ×250 (376 nm per pixel), ×1,000 (94 nm per pixel), ×3,000 (30 nm per pixel) and ×10,000 (9.4 nm per pixel). Quantitative analyses of the chemical composition of the phases were performed using a Cameca SXFive EPMA at the Raimond Castaing Center (Université Paul Sabatier, Toulouse, France). The operating conditions were: accelerating voltage 15 keV; beam current 20 nA; analyzed surface of $\approx 2 \times 2$ µm^2. Periclase, corundum, wollastonite, platinum and NiO were used as standards for Mg, Al, Ca and Si, Pt, and Ni respectively.

3.3 Dihedral angle measurement

3.3.1 Chemical and textural equilibrium

Chemical equilibrium was checked using EPMA on the two silicate phases (Table 3.1). The composition of the glass is found to not perfectly match the equilibrium composition expected at 1450 °C. This difference can be explained by crystallization of forsterite ($\approx$ 4 wt%) during sample quench. NiO was detected in forsterite and silicate glass, at levels of 2 wt% and 0.6 wt%, respectively (Table 3.1). No concentration profile was observed in either of these phases, which is in agreement with diffusion and partitioning coefficients previously obtained at similar experimental conditions (Dingwell et al., 1994; Petry et al., 2004; Borisov, 2006; Matzen et al., 2017), indicating chemical equilibrium. Textural equilibrium was checked using SEM images (Figure 3.1). In the 20:75:5 and 47.5:47.5:5 samples, nickel grains are elongated in comparison with the other samples. A remarkable feature of the 20:75:5 sample is that nickel is clustered at the center of the sample and forms an interconnected network. Looking at textures at the grain scale, similar features and forsterite triple junctions at 120° are observed in all samples. There are no differences in the textures or in the dihedral angle distributions (see section 3.3.2) between 24 hour- and 10 day-experiments. Hence, at triple junction scale, textural equilibrium is reached.

Table 3.1 – Composition in wt% of the starting materials and composition of the different phases after experiments. Error bars, expressed as 2σ standard deviation, were estimated based on repeated measurements of at least 30 points for each phase. Phase composition of samples are expressed in volume proportions following Fo:Melt:Ni.

Phase composition (wt%)	MgO	SiO_2	CaO	Al_2O_3	NiO	Sum
Commercial Forsterite	57.55 ± 0.78	43.03 ± 0.55	0.55 ± 0.16	0.00	0.00	101.17
Aimed silicate melt	22.92	45.49	14.55	17.04	0.00	100.00
Starting silicate melt	23.83 ± 0.32	44.72 ± 0.84	14.70 ± 0.31	16.75 ± 0.49	0.00	100.00
Forsterite in 20:75:5	54.68 ± 0.58	42.50 ± 0.52	0.50 ± 0.05	0.20 ± 0.07	2.12 ± 0.73	100.00
Forsterite in 47.5:47.5:5	54.78 ± 0.45	42.47 ± 0.53	0.50 ± 0.06	0.20 ± 0.08	2.04 ± 0.54	100.00
Silicate melt in 20:75:5	21.32 ± 0.57	44.58 ± 0.22	15.23 ± 0.44	18.26 ± 0.33	0.60 ± 0.26	100.00
Silicate melt in 47.5:47.5:5	21.43 ± 0.29	43.94 ± 0.19	15.50 ± 0.13	18.53 ± 0.15	0.60 ± 0.11	100.00

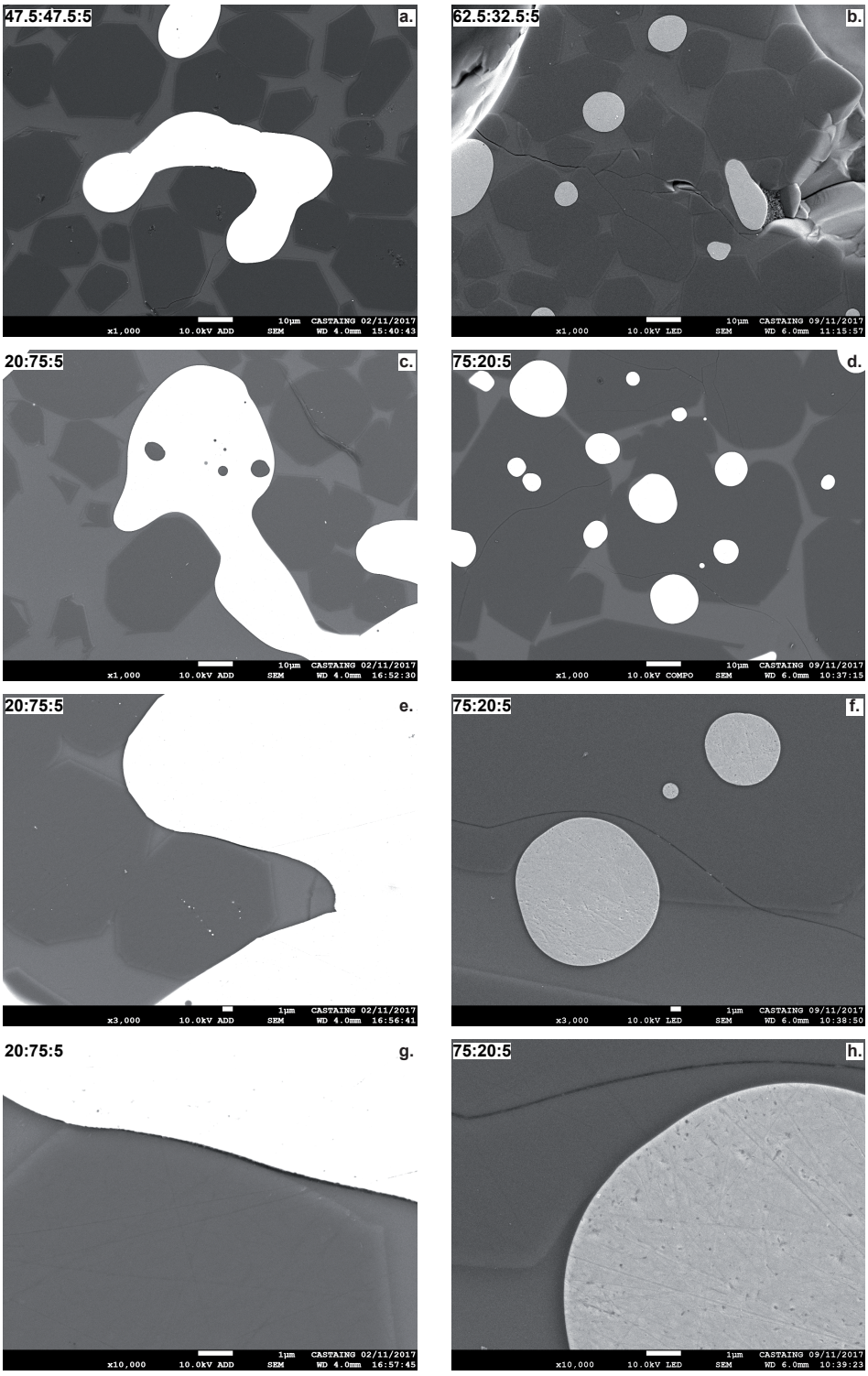

Figure 3.1 – SEM images representative of different samples. White: nickel; dark gray: forsterite and light gray: silicate melt. (a.) 47.5:47.5:5 sample at $\times 1,000$ (94 nm per pixel), (b.) 62.5:32.5:5 samples at $\times 1,000$ (94 nm per pixel), (c.) 20:75:5 sample at $\times 1,000$ (94 nm per pixel), (d.) 75:20:5 sample at $\times 1,000$ (94 nm per pixel), (e.) 20:75:5 sample $\times 3,000$ (30 nm per pixel), (f.) 75:20:5 sample at $\times 3,000$ (30 nm per pixel), (g.) 20:75:5 sample at $\times 10,000$ (9.4 nm per pixel), (h.) 75:20:5 sample at $\times 10,000$ (9.4 nm per pixel). Images on (g.) and (h.) highlight the hook shape of the silicate melt toward the apex of triple junctions. This kind of structure is typically of 100 nm at half-height of the hook, requiring a resolution threshold of 30 nm per pixel to have a proper imaging.

3.3.2 True dihedral angle measurement

Dihedral angles of silicate melt and forsterite were measured using the "angle tool" of the Fiji distribution of ImageJ, while the dihedral angle of nickel was inferred from the two others, considering that the sum of the three dihedral angles is 360°. In order to obtain sufficient statistics, measurements were repeated on at least 100 different triple junctions. These measured distributions are called apparent dihedral angle distributions, as they are representative of a 2D slice in a 3D volume. For a single population of dihedral angles, these apparent distributions can be fitted with a Gaussian function centered on the median value (Jurewicz and Jurewicz, 1986), that corresponds to the true dihedral angle, i.e. the dihedral angle in the 3D volume.

3.3.2.1 Transition between macroscopic and microscopic behavior of triple junctions

Figure 3.2a, 3.2b and 3.2c displays the true dihedral angle for each phase in each sample as a function of pixel size. With increasing detail (i.e. decreasing pixel size), the dihedral angle of the melt decreases from $\approx 70°$ to $\approx 25°$, and then reaches a steady value within uncertainty, from 30 nm per pixel. Dihedral angles of forsterite and Ni exhibit the opposite trend upon increasing resolution, increasing from 125° to 160° for forsterite and from 160° to 175° for Ni, until a constant value is reached. These observations indicate that microfilms and/or micro-channels of silicate melt are present between forsterite and/or Ni grains, as previously suggested by Cmíral et al. (1998). For low melt fractions, distribution of the melt can be anisotropic (Faul, 2000): some grain boundaries are still dry whereas the others are wetted by silicate melt, and the width of channels between grains may vary from 10 to 100 nm, making resolution a key parameter to image melt distribution (Garapić et al., 2013). In the present study, close to triple junctions, these structures represent hooks between forsterite and nickel grains that are thinner and thinner toward the apex of the triple junction (Figure 3.1g and 3.1h). Typically, the width of these structures at half-length of the hook is about 100 nm. To be accurately measured, we considered that at least 9 pixels are needed, i.e., a resolution threshold of 30 nm per pixel corresponding to a $\times 3,000$ magnification in our case. At lower resolution, the continuous evolution of dihedral angle as a function of magnification indicates a continuous evolution from the microscopic to the macroscopic energy balance.

It is also of note that at low resolution (376 and 94 nm per pixel), dihedral angles appear to be a function of phase proportions. For instance, the 20:75:5 and the 47.5:47.5:5 samples (i.e., where Ni grains are elongated and seem to form a network) show dihedral angles of roughly 60° for the silicate melt and 170° for the nickel, whereas the 62.5:32.5:5 and the 75:20:5 samples (i.e. samples with isolated beads of nickel) exhibit angles that are 20° higher for silicate melt and 15° lower for nickel (Figure 3.2a and 3.2c). At higher resolution this difference is no longer apparent, highlighting the same microscopic behaviors but different macroscopic ones.

Once all the small-scale details are unraveled, all samples display the same dihedral angle distribution and the same values of true dihedral angles, regardless of the proportions of each phase. In light of this result, the different datasets for a same magnification were merged to

provide better statistics on the dihedral angle distribution. In the remainder of the text, the median values of these new merged distributions are considered as the true dihedral angles (Figure 3.2 and Table 3.2).

Table 3.2 – Median dihedral angles (in °) at the triple junctions for different magnifications and all samples. The merged sections correspond to all datasets put together. In each column, the value of the dihedral angle is reported with its 2SE ($2SE = \frac{2SD}{\sqrt{N-1}}$ where SD is the standard deviation and N the number of measurements) uncertainty.

Composition		×250 (376 nm per pixel)	×1,000 (94 nm per pixel)	×3,000 (30 nm per pixel)	×10,000 (9.4 nm per pixel)
20:75:5	Fo	126.7 ± 11.0	149.6 ± 5.1	161.1 ± 5.0	164.7 ± 6.3
	Melt	62.6 ± 1.1	37.4 ± 5.5	24.1 ± 6.1	21.2 ± 5.2
	Ni	170.9 ± 0.6	175.3 ± 2.3	177.3 ± 4.0	179.2 ± 4.2
47.5:47.5:5	Fo	126.2 ± 1.5	145.9 ± 6.1	166.8 ± 7.2	164.4 ± 4.3
	Melt	63.4 ± 1.7	38.4 ± 6.3	19.3 ± 6.8	18.3 ± 7.4
	Ni	167.7 ± 0.8	174.2 ± 2.6	176.6 ± 3.0	180.0 ± 5.1
62.5:32.5:5	Fo	126.9 ± 1.5	150.2 ± 5.1	156.2 ± 5.9	157.6 ± 6.2
	Melt	80.0 ± 1.6	46.9 ± 5.2	27.8 ± 5.6	24.5 ± 5.5
	Ni	155.6 ± 0.8	165.8 ± 1.8	175.0 ± 1.7	175.6 ± 2.3
75:20:5	Fo	122.4 ± 1.1	145.5 ± 4.5	162.6 ± 5.5	163.6 ± 9.4
	Melt	84.3 ± 1.2	50.8 ± 4.6	26.5 ± 5.0	22.6 ± 6.6
	Ni	155.7 ± 0.5	164.5 ± 1.5	174.1 ± 2.2	176.2 ± 4.8
Merged	Fo	125.6 ± 1.2	148.4 ± 2.6	161.1 ± 3.0	161.7 ± 3.8
	Melt	70.5 ± 1.4	42.2 ± 2.7	24.7 ± 2.9	21.4 ± 3.1
	Ni	162.3 ± 0.7	168.8 ± 1.1	175.3 ± 1.3	176.9 ± 1.8

3.3.2.2 Macroscale behavior: apparent isotropy

Figure 3.2d and 3.2e shows the merged dihedral angle distributions at 376 and 94 nm per pixel and associated Gaussian fits for each phase. These distributions are fitted with an unimodal Gaussian curve, as suggested by Jurewicz and Jurewicz (1986). The quality of the fit is better for the 376 nm per pixel distributions than for that at 94 nm per pixel, due to a slight asymmetry of the latter and an intermediate behavior between macro- and micro-scales. The good agreement between data and unimodal Gaussian curves suggests that there is a single population of dihedral angles, so at this macroscale, olivine grains appear isotropic, as commonly assumed in most previous studies of dihedral angles in this type of system.

3.3.2.3 Microscale behavior: crystalline anisotropy of forsterites

At the microscale, i.e. close to the apex of the triple junctions (Figure 3.2f, 30 and 9.4 nm per pixel), distributions for forsterite and silicate melt become clearly asymmetric, with the emergence of a narrow peak and a shoulder towards lower values for forsterite, and higher values for silicate melt. In this case, data cannot be fitted by a unimodal Gaussian function. Similar features appear when angle distributions are mixed (Jurewicz and Jurewicz, 1986), indicating a possible difference of interfacial energies along crystal faces. In this respect, it has been shown that wetting behavior of olivine depends on crystal orientation (e.g. Jung and

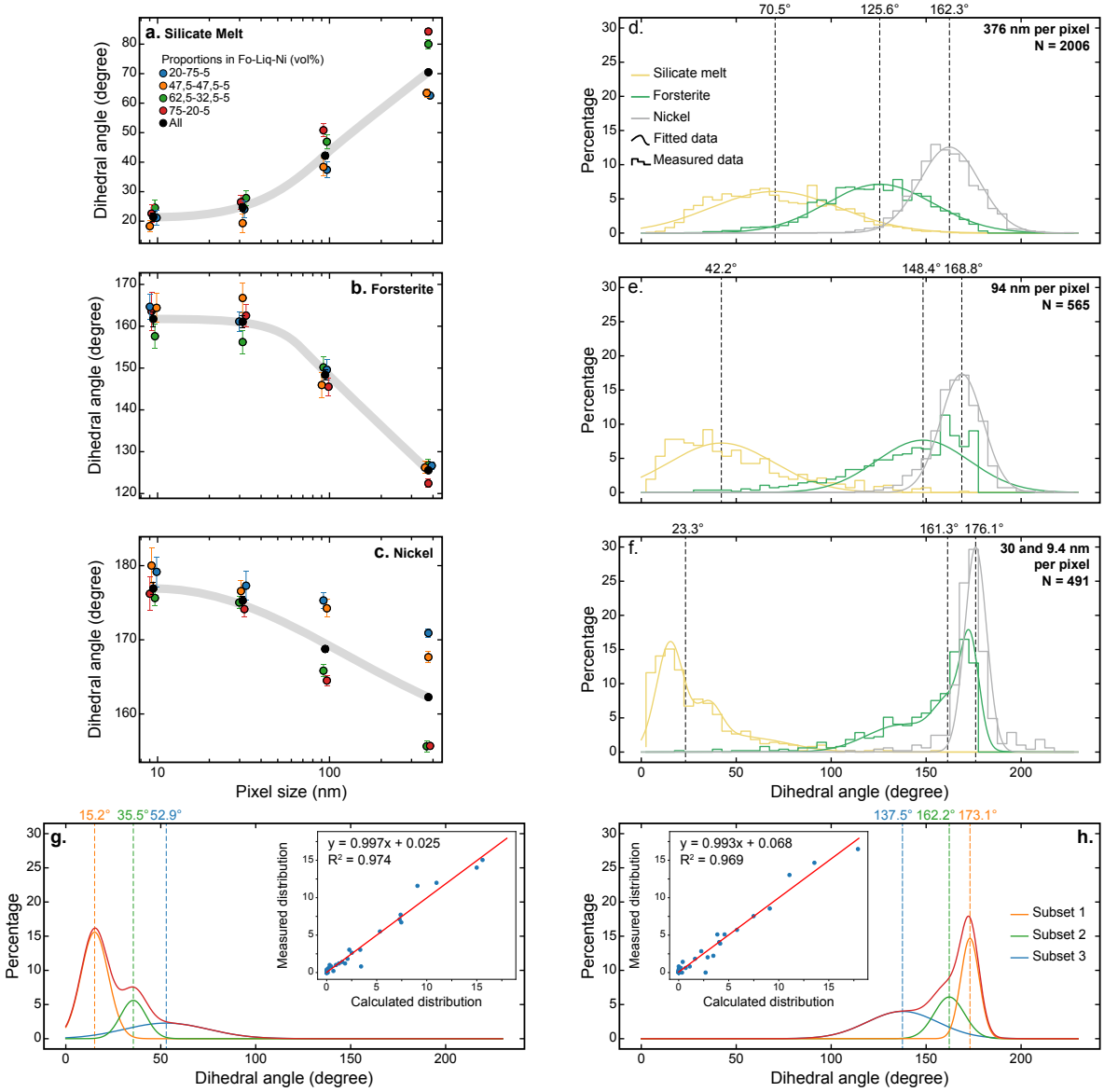

Figure 3.2 – Measured median dihedral angle as a function of pixel size (in nm) for (a.) silicate melt, (b.) forsterite, (c.) nickel and merged dihedral angles distributions at different pixel sizes: (d.) 376nm per pixel, (e.) 94nm per pixel and (f.) 30 and 9.4nm per pixel. Circle color symbols on (a.), (b.), (c.) correspond to different samples, black circle represents the median value of all datasets merged at a given magnification and gray lines are guides for the eyes. These three diagrams show that the dihedral angle reaches steady value at a pixel size of 30 nm per pixel, corresponding to the resolution at which the fine microstructure is entirely imaged. Scatter between different samples at lower resolution is due to measurement artifacts, as this small-scale geometry is not entirely imaged. Step curves on (d.), (e.) and (f.) correspond to the dihedral angle distribution, curly curves correspond to Gaussian fits, single Gaussian function for (d.) and (e.) and triple Gaussian function for(f.); black dotted lines represent the median value of the distributions. The agreement between data and triple Gaussian fit is shown in (g.) for the silicate melt distribution and in (h.) for the olivine distribution. Orange, green and blue dotted vertical lines correspond to median values of each subset of dihedral angle. Increasing the resolution makes the distribution more asymmetric, meaning that different populations of dihedral angle exist, representative of the forsterite crystalline anisotropy at microscale.

Table 3.3 – Dihedral angles of the different phases when crystalline anisotropy is considered and corresponding interfacial energy ratios. * Correspond to values calculated from dihedral angle data. Uncertainties are 2SE calculated using the derivative method.

Populations	Phase	Dihedral angle (in °)	Interfacial energy ratios	
	Fo	125.6 ± 1.2	$\gamma_{Melt-Fo}/\gamma_{Melt-Ni}$	0.374 ± 0.016
$\times 250$	Melt	70.5 ± 1.4	$\gamma_{Melt-Fo}/\gamma_{Fo-Ni}$	0.323 ± 0.013
	Ni	162.3 ± 0.7	$\gamma_{Melt-Ni}/\gamma_{Fo-Ni}$	0.862 ± 0.015
	Fo	148.4 ± 2.6	$\gamma_{Melt-Fo}/\gamma_{Melt-Ni}$	0.372 ± 0.044
$\times 1,000$	Melt	42.2 ± 2.7	$\gamma_{Melt-Fo}/\gamma_{Fo-Ni}$	0.290 ± 0.031
	Ni	168.8 ± 1.1	$\gamma_{Melt-Ni}/\gamma_{Fo-Ni}$	0.781 ± 0.070
	Fo	173.1 ± 0.7	$\gamma_{Melt-Fo}/\gamma_{Melt-Ni}$	0.358 ± 0.104
Subset 1	Melt	15.2 ± 1.1	$\gamma_{Melt-Fo}/\gamma_{Fo-Ni}$	0.265 ± 0.077
	Ni	176.1 ± 1.1	$\gamma_{Melt-Ni}/\gamma_{Fo-Ni}$	0.741 ± 0.071
	Fo	162.2 ± 1.5	$\gamma_{Melt-Fo}/\gamma_{Melt-Ni}$	0.140 ± 0.040
Subset 2	Melt	35.5 ± 1.2	$\gamma_{Melt-Fo}/\gamma_{Fo-Ni}$	0.125 ± 0.035
	Ni	176.1 ± 1.1	$\gamma_{Melt-Ni}/\gamma_{Fo-Ni}$	0.893 ± 0.050
	Fo	137.5 ± 2.7	$\gamma_{Melt-Fo}/\gamma_{Melt-Ni}$	0.093 ± 0.026
Subset 3	Melt	52.9 ± 3.2	$\gamma_{Melt-Fo}/\gamma_{Fo-Ni}$	0.087 ± 0.025
	Ni	176.1 ± 1.1	$\gamma_{Melt-Ni}/\gamma_{Fo-Ni}$	0.943 ± 0.060
	Fo	161.3 ± 2.4	$\gamma_{Melt-Fo}/\gamma_{Melt-Ni}$	0.214 ± 0.066
Merged	Melt	23.3 ± 2.1	$\gamma_{Melt-Fo}/\gamma_{Fo-Ni}$	0.174 ± 0.052
	Ni	176.1 ± 1.1	$\gamma_{Melt-Ni}/\gamma_{Fo-Ni}$	0.811 ± 0.121
Literature data representative of natural samples			Interfacial energy ratios	
Ballhaus and Ellis (1996)	Sulfide	68 to 86	$\gamma_{Ol-Ol}/\gamma_{Ol-Sulfide}$ *	1.463 to 1.658
Two-phase system	FeNi alloy	113 to 115	$\gamma_{Ol-Ol}/\gamma_{Ol-FeNi}$ *	1.075 to 1.104
Holzheid et al. (2000)	Ol	136 ± 5	$\gamma_{Melt-Fo}/\gamma_{Melt-Sulfide}$ *	1.221 ± 0.129
Three-phase system	Melt	102 ± 5	$\gamma_{Melt-Fo}/\gamma_{Fo-Sulfide}$ *	0.867 ± 0.050
	Sulfide	122 ± 5	$\gamma_{Melt-Sulfide}/\gamma_{Fo-Sulfide}$ *	0.710 ± 0.066

Waff, 1998; Wanamaker and Kohlstedt, 1991). Hence, the asymmetry of the distributions may be linked to different populations of dihedral angles reflecting the anisotropic behavior of forsterite. On the other hand, dihedral angle distribution of nickel remains very symmetric, which can be explained by its cubic crystalline system for which all crystal planes are equivalent. Finally, due to its low viscosity, silicate melt accommodates the anisotropy of forsterite and has thus different dihedral angle populations due to different olivine orientations. Three principal populations of interfacial energies exist in forsterite crystals (Jung and Waff, 1998), corresponding to Miller indices of (010), (110) and a family of minor crystal planes ((021), (120), (001), (101) and (100)). Hence, three Gaussian functions were fitted on both silicate melt and forsterite dihedral angle distributions (Figure 3.2f, 3.2g and 3.2h). The agreement between measured and calculated distributions is characterized by a correlation greater than 0.95 (inset in Figure 3.2g and 3.2h). The newly obtained median values for each population are 15.2°, 35.5° and 52.9° for the silicate melt and 173.1°, 162.2° and 137.5° for the olivine, each pair of dihedral angles corresponding to a new subset called 1, 2 and 3 respectively (Table 3.3). Calculating the area under each Gaussian provides the proportion of each population of interfacial energies, corresponding roughly to $\approx 33\%$ for each distribution. These values are in good agreement with the proportions of the crystallographic planes given by Jung and Waff (1998).

3.4 Determination of interfacial energies and consequences on phase relations

3.4.1 Theoretical approach in a three-phase system

In a three-phase system, the equilibrium geometry of a triple junction can be represented as in Figure 3.3. When textural equilibrium is reached, the three different dihedral angles θ_1, θ_2 and θ_3 vary as a function of the interfacial energies γ_{12}, γ_{13} and γ_{23} according to equation (3.2), assuming crystalline isotropy (Laporte and Provost, 2000; Smith, 1964).

$$\frac{\gamma_{12}}{\sin(\theta_3)} = \frac{\gamma_{13}}{\sin(\theta_2)} = \frac{\gamma_{23}}{\sin(\theta_1)} \tag{3.2}$$

In detail, given that olivine crystals are anisotropic (see above), this equation can be used for each pair of olivine-silicate melt dihedral angle population. Rearranging this equation yields a set of three equations:

$$\frac{\sin(\theta_1)}{\sin(\theta_2)} = \frac{\gamma_{23}}{\gamma_{13}} \qquad \frac{\sin(\theta_2)}{\sin(\theta_3)} = \frac{\gamma_{13}}{\gamma_{12}} \qquad \frac{\sin(\theta_1)}{\sin(\theta_3)} = \frac{\gamma_{23}}{\gamma_{12}} \tag{3.3}$$

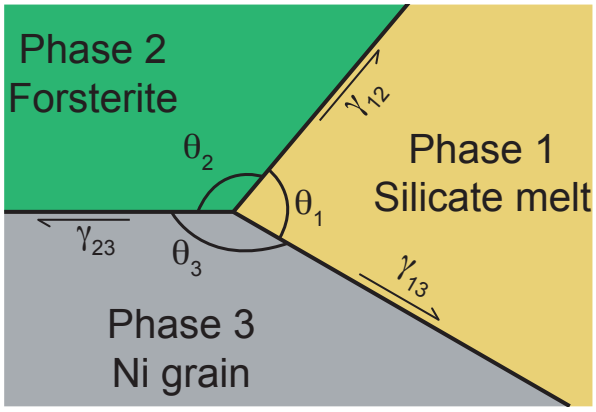

Figure 3.3 – Schematic vie of a triple junction between the silicate melt, a forstertite crystal and a nickel grain. Dihedral angles θ_1, θ_2 and θ_3 are related to interfacial energies γ_{12}, γ_{13} and γ_{23} when textural equilibrium is achieved, following equation 3.2

Based on this equation, the ratio of two interfacial energies can be inferred by calculating the ratios of sinuses of dihedral angles. From a theoretical point of view, it is thus possible to illustrate how variations in phase geometry translate into variations in the ratio of interfacial energies (Figure A.1). Given that an individual dihedral angle cannot be smaller than 0° and no larger than 180°, and that the sum of the three dihedral angles is constrained to be 360°, the variation of interfacial energy ratio can be represented using a ternary diagram. Due to the aforementioned conditions, only the inner triangle of the ternary diagram is of interest (Figure 3.4a). From equation (3.3), equality between two interfacial energies can be achieved when two dihedral angles are equal. Plotting these lines in the ternary diagram defines six

different energetic regimes. In each of these six domains, the relative order of interfacial energies differs (Figure 3.4b). The central point of this diagram represents the case where each phase has a dihedral angle of 120° (i.e. all interfacial energies are equal).

While a given ratio of interfacial energies always leads to the same geometry at the scale of an individual triple-junction, the larger-scale distribution of material will be affected by phase proportions, and limited by the least abundant phase. Given that olivine is always the major phase, the range of potential geometries is illustrated for the cases of nickel (Figure 3.4c) or silicate melt (Figure 3.4d) as the minor phase. For instance, we consider the case where two phases have dihedral angles of 180° and the third one has a dihedral angle of 0°. As displayed on Figure 3.4c and 3.4d, in this situation the third phase entirely wets the two others, preventing contact between them. If the third phase is present in small proportion, it will form a thin film along the interface between the two others. Alternatively, if one of the two other phases is limited in proportion, this phase will form an isolated sphere into the third phase (Figure 3.4c and 3.4d).

Figure 3.4c and 3.4d also represents a first order estimation of the interconnection threshold–dihedral angle dependence. When a phase has a dihedral angle close to zero, it has a thin lens shape, spreading along the interface of the two other phases. In this case, its interconnection threshold is very low. Increasing the value of the angle leads to an increasingly spherical shape and higher interconnection threshold.

3.4.2 Interfacial energy ratios

Interfacial energies can theoretically be calculated from the knowledge of the dihedral angles, if at least one interfacial energy is known independently. In this respect, the interfacial energy between silicate melt and olivine measured by Cooper and Kohlstedt (1982) seems a suitable reference point (0.5 ± 0.2 J.m^{-2}). However, this value assumes crystalline isotropy of olivine, a situation that does not reflect reality as discussed above. To our knowledge, no study reports different interfacial energies for different orientations of olivine crystals, so that it is preferable to stick to calculating ratios as follows:

$$\frac{\gamma_{\text{Melt-Ni}}}{\gamma_{\text{Melt-Fo}}} = \frac{\sin(\theta_{\text{Fo}})}{\sin(\theta_{\text{Ni}})} \qquad \frac{\gamma_{\text{Fo-Ni}}}{\gamma_{\text{Melt-Fo}}} = \frac{\sin(\theta_{\text{Melt}})}{\sin(\theta_{\text{Ni}})} \qquad \frac{\gamma_{\text{Melt-Ni}}}{\gamma_{\text{Fo-Ni}}} = \frac{\sin(\theta_{\text{Fo}})}{\sin(\theta_{\text{Melt}})} \tag{3.4}$$

Results of these calculations are shown in Table 3.3 for the different crystal plane families (i.e. subsets) and for the complete dataset (referred to as “merged”). When the raw data are treated, the sum of the three dihedral angles is greater than 360° for each subset. Given that this result is impossible, angles have been recalculated by fixing the nickel dihedral angle to 176.1° (corresponding to the measured value), then normalizing the two remaining values such that the sum is 360°.

The three-phase system considered composed of silicate melt, forsterite and nickel plots in the $\gamma_{\text{Melt-Fo}} < \gamma_{\text{Melt-Ni}} < \gamma_{\text{Fo-Ni}}$ domain as shown in Figure 3.5 (using data from Table 3.2, column "Merged", and from Table 3.4). At low resolution, nickel grains seem to be almost equally in contact with the forsterite and the silicate melt, whereas at high resolution, they

are more rounded and barely in contact with forsterite crystals. This behavior is illustrated through the variation of the interfacial energy ratios as a function of magnification. At low resolution (376 and 94 nm per pixel) both $\gamma_{\mathrm{Melt-Fo}}/\gamma_{\mathrm{Melt-Ni}}$ and $\gamma_{\mathrm{Melt-Fo}}/\gamma_{\mathrm{Fo-Ni}}$ ratios are almost equal, while at higher resolution (30 and 9.4 nm per pixel) these two energy ratios are lower and Ni has a higher interfacial energy than the rest of the system.

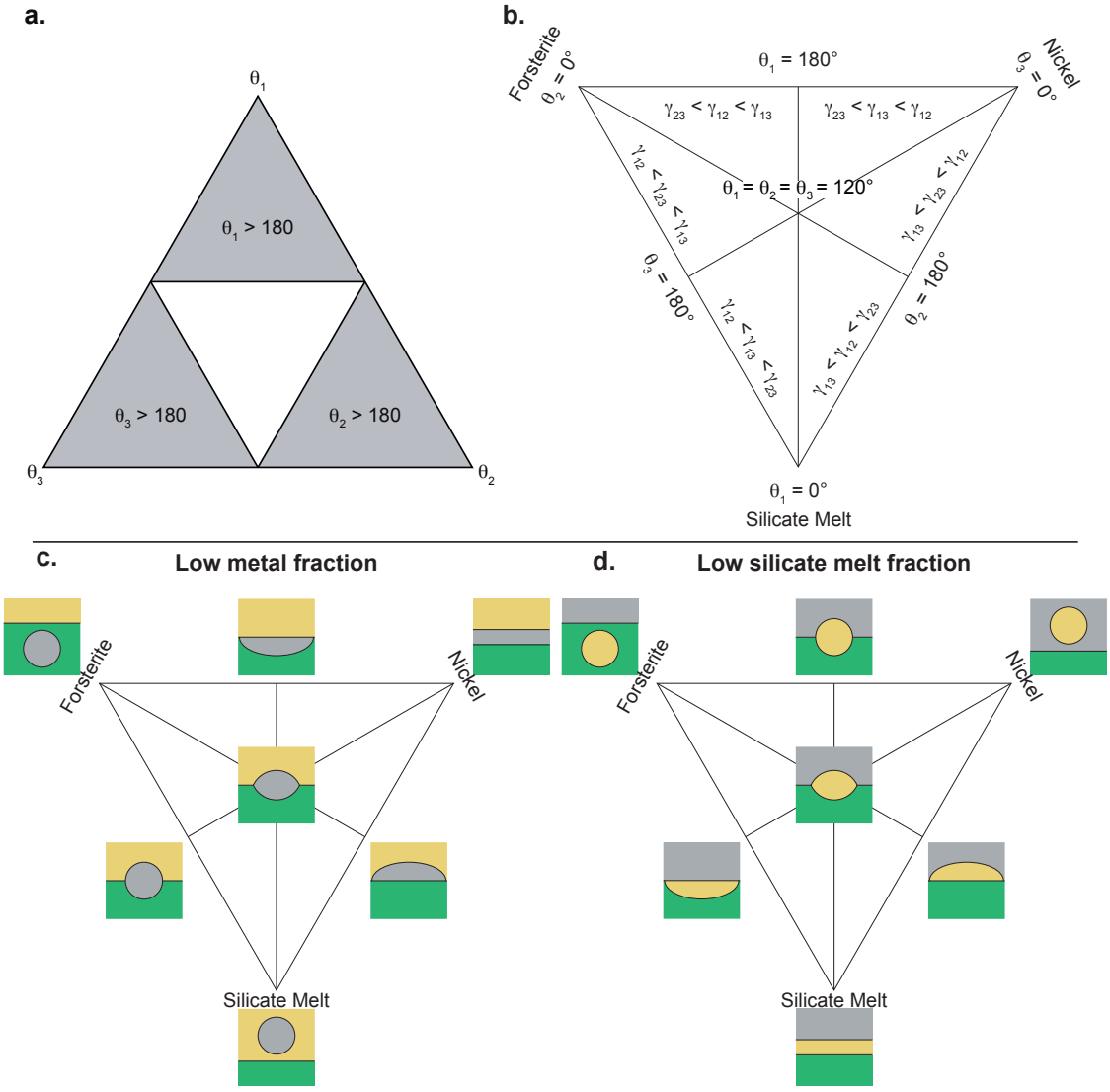

Figure 3.4 – (a.) Ternary diagram showing the inner triangle of possible space given the conditions $\theta > 0°$ and $\theta < 180°$. (b.) Reduced ternary diagram showing the different energetic regimes delimited by equation 3.3. Full lines separate these regimes and represent equality between two interfacial energies. Sketches explaining the geometry in remarkable points of the ternary diagram are represented in (c.) and (d.). Two end-member cases are considered: (c.) metal is the minor phase, (d.) silicate melt is the minor phase. If one angle is equal to 180°, the phase either forms a sphere or a film. When the dihedral angle is equal to 0°, the phase is highly wetting, its contact is punctual or inexistant, and this phase prevents the two others from being in contact with each other.

The energy ratios involving olivine are quite different de-pending on crystal orientation. From subset 1 to subset 3, the $\gamma_{\mathrm{Melt-Fo}}/\gamma_{\mathrm{Melt-Ni}}$ and $\gamma_{\mathrm{Melt-Fo}}/\gamma_{\mathrm{Fo-Ni}}$ ratios decrease from

0.3 to 0.1, and the $\gamma_{\text{Melt-Ni}}/\gamma_{\text{Fo-Ni}}$ ratio increases toward values close to 1, illustrating an evolution in the geometry toward the $\gamma_{\text{Melt-Ni}} = \gamma_{\text{Fo-Ni}}$ isovalue line (Figure 3.5). The changes of equilibrium geometries for the different subsets can be illustrated using Figure 3.4. For example, in case of low metal fraction, the metal grain becomes less embedded in forsterite from subset 3 to subset 1, making it easier to form an interconnected network in the latter case. This leads to an interconnection threshold that varies locally, increasing from subset 1 to subset 3. As interfacial energies are the lowest for subset 1, this geometry will most likely dominate the overall distribution. However, the energetic effect is countered by samples composed of an aggregate of randomly oriented crystals leading to metal grains in contact with various olivine crystal planes, including crystalline planes of high energy. To reach a state of lower energy, a dynamic process such as deformation would be required to re-orientate olivine grains. Despite these differences, it is of note that all subsets of olivine orientation fall in the same energetic regime where $\gamma_{\text{Melt-Fo}} < \gamma_{\text{Melt-Ni}} < \gamma_{\text{Fo-Ni}}$.

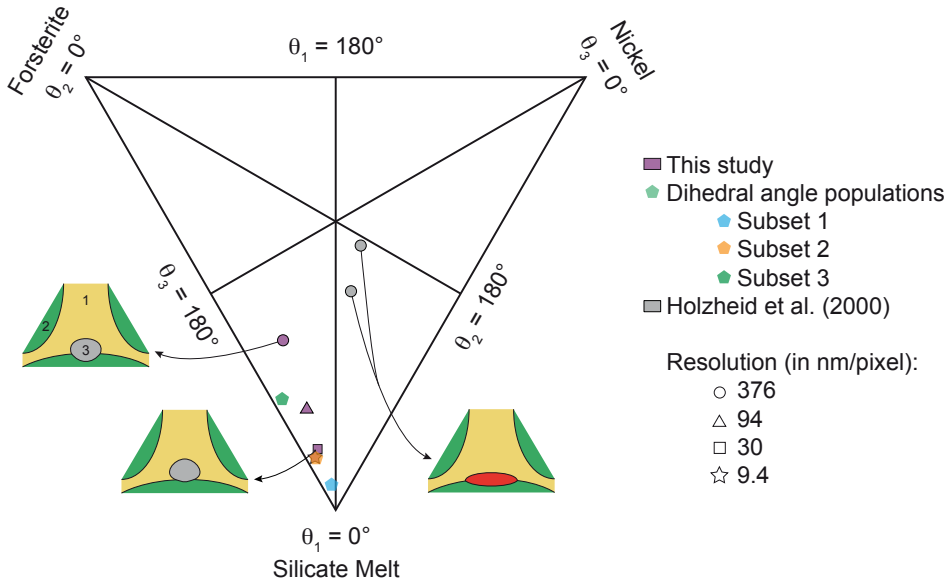

Figure 3.5 – Ternary diagram of the dihedral angles with the different energetic regimes. Pruple symbols represent data from this study. Pentagon symbols stand for the different populations of dihedral angle taking into account forsterite crystalline anisotropy (merged data at resolutions of 30 and 9.4 nm per pixel). Gray symbols correspond to the data from Holzheid et al. (2000). Error bars are smaller than symbols. Sketches show the geometry of the three phases according to their dihedral angles. Color code is the same as in Figure 3.3, except for sulfide, in red. Data with pure metal fall in the $\gamma_{\text{Melt-Fo}} < \gamma_{\text{Melt-Ni}} < \gamma_{\text{Fo-Ni}}$ domain, even when crystalline anisotropy is taken into account (shaded pentagons), which is clearly different from a system with sulfide: $\gamma_{\text{Melt-Sulfide}} < \gamma_{\text{Melt-Ol}} < \gamma_{\text{Ol-Sulfide}}$.

3.4.3 Comparison with literature data

In order to infer the mobility of sulfur-rich and pure metallic melts in an olivine matrix, the experimental results of Ballhaus and Ellis (1996) can be used. Calculating the interfacial energy ratios from their measured dihedral angles gives $\gamma_{\text{Ol-Ol}}/\gamma_{\text{Ol-Sulfide}} = 1.463$ to 1.658 and $\gamma_{\text{Ol-Ol}}/\gamma_{\text{Ol-Fe}} = 1.075$ to 1.104. Taking these ratios at face-value (note that calculated values are based on angles measured by Ballhaus and Ellis (1996) at a resolution that was

not specified) suggests that $\gamma_{\mathrm{Ol-Ol}} \approx \gamma_{\mathrm{Ol-Fe}} > \gamma_{\mathrm{Ol-Sulfide}}$. In such a two-phase system, the olivine–metal-rich phase interfacial energy is lower in the case of sulfide than of pure metal. Thus sulfide melts appear to wet olivine grains more than pure metallic ones do, and sulfur-rich melts thus have a lower interconnection threshold ($\approx$ 3 to 7 vol% from Laporte and Provost, 2000) than pure metallic melts in an olivine matrix ($\approx$ 12 vol% from Laporte and Provost, 2000, although the high dihedral angles determined in this study suggest a much higher interconnection threshold on the order of 25 vol%).

In natural systems (i.e. planetesimals in the early solar system), silicate and metal-rich phases fractions have close melting temperatures ($\approx$ 1000 °C). Furthermore, the first melt compositions produced upon heating of the metal-rich fraction are sulfur-rich, close to the Fe–FeS eutectic composition. To our best knowledge, a single study reports for measurements of dihedral angles in a three-phase system hosting sulfide melts (Holzheid et al., 2000). As dihedral angle measurement resolution is not specified, these values have to be used with caution. In their study, the $\gamma_{\mathrm{Melt-Ol}}/\gamma_{\mathrm{Melt-Sulfide}}$ ratio is greater than 1, whereas the $\gamma_{\mathrm{Melt-Ol}}/\gamma_{\mathrm{Melt-Ni}}$ is lower than 1 in the case of a pure metal implying that $\gamma_{\mathrm{Melt-Sulfide}} < \gamma_{\mathrm{Melt-Ni}}$. This switch in the value of the ratio $\gamma_{\mathrm{Melt-Fo}}/\gamma_{\mathrm{Melt-Sulfide}}$ compared to $\gamma_{\mathrm{Melt-Fo}}/\gamma_{\mathrm{Melt-Ni}}$ indicates a change in the order of interfacial energies, i.e. of energetic regime, relative to the case of pure metal, which then becomes $\gamma_{\mathrm{Melt-Sulfide}} < \gamma_{\mathrm{Melt-Ol}} < \gamma_{\mathrm{Ol-Sulfide}}$ (Figure 3.5). The sulfur-rich melt thus appears to have a low interfacial energy with silicate melt and a higher one with olivine so that the contact between sulfur-rich melt and solid silicates tends to be limited. In this case, the sulfide melts produced at low temperature near the eutectic will tend to spread along the surface of solid silicate grains in order to increase the contact surface with the silicate melt, thus having a tendency to interconnect in the presence of a silicate melt (Figure 3.5).

3.5 Metal-silicate differentiation in early accreted planetesimals

Comparing dihedral angle measurements carried out in this study for a pure metal with previous ones for a sulfur-rich phase shows that increasing the sulfur content of the metallic liquid increases its wettability, reducing its dihedral angle and its percolation threshold. Once this threshold exceeded, the sulfur-rich metallic liquid is able to percolate, leaving a metallic residue whose threshold increases due to decreased sulfur content. Therefore, in the absence of a large degree of silicate melting, the complete extraction of metal in a small body remains unlikely.

To explore deeper the consequences of a dependence of the inter-connection threshold on sulfur content, the evolution of a body heated by decay of ^{26}Al has been modeled. Upon heating, silicate and iron-sulfur begin to melt at similar temperature (see below). The behavior of each subsystem thus has to be modeled as their relative proportions depend on each other. Silicate melt is likely to form an interconnected network even at very low melt fraction (< 1 vol% estimated from Laporte and Provost, 2000; Wray, 1976), thus it is assumed to be continuously extracted. As the fraction of silicate decreases, that of sulfide melt increases until the interconnection threshold is reached. This behavior depends at the same time on

the relation between the sulfur content of the sulfide melt and its interconnection threshold and on the melting curve of silicates.

3.5.1 Modeling the behavior of metal and silicates

3.5.2 The metal-sulfide subsystem

The metallic subsystem is assumed to have an initial composition of H-type ordinary chondrites as they are a possible precursor material of primitive achondrites (Palme et al., 1981). Such a composition corresponds to volumetric phase proportions of 3 vol% troilite and 7 vol% metal (Guignard and Toplis, 2015), or 7 wt% S in the metallic subsystem (Wasson and Kallemeyn, 1988). As temperature rises, removal of silicate melt increases the volume fraction of metal, but the sulfur content of the sulfide melt decreases as well due to equilibrium melting of the metallic subsystem. The overall effect is an increase of the interconnection threshold of the molten fraction, from a lower limit at the Fe–FeS eutectic (3 vol% Roberts et al., 2007; Yoshino et al., 2003) to an upper limit for pure metal (25 vol% estimated from the large value of nickel dihedral angle measured in the present study, see section 3.3.2.3). Between these two endmembers, the sulfur content–interconnection threshold dependence is poorly constrained. For this reason, several different functions have been considered (Figure 3.6a). Threshold function (a) increases linearly with sulfur content from the Fe–S eutectic composition to pure iron, while other functions investigate non-linear trends. Altogether, they fall into two categories: a first one with a sharp increase of the threshold upon decreasing sulfur con-tent in the vicinity of the eutectic (threshold functions a and b), and a second one with a smooth increase of the threshold upon decreasing sulfur content in the vicinity of the eutectic (threshold functions c, d and e). The liquidus curve of the Fe–S phase diagram is taken from Buono and Walker (2011) at 1 bar (Figure 3.7, black curve) and allows plotting the different percolation threshold functions as a function of temperature (Figure 3.6b, full lines). The percolation thresholds increase with temperature until all the metallic subsystem is entirely molten ($\approx$ 1400 °C at 7 wt% of sulfur, dashed black thin vertical line Figure 3.6b), then the threshold functions reach constant values. In the following, it is considered that once the interconnection threshold reached, the network forming sulfide melt is extracted.

Another important issue is the efficiency of draining once the percolation threshold has been reached. Ghanbarzadeh et al. (2017) demonstrated that drainage is affected by an hysteresis effect, where not only the molten fraction exceeding the percolation threshold flows out, but almost all the fluid is lost, except for a small fraction trapped in network irregularities. This amount corresponds to the trapping threshold, which is null for a dihedral angle less than 60° as in the case of silicate melts, but up to 2 vol% for a dihedral angle of 120° (Ghanbarzadeh et al., 2017). In the present calculation, the trapping threshold is set to 1 vol%.

3.5.3 The silicate subsystem

The silicate melting curve has been calculated using a fractionate melting simulation on the *Rhyolite-Melts* thermodynamic software, with continuous extraction of the melt (Asimow

and Ghiorso, 1998; Ghiorso and Gualda, 2015; Ghiorso and Sack, 1995; Gualda et al., 2012). An initial composition of H-type chondrites (Wasson and Kallemeyn, 1988) is also assumed and temperature ranges from 950 °C to 2000 °C, at 1 bar, along the Iron-Wüstite (IW) buffer. The FeO content of the silicates is calculated from the FeO/(FeO+MgO) ratio (given in Wasson and Kallemeyn, 1988, Table 1). The melting curve is displayed in Figure 3.6c and 3.6d as a black curve. The different kinks in the curve correspond to the complete melting of the different silicate phases. This simulation shows a silicate eutectic at ≈ 1000 °C.

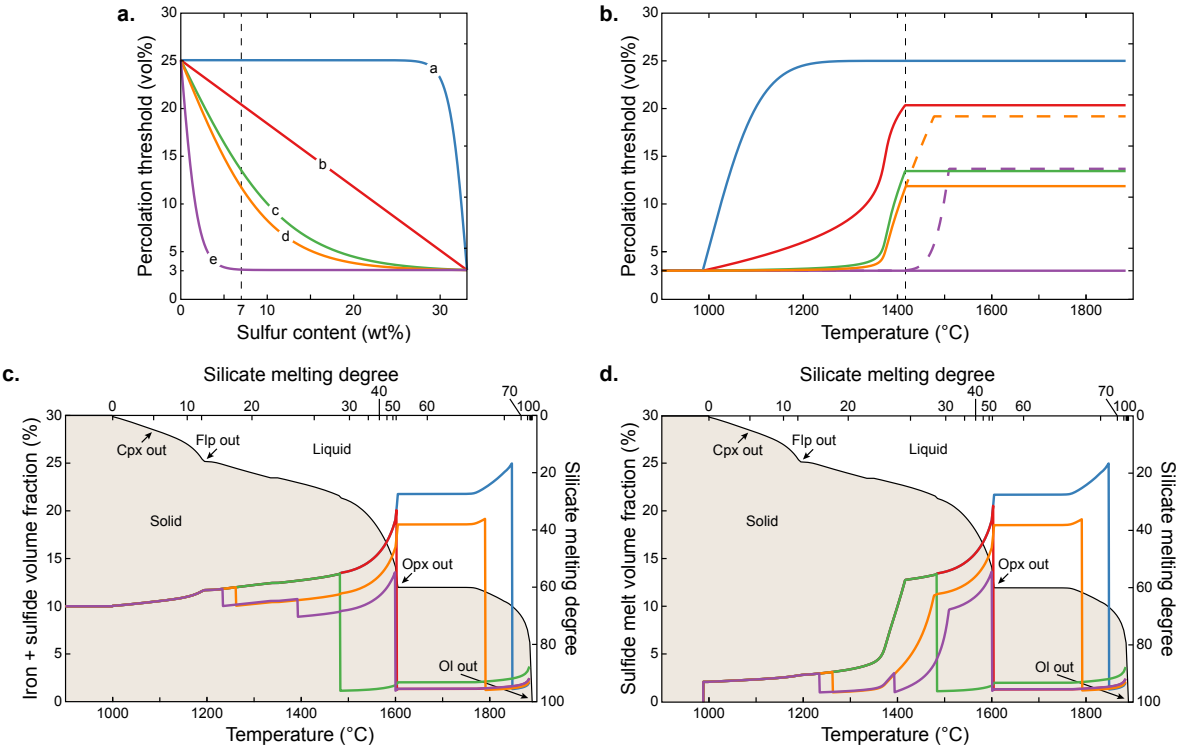

Figure 3.6 – Evolution of the metal volume fraction of a silicate-metal mixture as a function of temperature. Silicate melt is assumed to be continuously extracted so that the metal fraction increases with the melting degree of silicate. The metallic melt is completely drained when its percolation threshold is reached, except a trapped fraction set to 1 vol%. The percolation threshold is a function of the sulfur content. (a.) Different interconnection threshold evolutions as a function of sulfur content of the sulfide melt. (b.) Percolation threshold functions as a function of temperature. Full lines are for simulations that experienced sulfide melt extraction once all the iron is molten, while dashed lines represent the case where the extraction occurred when a solid iron residue was present. (c.) Evolution of the metal volume fraction (solid iron and sulfide melt) as the silicate is extracted through fractionated melting. (d.) Evolution of the sulfide melt volume fraction as a function of temperature. In (c.) and (d.) the black line represents the volume of silicate melt extracted as a function of temperature, the shaded area indicating the residual silicate. The different kinks in the silicate melting curves represent the disappearance of mineral species, arrows pointing them out. Color lines draw the volume fraction of the metallic subsystem in (c.) and of the sulfide melt in (d.) for the different percolation threshold functions depicted in (a.) and (b.).

3.5.4 Metal segregation

Upon removal of the silicate melt produced, the quantity of metal increases (whole metal, i.e. solid iron and sulfide on Figure 3.6c and sulfide melt on Figure 3.6d). Once the quantity of

sulfide melt reaches its interconnection threshold, all but 1 vol% is assumed to be extracted as explained above. This removal causes the loss of sulfur, changing the composition of the metallic subsystem (Figure 3.7, color curves for the different threshold functions) if it occurred while there was still some solid iron. In this case, the interconnection threshold is shifted towards higher values; this tendency is shown in Figures 3.6b (dashed lines) and A.2.

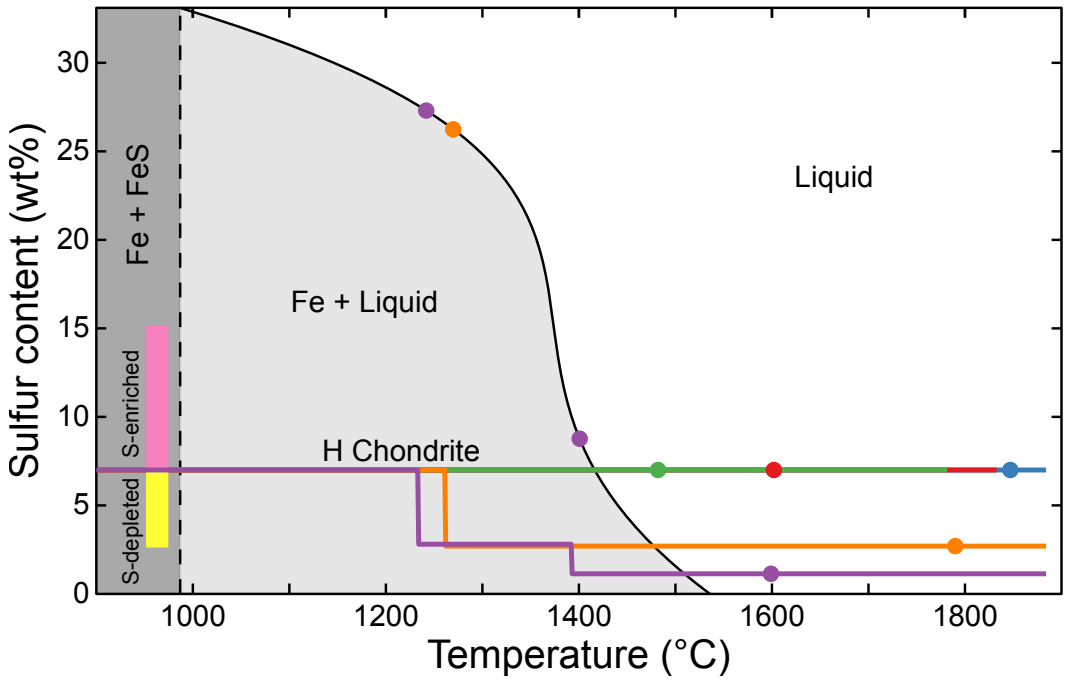

Figure 3.7 – Evolution of the sulfur content of metal plotted on the phase diagram of the Fe-FeS system. Color dots represent the composition of the extracted melt, following the color code for the different threshold functions of Figure 6a. Color bars represent the composition of different primitive achondrites, sulfur enriched ones in pink (Acapulco Guignard and Toplis (2015); Zipfel et al. (1995) and TIL99002 Patzer et al. (2004)) and S-depleted ones in yellow (Acapulco Palme et al. (1981), Lodran Bild and Wasson (1976); Guignard and Toplis (2015) and NWA 725 Patzer et al. (2004)). The discrepancy in the sulfur content of the different primitive achondrites can be accounted for given that the evolution of the interconnection threshold is close to threshold functions (d) or (e), allowing the fractionation of sulfur within the planetesimal.

The different threshold functions described here fall in two categories. In the first case, the interconnection threshold of the sulfide cannot be reached until a large fraction of silicate is melted. For example, threshold function (a) leads to the result that the high interconnection threshold of pure metal is preserved over a wide range of compositions (Figure 3.6a). In this pessimistic case, the conditions to extract the sulfur-bearing component would require 67 vol% melting of the silicate fraction, corresponding to an extreme temperature of $\approx$ 1850 °C (Figure 3.6b, 3.6c and 3.6d). In the case of threshold function (b) (linear increase with sulfur content), the threshold is constantly higher than the volume fraction of sulfide melt over a wide range of temperatures (Figure Figure 3.6b, 3.6c and 3.6d), such that the threshold is not reached before extraction of 55 vol% of the silicates, i.e. a temperature of 1600 °C. The same sort of behavior is also true for threshold function (c), that is a non-linear function of S-content, with lower interconnection threshold at high S-content. In this case, the onset of drainage occurs at 13 vol% of molten sulfide and a degree of silicate melting of 30 wt%, i.e. 1450 °C (Figure 3.6b, 3.6c and 3.6d). For the three cases described above (threshold functions

(a), (b) and(c)), sulfide melt extraction requires the removal of large volume of silicate melt and temperatures above 1420 °C, meaning that the metallic subsystem is fully molten and its extraction takes place in a single event, leaving only a small residual trapped fraction of 1 vol%. Such a scenario appears unlikely given that the loss of silicate melt also takes away theprincipal heat source, ^{26}Al that is transferred to the melt by plagioclase melting near 1200 °C. In the case of fractional melting assumed here, the ^{26}Al heat sources will thus be totally extracted for a melting degree no higher than 15 vol%. However, models on the percolation process in Vesta (Mizzon, 2015) show that silicate melt migration is not instantaneous. Even though the heat source is transferred towards the surface of the body, the degree of mantle melting can be as high as 50 vol% due to time-scale of melt extraction.

For the second family of cases, threshold functions (d) and (e) allow interconnection and extraction of the sulfide melt at lower temperatures, i.e. at lower silicate melting degrees and below the liquidus of the metallic subsystem. In details, function (d) is at first glance similar to (c), but it yields a very different extraction behavior (Figure 3.6b, 3.6c and 3.6d). In this case, a first episode of drainage occurs at 3 vol% of liquid sulfide, after extraction of 19 vol% of silicate melt (1250 °C). This concerns 2 % of the total volume, corresponding to 20 vol% of the metallic phase. This loss of iron-sulfide liquid reduces the sulfur content of the residual metallic subsystem by two-thirds of its initial value, thus raising the interconnection threshold to 18 vol% (Figures 3.6b and 3.7). Both factors inhibit a possible second extraction of sulfide melt that would occur at a silicate melting degree of 65 vol% and a temperature of 1800 °C (Figure 3.6b, 3.6c and 3.6d), conditions that cannot be reached easily for the aforementioned reasons. As a consequence, only the first episode of loss of molten sulfide remains plausible. In this case, it will leave behind a material with a metal volume fraction close to the initial state, i.e. 10 vol%, but depleted in sulfur ($\approx$ 2.5 wt%, Figure 3.7), and a silicate highly depleted in its feldspar and clinopyroxene com-ponents. Function (e) assumes that the interconnection threshold of the eutectic is preserved for a wide range of sulfur contents and allows three successive extractions at 1220 °C, 1380 °C and 1600 °C corresponding respectively to 17 vol%, 24 vol% and 50 vol% of silicate partial melting (Figure 3.6b, 3.6c and 3.6d). These stages result in a metal volume fraction of 10 %, 8 % and 1 % (trapped fraction) respectively, the final episode of drainage taking place after complete fusion of the metal. During these stages the sulfur content decreases to 2.3 wt% and then to 1 wt% (Figure 3.7). Interestingly, function (e) belongs to both threshold function categories, since it allows partial metal extraction at moderate silicate partial melting (17 vol%), and then complete drainage at a higher but perhaps still possible degree of silicate melting (50 vol%).

3.5.5 Comparison with experimental data and primitive achondrites

The present model indicates that the S-content dependence of the interconnection threshold plays a critical role on the drainage of sulfur-bearing liquids. In the absence of direct experimental determination concerning the effect of S-content, we turn to experiments in similar systems and data from natural samples. For example, experiments conducted by Rose and Brenan (2001) addressed the effect of oxygen on the wettability of metallic melts. They observed a sharp decrease in the dihedral angle from 0 to 5 mol% of oxygen, followed by a smooth decreasing linear trend at higher oxygen content, a behavior similar to that described

by functions (c), (d) or (e). Holzheid et al. (2000) built a data compilation addressing the effect of sulfur, but it lacks data on pure metal. Adding the data from the present study, a sharp decrease of the interconnection threshold is observed at low sulfur content, followed by a smooth decreasing linear behavior, again similar to curves (c), (d) and (e). In light of these considerations, it is concluded that this sort of dependence is the most plausible.

In turn, this sheds new light on the processes experienced by primitive achondrites and may potentially explain their composition. These meteorites are widely accepted to represent partial melting residues for both metallic and silicate subsystems. Sulfur contents of the Fe–FeS system is plotted in Figure 3.7 for different primitive achondrites. Note that the composition can be highly heterogeneous in the same meteorite, from one section to another: for instance Acapulco displays S-contents ranging from ≈ 6 wt% up to ≈ 15 wt% (Guignard and Toplis, 2015; Palme et al., 1981; Zipfel et al., 1995). Primitive achondrites can nonetheless be assigned to two categories following their S-content: they are either depleted or enriched relative to the H-chondrite primitive material (Figure 3.7). Depletion can be due to the extraction of a sulfide melt, whose composition is different from that of the bulk metallic subsystem. In a similar way, S-enriched meteorites can be viewed as regions that have locally concentrated sulfide melts draining down from upper parts of the parent body. Indeed, it should be appreciated that differentiation at moderate melt fraction operates through liquid migration inside a porous solid matrix. This migration is affected by compaction waves that form alternating horizons enriched and depleted in liquid (Šrámek et al., 2012) that may freeze if the heat source (i.e. ^{26}Al content) is insufficient to allow complete separation. S-enriched and S-depleted meteorites can thus sample different horizons of the same planetesimal. This feature may be simply understood in the case of a S-dependent threshold corresponding to function (d) or (e). Recent studies on Hf-W systematics (Kruijer et al., 2014) also support the idea that different sulfide melts extraction events may occur during differentiation. More precisely, data on IVB iron meteorites suggest two segregation steps: a first one with an early extraction of a S-rich liquid, and a second one, later, with an iron-rich melt. However, the present study outlines that the extraction of a silicate melt is a necessary condition to allow the metallic melt fraction to exceed its interconnection threshold.

Finally, the formation of a small core with a heterogeneous sulfur content is a natural outcome of the present model depending on the temperature of extraction, as melts with various compositions are extracted. This model thus provides a plausible explanation for the diversity of sulfur content in iron meteorites, even though one should keep in mind that these meteorites most likely formed by larger degrees of melting and are expected to have lost some sulfide due to the sulfur volatility and the mechanical weakness of troilite.

3.6 Conclusion

Laboratory experiments were performed to study the local geometry of a three-phase system composed of forsterite, silicate melt and nickel grains relevant to partially differentiated meteorites. The dependence of equilibrium geometries (dihedral angles) on interfacial energies was also considered from a theoretical point of view. Finally, the evolution of the metal fraction in a planetesimal was modeled assuming an interconnection threshold that is

a function of S-content. The main conclusions can be summarized as follows:

1. From an experimental and analytical point of view, a resolution of 30nm per pixel is necessary for accurate measurements of dihedral angles, in particular the complex shape of forsterite grains that precludes simple prediction of the different interconnection thresholds of the system. A theoretical approach shows that different energetic regimes exist and that the accurate measurement of dihedral angles is needed to predict the geometry.
2. Fe–FeS eutectic melt (first metallic liquid to form) and pure metal (last metallic liquid to form) belong to two distinct interfacial energy regimes. The comparison between the equilibrium geometries in a system containing Fe–FeS eutectic melt shows that the sulfide–silicate melt interfacial energy is energetically favorable when the metallic melt is sulfur-rich, meaning that such liquids will spread along the faces of silicate crystals, decreasing the interconnection threshold of the metallic melt. On the other hand, in the case of pure metal, grains remain largely spherical, increasing the interconnection threshold.
3. The variation of sulfur content of primitive achondrites from one sample to the other is best explained when the interconnection threshold significantly decreases at low sulfur content and remains close to the value of the Fe–FeS eutectic for a wide range of compositions at higher S contents. Different sulfide melt extractions are then possible at temperatures of 1200 - 1400 °C, requiring $\approx$ 25 vol% of silicate melt. These conditions can be reached even if the mobility of the heat source is taken into account. Successive extraction events provide a good explanation for the variability of sulfur content observed in primitive achondrites, which are either representative of a region that experienced sulfide extraction or from a region that accumulated sulfide melt from the outer parts of the body.

Chapter 4

A 3D X-ray microtomography reevaluation of metal interconnectivity in a partially molten silicate matrix

Contents

In the framework of metal-silicate differentiation in early-accreted small bodies, understanding the dynamics of interconnection and disruption of metallic networks is of prime importance. To this end, experiments have been performed to investigate the effect of varying silicate melt content, metal fraction (i.e. closer to or further away from the interconnection threshold) - both above or below the melting temperature of metal - and run duration on the stability and textural maturation of metallic networks and isolated beads. Experiments using a three-phase system (forsterite + silicate melt + nickel) were run in a 1-atmosphere controlled high temperature furnace (AF, $\Delta_{\mathrm{NNO}} = -3$, 1713 or 1743 K), in a 3/4-inch piston-cylinder (PC, carbon capsule buffered, 1 GPa, 1480 or 1773 K) and in a Paris-Edinburgh press (PE, carbon capsule buffered, 1 GPa, from 25 to 2123 K, beamline PSICHE - SOLEIL Synchrotron). Recovered samples of AF and PC experiments were analyzed with ex-situ 3D X-Ray microtomography, while in-situ analyses were conducted on PE experiments. Starting from ground powders, gas bubbles were trapped in the AF samples. These bubbles stirred the sample while trying to escape. This agitation brought the metallic grains together, whether solid or molten, forming large blobs that represent up to 80 vol% of the metal content of the sample. In this case, coalescence mechanisms occur on a much shorter timescale than normal grain growth and are much more efficient, opening pathways to the formation of large metal aggregates in magma oceans. Such clusters may be able to settle and form a metallic core if their size is large enough (1 mm to 1 cm). PC experiments show that varying silicate melt and metal contents (in terms of distance to interconnection threshold for the metal) affect the rate of textural maturation. Increasing silicate melt fraction and getting further to the interconnection threshold of metal enhances the textural maturation rate. A similar result was obtained with PE experiments, which demonstrated that cold compression at the beginning of the run caused metal grains to adopt elongated shapes between silicate grains, forcing interconnection at only 10 vol% of metal. Increasing the textural maturation rate favored the disruption of the network, proving its instability; remnants became more spherical with time. Playing with the textural maturation rate to assess the true interconnection threshold of pure metal gives a value between 20 and 25 vol%. Taking the effect of of textural maturation rate into account may explain the variability of textures observed in natural samples (e.g. chondrules, metamorphosed chondrites and primitive achondrites). This Chapter is presented here in the state of the draft of the paper to be submitted soon.

4.1 Introduction

Differentiated bodies are common throughout the Solar System. Terrestrial planets and their natural satellites (e.g. the Earth's Moon (Righter, 2002) or icy moons such as Ganymede (Kivelson et al., 1996)) show evidence for metallic cores, as inferred from their magnetic fields or their geochemical composition. However large-scale evolution processes have affected these bodies, erasing all traces of the metal-silicate differentiation processes. Meteorite collections display a large variety of objects that can be classified in three main categories following their degree of differentiation: chondrites (undifferentiated), achondrites (fully differentiated) and primitive achondrites (partially differentiated, achondritic textures). From these objects, two scenarii of metal-silicate differentiation can be distinguished:

(1) Achondrites in general are commonly thought to be the result of large-scale melting

processes on their parent bodies. The formation of iron meteorites requires the complete melting of the iron-sulfur subsystem (Chabot and Haack, 2006; Goldstein et al., 2009, and references therein), implying the presence of a large fraction of silicate melt. Similarly, the homogeneous oxygen isotopic composition of the HED clan argues in favor of a global magma ocean stage (Greenwood et al., 2014). Metal segregation may therefore have occurred by particle settling. Monnereau/Néri (in prep., Chapter 5) modeled the evolution of a magma ocean in the case of internal heating by the decay of short-lived radionuclides and assuming equilibrium heat fluxes. Results show that a large fraction of the silicates remain solid (about 50 vol%). In this case, metal particles might still be able to sink if they reach large sizes (Solomatov, 2015); and differentiation most likely occurred through percolation of an interconnected network.

(2) Primitive achondrites are the result of incomplete metal-silicate segregation at low melting degree. Among the subgroups of this clan, acapulcoites and lodranites are of particular interest, as they have not been subject to shock, oxidation or large-scale alteration (Keil and McCoy, 2018). Acapulcoites exhibit the lowest degree of differentiation. They are thought to have heated barely to onset the melting of both silicate and iron-sulfide subsystems, i.e. at T $\approx$ 1273 K (e.g. McCoy et al., 1996; Mittlefehldt et al., 1996). Some objects show evidence for removal of silicate ($<$ 5 vol%) and iron-sulfide melts, as evidenced by depletion in incompatible elements (Palme et al., 1981; Zipfel et al., 1995; Mittlefehldt et al., 1996; Patzer et al., 2004). In contrast, lodranites represent a more evolved subgroup with complete loss of early melting silicates such as feldspars and clinopyroxenes and with a metallic subsystem depleted in sulfur. Such features point to simultaneous extraction of both silicate and iron-sulfide melts (Bild and Wasson, 1976; McCoy et al., 1997) at temperatures of 1473 K, consistent with a silicate melting degree of 20-25 vol% (Bild and Wasson, 1976; Papike et al., 1995; McCoy et al., 1996, 1997). At such high crystal contents, the metal had to form a network to be extracted.

Interconnection of the metallic phase is thus a major issue for metal-silicate differentiation. Overall, the connectivity of a phase depends on its interconnection threshold, i.e. the phase fraction at which it forms a network. This threshold is the result of the minimization of interfacial energies between the different phases (Smith, 1964; Bulau et al., 1979; Jurewicz and Watson, 1985). This energetic balance favors the low-energy contacts at the expense of high energy ones and is expressed physically by the dihedral angles at triple junctions. In a two-phase system, the dihedral angle θ of the liquid between two solid grains is a function of the interfacial energy between two solid grains $\gamma_{\mathrm{Solid-Solid}}$ and that between the solid and the liquid $\gamma_{\mathrm{Solid-Liquid}}$ (in J.m$-$2), following (Smith, 1964):

$$2\cos\left(\frac{\theta}{2}\right) = \frac{\gamma_{\mathrm{Solid-Solid}}}{\gamma_{\mathrm{Solid-Liquid}}} \tag{4.1}$$

It is considered that for low dihedral angles ($< 60°$), the interconnection threshold is extremely low ($<$ 1 vol%, see Laporte and Provost, 2000, and references therein), while for large dihedral angles ($> 60°$) a significant amount of a phase is required to form an interconnected network.

Dihedral angle values reported for mafic and ultramafic silicate melts in an olivine matrix are lower than 60° (Faul, 2000; Laporte and Provost, 2000); the formation of an interconnected network for the silicate melt is thus easily achieved. On the contrary, metallic melts have

dihedral angles greater than 60°, with values varying as a function of their sulfur content (Holzheid et al., 2000; Rose and Brenan, 2001). This dependence of the sulfur content on the interconnection threshold has huge consequences for the segregation of iron-sulfide melts, as the composition of the latter varies as a function of temperature. The first iron-sulfide melt produced is sulfur-rich (eutectic composition) and has a low dihedral angles (Ballhaus and Ellis, 1996; Minarik et al., 1996; Gaetani and Grove, 1999; Holzheid et al., 2000), ranging from 60° to 100°, i.e. interconnection thresholds from 0 to 7 vol%, as estimated from Wray (1976) and Laporte and Provost (2000). Their segregation is likely to be achieved more easily than for the other end-member, pure metal, that displays much larger dihedral angles (Shannon and Agee, 1996; Gaetani and Grove, 1999; Néri et al., 2019) from 110° up to 176° corresponding to interconnection thresholds ranging from 10 to 25 vol%. It is of note that large discrepancies exist between dihedral angles inferred in different studies for the same composition of the metallic melt, a situation which is most likely due to the different resolutions used to assess dihedral angles on SEM images (Cmíral et al., 1998; Néri et al., 2019). Electrical conductivity measurements can also be used to determine the interconnection threshold, but literature data also show large variations in the obtained values for the same composition. For instance for the Fe-FeS eutectic composition, a low threshold of 3 to 6 vol% has been estimated by Yoshino et al. (2003) and Watson and Roberts (2011), while Bagdassarov et al. (2009a) reported a much higher value of 17.5 vol%. This discrepancy is possibly explained by different degrees of textural maturation (Bagdassarov et al., 2009a).

All of these techniques are based on 1D or 2D characterization of the samples. More data are required to reconcile the microstructural observations (dihedral angles) with bulk properties (electrical conductivity). Indeed, similar microscopic properties can lead to different macroscopic ones (Néri et al., 2019). The present study aims to bring new constraints on this problem by studying the effect of varying textural maturation rates (illustrated by different silicate melt contents, metal states, distance to interconnection threshold and run duration) on the 3D distribution of the metallic phase in a system composed of forsterite, silicate melt and pure metal. 2D-microstructures of this system have already been characterized (Néri et al., 2019) and show no variations with regard to varying silicate melt content and run duration. Hence the present study focuses on the meso- to macro-scale behavior of metal. Experiments were performed at 1 bar using a controlled-atmosphere, high temperature furnace and at 1 GPa using a piston-cylinder and a Paris-Edinburgh press. The characterization of the 3D distribution of the metal was then performed using ex-situ 3D X-Ray microtomography on recovered samples (1-atmosphere furnace and piston-cylinder experiments), as well as in-situ microtomography at beamline PSICHE (Pairs-Edinburgh press experiments at the SOLEIL synchrotron) to obtain time-resolved information on textural evolution upon silicate melting.

4.2 Experimental setup

4.2.1 Starting material

Samples are composed of a mixture of crystalline forsterite (Fo), synthetic silicate melt (Melt) and nickel metal (Ni). Different compositions have been studied to vary the silicate melt / forsterite ratio. Forsterite and nickel are commercial powders, respectively

Neyco CERAC, Inc., 325 mesh, 99% pure; grain size 0-40 µm and Goodfellow, 99.8% pure, grain size 1-70 µm. The silicate melt has been synthesized by mixing oxide (SiO2 99.8% - Alfa Aesar, Al2O3 99.999% extra pure - Acros) and carbonate (CaCO3 99+% - Acros, 4(MgCO3).Mg(OH)2.5(H2O) - Acros) powders in appropriate proportions. Two compositions of silicate melt in the Anorthite-Diopside-Forsterite (An-Di-Fo) diagram are used; both are in equilibrium with forsterite. The first one is in equilibrium with forsterite at 1713 K (Morse, 1980) for the AF and PC experiments, allowing to vary the relative proportions of forsterite and silicate melt without changing their composition. The second one has the composition of the An-Di-Fo eutectic at 1 GPa (Presnall et al., 1978) to allow progressive melting of the silicates in the PE experiments. The mixtures of oxide and carbonate were first fired at 1373 K for two hours to allow complete dehydration and decarbonation, then heated to 1773 K for two hours for melting, then quenched. This last step was repeated to ensure chemical homogeneity (for more details on the glass synthesis, the reader can refer to Néri et al., 2019). Finally, the quenched materials obtained were finely ground and mixed with Fo and Ni in the desired proportions.

Although iron is the most abundant metal in natural samples, nickel is used in the present experiments as its lower melting temperature and its stability at higher oxygen fugacity (fO_2) allow a better control of the chemistry and mineralogy of the samples. Indeed, previous work with similar experimental systems (Néri et al., 2019) showed that the diffusion of nickel into the silicate phases is not significant (2 wt% NiO in forsterite and 0.6 wt% NiO in silicate glass at equilibrium).

4.2.2 Experiments

To constrain the influence of varying silicate melt content, distance to interconnection threshold, metal state, run duration and the effect of agitation, experiments were performed using different assemblies at 1 bar and 1 GPa, as shown in Figure 1. A total of 24 experiments were conducted; the experimental conditions and type of assemblies are reported in Table 4.1.

4.2.2.1 Annealing experiments in a 1-bar atmosphere controlled high temperature vertical furnace (AF)

Experiments have been performed in a 1-bar controlled atmosphere vertical high temperature furnace (AF). This pressure is relevant in the case of small bodies with modest radii (no larger than 300 km). Oxygen fugacity was controlled by mixing CO/CO_2 in appropriate proportions to limit the solubility of nickel in the silicates. All experiments were performed at $\log(fO_2)$ = -8.5, i.e. 3 orders of magnitude below the Ni-NiO (NNO) buffer ($\Delta_{NNO} = -3$), at 1713 K and 1743 K, i.e. 15 K below and above the melting point of nickel. Temperature was measured with an S-type thermocouple ($PtRh_{10}$ / Pt), ensuring a low error on temperature value (± 1 K). Samples were held in the furnace using the wire loop technique (Figure 2.4), as described in Néri et al. (2019). Sample size is typically 5-6 mm^3. A multiquench rod was used, allowing five samples to be placed in the furnace simultaneously and to quench them at different times.

In a first set of runs, 24-hours experiments were run on all compositions (in Fo:Melt:Ni vol%: 20:75:5, 47.5:47.5:5 and 62.5:32.5:5) to study the textures after this duration. Then, time-series experiments were conducted to follow the kinetics of textural evolution for a single mixture (20:75:5). A first series was performed below the melting temperature of nickel (1713 K). Samples were recovered after 1 minute (taken as initial state), 30 minutes, 2 hours, 6 hours and 24 hours. The second series of runs was conducted to study the fate of the formed solid nickel network when temperature exceeds its melting temperature (1743 K). In this case, samples were equilibrated at 1713 K for 24 hours (one was recovered), then temperature was increased to 1743 K and samples recovered after 30 minutes, 3 hours, 9 hours and 24 hours.

Table 4.1 – Starting phase proportions and 3D X-Ray microtomography resolutions of the different experiments. Proportions are expressed as forsterite (Fo) : silicate melt (Melt) : nickel (Ni) in volume percent. AF is for the 1-bar atmosphere controlled high temperature furnace experiments, PC is for the piston-cylinder experiments and PE for the Paris-Edinburgh press experiments. N.D. are for experiments which were not analyzed with 3D X-Ray microtomography.

Fo:Melt:Ni (vol%)	Set up	Type	Pressure (GPa)	Temperature (K)	Time (h)	Voxel (µm)
20:75:5	AF	Time-series 1	10^{-4}	1713	0.02	N.D.
20:75:5	AF	Time-series 1	10^{-4}	1713	0.5	N.D.
20:75:5	AF	Time-series 1	10^{-4}	1713	2	N.D.
20:75:5	AF	Time-series 1	10^{-4}	1713	6	N.D.
20:75:5	AF	Time-series 1	10^{-4}	1713	24	1.54
20:75:5	AF	Time-series 2	10^{-4}	1713 then 1470	24 then 0.5	1.54
20:75:5	AF	Time-series 2	10^{-4}	1713 then 1470	24 then 3	2.56
20:75:5	AF	Time-series 2	10^{-4}	1713 then 1470	24 then 9	1.54
20:75:5	AF	Time-series 2	10^{-4}	1713 then 1470	24 then 24	2.56
47.5:47.5:5	AF	Long run	10^{-4}	1713	24	4.25
62.5:32.5:5	AF	Long run	10^{-4}	1713	24	3.76
20:75:5	PC	Static	1	1753	5	1.23
47.5:47.5:5	PC	Static	1	1753	5	1.50
62.5:32.5:5	PC	Static	1	1753	5	1.50
81:9:10	PC	Static	1	1773	4	1.75
76.5:8.5:15	PC	Static	1	1773	4	1.50
68:17:15	PC	Static	1	1773	4	1.80
59.5:25.5:15	PC	Static	1	1773	4	1.50
72:8:20	PC	Static	1	1773	4	1.67
64:16:20	PC	Static	1	1773	4	1.80
56:24:20	PC	Static	1	1773	4	1.70
65:25:10	PE	Melting	1	298 to 2123	8	1.30
70:5:25	PE	Melting	1	298 to 1823	7	1.30
65:5:30	PE	Melting	1	298 to 1973	8	1.30

4.2.2.2 Piston-cylinder experiments (PC)

High-pressure experiments were also conducted to remove porosity, or at least preventing porosity from expanding due to thermal dilation. Textures of these experiments will be compared with those obtained from low-pressure bubble containing runs. Piston cylinder (PC) experiments have been performed in a 3/4-inch solid medium apparatus at the *Laboratoire Magmas et Volcans* (LMV, Clermont-Ferrand, France). Experiments were run for 5 hours at 1 GPa and 1723 K, i.e., 30 K below the melting point of nickel at such high pressure (Strong and Bundy, 1959). Pressure is larger than what is expected at the center of a 300 km radius, but there are no significant effects on the silicates between 1 bar and 1 GPa. Temperature was measured using a type C thermocouple (WRe_5 / WRe_{26}) and controlled using a PID

Eurotherm controller. The uncertainty on temperature was ±5 K. Powder mixtures were directly enclosed in a graphite capsule, making the sample size about 3 mm^3. Graphite has been chosen to set the oxygen fugacity to reducing conditions and to limit interactions with silicates. Although carbon is expected to dissolve into molten nickel, this effect was limited during the duration of the experiment: no graphite crystals were found as inclusions in the nickel beads. The graphite capsule was then put in MgO to isolate it from the graphite furnace and to align the sample with the hot zone. To limit shear and to mechanically stabilize the assembly, pyrex tubes were added on both sides of the graphite furnace. This assembly was contained in a NaCl cell pressure media to ensure hydrostatic conditions (Figure 2.6).

4.2.2.3 Paris-Edinburgh press experiments (PE)

Experiments similar to the piston-cylinder ones were conducted in a Paris-Edinburgh (PE) press at beamline PSICHE (SOLEIL Synchrotron) to have a series of time-resolved 3D X-Ray microtomography. In this case, forsterite powders were sieved to have grain sizes larger than 30 µm, allowing a better imaging of grains. The Ultrafast Tomography Paris-Edinburgh Cell (UToPEC) was used. This equipment allows the acquisition of a full image of the sample in a few tens of seconds, and also offers a 165° angular opening (upon a 180° rotation) that reduces artifacts during reconstruction (Boulard et al., 2018). Samples were taken to 1 GPa. Pink beam (filtered white beam) illumination was used to obtain a high X-Ray flux, necessary for high temporal (< 1 min tomogram) and spatial resolution (1.3 µm/voxel). Pressure and temperature were determined using the cross calibration method (Crichton and Mezouar, 2002) on Pt and hBN (hexagonal Boron Nitride) powders. The P-T calibrants were placed near the furnace but not in direct contact with the sample. The equations of state of these calibrants are taken from Le Godec et al. (2000) and Zha et al. (2008). As for PC experiments, powder mixtures were enclosed in an inner graphite capsule, which was in turn enclosed in a hBN outer capsule to isolate it from the graphite furnace. Sample size was about 2.5 mm^3. Graphite and molybdenum disks and steel rings were placed on both vertical ends of the furnace to align the sample vertically and to ensure electrical conductivity. This assembly was contained in a boron epoxy cell pressure media to ensure hydrostatic conditions (Figure 2.7). A peek plastic ring was added around the boron epoxy cell to limit the extrusion of the assembly. For these experiments, the silicate melt had the composition of the An-Di-Fo eutectic at 1 GPa (Presnall et al., 1978), allowing to know the temperature - composition - melt proportion relation.

4.2.3 Analytical techniques

4.2.3.1 Ex-situ 3D X-ray microtomography

After experiments, spatial distribution of the metal was first characterized with non-destructive 3D X-ray computed microtomography, using a Phoenix/GE Nanotom 180 at CIRIMAT (Toulouse, France) and operating conditions of 100 kV voltage and 130 µA energy current. Resolution could go down to 1.5 - 4 µm/voxel due to the small sample size. Typical acquisition time was about 1.5 hours, measuring 1440 slices (i.e. a step of 0.25° between each

slice). Each slice corresponds to the acquisition of 5 images (750 ms per image), out of which the first one is skipped to avoid remanence effects on the detector, and the other four are stacked to increase the signal to noise ratio. To allow precise segmentation (see below) of nickel in the samples, a nickel wire with a diameter of 250±3 µm has been used as a reference material. The nickel wire was measured with a micrometer caliper and then put into an alumina rod used to hold the samples for each acquisition. Data were processed with Datosx reconstruction software in order to obtain the 3D reconstructed volumes of the samples.

4.2.3.2 In-situ 3D X-ray microtomography

In the case of a high flux Synchrotron X-Ray pink beam, typical acquisition times (of about 50 s) are much shorter than for ex-situ microtomography. For each volume 1500 slices were acquired, resulting in a step of 0.24° between two successive slices. Each slice is composed of only one image with an exposure time of 35 ms. For these PE experiments, no reference material was used as it could cause instabilities in the experiment assembly. Data were processed with a Paganin filter to enhance phase contrasts (Paganin et al., 2002) and the PyHST2 python library (Mirone et al., 2014) was used to obtain the 3D reconstructed volumes of the samples.

4.2.3.3 3D data processing

For all samples, the 3D volume was converted to a stack of 8-bit images using ImageJ (Eliceiri et al., 2012; Schindelin et al., 2012). In the case of PC experiments, Regions of Interest (RoIs), representative of the samples, with dimensions of 500 x 500 x 500 voxels (≈ 0.2 - 0.4 mm^3) were also extracted with ImageJ. These 8-bit stacks were then loaded to Blob3D (Ketcham, 2005) for quantitative data analysis. Data treatment using Blob3D consisted of into three steps: segmentation, separation and extraction. For "segmentation", the software analyzed the data to affect a given set of voxels (corresponding to a range of grayscale values) to a given phase. In the present case, the grayscale difference between forsterite and silicate melt cannot be resolved due to similar X-rays absorption coefficients and densities. Hence, for the 3D X-ray microtomography data, the system has been considered in terms of only two phases: nickel and "silicates", the latter covering forsterite and silicate melt. Segmentation of the present samples was performed by simple thresholding, such that the volume of total nickel corresponds to the initial content of the sample. For the AF and PC samples, measurement of the diameter of the reference nickel wire allows to check the quality of the thresholding. For the "separation" step, the different sets of contiguous voxels are distinguished in terms of distinct objects, or blobs (see Ketcham, 2005, for more details). Finally, "extraction" quantifies the characteristics of the different objects: their volume, surface, Sphere Normalized Aspect to Volume Ratio (SNSVR, the equivalent of a 2D aspect ratio, i.e. the deviation of the blob from a sphere), their orientation, maximum and minimum length, etc. Of these parameters, only volume, surface and SNSVR were extracted and analyzed here. Indeed, a close look at the shape of nickel grains shows that their shape is far from being simple (e.g. a sphere or an ellipsoid). Extracting these data at the scale of the sample or RoIs is an efficient way to have statistical information and to determine trends between the different experiments.

4.2.3.4 Electronic analyses

Samples have also been characterized using Field Emission Gun Scanning Electron Microscopy (FEG-SEM) coupled with Electron BackScattered Diffusion (EBSD) in order to assess textural equilibrium at the micro-scale and to have information on the deformation processes due to potential shear in the samples. EBSD was mostly used for the AF time-series experiments with solid nickel. As the quality of the surface of the samples is very important for these electronic analyses, they were mounted in epoxy resin and polished with SiC grit down to 5 µm, then with alumina 1 µm for one hour, alumina 0.3 µm for two hours, and finally with colloidal silica for two additional hours.

FEG-SEM images were acquired at the Raimond Castaing Center (Toulouse, France) on a JEOL JSM-7800F Prime FEG-SEM, using a 10 keV accelerating voltage and a 10 nA beam current. Analyses of the textures with EBSD were conducted on a FEG-SEM JEOL JSM 7100F TTLS LV at the Raimond Castaing Center (Toulouse, France) as well, with operating conditions of 20 keV accelerating voltage and 18 to 20 nA beam current.

4.3 Results

4.3.1 Attainment of textural equilibrium

FEG-SEM images were used to assess textural equilibrium and showed olivine triple junctions at 120° in all samples, regardless of the duration of the experiment. Measurements of dihedral angles at triple junctions between forsterite, silicate melt and nickel on high resolution images (30 nm per pixel) yielded the same results within uncertainty, as in Néri et al. (2019), indicating textural equilibrium. Although the macro-scale organization of metal beads is different from one experiment to another, the grain-scale distributions are similar, indicating that the same micro-textural equilibrium can lead to different macroscopic textures.

4.3.2 Metal coalescence due to agitation

4.3.2.1 Large-scale properties of the local metal networks

Metal particles in the 20:75:5 and 47.5:47.5:5 samples are gathered under the form of localized networks (Figure 4.1a and 4.1b AF insets). Complementary experiments carried out in piston-cylinder with the same phase proportions do not exhibit similar results; grains are evenly distributed and form spheres (Figure 4.1a and 4.1b PC insets). AF samples bear gas bubbles trapped in the silicate matrix, which may have agitated the silicates and cause the observed interconnection of small metallic networks.

In detail, 3D data of static AF and PC experiments with solid nickel are represented in Figure 4.1. Efficient clustering of nickel in the 20:75:5 and 47.5:47.5:5 mixtures can be observed on Figure 4.1a and 4.1b (AF insets) with the three largest blobs of each sample

represented in red, orange and yellow (from largest to smallest). The largest blobs of the PC experiments are clearly smaller than in AF experiments, they are blending in among all the particles (Figure 4.1a and 4.1b, PC insets). Similarly, figure 4.1c shows the 62.5:32.5:5 mixture which displays the presence of bubbles due to areas with low Ni density, but the nickel grains are not interconnected at all. On the contrary, textures are very similar to that in the PC sample, indicating that the forsterite to forsterite plus silicate melt ratio is also of significant influence.

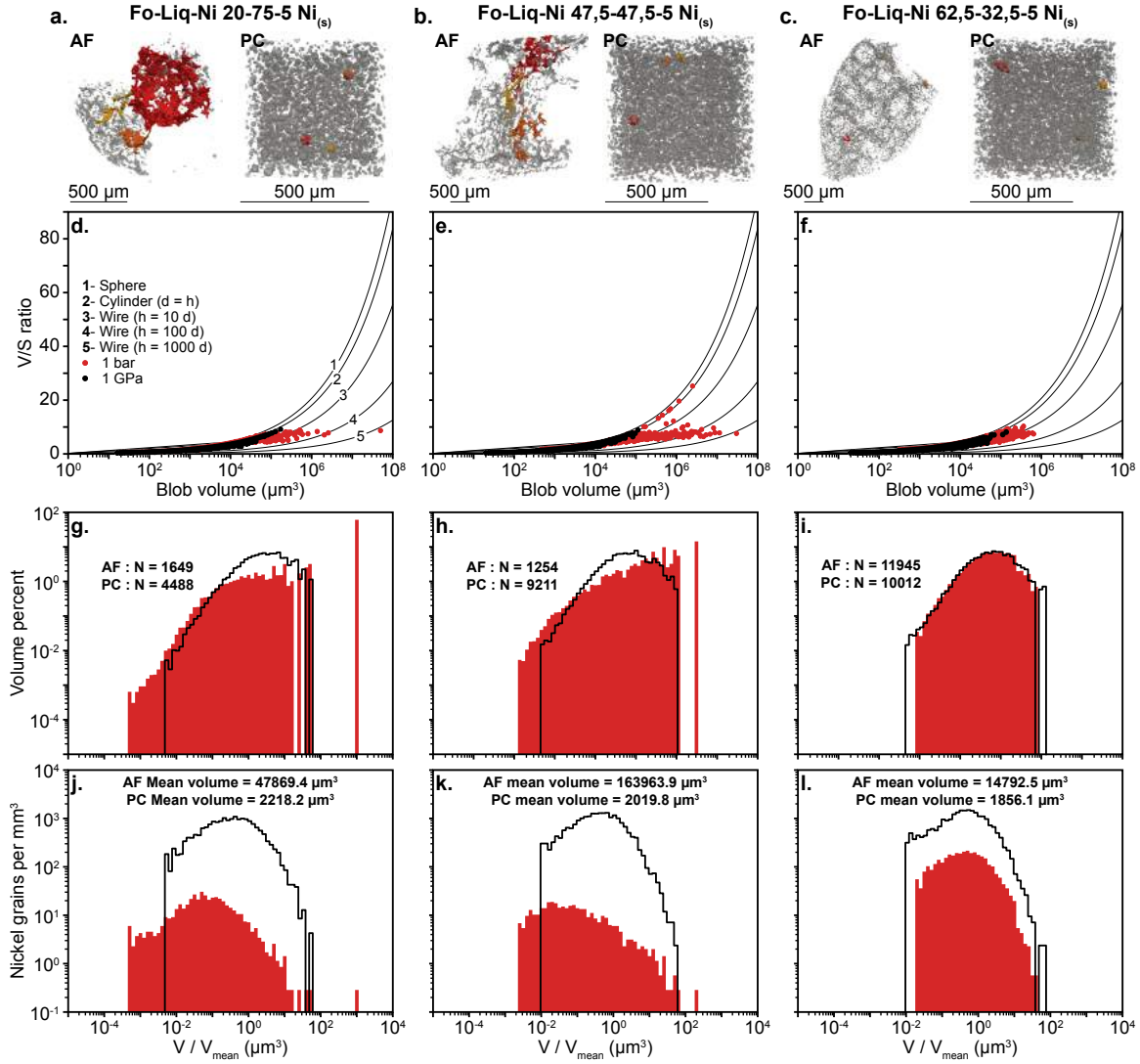

Figure 4.1 – Textures comparison of nickel phase (5 vol% in all samples) between stirred by gas bubbles samples (1-bar furnace, AF) and immobile samples (piston cylinder, PC) for different proportions of silicate melt in the system and after 24 hours (AF) and 5 hours (PC) of experiments at 10-15 K below the melting point of nickel. (a-c) show images of the 3D X-ray microtomograms. In gray is represented all the nickel of the sample. The three biggest blobs of nickel are represented in red, orange and yellow in each sample. (d-f) represent the volume to surface ratio (V/S) as a function of blob volume, with data points for AF experiments in red and data points for PC experiments in black. Normalized distributions (V/V_{mean}), in volume or in number are represented in (g-i) and (j-l), respectively. Here also, AF data are plotted in red and PC data in black.

Figure 4.1d, 4.1e and 4.1f represents the volume to surface (V/S) ratio as a function of blob volume. This ratio provides information on the shape of the grain relative to a sphere. Thin black lines represent evolutionary trends of the V/S ratio as a function of the blob volume for different simple geometrical shapes, i.e. a sphere and cylinders with different height to diameter ratios. The largest nickel blobs in AF samples (red dots) plot on an evolutionary trend that deviates significantly from trends expected for spheres, with inferred aspect ratios up to 1,000 if the shape is assumed to be an elongated cylinder, i.e. a wire. This feature indicates that blobs have been highly sheared by motion of the bubbles. In the 47.5:47.5:5 sample, some large blobs (with volumes around 106 μm^3) kept a spherical shape, indicating that stirring was not homogeneous within this sample. However, these blobs represents less than 1 vol% of the whole nickel in these samples, and may result from the lower fraction of silicate melt, leading to less efficient bubble stirring. The 62.5:32.5:5 AF mixture and PC experiments show very similar V/S ratio trends, both consistent with spherical shapes. This feature indicates that the larger presence of silicate crystals in the AF experiment drastically hindered bubble stirring, leaving nickel grains with their equilibrium spherical shapes. Within the 62.5:32.5:5 mixtures, the AF experiment shows larger grains than the PC one due to longer run duration: 24 hours compared to 5 hours for the PC ones.

Grain size distributions of the different samples bring additional information. To correct for the effect of different experimental duration, volumes of the blobs were normalized to mean blob volumes of the samples. From this, two different types of distribution are represented: the volume fraction distribution (Figure 4.1g, 4.1h and 4.1i), which provides the nickel volume fraction of each bin, and the density distribution of nickel grains (Figure 4.1j, 4.1k and 4.1l), showing the number of nickel grains per bin in a normalized unit volume of 1 mm^3. Both types of distribution are narrow and similar for the PC samples, with mean volumes of 2000 μm^3 (i.e. a sphere equivalent radius of 8 µm), and grain volumes that range from 10 μm^3 to 200,000 μm^3 (i.e. sphere equivalent radii that range from 1.3 µm to 36 µm), no matter their silicate melt content. Overall, a normal distribution shape (lognormal in log scale) is preserved, which is the expected result for normal grain growth mechanisms. The AF 62.5:32.5:5 sample distribution (red step curve in Figure 4.1i) is a perfect match to PC samples; it has the exact same characteristics, except for the average grain volume that is the result of a longer run duration (24 hours). Note that slight variations between these distributions are due to the resolution of the 3D data volume (see Table 4.1). Distributions for the other AF experiments, with larger amounts of silicate melt (75 vol% and 47.5 vol%, red bars in Figure 4.1g, 4.1h, 4.1j and 4.1k), show two interesting features. Firstly, grains span a wider range of sizes that reach 107 μm^3, yielding a different shape in a lognormal diagram, with a large gap in size between the largest grain and the rest of the distribution. In these experiments, the largest nickel grains can thus represent a significant amount of the total nickel. For example, the largest blob of the 20:75:5 sample (red blob on Figure 4.1a AF inset) is a solid network of nickel formed of multiple grains (see section 4.3.2.2), that concentrates 80 vol% of the total nickel (Figure 4.1g), while the second largest concentrates only 5 vol%. The largest blob of the 47.5:47.5:5 sample represents a lower fraction of the total nickel but still reaches $\approx$ 20 vol% (Figure 4.1h). All these properties underline grain growth mechanisms that deviate from normal ones. In comparison, there is no gap between the largest blob of the 62.5:32.5:5 AF distribution or of each PC distribution and the rest of the population. Also, this largest blob represents at most 1 vol% of the total nickel volume. These features highlight the extreme efficiency of stirring in creating local concentrations of metal.

The differences in the density of nickel grains at a given V/V_{mean} ratio between the different samples are also of great importance (Figure 4.1j-l). Overall, for the same normalized volume, the number of blobs per unit volume are similar in all PC experiments, about 1000 blobs per mm^3. However, there are differences among the AF density distributions and between the AF and PC ones. The 62.5:32.5:5 AF sample (Figure 4.1l) shows a density distribution with a maximum at about 100 blobs per mm^3, which is one order of magnitude lower than the PC experiments, but one order of magnitude higher than the silicate melt rich AF experiments (Figure 4.1j and 4.1k, with a grain density of about 10 per mm^3). This discrepancy between the silicate melt poor AF and the piston-cylinder samples is probably due to different experiment duration times: longer experiments allow the nickel grains to grow larger, lowering the number of grains per volume unit. However, differences in the amplitudes of density distributions of nickel grains per volume unit between high and low silicate melt contents between the AF samples highlights once more the efficiency of gathering nickel grains in agitated systems, as these experiments have the same duration.

4.3.2.2 Micro-scale properties

A time-series experiment was conducted in the 1-bar high temperature atmosphere controlled furnace to study the textural evolution of nickel grains due to stirring (20:75:5 mixture - 1713 K - solid Ni). These experiments were analyzed with FEG-SEM imaging coupled with EBSD to evaluate the deformation that affected the samples. EBSD data and high-resolution FEG-SEM images show clusters of nickel actually made of an agglomeration of individual solid nickel grains. Textures of these samples are illustrated in Figure 4.2a-d. Grain-to-grain junctions can be detected by different grayscale contrasts on the FEG-SEM images due to different grain orientations or by direct measurement of grain orientation with EBSD (Figure 4.2e-h). Such clusters of solid nickel grains can be explained in terms of interfacial energies: nickel has the highest interfacial energy with the silicates, either solid or molten (Néri et al., 2019), but its interfacial energy with itself is likely to be relatively low (Murr, 1975). Hence, nickel grains will tend to be in contact in solid state for energetic reasons, coalescing to form a single large bead when molten. A consequence of stirring by bubbles the samples is nickel shearing detected by EBSD with the appearance of a significant local misorientation in grains up to 5° (Figure 4.2e-h). Forsterite grains are clearly not affected by this deformation, their local misorientation remaining lower than 1°. Once the solid nickel network is formed, textural evolution is restricted to the evolution of aspect ratio distributions (Figure 4.2i-l) and of finite shear strain with time. Indeed, assuming simple shear and homogeneous strain, the finite shear strain (γ), i.e. the quantity of deformation undergone by the grain, can be estimated from the aspect ratio (R) using the following equation:

$$R^2 = \frac{\gamma^2 + 2 + \gamma\left(\gamma^2 + 4\right)^{1/2}}{\gamma^2 + 2 + \gamma\left(\gamma^2 + 4\right)^{1/2}} \tag{4.2}$$

Dividing the finite shear strain by the time of experiments gives the finite shear strain rate. At the beginning of the experiment (0.5 hours), nickel grains have an average aspect ratio of 2, spanning a range from 1 to 6. This corresponds to a mean shear finite strain rate of 4.10-4 s^{-1} (shear finite strain of 0.7). After 2 hours, the aspect ratio distribution does not

change significantly. However, 6 hours after the beginning of the experiment, the proportion of grains with low aspect ratios has decreased in favor of grains with larger ones, shifting the average aspect ratio to 2.2 and also modifying the average shear finite strain rate to 4.10-5 s^{-1}. The effect of elongating grains with time is even more obvious after 24 hours of experiment: only 40% of the grains kept a low aspect ratio, with an average value of 2.6 corresponding to a mean shear finite strain rate of 10-5 s^{-1}. The decrease of shear finite strain rate with time indicates that the agitation due to gas bubbles also decreases with time. Indeed, over time, gas bubbles escape from the sample. The aspect ratio distributions of forsterite evolve as well: grains become more and more rounded due to textural maturation. The overall effect is an increased gap between the average aspect ratio values of forsterite and nickel (Figure 4.2i-l dashed lines). As elongated and locally deformed grains are observed to be rapidly formed, typically in less than one hour, stirring mechanisms are apparently extremely effective to concentrate nickel grains in the solid state. However, the formation of a network with only 5 vol% of a phase that has a high dihedral angle, thus a high interconnection threshold, is unexpected. This network is unlikely to remain stable under static conditions.

4.3.2.3 Evolution of the coalesced network

To investigate the stability of the network at low metal fraction, another AF time-series experiment was conducted at 1, using the same proportions as before (20:75:5 Fo:Melt:Ni vol%), but with molten nickel to increase the textural maturation rate of metal. For this experiment, samples were first equilibrated at 1713 K for 24 h in order to form a solid network. Temperature was then increased to 1743 K, i.e. 15 K above the nickel melting temperature. Samples were quenched at different times (Table 4.1, Figure 4.3).

Figure 4.3 shows the data extracted from this time-series experiment. Data for the sample recovered after 24 hours with solid nickel are identical to Figure 4.1a, 4.1d, 4.1g and 4.1j (AF). Half an hour after melting the nickel (Figure 4.3b), the previously formed network is disrupted and separated into smaller blobs, causing the number of blobs to increase by a factor of almost 2 (from 1649 at solid state to 3721 after 0.5 hours, Figure 4.3a and 4.3b). Most likely, nickel separated along grain boundaries, as they may constitute weak points. This interpretation is supported by the mean volume of blobs that drops by one order of magnitude to 3.5×10^3 µm^3 (sphere equivalent radius of 10 µm instead of 134 µm for the initial large-cluster), corresponding to the mean grain size of the starting nickel powder. V/S ratios are also drastically affected by the melting of nickel: once molten, all of the blobs tend toward spherical shapes (Figure 4.3b). Regardless of the time spent above the melting temperature, grains of nickel remain spherical (Figure 4.3b-d), but time affects the size and number of blobs. Indeed, with increasing time the number of nickel blobs decreases and their average volume fraction increases. After 9 hours above the melting temperature of nickel, only 56 blobs remain with a mean volume that reached 5×10^5 µm^3, i.e. a sphere-equivalent radius of 50 µm that is much larger than the initial mean grain size of 8 µm. Such a strong increase in such a short time cannot arise from normal grain growth, about a thousand years would have been necessary (Guignard et al., 2012, 2016). Stirring is thus a highly efficient mechanism to make molten nickel blobs coalesce on extremely short timescales of typically a few hours.

With molten nickel, volume fraction and density distributions (Figure 4.3e-l) have similar shapes to that observed after 24 hours at solid nickel state, with a single large grain representing a significant fraction of total nickel, and a gap between this grain and the rest of the population. However, the volume percent of the largest grain is smaller. After 0.5 h with molten nickel, the size of the largest blob reached about 20 vol% of the whole metal fraction (Figure 4.3f). Then, the volume of the largest blob is doubled to reach 40 vol% after 3 hours (Figure 4.3g) and remains about the same after 9 hours (Figure 4.3h). This fraction is likely to be a maximum. Indeed, although the number of grains after 9 hours of Ni melting decreased, none of them exceeded 40 vol% of the whole nickel; instead, the proportion of large grains increased. The shift of the distributions toward higher mean volumes leads to a decrease of the density of nickel particles per volume unit, by almost one order of magnitude between each time step. The odd shapes of the size distributions in Figure 4.3h and 4.3g are likely due to a lack of statistics (only 56 grains).

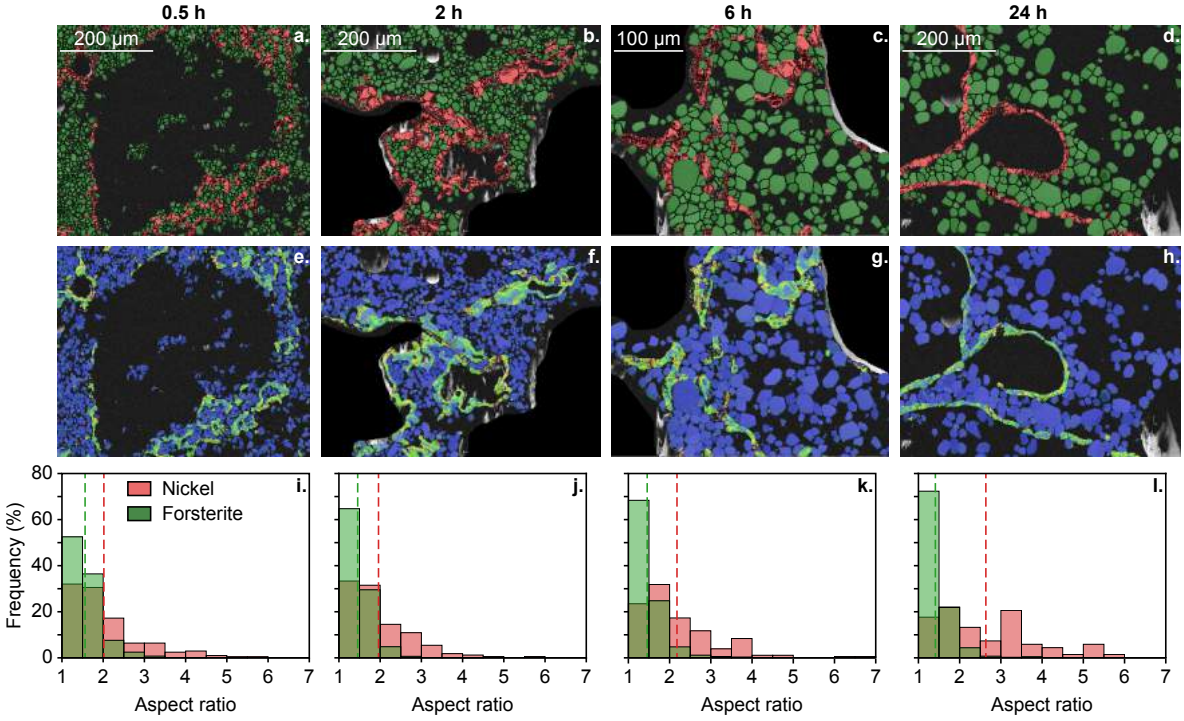

Figure 4.2 – Results of the EBSD data acquired on the 20:75:5 (Fo:Melt:Ni vol%) AF time-series experiments at 1713 K (with solid nickel). The first column correspond to a run duration of 0.5 hours, the second column to a run duration of 2 hours, the third column to a run duration of 6 hours and the last column to a run duration of 24 hours. (a-d) Phase identification of the analyzed surfaces, with nickel grains in red and forsterite crystals in green. Silicate melt and air bubbles are represented in black. (e-h) Local misorientation maps of the phases, with low misorientation angles in blue and high misorientation angles in red. The color scale is normalized to the same maximum value of 5° for both phases and for the different maps. Grain boundaries appear in thick black lines while sub-grain boundaries in thin black lines. (i-l) Distributions showing the evolution of aspect ratios of forsterite and nickel with time. Forsterite is represented in green and nickel in red. Dashed lines correspond to the mean aspect ratio of a phase.

All these features indicate that agitated systems are highly efficient to make metal grains coalesce and have higher average grain sizes than with classical grain growth mechanisms, whether the metallic phase is molten or not. However, agitation also fosters the formation of

a localized metallic networks that are unstable and can be broken provided that the rate of textural maturation of the phases is larger than that of deformation.

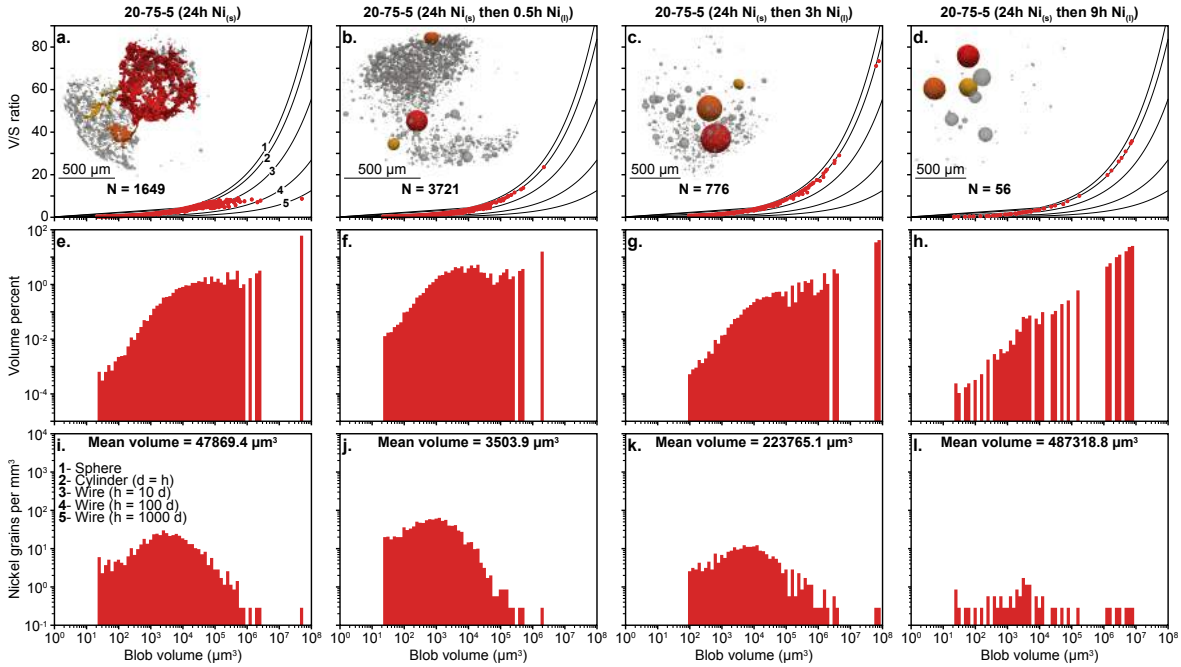

Figure 4.3 – Time-series textural evolution of nickel phase across the melting temperature of nickel in sample containing 75 vol% of silicate melt and stirred by gas bubbles (AF experiments). (a, e and i) are the same diagrams that in Figure 4.1. (a-d) show images of the 3D X-ray microtomograms and the V/S ratio as a function of blob volume. In gray is represented all the nickel of the sample. The three biggest blobs of nickel are represented in red, orange and yellow in each sample. Normalized distributions (V/V_{mean}), in volume or in number are represented in (e-h) and (i-l), respectively.

4.3.3 The effect of varying silicate melt content and metal fraction

4.3.3.1 Ex-situ analyses

A series of experiments with molten nickel was conducted to study the effect of varying silicate melt contents on the equilibrium texture and the formation of an interconnected network. To do so, PC experiments were run with 10, 15 and 20 vol% of nickel and three different forsterite to forsterite plus silicate melt ratios (noted as Fo/(Fo+Melt)): 90, 80 and 70 %. These experiments were kept at 1773 K and 1 GPa for 4 hours.

Figure 4.4 shows results for the PC experiments with molten nickel. V/S ratios of the detected blobs as well as the largest blob for each sample (with the corresponding color code) are represented in Figure 4.4a-c. The shape of the largest blob seems to depend on the fractions of nickel and silicate melt. At a given metal fraction, large silicate melt contents (color blobs and green dots, Figure 4.4b and 4.4c) result in nickel grains with shapes closer to spheres (wire equivalent aspect ratio lower than 10), while low silicate melt contents (color blobs and red dots, Figure 4.4b and 4.4c) yield nickel grains with twisted shapes that decrease the V/S ratio (with wire equivalent aspect ratios up to 100). Different final results on the exact

same experimental system and for identical experimental duration indicate different textural maturation. It is of note that the detected blobs are actually composed of smaller individual grains, with spherical shapes, linked by narrow necks. With time, grains should toward their minimal interfacial energy geometry and form spheres. There are two pathways to do so: either break the grains with large V/S ratios into smaller spherical ones or gather them into a single spherical larger one. This latter scenario is limited because the minimization of interfacial energy is not sufficient to cause a local deformation of the solid silicate framework. Varying amounts of silicate melt affect the viscosity of the rigid silicate matrix, also affecting the timescales of metal reorganization. The state, solid or molten, of nickel grains also affect this timescale as molten nickel pools can be deformed more easily than solid grains. Finally, the fraction of nickel and most precisely to distance to the interconnection threshold affects the textural maturation rate. Indeed, close to the interconnection threshold, small and localized networks start to form, which are likely to destabilize and reorganize on larger timescales than isolated grains. Hence, the effect of the silicate melt content is best observed on the experiments with 20 vol% Ni (Figure 4.4c, 4.4f and 4.4i). This effect is likely a function of the distance to the interconnection threshold, rather than a function of an absolute phase fraction as it depends on each different phase and system.

The representation of the nickel volume fraction and density distributions (Figure 4.4d-i) supports the idea of different textural maturation rates conclusion, with the nickel volume fraction and size of the largest blob increasing with decreasing silicate melt content. The experiment with large silicate melt fraction has a largest blob with a volume of 10^6 µm^3, which represents about 1 vol% of the total nickel; while at low silicate melt fraction, the largest blob has a volume of 5×10^6 µm^3 and represents about 10 vol% of the total nickel.

4.3.3.2 Time-resolved in-situ analyses

Complementary PE experiments were conducted on beamline PSICHE with the following starting materials (Fo:Melt:Ni in vol%): 65:25:10, 70:5:25 and 65:5:30. These experiments were kept at 1 GPa and temperature was progressively raised to allow progressive melting of the silicates and the in-situ study of textural evolution. In the PE experiments, the silicate melt content corresponds to the eutectic silicate melt content. For example, for the 65:25:10 mixture, just above the eutectic temperature, there will be 25 vol% of silicate melt, a fraction that will then increase with increasing temperature.

Upon progressive melting of the material and increasing textural maturation rate, tomograms were taken to study the evolution of the metallic networks. For simplicity, only the characteristics of the largest blob are represented. Considering the 65:25:10 experiment (Figure 4.5), the trend defined by the nickel volume fraction of the largest blob is very illustrative: at the beginning of the experiment, most of the nickel is gathered as a network, which represents about 70 vol% of the total nickel (Figure 4.5a). However, upon increasing temperature and silicate melt fraction, the network breaks apart at about 1773 K (after nickel melting and the silicate eutectic): the nickel volume fraction of the largest blob drops to 5 vol% and continues to decrease until it reaches ≈ 1 vol%. The SNSVR (Figure 4.5b) shows a similar trend with a huge drop at the same temperature indicating that disconnection of the network forms blobs with shapes close to spherical (SNSVR = 1). Oscillations of the SNSVR before

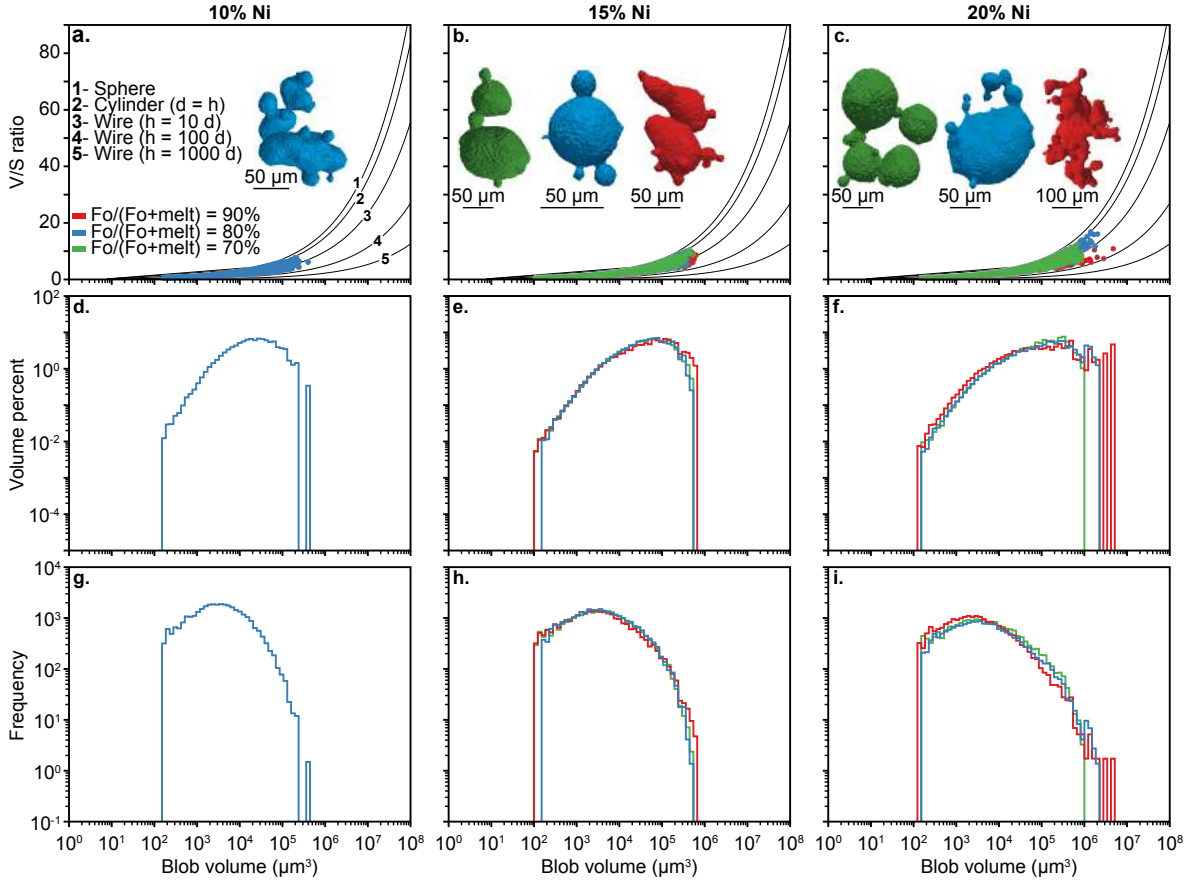

Figure 4.4 – Textural evolution of nickel phase with varying forsterite to forsterite plus silicate melt ratios (noted as Fo / (Fo + Melt); 90% in red, 80% in blue and 70% in green) and varying nickel content (10 vol% in the first column, 15 vol% in the second one and 20 vol% in the third one). The three rows show similar representations to those used in Figure 4.3. (a-c) The largest blob of each experiment is represented in color corresponding to the Fo / (Fo + Melt) ratio, along with the V/S ratios of the blobs in the different samples. Normalized distributions (V/V_{mean}), in volume or in number are represented in (d-f) and (g-i), respectively.

its dramatic decrease indicate that the unstable network is constantly reorganizing itself, with a dynamic of disruption and interconnection. After the network breaks apart, the mean blob volume corresponds to the initial nickel grain size; V/S grain populations and nickel volume fraction and density distributions are similar to those obtained at the end of PC experiments (Figure 4.1 and Figure 4.4). The formation of a metallic network at the beginning of this experiment is due to the cold compression. Indeed, nickel is the "soft" phase and will spread along grains of the solid silicate matrix. An additional point of note is that this unstable network is not global and is far from concentrating all the nickel of the sample. However, once the textural maturation rate is high enough (molten nickel and / or enough silicate melt) the metal can reorganize itself quickly.

The effect of silicate melt is thus to increase the textural maturation rate, allowing the metal to reorganize more rapidly in the presence of large silicate melt contents. On the other hand, low silicate melt content slows considerably slows down the reorganization of metallic beads, preventing them from forming spheres.

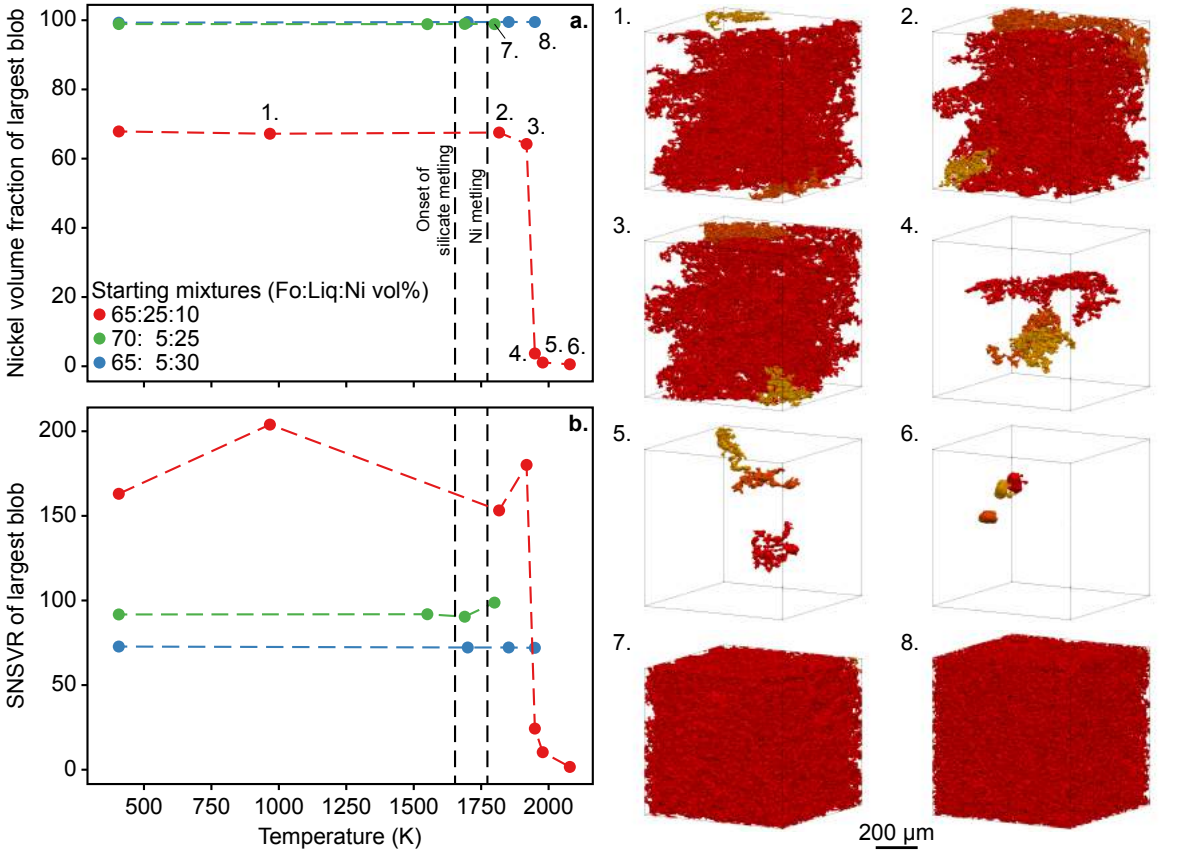

Figure 4.5 – Textural evolution of nickel phase in the Paris-Edinburgh press experiments conducted on beamline PSICHE (SOLEIL Synchrotron) for three different mixtures (in Fo:Melt:Ni vol%): 65:25:10 (in red), 70:5:25 (in green) and 65:5:30 (in blue). Results here are plotted as a function of temperature, which corresponds also to a different silicate melt content due to progressive melting. For simplicity, the nickel volume fraction (a) and the SNSVR (b) of the largest blob are plotted as a function of temperature. Numbers represent images of the 3D tomograms in different conditions and for the different samples. For clarity of the figure, only the three largest are represented in red, orange and yellow, from largest to third largest.

4.3.4 Formation of stable networks

Figure 4.5 also shows the result for the PE experiments with 25 and 30 vol% of nickel. In these two experiments, the largest grain concentrates more than 99 vol% of the whole nickel in the sample (Figure 4.5a), making this blob a widespread network. The volume fraction of the largest blob does not seem to be affected by temperature. The SNSVR of these two largest blobs (Figure 4.5b) are high: between 75 and 100, corresponding to a wire equivalent aspect ratio of 10,000. These values do not seem to be affected by temperature either. The starting material only contained 5 vol% of eutectic silicate melt, resulting in about 8 to 10 vol% of silicate melt at the end of experiment. Such low silicate melt fraction is enough to break an unstable network in a few hours (as seen on Figure 4.4). However, the networks formed in these experiments remain, indicating that they are stable. The interconnection threshold to form a stable network is then between 20 and 25 vol% for pure nickel.

4.4 Discussion

4.4.1 A reevaluation of interconnection threshold in literature

A precise knowledge of the interconnection threshold is essential to address metal-silicate differentiation processes. No consensus exist in the literature and various threshold values are proposed for the same system (e.g. Yoshino et al., 2003; Bagdassarov et al., 2009a; Watson and Roberts, 2011). How can these data be reconciled? The present study highlights that the cold compression at the beginning of the experiment leads to the formation of an unstable interconnected network of the metallic phase (Figure 4.5), due to the low viscosity of the metallic phases. On a broader scale, deformation may affect the dynamics of interconnection. Stress and surface tension affect drastically the rate of textural maturation, giving rise to two regimes depending on the dominating force (Walte et al., 2011). These effects may lead to a misinterpretation of the equilibrium interconnection threshold.

With similar systems of Fe-FeS eutectic in San Carlos olivines, the literature reports values of interconnection thresholds that range from 3-6 vol% (Yoshino et al., 2003; Roberts et al., 2007; Watson and Roberts, 2011) to 17.5 vol% (Bagdassarov et al., 2009a). The formation of a sulfide network during compression can be expected, as in the present study with nickel. The existence of a forced and unstable network provides a good explanation for the discrepancies among literature data. Instead, Bagdassarov et al. (2009a) invoked different degrees of textural maturation to explain the discrepancy. To circumvent this issue and increase the rate of textural maturation, fine-grained olivines grain sizes were used (mean particles diameter of 1.8 µm) and experiments ran for longer equilibration times (about 100 hours with temperatures between 1243 and 1373 K). The resulting grain sizes at the end of experiment are equivalent to the disappearance of more than 99 % of the olivine grains. In this two-phase system case, textural maturation is driven by grain boundary migration (Walte et al., 2007; Bagdassarov et al., 2009a). Using small starting grain sizes is a way to enhance grain boundary migration and to increase the rate of textural maturation.

In AF and PC experiments, dihedral angle values at triple junctions are identical within error bars, indicating similar micro-textural equilibrium. While this micro-scale equilibrium is reached on short timescales (e.g. 4 hours in the case of PC), the macro-textural one may require more time. By contrast to the study of Bagdassarov et al. (2009a), a few hours were sufficient to reach textural equilibrium in the present study. In fact, different parameters act to reduce the equilibration time: varying contents of silicate melt and metal, shifting from solid to molten of the latter and grain growth. The addition of a silicate melt drastically increases the grain growth rate (Faul and Scott, 2006) and grain boundary migration of silicates. The minimization of interfacial energy along a silicate melt - metallic melt interface is also faster due to the low viscosity of both phases. Indeed, in the AF time-series experiments, after 24 hours of equilibration below the melting temperature of nickel, the shift to 1743 K (i.e. above the melting temperature of nickel) disrupted the network on extremely short timescales, less than 0.5 hours. The PE experiment with 10 vol% nickel (Figure 4.5 red dots) shows similar results with the disruption of the network once both metal and silicates are molten. The two parameters silicate melt content and state (solid or molten) of the phase constituting the network seem to have similar effects on the textural maturation rate. Large silicate melt

contents increase drastically the maturation rate, while low contents decrease it. A molten network is able to disrupt rapidly (< 1 h), while a solid one will take more time to disrupt, due to slow grain boundary migration and to interfacial energies that will make the grains hold together. In the present study, all these parameters ensure the disruption of the unstable networks and the acquisition of spherical shapes for nickel grains in a matter of a few hours.

To assess the stability of a network, the presence and quantity of silicate melt along with the state of the network are critical parameters to play with. Their respective effects allow the increase of the textural maturation rate by a few orders of magnitude, reducing in the same the time of experiment necessary to approach textural equilibrium. PE experiments thus showed that a molten metallic network is stable above 25 vol% of metal. The true interconnection threshold of pure metal in a partially molten silicate matrix is between 20 and 25 vol%, in agreement with the dihedral angle measured in Néri et al. (2019).

4.4.2 Coalescence mechanisms

4.4.2.1 Origin of coalescence in experimental samples

The gas bubbles trapped in the samples are likely what drove the metal grains to form localized networks. It seems that the porosity trapped in the ground powdered starting material expanded during the experiment due to thermal expansion at high temperature. Thus, gas bubbles trying to escape stirred the samples when there is sufficient silicate melt content, leading to local interconnection of nickel grains. However, this effect is only seen for samples bearing enough silicate melt and not the 62.5:32.5:5 one. Indeed, if the viscosity of the melt-crystal mush is too high, bubbles remain trapped and are not able to deform the solid silicate framework to escape the sample, as observed on Figure 4.1c (AF inset). Viscosity depends on the crystal fraction and more specifically on the maximum packing fraction, noted ϕ_m. If the forsterite crystal fraction exceeds ϕ_m, then all crystals are in contact with one another. In this case viscosity is extremely high, roughly that of the solid silicate, on the order of 10^{18} Pa.s (Hirth and Kohlstedt, 2003), precluding any deformation or shear due to bubble motion. On the other hand, if the crystal fraction is lower than ϕ_m, then viscosity remains sufficiently low for stirring by gas bubbles. Based on literature data, the maximum packing fraction ranges from 0.4 to 0.74 with a value of ≈ 0.6 for relevant geological materials (Marsh, 1981; Scott and Kohlstedt, 2006; Champallier et al., 2008; Costa et al., 2009). Here, the 62.5:32.5:5 mixture seems extremely close to ϕ_m, explaining why the bubbles could not deform the forsterite skeleton during the AF experiment.

4.4.2.2 Implications for differentiation in magma oceans

Different metal-silicate differentiation scenarios are conceivable depending on the size and accretion time of the planetesimal and on the grain size of the matrix. The accretion time controls the quantity of heat source (^{26}Al, $t_{1/2} = 0.73$ Myr) while the size controls the ability of the body to evacuate its internal heat. In turn, the grain size of the crystalline silicates controls the timescale of melt migration (Lichtenberg et al., 2019), whether it be silicate or

iron-sulfide melt. Note that grain sizes of about a millimeter are very efficient to extract melts. In general terms, the evolution pattern of a planetesimal thus depends on the ratio between the timescale of melt migration and that of heating (and / or time spent at high temperature). For example, for a large body accreted in the time-window that leads to temperatures just above the partial melting temperatures of both silicate and iron-sulfur subsystems, the heating rate is relatively low. The body then remains hot for long periods of time, allowing grains to grow to sizes large enough to promote efficient migration of silicate melt, this efficiency is enhanced by the extremely low interconnection thresholds of silicate melts (Laporte and Provost, 2000). In this case, differentiation of metal-rich melts occurs by the formation of an interconnected iron-sulfide network that results from indirect concentration induced by the removal of silicate melt (Néri et al., 2019). In the case of a small early-accreted body, the heating timescale is much shorter than that of melt migration. In this case, the planetesimal will reach large degrees of local silicate melting and potentially form a convective magma ocean(e.g. Hevey and Sanders, 2006). The fate of metal in a magma ocean is discussed in detail in a companion paper (Néri et al. (in prep.), Chapter 5).

In light of the results presented here it is clear that convective motion will act to foster the coalescence of iron-sulfide beads as observed in the AF experiments, whether the metal is solid (Figures 4.1 and 4.2) or molten (Figure 4.3). This process occurs on much shorter timescales than normal grain growth mechanisms (e.g. Ostwald ripening), allowing the rapid formation of large iron-sulfide blobs. For instance, in the present study, aggregates were able to reach volumes as large as 5×10^7 µm^3 in 24 h (Figure 4.1d), corresponding to a sphere equivalent radius of ≈ 230 µm, noting that normal grain growth would have taken a few million years to reach such sizes. The former time-scales (days) are ridiculously short compared to the lifetime of a magma ocean in a small body (a few million years, M. Monnereau personal communication). Coalescence is thus expected to occur to form large blobs of iron-sulfide, although a dynamic environment also creates shear forces that counteract surface tension and lead to fragmentation (Liao and Lucas, 2010). In detail, numerical simulation of the balance between formation and destruction of falling metallic blobs in a crystal-free silicate melt shows a critical stable drop radius of about a centimeter that is reached in tens of seconds (Ichikawa et al., 2010).

Following Solomatov (2015), the condition for a particle to escape convective motions depends on its size, density difference with the surrounding magma ocean, viscosity of the magma ocean, acceleration due to gravity (i.e. radius) and Rayleigh number. Assuming a 100 km radius planetesimal and iron-sulfide particles sinking in an entirely molten magma ocean ($\Delta\rho = 2000$ kg.m^{-3} for Fe-FeS eutectic to $\Delta\rho = 5000$ kg.m^{-3} for pure iron, $\eta = 10$ Pa.s), the critical size for a particle to sink is about a millimeter. If the equilibrium temperature of the magma ocean does not lead to entire melting, the presence of silicate crystals can affect its viscosity according to the Einstein-Roscoe equation (Roscoe, 1952):

$$\eta = \frac{\eta_l}{(1 - \phi/\phi_m)^{2.5}} \tag{4.3}$$

with η the viscosity of the crystal-melt mixture, η_l the viscosity of the silicate melt, ϕ the crystal fraction and ϕ_m the maximum packing fraction. This latter variable corresponds to the crystal fraction at which all crystals are in contact leading to viscosities that approach that of the solid. In geological materials, this fraction varies between 0.5 and 0.7 (Marsh,

1981). Assuming a mean value of $\phi_m = 0.6$, the viscosity of the magma ocean will increase dramatically as ϕ_m is approached (increasing by a few orders of magnitude for an initial viscosity of 500-1000 Pa.s at a crystal fraction of 0.5). In this viscous regime, the critical grain size to escape convective motions is increased to the centimeter. Such sizes, millimeter or centimeter, cannot be reached by normal grain growth mechanisms in the lifetime of a magma ocean, but are permitted by coalescence. Noteworthy, olivine crystals are likely entrained during the fall of iron-sulfide particles due to the interfacial energy ratios (Néri et al., 2019). In summary, coalescence is an efficient mechanism to make iron-sulfide particles grow large enough to remove them from the magma ocean, along with olivine crystals.

4.4.3 Textures in natural samples

An important issue of natural samples is that textures of iron or troilite grains differ from one sample to another, indicative of different evolutionary processes. Comparison of natural and experimental textures may shed light on such processes. For example, a striking feature of chondrules is that metallic particles are very close to being perfect spheres (e.g. Zanda, 2004). Furthermore, the presence of silicate glass in these objects indicates a high degree of silicate melting. These conditions are similar to those of the AF experiments, in which textural maturation of metallic phases was rapid, reaching spherical shapes in a matter of a few hours or less. However, note that this does not preclude deviation from sphericity, if the silicate melt is not distributed homogeneously. In opposition, iron or troilite grains in primitive achondrites or metamorphosed H chondrites (type 4 to 6) have irregular shapes.

In contrast, primitive achondrites have metallic phases that are irregular in shape. These natural samples are thought to originate from a precursor H chondrite material, which was partially molten and may have have lost a silicate phase and/or an iron-sulfide component. In detail, acapulcoites are generally thought to be the residue of low degrees of partial melting, typically up to 5 vol%. In turn, lodranites experienced greater extents of partial melting, as highlighted by the loss of almost all the sulfide phases, low melting temperature silicates (e.g. clinopyroxene and feldspar) and depletion in light Rare-Earth Elements. These features indicate that both silicate and iron-sulfide subsystems were molten at the same time. Acapulcoites and lodranites are then expected to have iron and troilite grains with textures more evolved than in H-chondrites, due to greater peak temperatures. However, grains of iron-rich phases in acapulcoites and lodranites have intermediate irregular shapes, between H4 and H6 (Guignard and Toplis, 2015). Some metal grains seem to be forced to have a given shape, following the boundaries of neighboring silicate grains, as seen on sections of Acapulco and Lodran (MNHN, sections Acapulco -2 and Lodran ns 2 respectively, see Chapter 6).

The odd textures of metal-rich phases in these primitive achondrites can be explained by the loss of silicate melt. Indeed, the removal of a phase will induce a compaction of the matrix, applying a stress on the iron and troilite grains. As seen in the experiments, such stress results in deformation of metallic phases along the boundaries of silicate crystals. The efficiency of this process is directly linked to the quantity of the mobile phase that is extracted. For instance, greater loss of silicate melt will lead to greater deformation of iron and troilite grains. An additional effect that may increase this effect is the proximity to the interconnection threshold (see Figure 4.4a, 4.4b and 4.4c). Indeed, upon removal of silicate

melt, in the absence of mobility of the metallic phase, the relative amount of iron and troilite will increase, getting closer to the interconnection threshold. Hence, localized networks will start to form, with irregular shapes and longer equilibration times. Although natural samples were maintained at relatively high temperature for long times (probably a few million years), iron and troilite did not adopt a spherical shape. Either a deformation mechanism maintained the non-sphericity of the phases, or limited mobility of silicate grain boundaries prevented the formation of spherical grains. Acapulcoites and Lodranites show no signs of deformation or shock (e.g. Keil and McCoy, 2018, and references therein), hence the second scenario is more likely. The growth of crystalline silicates is significantly faster in the presence of silicate melt (Guignard et al. in prep) allowing to reach grain sizes on the order of a few hundred microns in a few million years, which is relevant to acapulcoites and lodranites (Bild and Wasson, 1976; Palme et al., 1981). With such grain sizes, once silicate melt had been extracted, grain growth of residual grains must have been significantly hindered (Guignard et al., 2012, 2016). Grain boundary migration being almost inexistent, subsequent textural maturation is expected to be extremely slow, leading to irregular shapes that are stable over time.

4.5 Conclusion

Experiments were performed to determine the interconnection threshold of pure metal and to study the influence of different parameters. The experimental system was composed of forsterite, silicate melt and nickel grains, which is relevant to metal-silicate differentiation processes. Overall, the main conclusions can be summarized into the following points:

(1) Convection motions, mimicked by gas bubbles stirring in the experiments, provide a very efficient way to cluster the metal, whether it is solid or molten. With time, nickel grains become more and more elongated, as they are transported. Once two solid nickel grains are put in contact, they will stick together because the nickel-nickel solid interfacial energy is favorable compared to contacts with the other silicate components of this system. Upon melting of the metal, the previously formed chain of grains is disrupted into smaller spheres due to re-equilibration, on an extremely short timescale: less than one hour. The efficiency of this re-equilibration is likely to be affected by the fraction of silicate melt. In any case, coalescence of metallic blobs, whether they are molten or not, is likely to occur in a magma ocean stage. Although the metal aggregates are also in contact with silicate crystals due to interfacial energies, they may be able to sink under their own weight.

(2) The formation of a metallic network can be forced even when the metal content is lower than its interconnection threshold. Indeed, time-resolved in-situ 3D X-Ray microtomography proves that nickel forms a network at the beginning of the experiment due to cold compression. Metal being the "soft" phase in the present system, it will be squished between silicate grains. However, once this network and the silicate melt are molten, the network is disrupted into smaller blobs, which do not become perfect spheres as quickly as in the experiments with 75 vol% of silicate melt. Indeed, the distance to the interconnection threshold and the silicate melt content affect the rate of textural maturation. Close to the interconnection threshold, some local networks may form throughout the samples; the more metal, the larger the networks, requiring more time to destabilize them. In turn, large quantities of silicate melt make

the metallic grains reorganize into spheres on short timescales, while lower contents hinder this process. Experiments of progressive melting show that a stable network is formed at 25 vol% of metal and above (30 vol%). Hence, the interconnection threshold of pure metal is likely to be between 20 and 25 vol%.

(3) Natural objects show iron and troilite grains that range from close to spherical, to largely irregular. In chondrules, metal grains are spherical because they were most likely molten and also because significant amounts of silicate melt are present. Hence, they have a high textural maturation rate, allowing the iron and troilite pools to equilibrate rapidly. On the other hand, primitive achondrites show metallic grains with irregular shapes. This can be explained by the extraction of silicate melt during compaction of the silicate matrix, that leads to iron and troilite beads spreading between the silicate crystals. With time and grain boundary migration, these irregular grains should retrieve a spherical shape. However, as the grain growth mechanisms are much more efficient for the silicates in the presence of silicate melt, once the melt has been removed, the grain sizes are likely to be frozen. Hence, grain boundary migration is hindered and the metallic grains cannot re-equilibrate to form spheres, leaving irregular grains.

Chapter 5

Magma oceans in early-accreted small bodies and Pallasite formation

Contents

5.1 Introduction

The presence of achondrites in meteorite collections indicates that early accreted planetesimal were largely molten. Indeed, the formation of iron meteorites requires that the iron-sulfur subsystem was entirely molten, indicating that temperature was above $\approx$ 1673 K (liquidus temperature for the Fe-FeS composition of H chondrites) and that silicates were significantly molten. In turn, the high homogeneity of the oxygen isotopic compositions within the HED meteorite clan is most likely due to a large-scale melting of the parent body and a potential magma ocean stage (Greenwood et al., 2014). In this context of large silicate melt fractions, metal-silicate differentiation processes are not confined to the percolation of an interconnected network of iron-sulfur melt, but extend to the settling of metallic droplets as thought to have occurred for Earth's core formation (e.g. Rubie, 2015, and references therein). However, the question of the physical properties of magma oceans in small bodies has received little attention. The study of Taylor (1992) addressed the critical size a metallic droplet has to be to settle in a crystal mush as a function of the crystal content and for different body radii. The obtained sizes are large, from 1 cm to 1 m for crystal contents ranging between 10 and 50 vol% respectively, at a fixed body radius of 100 km. For a body similar in size to Vesta, i.e. a radius of 250 km, these sizes are only divided by $\approx$ 2. Based on grain growth laws, Taylor (1992) argues that coalescence of metallic blobs most likely helps in forming large droplets that may segregate and form the core. However, when it comes to coalescence, fragmentation must also be taken into account (Liao and Lucas, 2010). Ichikawa et al. (2010) considered the coalescence - fragmentation balance of metallic droplets inside a crystal-free magma ocean. The equilibrium size of the blobs is found to be about a centimeter, making growth to the sizes required for settling difficult. In addition, this equilibrium is likely to depend on the parameters of the magma ocean, i.e. heat flux to evacuate, controlling the vigor of convection, and / or crystal fraction.

The formation of achondrites, principally iron and stony meteorites, is the direct evidence of efficient metal-silicate differentiation in environments with large silicate melt fractions, i.e. magma oceans. Hence, although the differentiation processes do not seem favored, they took place. The present Chapter will address the equilibrium parameters of magma oceans in early-accreted small bodies and discuss the implications in the context of metal-silicate differentiation processes and the formation of achondrites, with emphasis on Pallasites.

5.2 Magma ocean modeling

A magma ocean stage is likely to have been experienced by terrestrial planets. On large planets the heat brought by impacts is of great importance and is likely to have allowed the complete melting of these bodies. However, when it comes to planetesimals, the contribution of impacts to the heat budget is negligible, the decay of ^{26}Al is most likely the main heat source (see Chapter 1). Hence, before differentiation, the heat source is distributed homogeneously throughout the whole volume of the planetesimal. Melting will thus occur throughout the body, with the exception of the external zones cooled by conduction to the surface. Convection may onset during the partial melting of the silicates due to the deconsolidation of the rigid

silicate framework and a huge drop in viscosity once a certain silicate melt fraction is reached. The viscosity at which convection onsets depends on the rheological properties of the partially molten material, as shown in this section.

5.2.1 Temperature - crystal fraction - viscosity relation

The migration of silicate melts depends on their viscosity, grain size of the matrix and size of the planetesimal. These melts may not be redistributed if the parent body is small, if grain sizes are small, or even if the heating timescale is smaller than the melt migration timescale. In these conditions, ^{26}Al remains spread throughout the whole volume and temperature can rise along with the melting degree. The parameter that varies most with the melting degree is viscosity of the silicate, from $\approx 10^{18}$ Pa.s for an entirely solid matrix (Hirth and Kohlstedt, 2003) to ≈ 10 Pa.s for an entirely molten body (Dingwell et al., 2004). As long as the crystal fraction ϕ exceeds the maximum packing crystal fraction ϕ_m, viscosity does not vary much and remain on the order of $\approx 10^{18}$ Pa.s. This maximum packing fraction corresponds to a rheological threshold above which the material behaves as a solid and below which it behaves as a liquid. In other words, it is the crystal fraction below which the rigid silicate framework is not consolidated anymore and can be easily deformed. Hence, below this threshold, viscosity decreases by several orders of magnitude and evolves toward that of the liquid η_l. The behavior for crystal fractions lower than the rheological threshold ($\phi < \phi_m$) is typically described in the literature by the equation of Roscoe (1952):

$$\eta = \frac{\eta_l}{(1 - \phi/\phi_m)^{2.5}} \,. \tag{5.1}$$

This equation shows that small variations of ϕ below ϕ_m causes the viscosity to decrease by several orders of magnitude, then further away from ϕ_m, viscosity evolves smoothly toward that of the liquid η_l.

The maximum packing fraction depends on size and aspect ratio of the silicate crystals (Marsh, 1981; Vigneresse et al., 1996). Literature data indicate that ϕ_m varies between 0.4 and 0.74 with a classical value of ≈ 0.6 for geological materials of interest (Marsh, 1981). In order to describe the evolution of viscosity as a function of crystal fraction and temperature, the equilibrium melting curve of the silicates was modeled using *Rhyolite MELTS* (Asimow and Ghiorso, 1998; Ghiorso and Gualda, 2015; Ghiorso and Sack, 1995; Gualda et al., 2012) and assuming a H chondrite bulk composition (Figure 5.1, green curve). Then, viscosity was calculated using equation 5.1 and assuming three different values of ϕ_m (Figure 5.1, black, red and pink curves) in the range of geological materials: 0.5, 0.6 and 0.7. Noteworthy, equation 5.1 tends toward infinity approaching ϕ_m, which is the reason why an extremely small variation of temperature or crystal fraction around ϕ_m changes viscosity by several orders of magnitude. An interesting feature of figure 5.1 is that the huge viscosity drop occurs over a very narrow range of temperature ≈ 100 K. Here, it is reasonable in a first approximation to not consider the effect of the metal viscosity as it would not affect much the rheology of the bulk material.

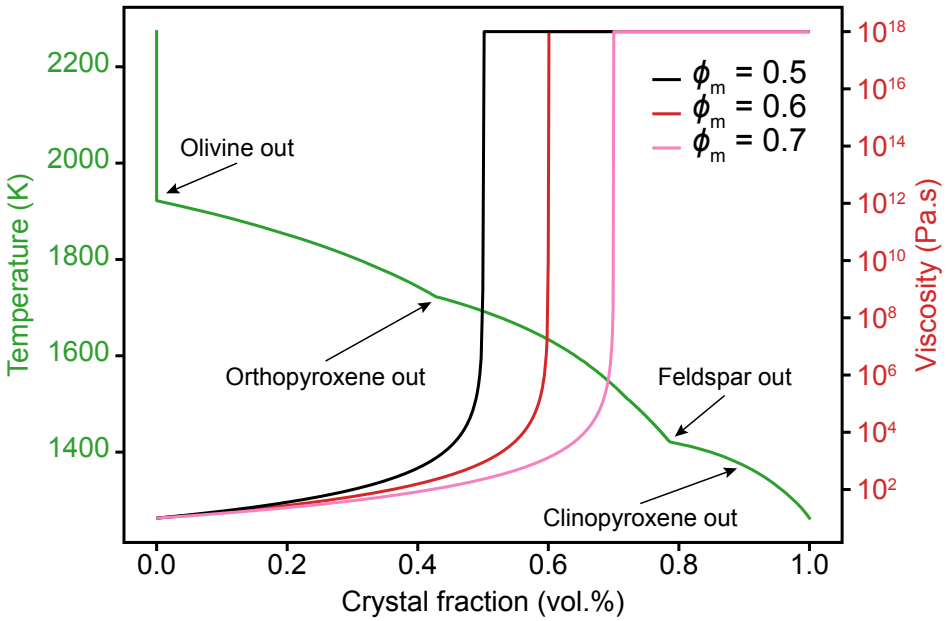

Figure 5.1 – Temperature (green curve) and viscosity as a function of crystal fraction for different rheological thresholds (black, red and pink curves). The green curve is the result of an equilibrium melting simulation of a chondritic material (H chondrite) using the *Rhyolite MELTS* thermodynamical simulator (Asimow and Ghiorso, 1998; Ghiorso and Gualda, 2015; Ghiorso and Sack, 1995; Gualda et al., 2012). The different kinks in the curve correspond to the complete melting of a mineral phase. The viscosity - crystal fraction relation is drawn from the Einstein-Roscoe equation (eq. 5.1 Roscoe, 1952). The temperature and viscosity y-axis are not correlated.

5.2.2 Convection

As viscosity decreases, and the rigid crystalline framework disappears, convective motion may begin, the condition being that the Rayleigh number (Ra) exceeds a critical value. This dimensionless number can be viewed as the ratio of the timescale for thermal transport via conduction to the timescale for thermal transport via advection and characterizes the vigor of convection. In the case of an internally heated sphere with a constant distribution of mass and heat source, it expresses as follows:

$$Ra = \frac{4\pi G \rho^2 \alpha \dot{Q} R^6}{9 \kappa k \eta}, \tag{5.2}$$

with α the thermal expansion of the fluid ($\approx 10^{-5}$ K^{-1} for silicate melts), ρ the density of the fluid (≈ 2700 kg.m^{-3}), G the gravitational constant (6.67430×10^{-11} in m^3.kg.$^{-1}$.s^{-2}, $\dot{Q}$ the heat power of the internal heat source (in W.kg^{-1}), R the radius of the planetesimal (in m), η the viscosity (in Pa.s), κ the coefficient of thermal diffusivity, expressed as $\kappa = \frac{k}{\rho C_p}$, k being the thermal conductivity (≈ 3 W.m^{-2}) and C_p the heat capacity of the material (≈ 1000 J.kg^{-1}.K^{-1} for the bulk material). With this definition of the Rayleigh number, its critical value is about $\approx 10^4$ (Chandrasekhar, 1961).

For planetesimals, as long as the crystal fraction is lower than ϕ_m, the Rayleigh number is greater than 10^{15} and exceeds its critical value, thus convection occurs provided that the accretion date allows a sufficient degree of melting. In the magma ocean, temperature is

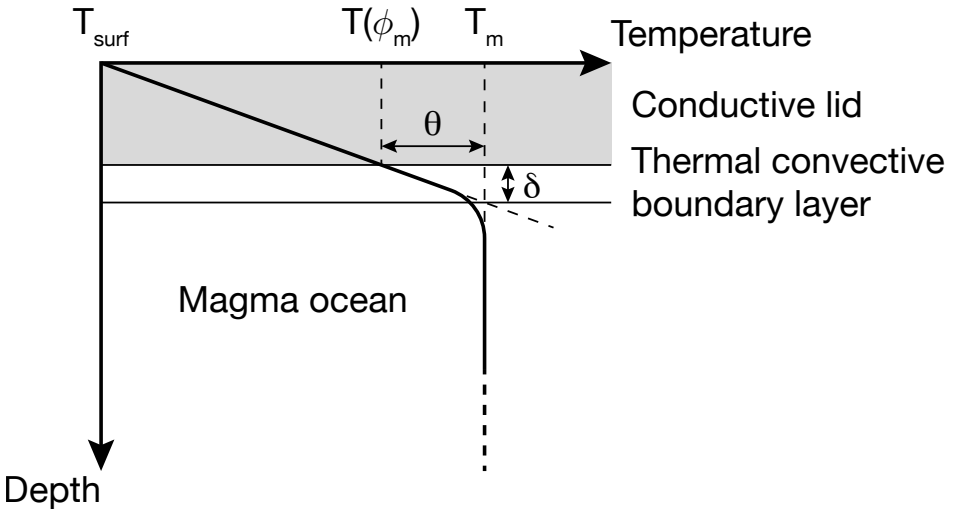

Figure 5.2 – Sketch showing the thermal structure of a planetesimal that melted enough to have a deep magma ocean (crystal fraction $\phi <$ maximum packing fraction ϕ_m). The grey shaded layer corresponds to the conductive lid, T_{surf} is the surface temperature, $T(\phi_m)$ is the temperature at which the crystal fraction corresponds to ϕ_m, T_m is the temperature of the magma ocean, δ is the boundary layer thickness and θ is the temperature difference within this boundary layer ($\theta = T_m - T(\phi_m)$).

homogenized by convection and does not depend on the radius, except in the top boundary layer where the heat is not evacuated by advection, but by conduction only. Above, in the conductive lid, the temperature decreases quasi-linearly with the radius, leading to a temperature profile as depicted on Figure 5.2. Actually, because of the spherical geometry, the conductive profile is quadratic, but the linear approximation remains valid over small parts of the body radius. At the steady state, the conservation of the heat imposes the equality of heat fluxes at the top of the magma ocean, through the lid if we neglect the radiogenic heat released in that part, and at the surface of the body. This assumption implies that all the heat produced internally due to the decay of the short-lived ^{26}Al goes through the convective boundary layer. The characteristics of this layer depends on the vigor of the convection. It is usually seen as the horizon where convective instabilities develops, i.e. a layer that remains with a crystal fraction below the critical threshold for convection. It is characterized by its thickness δ and the temperature drop across it θ. θ corresponds to the temperature difference between that of the magma ocean and the temperature at which ϕ_m is reached, defining the beginning of the convective regime. δ is such that the Rayleigh number of the layer corresponds to the critical value:

$$Ra_c = \frac{\rho g \alpha \theta \delta^3}{\kappa \eta}\,. \tag{5.3}$$

At equilibrium, the physics of the magma ocean is dictated by θ and δ that allow the efficient extraction of the internally produced heat. Assuming equilibrium fluxes, the heat flux F can be expressed as follows:

$$F = \frac{k\theta}{\delta} = \frac{\dot{Q}_v R}{3}\,, \tag{5.4}$$

where $\dot{Q}_v$ is the heat power (in W.kg^{-1}). Both the conductive thickness δ and the temperature

difference within the limit layer θ can be expressed as a function of the system parameters:

$$\delta = \frac{3k\theta}{R\dot{Q}v} = \left(\frac{Ra_c}{Ra}\right)^{\frac{1}{4}} R\,, \tag{5.5}$$

$$\theta = \left(\frac{Ra_c}{Ra}\right)^{\frac{1}{4}} \frac{R^2\dot{Q}v}{3k}\,. \tag{5.6}$$

As the fluid is supposed to be convecting for crystal fractions lower than the maximum packing fraction, the temperature of the fluid can be calculated following $T = T(\phi_m) + \theta$. Using the previous set of equations, θ increases along with η for a fixed radius and thermal parameters. However, the Rayleigh number decreases with increasing viscosity, making it anticorrelated to θ and the temperature of the magma ocean.

5.3 Equilibrium magma ocean

5.3.1 Parameters of the magma ocean

Figure 5.3 shows the evolution of the viscosity as a function of temperature ($\eta(T)$ dashed lines from equation 5.1) from data shown on Figure 5.1 and the evolution of the fluid temperature as a function of the Rayleigh number ($T(Ra)$ full lines from equation 5.6), for different maximum packing fractions (Figure 5.3a) and different planetesimal radii (Figure 5.3b). It can first be seen that for a given body radius and a given heat power, the fluid temperature increases with decreasing Rayleigh number, which is due to a feedback between $T(Ra)$ and $\eta(T)$. Indeed, if the Rayleigh number is higher than the equilibrium one, convection is too vigorous and the system extracts more heat than is produced. Hence, temperature decreases and viscosity rises, causing a decrease in the Rayleigh number (eq. 5.2) toward its equilibrium value. On the other hand, if the Rayleigh number is lower than its equilibrium value, all the heat produced by the decay of the short-lived radionuclides is not extracted, causing a temperature increase, and a drop in viscosity. The Rayleigh number then increases toward its equilibrium value.

Although there is a feedback between Rayleigh number and viscosity, no analytical solutions exist to equation 5.6. A comparison between this law and temperature - viscosity relations, e.g. that of Roscoe (1952) (eq. 5.1) allows to find a single solution by the graphical intersection of these two laws. This single solution depends on ϕ_m at fixed radius (Figure 5.3a) and on the radius of the planetesimal at fixed ϕ_m (5.3b). Note that the temperature range over which the two laws intersect for different ϕ_m or radii is narrow: from ≈ 1550 K up to ≈ 1700 K, giving rise to a range of possible viscosities that is narrow as well: from $\approx 10^4$ Pa.s to $\approx 10^5$ Pa.s. Varying the accretion date, slightly changes the equilibrium position. For an early accretion at 0.3 Myr, the heat flux to dissipate is more important, hence viscosity is slightly lower, between 0.3×10^4 to 3×10^4 Pa.s (Figure 5.3c). This results in a slightly higher silicate melting degree than the maximum packing fraction. The effect of varying the radii of the planetesimal is similar to that of varying ϕ_m for an accretion date of 0.3 Myr (Figure 5.3d). In turn, for a later accretion, the heat flux to evacuate is lower, and the deviation to the

maximum packing fraction is smaller. In the extreme case where the planetesimal accreted late and that temperature cannot reach large melting degrees, convection does not occur.

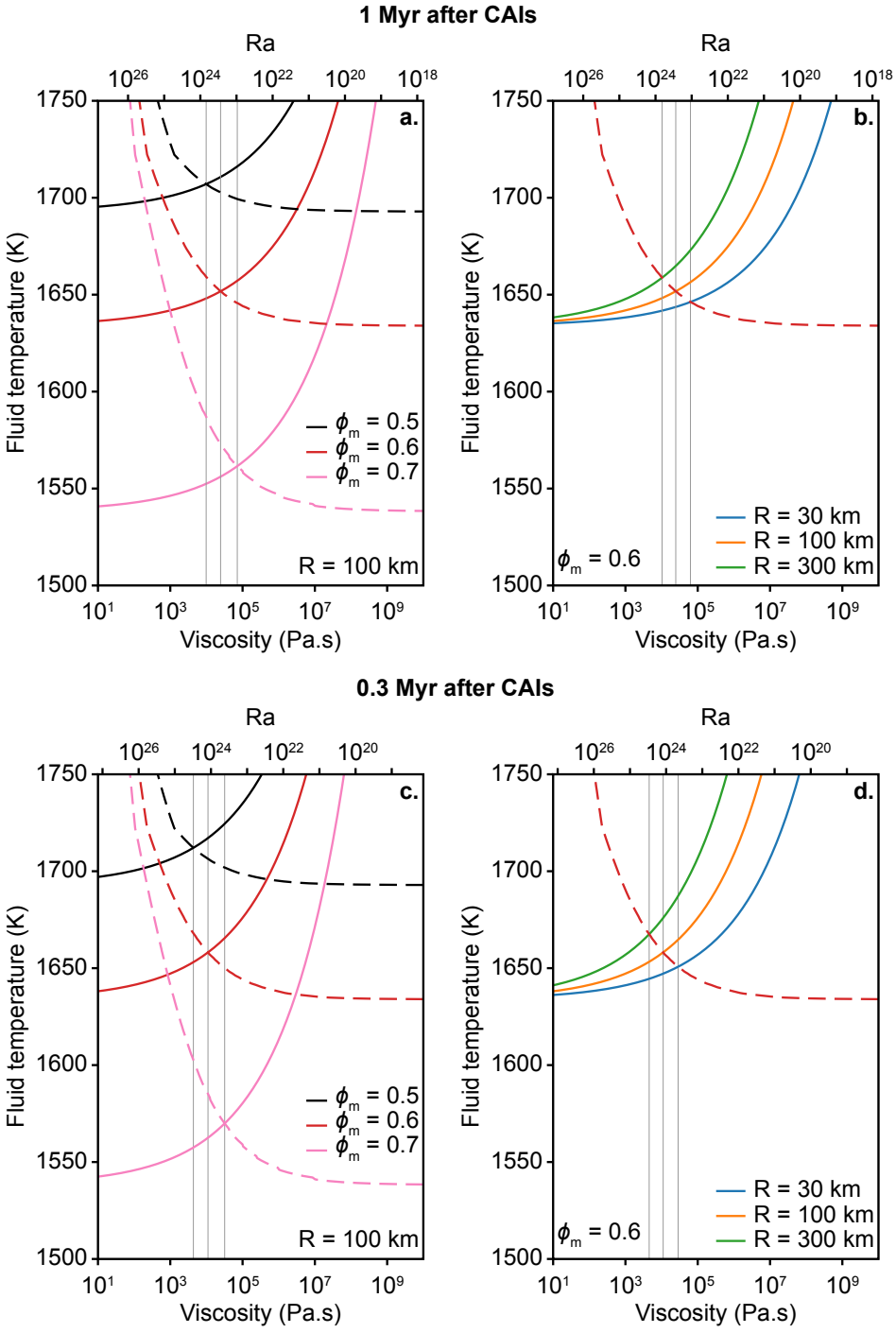

Figure 5.3 – Viscosity as a function of temperature following Roscoes's law (equation 5.1, dashed curves) and fluid temperature as a function of the Rayleigh number, (a.) for different maximum packing fraction at a fixed radius of 100 km and (b.) for different radii at fixed ϕ_m. The gray thin lines show the equilibrium parameters for the different cases studied here. These calculations are for an accretion date of 1 Myr after CAIs.

These temperatures and viscosities correspond to a crystal fraction range that is slightly lower than ϕ_m, meaning that once convection onsets, the planetesimal is locked into a convective regime that efficiently extracts all the heat produced. The body is not able to have greater temperatures than that allowing melting degrees in the vicinity of the assumed maximum packing fraction.

Noteworthy, the heat flux calculated here is an instantaneous one, which does not take into account all the heat released earlier. Results presented here are likely biased. A complete resolution of the heat equation to model the evolution of the magma ocean with time is currently in progress in collaboration with Marc Monnereau. Preliminary results show an extremely similar dependence of the equilibrium configuration on the maximum packing fraction. Upon global melting, a small temperature overshoot of the magma ocean occurs, but is on the order of a few Kelvin. This work will be the object of a scientific publication currently in progress.

5.3.2 Mobility of the metallic phases

In a convecting magma ocean, there are two processes that may lead to metal - silicate differentiation: the formation of an interconnected network and the settling of metallic droplets. The question of the formation of an interconnected network has already been addressed in the previous Chapters 3 and 4. Hence, here the question of the settling is treated.

Using a simplified approach, the condition for settling of a metallic particle is that its sinking velocity (approximated by the Stokes velocity v_s) is greater than the vertical velocity of the convective fluid w (as defined by Kraichnan (1962)), giving:

$$\frac{2r^2 g \Delta\rho}{9\eta} = v_s > w = 3\frac{\kappa}{\delta}\,. \tag{5.7}$$

Hence, the critical radius r_c for a particle to escape the convective motion is such that:

$$r_c^2 > \frac{27\kappa\eta}{2\delta g \Delta\rho}\,. \tag{5.8}$$

Then, knowing the viscosity of the magma ocean and the height of the limit layer from section 5.3.1, the critical size of the metallic droplets that lead to settling can be predicted.

The metal critical grain size for settling as a function of viscosity is plotted on Figure 5.4. For a fixed body radius of 100 km (Figure 5.4a), the critical grain size is on the order of a centimeter, between 0.9 cm for a maximum packing fraction of 0.5 to 2 cm for a ϕ_m of 0.7. At a fixed maximum packing fraction, e.g. 0.6 (Figure 5.4b), the radius has a similar effect. Indeed, critical grain sizes are also on the order of a centimeter, but with a wider range of sizes. In the case of a large body with a relatively strong gravity field (radius of 300 km), the grain size required for settling decreases to 0.7 cm, while it increases to almost 3 cm for a small body with a weak gravity field (radius of 30 km). Hence overall, no matter the radius or the maximum packing fraction, metallic droplets must be on the order of a centimeter to be able to settle and form a metallic core.

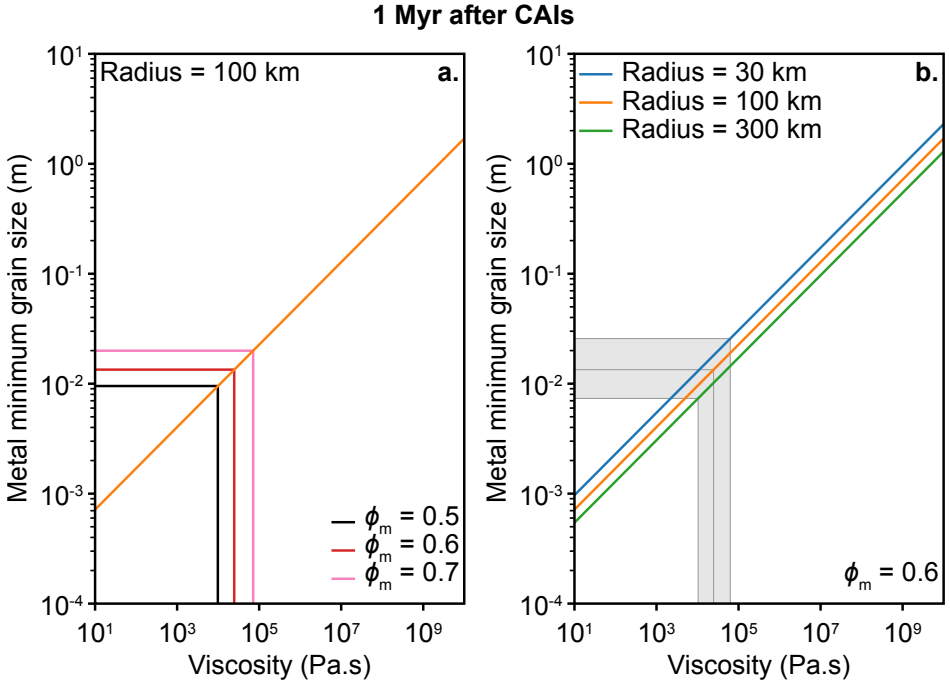

Figure 5.4 – Metal minimum grain size to escape convective motions as a function of viscosity for (a.) different ϕ_m at fixed radius and (b.) for different radii at fixed ϕ_m. Vertical and horizontal lines show the equilibrium parameters for the different cases studied here. These calculations are for an accretion date of 1 Myr after CAIs.

5.4 Implications for differentiation

5.4.1 Maximum packing fraction and viscosity laws for small bodies

In the present study, different values of the maximum packing fraction were assumed following the common values proposed for geological materials (Marsh, 1981). The true value of this fraction is difficult to assess as it depends on the size and aspect ratio of the silicate crystals (Marsh, 1981; Vigneresse et al., 1996). An additional parameter of great importance is the strain rate (e.g. Vigneresse and Burg, 2004; Caricchi et al., 2007; Costa et al., 2009). There is a consensus on the effect of strain rate on the viscosity: for a given crystal fraction, the lower the strain rate, the higher the viscosity. This can be understood because it is easier to deform an aggregate with more strength applied. The main consequence is a shift of the maximum packing fraction toward low values for low strain rates. Strain rate values for magma oceans in small bodies are difficult to determine, but a lower estimate can correspond to the mantellic convection on Earth (10^{-14} to 10^{-12} s^{-1}). From the parametrization of Costa et al. (2009), it would appear that from 10^{-7} s^{-1}, decreasing strain rates do not affect the rheological behavior of the material. Under these conditions, the maximum packing fraction of magma oceans in small bodies is expected to be low, about 0.5 to 0.6 (e.g. Caricchi et al., 2007; Costa et al., 2009).

As ϕ_m depends on each mineral assemblage, it may be easier to assess it from similar systems. Deformation experiments on partially molten peridotite were conducted by Scott

and Kohlstedt (2006). The maximum packing fraction was found to be in the range 0.70 to 0.75. However these experiments were conducted in a gas creep apparatus with large strain rates, on the order of 10^{-6} to 10^{-4} s^{-1}. Hence these values are most likely an overestimation of the maximum packing fraction for a magma ocean in a small body. Another good analogue material would be terrestrial basaltic lavas. Marsh (1981) studied the crystallinity (defined as the phenocryst content) of such materials and showed that most basaltic lavas have less than 55 vol% phenocrysts. Hence, this crystal content is likely to be an upper bound for the maximum packing fraction in basaltic systems undergoing low strain rates. The value of ϕ_m is then estimated to be around 0.5 for the magma oceans in small bodies.

The Einstein-Roscoe equation (eq. 5.1 Roscoe, 1952) does not accurately describe the viscosity near the maximum packing fraction (e.g. Solomatov, 2015) and does not take into account the effect of the strain rate. Hence efforts have been made to construct parametrizations that allow a better description of the evolution of viscosity as a function of crystal fraction and strain rate. For instance, Costa et al. (2009) built a parametrization that fits many experimental data, with different mineral assemblages and a relatively wide range of strain rates (from 10^{-8} to 10^{-3} s^{-1}). Close to the maximum packing fraction, the increase in viscosity is smoother than the sharp step of the Einstein-Roscoe equation (eq. 5.1 Roscoe, 1952). Using this parametrization on the present magma ocean equilibrium model, with an extrapolation of the parameters obtained for Scott and Kohlstedt (2006) to have a maximum packing fraction close to 0.5, shows no large difference compared to the simple Einstein-Roscoe equation (eq. 5.1, Roscoe, 1952). The magma ocean is also locked in a configuration with a crystal fraction slightly lower than ϕ_m. This exercise indicates that the results shown earlier (section 5.3.1) do not depend on the viscosity law used. Besides, more than an absolute crystal fraction, what controls the onset of convection here is viscosity and must be on the order of $\approx 10^4 - 10^5$ Pa.s.

Assuming a maximum packing fraction of 0.5 from literature data, a magma ocean in a small body has an equilibrium temperature of about 1700 K and a melting degree of the silicate fraction of $\approx 50 - 53$ vol% for an accretion date of 1 Myr and a body radius of 100 km. At these conditions, the metallic subsystem should be entirely molten: assuming a H chondrite precursor material, with 7 wt% sulfur (Wasson and Kallemeyn, 1988), the melting temperature of the iron-sulfur subsystem is ≈ 1680 K at 1 bar (Buono and Walker, 2011).

5.4.2 Coalescence as a mechanism to foster rapid grain growth

As discussed above, metallic droplets have to reach a size of about a centimeter to be able to settle and segregate from the convecting magma ocean (Figure 5.4). The time necessary to obtain such grain sizes in a partially molten silicate matrix can be calculated using the grain growth laws of Guignard et al. (in prep.). Figure 5.5 then shows the grain growth of olivine and nickel grains at a temperature of 1700 K, i.e. that of the equilibrium magma ocean, and assuming an initial grain size of ≈ 1 µm. In the case of metal, the centimeter size required to separate the metal and the silicate would require time greater than the age of the Solar System (Figure 5.5, red curve and shaded area). However, natural samples indicate that reaching large melting degrees, in the vicinity of the maximum packing fraction, fosters efficient metal-silicate segregation. Hence, either a population of natural samples with

large melting degrees and evidence for inefficient differentiation is not sampled, or there is a mechanism that promotes fast grain growth of the metallic droplets, allowing the metal to be extracted.

Coalescence is likely to be a mechanism that would allow extremely fast grain growth. Indeed, the experimental results in one-atmosphere high temperature furnace with an initial porosity shows the formation of large metallic aggregates, whether this latter phase is solid or molten. Within 24 hours, almost all the metal of a millimeter-sized sample has coalesced (see Chapter 4). At the scale of a magma ocean on a planetesimal, large metallic blobs on the order of a centimeter are likely to be easily formed. The study of Ichikawa et al. (2010) showed that blobs larger than 1.5 cm are no more stable into a crystal-free magma ocean and will be subject to fragmentation. The centimeter size is thus also an upper limit for the formation of large metallic blobs and might depend on the crystal fraction.

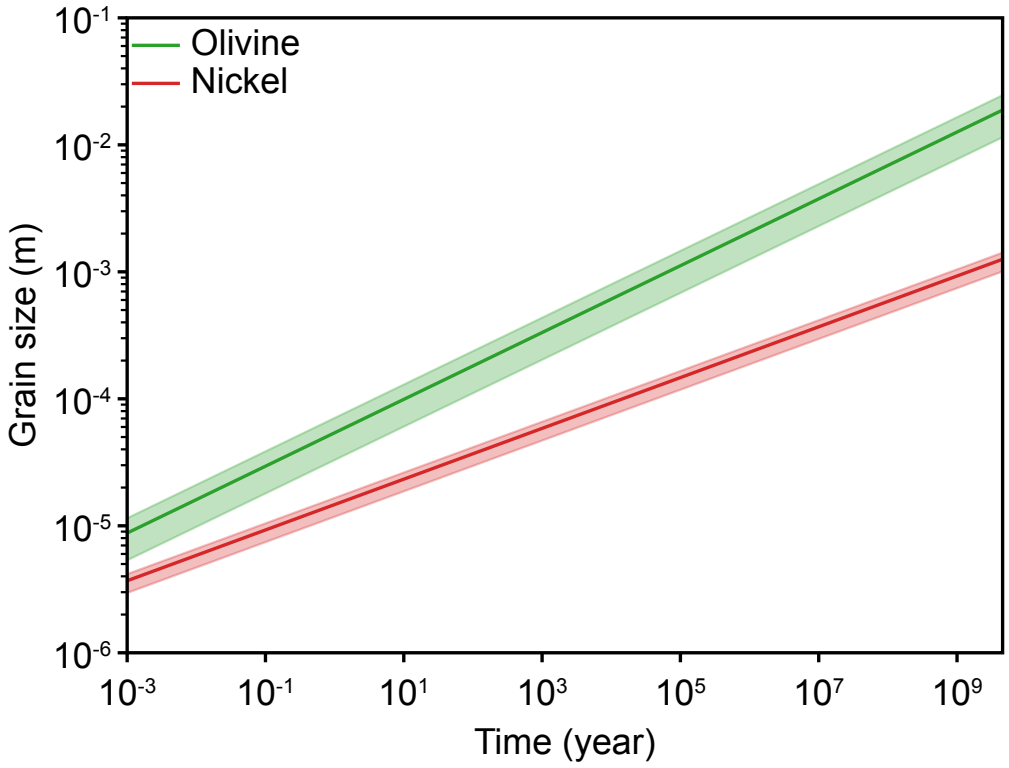

Figure 5.5 – Grain growth laws for olivine (green curve, Faul and Scott, 2006) and nickel (red curve, Guignard et al., in prep.) as a function of time. Temperatures are taken from the equilibrium configuration of magma oceans. Full lines are for the equilibrium temperature with a maximum packing fraction of 0.6; while shaded areas are for equilibrium temperatures with ϕ_m ranging from 0.5 to 0.7.

The need for rapid growth of nickel droplets is emphasized by the fast grain growth of olivine in the presence of silicate melt (Faul and Scott, 2006). Indeed, in one million years the olivine can reach a mean grain size of $\approx 2-3$ mm (Figure 5.5, green curve and shaded area). Such large silicate grain sizes allow efficient silicate melt extraction (Lichtenberg et al., 2019). Hence, to allow the settling of metallic droplets, they must have reached centimeter sizes in less than a million year, which may only be possible by coalescence.

The efficiency of gravitational settling using a Stokes velocity is quite uncertain. Indeed, Faroughi and Huber (2015) studied the settling velocity in a dense suspension. Results show that the sinking velocity is drastically hindered and is less than 10% that of Stokes velocity in a crystal-free environment. Critical sizes to allow their settling would then be increased by a factor of more than ten. Such large droplets are not stable and will undergo fragmentation, forming smaller blobs. Hence, although metal coalescence is likely to occur, its contribution to the metal-silicate differentiation is uncertain. The formation of an interconnected network can be a process that circumvents this issue.

5.4.3 A metal-silicate differentiation enhanced by compaction

Chung and Mungall (2009) calculated the critical height a coalesced network must be to segregate under its own weight as a function of crystal fraction and grain size. With a crystal fraction of 0.5, a metallic network must have a height larger than a meter for silicate grain sizes lower than a millimeter to be able to percolate (radius between 100 and 300 km and considering either the Fe-FeS eutectic or pure iron). This critical height is much larger than the equilibrium droplet size determined by Ichikawa et al. (2010), meaning that such large networks are most likely subject to fragmentation. Besides, at the equilibrium temperature allowing a silicate partial melting of 50 vol%, the metallic subsystem is entirely molten and has high interfacial energies with the silicate phases. Hence, its equilibrium geometry is a sphere (Néri et al., 2019), which would also prevent the formation of such networks. Another process must then take place to allow efficient metal-silicate segregation.

Experiments on a simplified experimental system at room temperature and numerical modelings show that even during convection, there is a gradient of particle density that develop rapidly (Höink et al., 2005; Lavorel and Le Bars, 2009). Because the mean crystal fraction is very close to ϕ_m, if such gradient of particle density would occur, the deeper region would exceed this critical fraction, ending convection. Hence, the inner regions are likely to get compacted, with an efficient extraction of the silicate melt provided that grain sizes are large enough. Following Lichtenberg et al. (2019), to allow an efficient melt segregation on short time-scales, grain sizes of the silicates have to be about a millimeter. The question is then, can the grains grow large enough before the onset of a gradient of particle density? In a convective magma ocean, grains that settled may be reentrained if they are small enough. Solomatov et al. (1993) studied the reentrainment of polystyrene spheres in an aqueous $CaCl_2$ convecting solution and determined a critical condition for reentrainment. It requires that the convection stress scale is about ten times lower than the weight per unit area of the particles. Using the parameters of the present magma ocean, critical sizes for reentrainment on the order of a few centimeters (2.5 to 7 cm for planetesimal radii ranging between 300 and 30 km respectively) are obtained. Hence, silicate grains are likely to grow to sizes allowing efficient silicate melt segregation before settling.

The grain growth law of Faul and Scott (2006) on olivine indicates that grain sizes are likely to reach centimeter-scale in $\approx$ 100 Myr, which is much larger than the lifetime of a magma ocean in a small body (Marc Monnereau, personal communication). Most likely, silicate grains will grow over the lifetime of the magma ocean and then settle when the heat source is exhausted. Indeed, vigor of convective motions decreases with decreasing quantities

of ^{26}Al, allowing the settling of millimeter to plurimillimeter silicate grains. Under these conditions, the silicate melt is extracted (Lichtenberg et al., 2019) and the relative proportion of iron-sulfur melts increase. Assuming an H chondrite precursor material with 10 vol% of iron-sulphide phases (3 vol% troilite and 7 vol% kamacite-taenite, Guignard and Toplis, 2015), the removal of 50 vol% of the silicate in the form of silicate melt causes the increase of the iron-sulfide melt proportion to 20 - 23 vol%. This fraction is likely to be enough for the formation of an interconnected network of iron-sulfur melts, given its sulfur content (Néri et al., 2019), which will then segregate inward to form the core. Because the silicate material was not consolidated before settling and due to the pressure of the overlying silicate column, a fraction of the grains is likely to be in suspension inside the molten metallic core.

5.4.4 Pallasite formation

5.4.4.1 General scheme

From a petrological and meteoritic point of view, silicate grains suspended in a molten metallic melt would constitute a material very similar to pallasites. To test the present model and check if mineralogy and composition would match, the melting curve of the silicates assuming a H chondritic precursor can be considered. Figure 5.1 indicates that at a silicate melt fraction of 50 vol%, a majority of olivine is left, but some orthopyroxene also. Besides basic mineralogical arguments, composition of the olivines, in terms of Mg#, should be checked. For this exercise, *Rhyolite MELTS* simulations were conducted (Asimow and Ghiorso, 1998; Ghiorso and Gualda, 2015; Ghiorso and Sack, 1995; Gualda et al., 2012) on a H chondrite precursor material with varying oxygen fugacities. Here the fO_2 was varied by changing the $Fe^{2+}O$ - Fe^0 relative proportions by mass balance. Oxygen fugacity was calculated considering the Iron-Wustite equilibrium (Fe-FeO, noted a IW, O'Neill and Pownceby, 1993). Then the system was considered to be self buffered, i.e. not following a known buffer to avoid that the *Rhyolite MELTS* algorithm would add or remove oxygen from the composition. Temperature was varied from entirely solid ($\approx$ 1223 K) to entirely molten ($\approx$ 1973 K) and pressure was set at 1 bar. From the mass balance performed earlier, the quantity of reduced iron can be calculated, which will change the modal proportions of the kamacite-taenite. Hence the the volume fraction of molten iron-sulfur upon extraction of the silicate melt after the crystals settling can also be predicted. Comparing this proportion to an interconnection threshold ($\approx$ 17 vol%, see Chapter 3) provides information about the mobility of this metallic melt.

Results are shown on Figure 5.6 which plots the silicate melt fraction as a function of the fraction the metal would represent after removal of the silicate melt. The color code then represents the fayalite content of the olivine. At a fixed silicate melt fraction, reducing conditions cause a simultaneous increase of the metal fraction and decrease of the fayalite content of the olivines. Gray areas on the color curves represent the solutions that match the Mg# of olivines in pallasites ($\approx$ 12 mol%, Boesenberg et al., 2000, 2012). At the silicate melt fraction of the equilibrium magma ocean, i.e. 50 vol% (Figure 5.6), there are oxygen fugacity conditions that show fayalite contents close to 12 vol%. This solution is extremely close to the complete melting of orthopyroxenes, explaining that this phase is so scarce in pallasites ($<$ 2 vol%, Boesenberg et al., 2000).

Under these conditions, the efficient extraction of the silicate melt due to the large grain sizes of the solid silicates increases the relative metal fraction to amounts slightly larger than 20 vol% (Figure 5.6 horizontal line). The oxygen fugacity conditions required for the solution at 50 vol% of silicate melt causes the sulfur content of the metallic subsystem to decrease to ≈ 5 wt%, assuming that no early sulfur-rich melt extraction occurred. Following the best match interconnection threshold - sulfur content of the metallic melt found by Néri et al. (2019) (Chapter 3), an iron-sulfur melt with this sulfur content has an interconnection threshold lower than 20 vol%. Hence, it is able to form an interconnected network and to segregate due to the large silicate grain sizes, forming the core. The interfacial energy relations within such system would suggest that upon the migration of the iron-sulfide melt, the silicate melt may be dragged down to switch places with the sulfur-rich metallic melt.

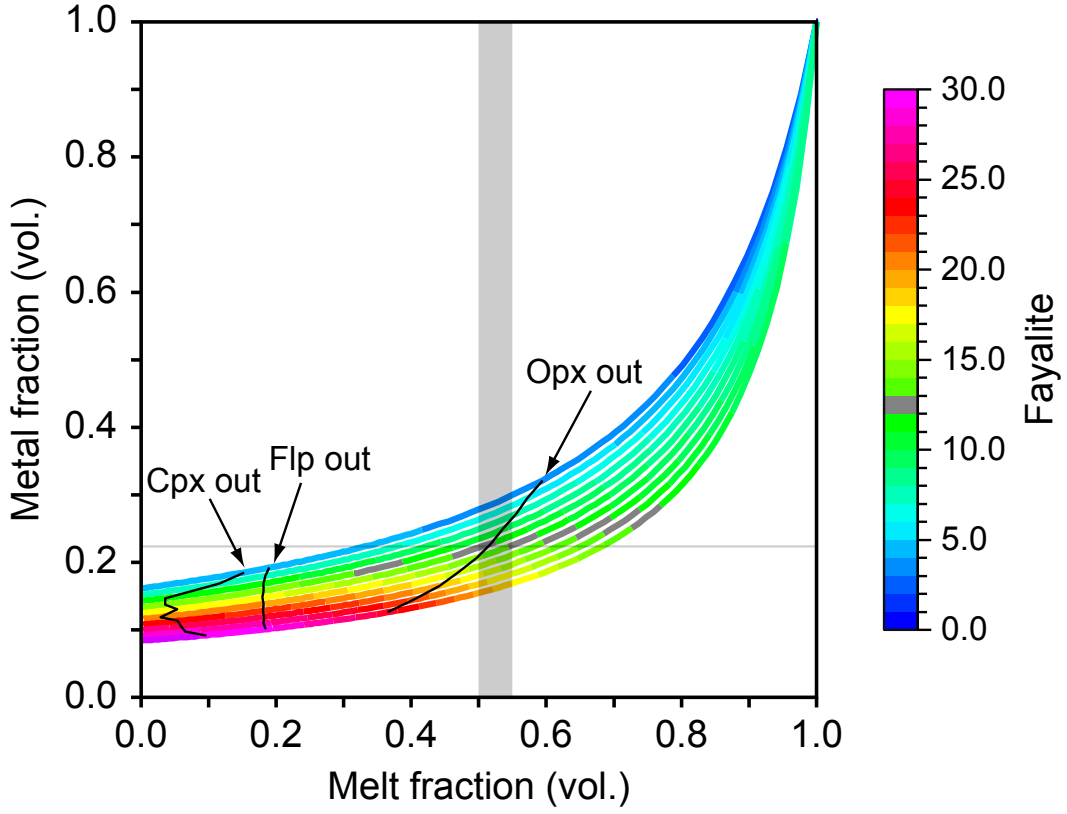

Figure 5.6 – Metal volume fraction as a function of silicate melting degree. The metal volume fraction does not correspond to the absolute content as it represents the fraction after removal of a given silicate melt fraction, corresponding to that of the x-axis. The color map shows the evolution of the fayalite content of olivine, with the gray areas showing the value corresponding to that of main group pallasites (12 mol%, Boesenberg et al., 2012). The thin black curves show the complete melting of the different silicate phases: Cpx for clinopyroxene, Flp for feldspar and Opx for orthopyroxene. Gray shaded areas show the melt fractions corresponding to the equilibrium magma ocean with the effect of accretion date and size as lateral variations; the horizontal area shows the corresponding metal fraction after silicate melt extraction.

A simple hydrostatic pressure balance based on the relative phase proportions indicate that there is a region composed of a mixture of olivine and iron-sulfur melt. Indeed, due to the column height of olivine, the pressure is sufficient to force the lower end to be suspended in the metallic core. In terms of proportions with respect to the whole planetesimal, the metallic

core would represent 6 vol% and would be overlained by the region forming the pallasites, representing another 6 vol%; then the overlying mixture of olivine and silicate melt would represent 63 vol% and the uppermost material would be composed of a molten silicate layer that is about 25 vol% of the planetesimal (Figure 5.7).

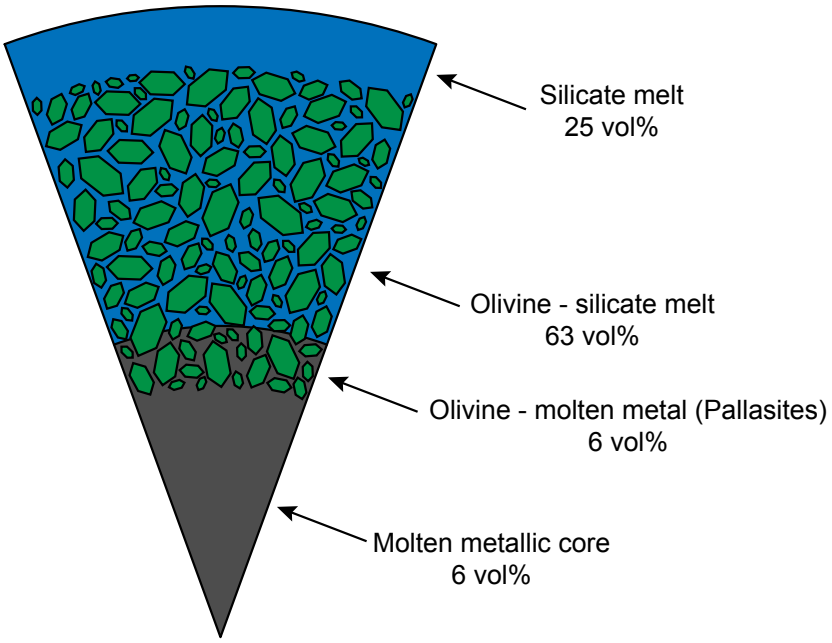

Figure 5.7 – Sketch showing the final structure of a planetesimal that underwent a magma ocean stage.

5.4.4.2 Comparison with literature data

Boesenberg et al. (2012) proposed a model with fractional melting processes to form a multi-layered parent body that will later on undergo fractional crystallization and lead to a region with a mixture of olivine and metal. Results presented and discussed above are in agreement with this model, but provide additional constraints on the conditions for pallasite formation, which are discussed further here.

Regarding the silicate subsystem, pyroxenes can be found in pallasites under two different forms. The first one is the millimeter-sized crystals within the pyroxene pallasites (Boesenberg et al., 2000), while the second is in the form of small grains, a few tens of microns in diameter within the main group pallasites (Boesenberg et al., 2012). The millimeter sized orthopyroxenes of the pyroxene pallasites indicate that these grains were able to grow over time, most likely in the presence of a silicate melt. Size and accretion date of the planetesimal may slightly change the equilibrium parameters of the magma ocean, from 50 to 53 - 55 vol% silicate melting degree. This small shift does not affect much the Mg# of the olivine, which still matches the mean value of main group and pyroxene pallasites. Hence the orthopyroxene can either be still present in low quantities, a few percent, or completely molten (Figure 5.6 gray shaded area). Then, in the first case (pyroxene pallasites), as this phase was never entirely molten, the remaining grains may have grown over time to reach millimeter sizes. In the second case (main group pallasites), orthopyroxenes are found at the margins

of some olivine crystals (Buseck, 1977), most likely indicating a secondary process implying more reducing conditions (Boesenberg et al., 2012). Invoking different sizes or accretion date shows that these two groups of pallasites should originate from different parent bodies, which is in agreement with their different oxygen isotopes signatures (Weisberg et al., 2006). The wide range of olivine content of pallasites (Weisberg et al., 2006) can be explained by a simple particle gradient within the mixture of olivine and molten iron-sulfide. Indeed, more olivines are floating at the surface of the molten core due to the density difference.

On the basis of oxygen isotopes, main group pallasites have compositions similar to the HED meteorite clan (Weisberg et al., 2006), which is likely to indicate a similar precursor material but not necessarily a common parent body. The present model indicates that a body with an outer crust of a similar silicate melt composition (i.e. bearing orthopyroxene, clinopyroxene and feldspar) is likely to be overlying an olivine-rich mantle and, in turn, a pallasite region, in agreement with the model of Mizzon (2015) for (4) Vesta. Hence, there should be an olivine rich region buried deep in (4) Vesta, which may be overlying a pallasite region.

Isotopic systems used to date high temperature events (e.g. Mn-Cr and Hf-W for silicate-silicate and metal-silicate differentiation respectively) are likely to support a magmatic origin for pallasites (McKibbin et al., 2016; Homma et al., 2019). However, at lower temperatures, other events may have affected this material. Based on paleomagnetism of some pallasites, other models proposed an impact origin of this meteorite clan (Tarduno et al., 2012; Bryson et al., 2015; Nichols et al., 2016). Indeed the record of a paleomagnetic field by pallasites indicate that these objects were subject to a magnetic field when tetrataenite formed, i.e. at temperatures below 593 K (Uehara et al., 2011; Maurel et al., 2019). Under these conditions, it is difficult to imagine that a magnetic field was recorded at the core mantle boundary as the core is likely to be crystallized as well. Hence, models argue in favor of an impact history that would allow a metal-olivine material from an impactor to be found close to the surface of the impacted planetesimal (Solferino and Golabek, 2018). Following the model of Bryson et al. (2015), a depth of 30 - 40 km on a parent body with a radius of 200 km best explains the paleomagnetic field recorded by the Imilac and Esquel pallasites. The magmatic origin of a pallasite forming region presented earlier (section 5.4.4.1) is not incompatible with the impact model of Solferino and Golabek (2018). Indeed, in order to have the olivine as the single crystalline phase left (and potentially small amounts of orthopyroxene), large-scale melting of $\approx$ 50 vol% is required. As the olivine - silicate melt mixture region is about 63 vol% of the planetesimal, it can easily be imagined that the injection of the impactor core into this area would form a material corresponding to pallasites. Such impact models would explain the presence of small angular grains in pallasites.

5.5 Conclusion

The present study aimed at characterizing magma oceans in early accreted small bodies, with application to their subsequent metal-silicate segregation. Results show that due to the dependence of viscosity on crystal fraction, the degree of melting of the magma ocean is buffered to a value close to that corresponding to that of the maximum packing fraction

considered. Slight variations in the melting degree can be caused by different body radii or accretion date of the planetesimal. The low strain rate of convection in magma oceans is likely to indicate a low maximum packing fraction, on the order of 0.5 by comparison with terrestrial basalts. Hence, the variation in accretion date and size of the planetesimal may cause the melting to vary between 50 and 55 vol%. At these temperatures, the metallic subsystem is entirely molten, which is not the case for the silicates: olivine is the only crystalline phase left. Orthopyroxene grains may still be present for a small body or with a relatively late accretion date.

Due to the grain growth of olivine crystals, their sizes are likely to be large enough to allow an efficient silicate melt migration when convection stops. The removal of this molten phase would allow the iron-sulfur melt content to be greater than its interconnection threshold, triggering its segregation and the formation of a metallic core. A hydrostatic pressure balance that a part of the olivine column is wetted into the metallic core. Such a region is likely to form a material very similar to pallasites. Modelling the evolution of the Mg# of the olivines with increasing melting degree indicates that the composition of pallasites can be easily matched at a degree of silicate melting of 50 to 55 vol%, even explaining the presence of millimeter sized orthopyroxene crystals in the pryoxene pallasites. This magmatic origin for pallasites is in agreement with isotopic data on high temperature chronometers (e.g. Hf-W and Mn-Cr). However, the presence of a paleomagnetic field recorded by tetrataenite grains and the presence of small irregular olivine grains may be indicative of a more complex history, involving impacts. The present model is compatible with such history as a similar structure to a Figure 5.7 is likely to be required prior to the impact for both the impactor and the target planetesimal.

Chapter 6

A petrographic analysis of primitive achondrites

Contents

6.1 Introduction

Winonaites, acapulcoites and lodranites are classified as primitive achondrites. These meteorites are widely known to be partially differentiated and partial melt residues (e.g. Keil and McCoy, 2018, and references therein). Each category has experienced a different degree of differentiation, with winonaites and acapulcoites having the lowest and lodranites the highest differences compared to chondritic compositions. In detail, winonaites have an overall chondritic mineralogy, but achondritic textures, although some relict chondrules may persist. These samples are thought to have heated slightly above the Fe-FeS eutectic temperature, as shown by the formation of kamacite-taenite or troilite veins (Benedix et al., 1998). In turn, acapulcoites are thought to have reached temperatures of the iron-sulfide eutectic and potentially also that of the silicate fraction. The melts were not or poorly mobile and crystallized where they formed. On the contrary, lodranites reached temperatures allowing a silicate melting degree of about 20-25 vol%. At these conditions, the samples lost a fraction of silicate melt, but also a sulfur-rich iron-sulfide melt, as evidenced by the lack of clinopyroxene, feldspar and troilite. For more details on the textural arguments for these processes, see Chapter 1. In order to extend the petrological and textural survey of these meteorites, six thick sections were obtained from the MNHN: Acapulco (reference specimen of acapulcoites), Dhofar 125, Dhofar 1222, Lodran (reference specimen of lodranites), Monument Draw and NWA 725. Among these, only Lodran is classified as a lodranite. Three additional primitive achondrites were provided by other institutes. One acapulcoite A 881902 was provided by the National Institute of Polar Research (NIPR, Tokyo) and was analyzed in the framework of the bachelor internship of Fiona Bonnet under my supervision. Another acapulcoite MET 01198 along with a lodranite GRA 95209 were provided by NASA (Antarctic Meteorite Collection; JSC Houston), these sections were analyzed in the framework of the master internship of Pauline Robert, under the supervision of Ghylaine Quitté. On the basis of oxygen isotopic compositions that differ from the acapulcoite-lodranite reservoir, Greenwood et al. (2012) proposed to classify Dhofar 1222 and NWA 725 as winonaites. Hence, these samples will be considered as winonaites in the remainder of the text. These samples are interesting to study in the framework of differentiation as they likely sample a stage that is closer to chondritic than acapulcoites.

In order to have information on the textures of these sections, they were analyzed with SEM-EDS and EBSD mapping. Chemical compositions of the different phases were measured with EPMA. Analytical data will be discussed in the context of formation models for these objects (e.g. Golabek et al., 2014; Neumann et al., 2018).

6.2 Methods

The sections of primitive achondrites were re-polished using Al_2O_3 1 µm for one hour and Al_2O_3 0.3 µm for two hours. A881902 was first polished using silicon carbide abrasive paper down to 2.5 µm before using the alumina powders as described above. This fine-grain polishing is a necessary step to have good quality electronic analyses (Scanning Electron Microscopy, Electron BackScattered Diffusion and Electron MicroProbe Analysis). Coloïdal

silica was not used to avoid any contamination on the surface of the thick sections. The section ID of the different sections along with their surface are specified in Table 6.1.

Table 6.1 – List of Primitive Achondrite samples used in this study.

Meteorite	Group	Section	Sample Area (mm^2)
A881902	Acapulcoite	-	≈25
Acapulco	Acapulcoite	Acapulco -2	≈79
Dhofar 125	Acapulcoite	Dhofar 125 3752-3	≈110
Dhofar 1222	Acapulcoite	Dhofar 1222 ns	≈122
MET 01198	Acapulcoite	MET01198, co#17501	≈10
Monument Draw	Acapulcoite	Monument Draw 3783-1	≈139
NWA 725	Acapulcoite	NWA 725 3762	≈151
GRA 95209	Lodranite (transitional acapulcoite)	GRA 95209, 242	≈154
Lodran	Lodranite	Lodran ns 2	≈104

6.3 Petrographic features

Polished thick sections were studied optically in reflected light. Global mineral and deformation maps were then acquired with SEM-EDS and SEM-EBSD, respectively. Results of the analysis of the different maps are presented in the following sections.

6.3.1 Textural properties and modal compositions of thick sections

All characteristics of the different sections are summarized in Table 6.2.

6.3.1.1 Winonaites

Dhofar 1222: The section (Figure 6.1a and 6.1b) is composed of olivine, orthopyroxene, clinopyroxene, feldspar, chromite, troilite, kamacite-taenite and phosphate grains that are evenly distributed on the surface of the sample. Olivines and orthopyroxenes have rounded and equigranular shapes. Triple junctions at 120° between olivine crystals indicate textural equilibrium. Some grains are much larger than the rest of the population. Feldspar and clinopyroxene appear in the form of pools that wet the silicate phases. The grain population can be separated into two subgroups as a function of their size: on the one hand, large pools that enclose orthopyroxene or olivine grains, and on the other hand small grains trapped between silicate crystals. Chromite grains have irregular shapes and are found in contact with troilite and kamacite-taenite. As for clinopyroxenes and feldspars, the phosphates have a bimodal size distribution with large pools and smaller grains, both having rounded shapes. Troilite and kamacite-taenite crystals have irregular shapes that are often contacting each other with sharp grain boundaries. Kamacite-taenite grains form much larger patches than troilite. Small rounded grains of the iron-rich phases can be found included within the orthopyroxenes and olivines. This section hosts numerous relict chondrules. Including a metallic one, some with a troilite crown, or only formed of silicates. Chondrules are either formed of large olivine grains with an interstitial small intergrowth of feldspars and clinopyroxenes or

of a mixture of dendritic crystals of olivine, orthopyroxene, clinopyroxene and feldspar. An alteration crust seem to appear along a border of the section, with veins oriented towards the center of the specimen. This secondary process mostly affects the iron-rich phases and presumably precipitated oxides or hydroxides within the veins that run along grain boundaries.

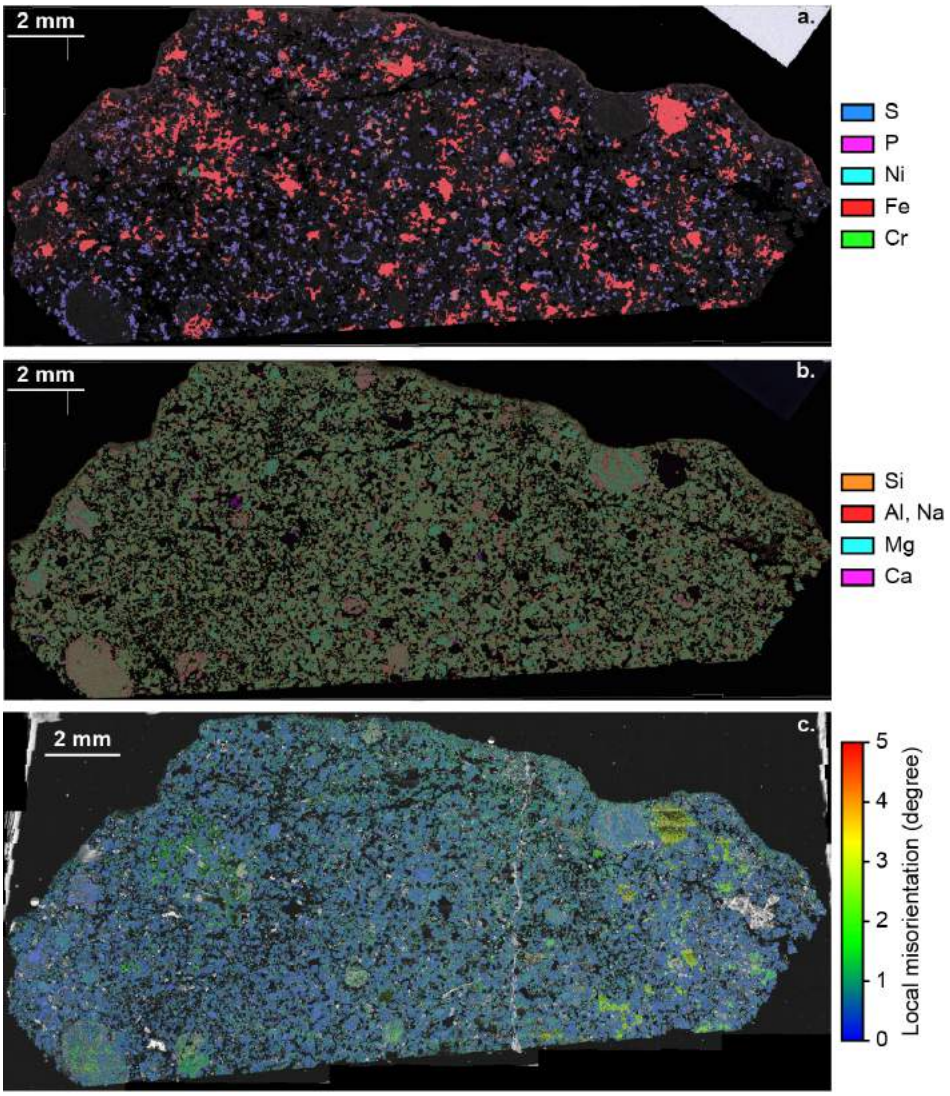

Figure 6.1 – (a.) Fe-Ni-Cr-P-S-Cr EDS map, (b.) Si-Al-Na-Mg-Ca EDS map and (c.) local misorientation map of Dhofar 1222. The local misorientation plots only the phases with the best EBSD signal, i.e. olivine, orthopyroxene and kamacite-taenite.

NWA 725: The section (Figure 6.2a and 6.2b) is composed of olivine, orthopyroxene, clinopyroxene, feldspar, chromite, troilite, kamacite-taenite and phosphate grains that are evenly distributed on the surface of the sample. Olivines and orthopyroxenes have rounded and equigranular grains, with triple junctions at 120° between olivine crystals. Clinopyroxene and feldspar grains have shapes that are close to rounded, i.e. not much wetting, which indicates a strong recrystallization of the material. Some large patches of clinopyroxene appear throughout the section. Chromites and phosphates have irregular shapes with rounded

extremities and are in contact with troilite and kamacite-taenite crystals. Troilite grains are small and have irregular shapes, while the kamacite-taenite ones form large patches that may form an interconnected network throughout the specimen. These two phases are often found contacting each other, with contacts forming sharp grain boundaries. No large Fe-Ni zonings are observed. This section also shows numerous relict chondrules, but with a single type this time: large olivine crystals are wetted by an intergrowth of fine-grained clinopyroxenes and feldspars. One of them has parallel elongated olivine crystals, similar to barred chondrules.

General characteristics: Winonaites do not show any signs for the loss of a silicate or a sulfur-rich component. These samples have a pristine dry mineralogy and host relict chondrules in various proportions (Dhofar 1222 hosts many more relict chondrules than NWA 725). This feature indicates a low degree of thermal metamorphism: temperature rose enough to allow the crystallization of feldspar and clinopyroxene but not enough to erase the chondritic texture. Textures of the metallic phases are in agreement with this low degree of thermal metamorphism. Indeed, the sharp grain boundaries between troilite and kamacite-taenite is likely to indicate a reequilibration of the textures within the iron-sulfide subsystem. Temperature may have reached that of the Fe-FeS eutectic, i.e. at most 988 °C.

6.3.1.2 Acapulcoites

All these samples are composed of olivine, orthopyroxene, clinopyroxene, feldspar, chromite, troilite, kamacite-taenite and phosphates grains that are evenly distributed on the surface of the samples. Olivines and orthopyroxenes have rounded and equigranular grain shapes. Olivine triple junctions at 120° indicate textural equilibrium.

Acapulco: This meteorite is the reference specimen of acapulcoites (Figure 6.3a and 6.3b). Feldspar and clinopyroxene have irregular shapes and seem to wet the orthopyroxene and olivine grain boundaries and may form large patches that are similar in shape to silicate melt pools. The different silicate phases can be found included in each other, indicating simultaneous growth. Phosphates are found in contact with iron-sulfide phases and have irregular shapes, similar to that of feldspar and clinopyroxene, looking like they are wetting olivine and orthopyroxene grains. Chromites can be found in the form of tiny grains at silicate grain junctions as well as larger patches in contact with iron-sulfide phases. They have irregular shapes that do not seem as wetting as the feldspar and clinopyroxene large patches. Troilite and kamacite-taenite grains have similar sizes and irregular shapes. These two phases are often found in contact with each other, with a sharp limit. From the SEM-EDS mapping, Fe-Ni zonings appear in the kamacite-taenite grains, but they do not form well defined Widmanstatten patterns. There is a population of small rounded grains that is trapped within the silicate phases, mostly within othropyroxenes. There are some cracks over the sample that do not follow grain boundaries and cross-cut some silicate phases. No alteration products precipated within them. Acapulco does not display any sign of alteration processes or relict chondrules.

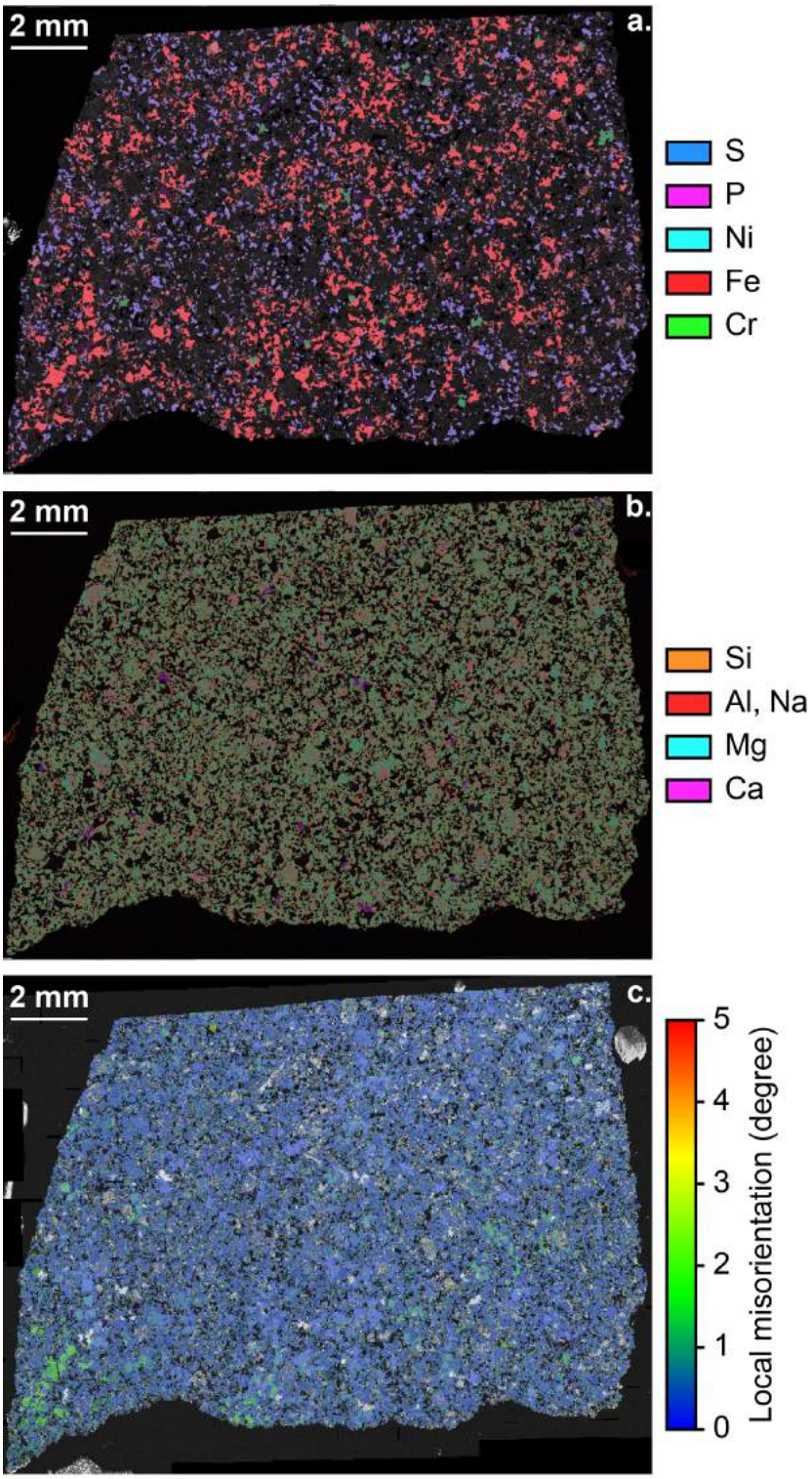

Figure 6.2 – (a.) Fe-Ni-Cr-P-S-Cr EDS map, (b.) Si-Al-Na-Mg-Ca EDS map and (c.) local misorientation map of NWA 725. The local misoriention plots only the phases with the best EBSD signal, i.e. olivine, orthopyroxene and kamacite-taenite.

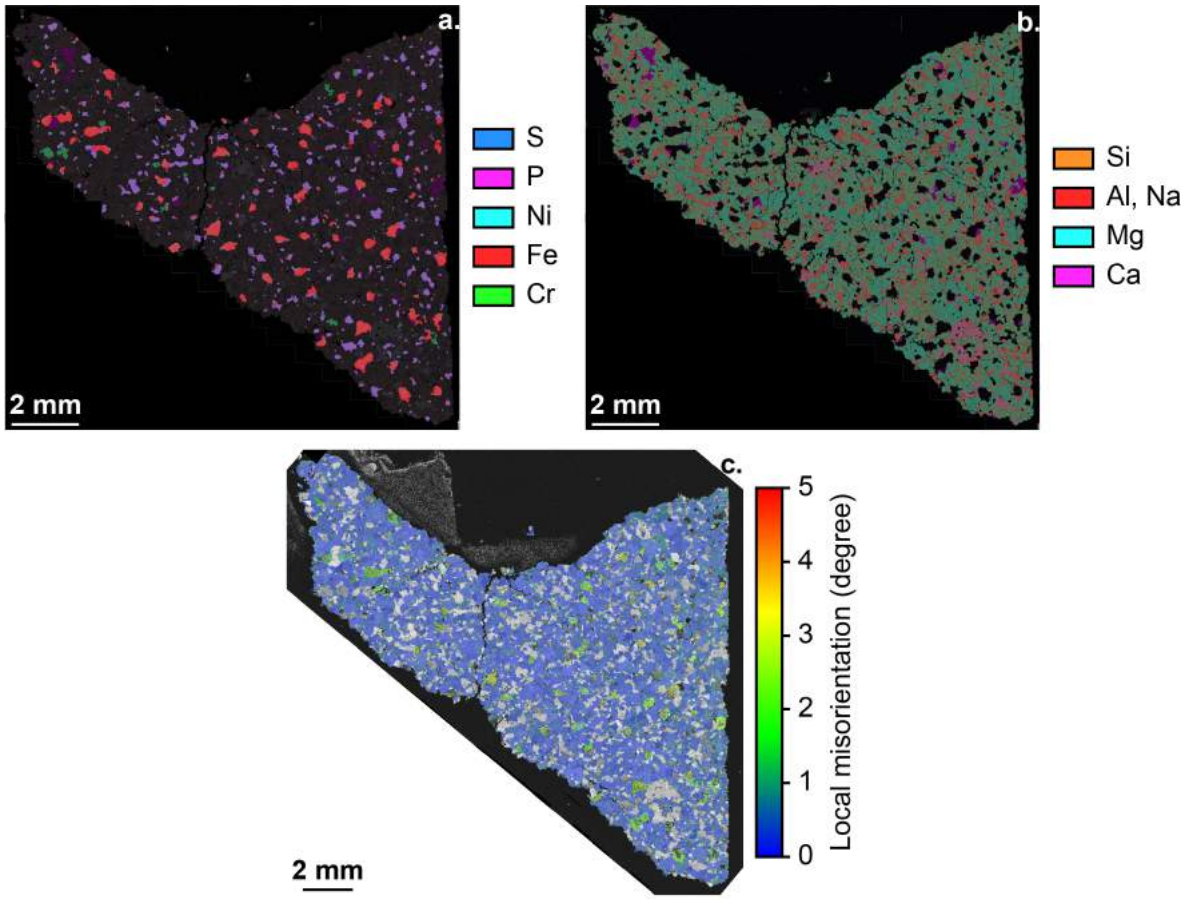

Figure 6.3 – (a.) Fe-Ni-Cr-P-S-Cr EDS map, (b.) Si-Al-Na-Mg-Ca EDS map and (c.) local misorientation map of Acapulco. The local misoriention plots only the phases with the best EBSD signal, i.e. olivine, orthopyroxene and kamacite-taenite.

A 881902: This section (Figure 6.4a and 6.4b) shows clinopyroxenes and feldspars that have irregular shapes and occur in the form of large pools that seem to form an interconnected network throughout the sample. Although some olivines and orthopyroxenes are included within large pools of feldspar and clinopyroxene, the latter phases do not exhibit wetting shapes, indicating a strong recrystallization. In this section, the amount of feldspar is clearly higher than that of clinopyroxene, which may indicate a partial extraction of a silicate melt. There are only two chromite grains, a large one and a smaller one, both in contact with troilite. Phosphates grains are more numerous and are typically in contact with both troilite and kamacite-taenite. Within the iron-sulfide phases, troilite dominates the mineralogy, with irregular grains. Both phases are often found in contact with each other with sharp grain boundaries. The large amount of troilite may indicate that this specimen originates from a region that accumulated a sulfur-rich metallic melt. Kamacite-taenite crystals can be separated into two subgroups: one that does not show any Fe-Ni zoning and a second one that does. Here also, these zonings do not form well defined Widmanstatten patterns. Similarly to Acapulco, there is a population of rounded iron-sulfide grains that is included within silicate crystals (mostly olivines and orthopyroxenes). A 881902 does not show any sign of alteration

but seems to host some relict chondrules. Indeed, there are some areas with large rounded olivine crystals that are wetted by small intergrowth of feldspar and clinopyroxene. These textures are similar to what would be expected by the recrystallization of the vitreous phase contained in chondrules.

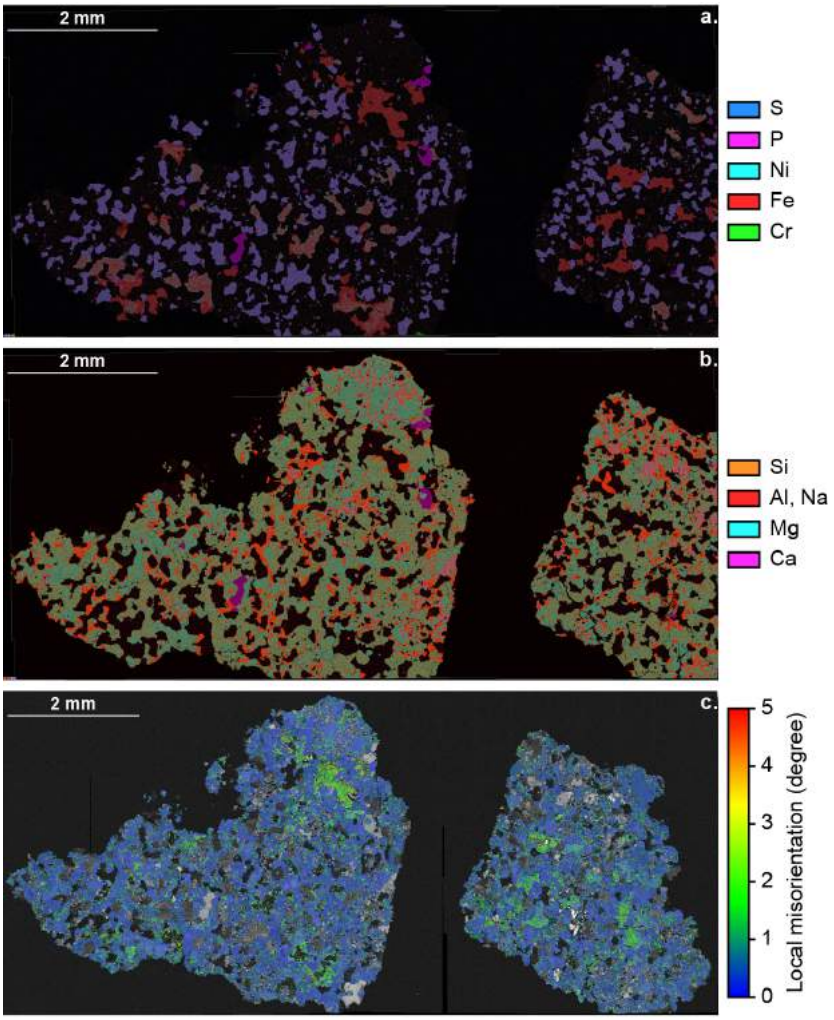

Figure 6.4 – (a.) Fe-Ni-Cr-P-S-Cr EDS map, (b.) Si-Al-Na-Mg-Ca EDS map and (c.) local misorientation map of A 881902. The local misoriention plots only the phases with the best EBSD signal, i.e. olivine, orthopyroxene and kamacite-taenite.

Dhofar 125: This section (Figure 6.5a and 6.5b) displays feldspars and clinopyroxenes with irregular shapes that wet olivine and orthopyroxene grain boundaries. There are two different populations of grains depending on their size, small grains that are trapped along grain boundaries and larger patches that may enclose other silicate phases. Chromites and phosphates appear in the form of irregular grains in contact with kamacite-taenite or troilite. Contrary to Acapulco, phosphates do not form large patches. Troilite and kamacite-taenite grains have irregular shapes and are found associated to each other with sharp boundaries. No Fe-Ni zoning is apparent. In this section, there is a single population of iron-sulfide grains,

silicate crystals do not show any metallic inclusions. Dhofar 125 does not show any signs of relict chondrules. However, borders of metallic grains are altered. The alteration product (most likely oxides or hydroxides) forms small veins that run along silicate grain boundaries.

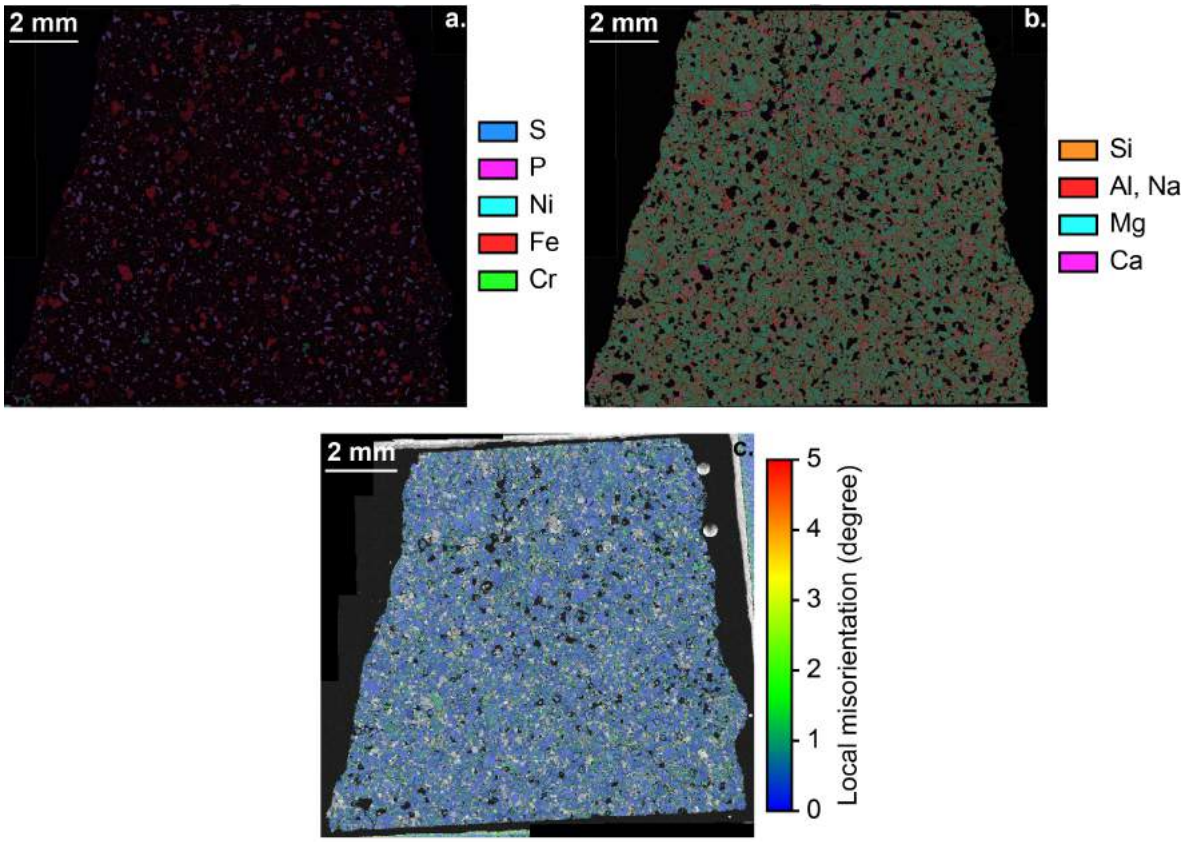

Figure 6.5 – (a.) Fe-Ni-Cr-P-S-Cr EDS map, (b.) Si-Al-Na-Mg-Ca EDS map and (c.) local misorientation map of Dhofar 125. The local misoriention plots only the phases with the best EBSD signal, i.e. olivine, orthopyroxene and kamacite-taenite.

MET 01198: This section (Figure 6.6a and 6.6b) exhibits small rounded crystals of olivine and orthopyroxene that are found included in each other, indicating simultaneous growth. Clinopyroxenes and feldspars have irregular shapes and seem to wet the other silicates. Feldspar grain sizes seem to be larger than those of clinopyroxene, but no olivine or orthopyroxene are included within the two former phases. The section displays a single chromite grain but several phosphate grains that are in contact mostly with kamacites-taenites. Troilite and kamacite-taenite grains have irregular shapes with their extremities that seem to wet the silicates. Both phases are often found associated with each other with sharp contacts. Kamacite-taenite has much larger grain sizes than troilite and does not show signs of Fe-Ni zoning. However, similarly to Acapulco, there is a small fraction of iron-rich grains that is included within orthopyroxenes. No relict chondrules or alteration veins are observed in this section.

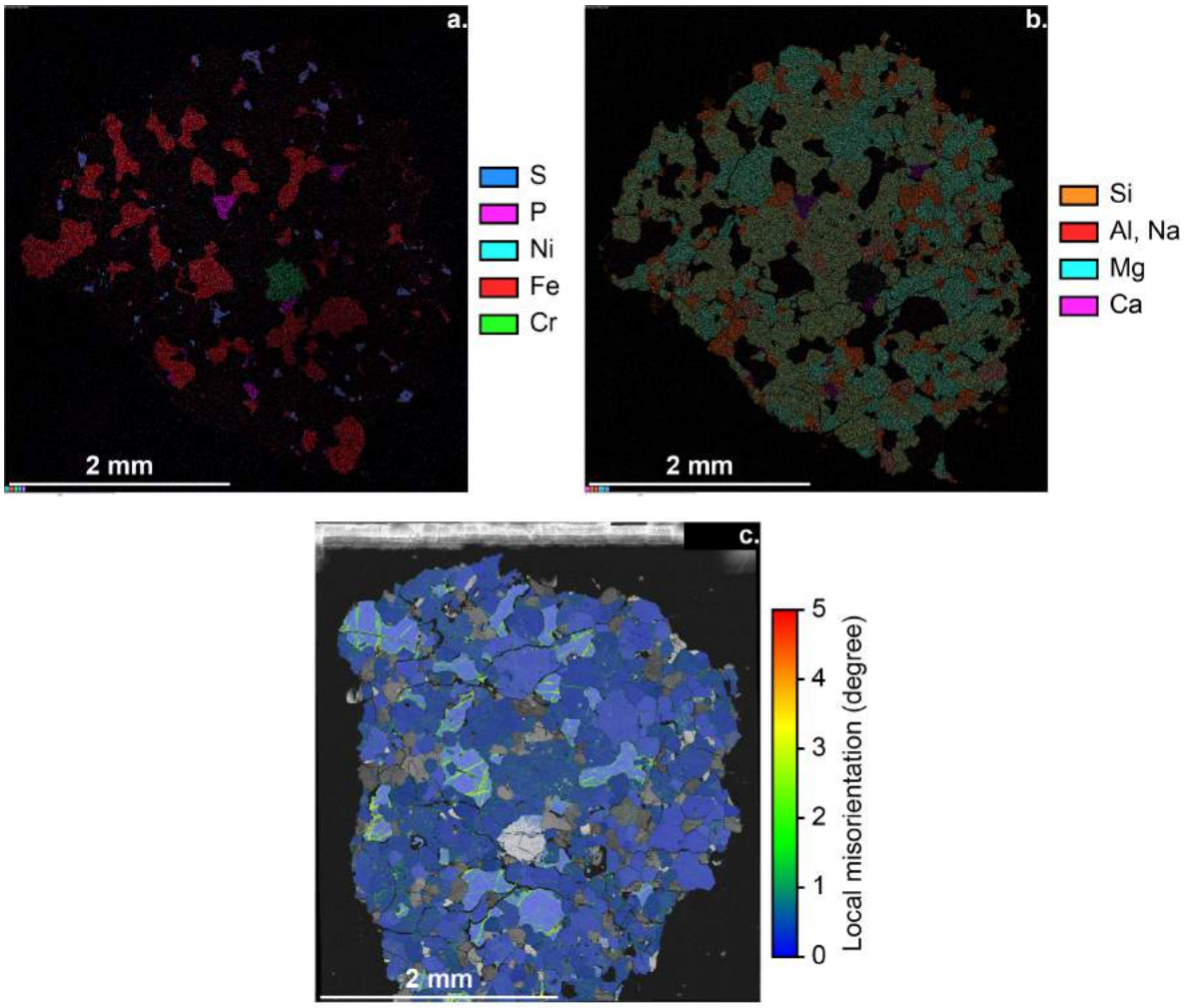

Figure 6.6 – (a.) Fe-Ni-Cr-P-S-Cr EDS map, (b.) Si-Al-Na-Mg-Ca EDS map and (c.) local misorientation map of MET 01198. The local misoriention plots only the phases with the best EBSD signal, i.e. olivine, orthopyroxene and kamacite-taenite.

Monument Draw: Although clinopyroxene and feldspar crystals can form large patches in this section (Figure 6.7a and 6.7b), they also have rounded shapes. This area is particularly rich in iron-rich phases and also gathers most of the chromites and phosphates of the section. These phases have irregular shapes that seem to be wetting the silicates. Troilite and kamacite-taenite crystals form large patches that seem to be largely interconnected throughout the surface of the section. Both phases are often found in contact with each other, grain boundaries being sharp. Some large veins of metal seem to be oriented in a specific direction. Zonings in Fe-Ni are also observed on the EDS mapping but they do not form well defined Widmanstatten patterns. As in Acapulco, there is a small fraction of small rounded metallic grains included within olivine and orthopyroxene crystals. The second area is composed of a material which do not bear large iron-rich phases patches. Olivine and orthopyroxene grains are rounded and seem to display an equivalent textural equilibrium to the metal-rich area. Feldspar and clinopyroxene seem to have more wetting shapes and may form large patches. Overall, Monument Draw seem to be highly heterogeneous. No relict chondrules are

observed. However, alteration veins cross-cut the whole surface of the sample, sectioning the silicate phases.

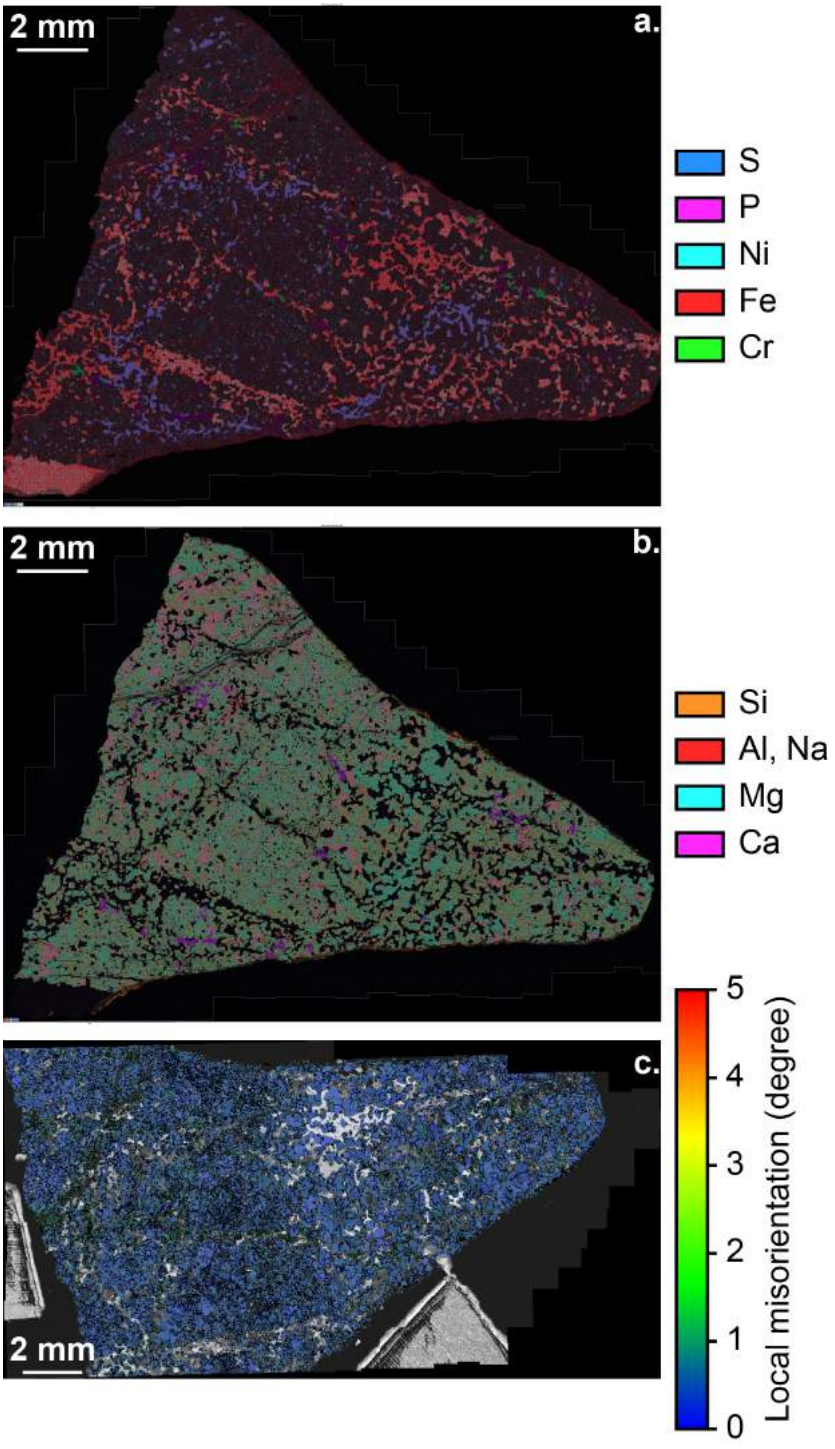

Figure 6.7 – (a.) Fe-Ni-Cr-P-S-Cr EDS map, (b.) Si-Al-Na-Mg-Ca EDS map and (c.) local misorientation map of Monument Draw. The local misorientation plots only the phases with the best EBSD signal, i.e. olivine, orthopyroxene and kamacite-taenite.

General characteristics: In general, acapulcoites do not show signs of an important loss of a silicate or a sulfur-rich component. These objects have a pristine dry mineralogy and may show some relict chondrules (e.g. A 881902). In more details, from a textural point of view, the sharp grain boundaries between kamacites-taenites and troilites indicate that temperature reached at least the Fe-FeS eutectic. In turn, some sections have relative phase proportions that differ from what is generally expected. For instance, A 881902 has a high amount of troilite with respect to the reference specimen Acapulco. Such depletion or enrichment in given phases are likely to arise from the migration of melts and may be indicative of a region that lost or accumulated a given component. The presence of chondrules in some sections is indicative of a poorly metamorphosed material, as for the winonaites. However, other samples show signs for a larger degree of thermal metamorphism that allowed to erase the chondritic texture and the potential melting of feldspar and clinopyroxene, due to their wetting textures.

6.3.1.3 Lodranites

Lodran: This meteorite is the reference specimen of lodranites. The present section (Figure 6.8a and 6.8b) is composed of olivine, orthopyroxene, clinopyroxene, chromite, troilite, kamacite-taenite and phosphate grains. Olivine and orthopyroxene represent the majority of the silicate phases and form rounded and equigranular grains, with olivine triple junctions at 120°. These two phases are found included in each other; the small inclusions are extremely rounded. Silicates have highly recrystallized and equilibrated textures. Clinopyroxenes are found as small rounded inclusions in larger olivine and orthopyroxene crystals. This section distinguishes Lodran from the acapulcoites by the lack of feldspar and the scarcity of clinopyroxene, indicating the removal of a low-temperature basaltic component. Some chromite and phosphate grains are present, often in contact with iron-rich phases. Troilite and kamacite-taenite have irregular shapes that seem to be wetting the silicates along grain boundaries. Both phases are typically found in contact each other with a sharp boundary. Fe-Ni zonings appear within kamacite-taenite crystals but do not form well defined Widmanstatten patterns. The present section contains large amounts of troilite and does not seem to be depleted in a sulfur-rich compound as indicated by Bild and Wasson (1976). No relict chondrules or alteration products are found in this section of Lodran.

GRA 95209: The section (Figure 6.9a and 6.9b) is composed of olivine, orthopyroxene, clinopyroxene, feldspar, chromite, troilite, kamacite-taenite and phosphate grains that are evenly distributed at the surface of the specimen. Olivine and orthopyroxene represent the majority of the silicate phases and form rounded and equigranular grains, with olivine triple junctions at 120° indicating textural equilibrium. Olivines and orthopyroxenes can be found included within each other in the form of small rounded grains. Feldspars and clinopyroxenes have irregular shapes that wet the other silicates. Both of these phases may enclose each other. Contrary to feldspars, clinopyroxenes form large patches with rounded shapes that may enclose olivine and orthopyroxene grains. Chromite and phosphate grains are small and found along grain kamacite-taenite boundaries. Troilite and kamacite-taenite have irregular grains which seem to be wetting the silicates, with no Fe-Ni zoning within the latter. These two phases are often found in contact with each other, forming sharp grain boundaries. At the scale of the section, there is a gradient of iron-rich phases, with on one side kamacite-taenite

grains that form large patches and a strong depletion in troilite, and on the other side small kamacite-taenite grains and a greater abundance of troilites. Within the kamacite-taenite-rich area, the large patches seem to form an interconnected network. These features seem to indicate a mobilization of the metallic phases. No relict chondrules are found in this specimen but some secondary processes seem to have altered the iron-phases in some areas with the formation of small veins that cross-cut the different phases (silicates and iron-rich ones).

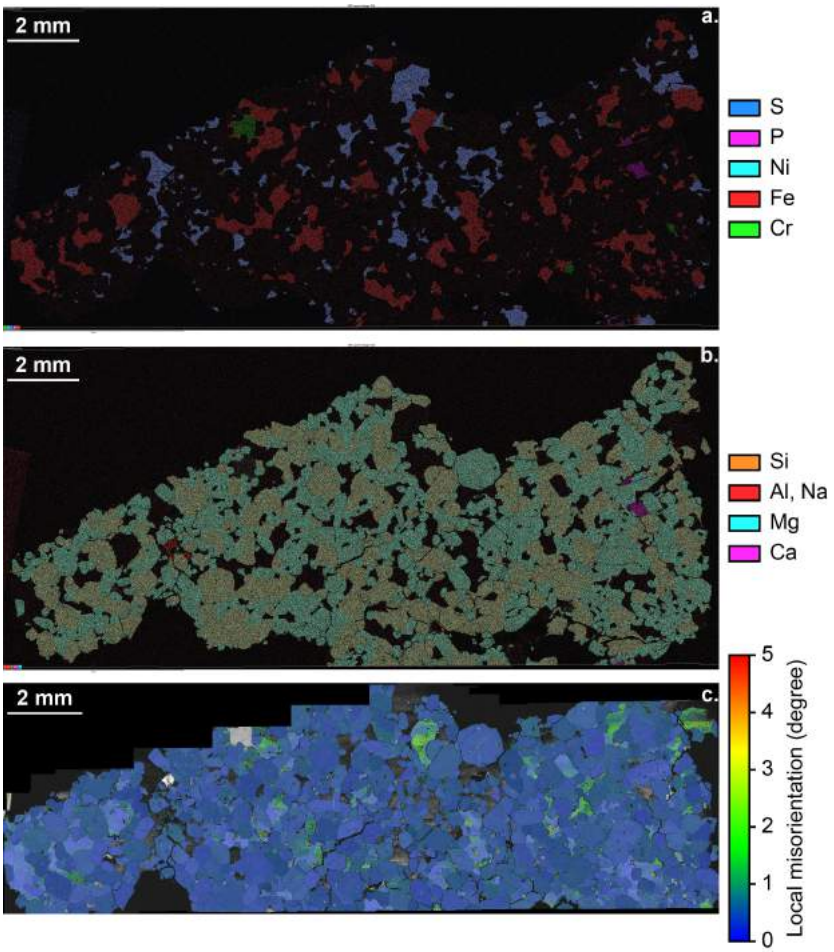

Figure 6.8 – (a.) Fe-Ni-Cr-P-S-Cr EDS map, (b.) Si-Al-Na-Mg-Ca EDS map and (c.) local misorientation map of Lodran. The local misorientation plots only the phases with the best EBSD signal, i.e. olivine, orthopyroxene and kamacite-taenite.

General characteristics: In general, lodranites show igneous processes with the loss of a silicate and / or an iron-rich melt (due to the lack of clinopyroxenes, feldspars or troilite). Previous studies reported an important loss of iron-rich phases, revealed by a low amount of troilite. This feature is not observed in the present lodranite sections, however the lack of feldspars and clinopyroxenes indicate the migration of a silicate melt. Although biased due the low amount of lodranite sections in this survey, these samples indicate a larger degree of thermal metamorphism than acapulcoites through the lack of chondrules and the mobilization of silicate and metallic melts.

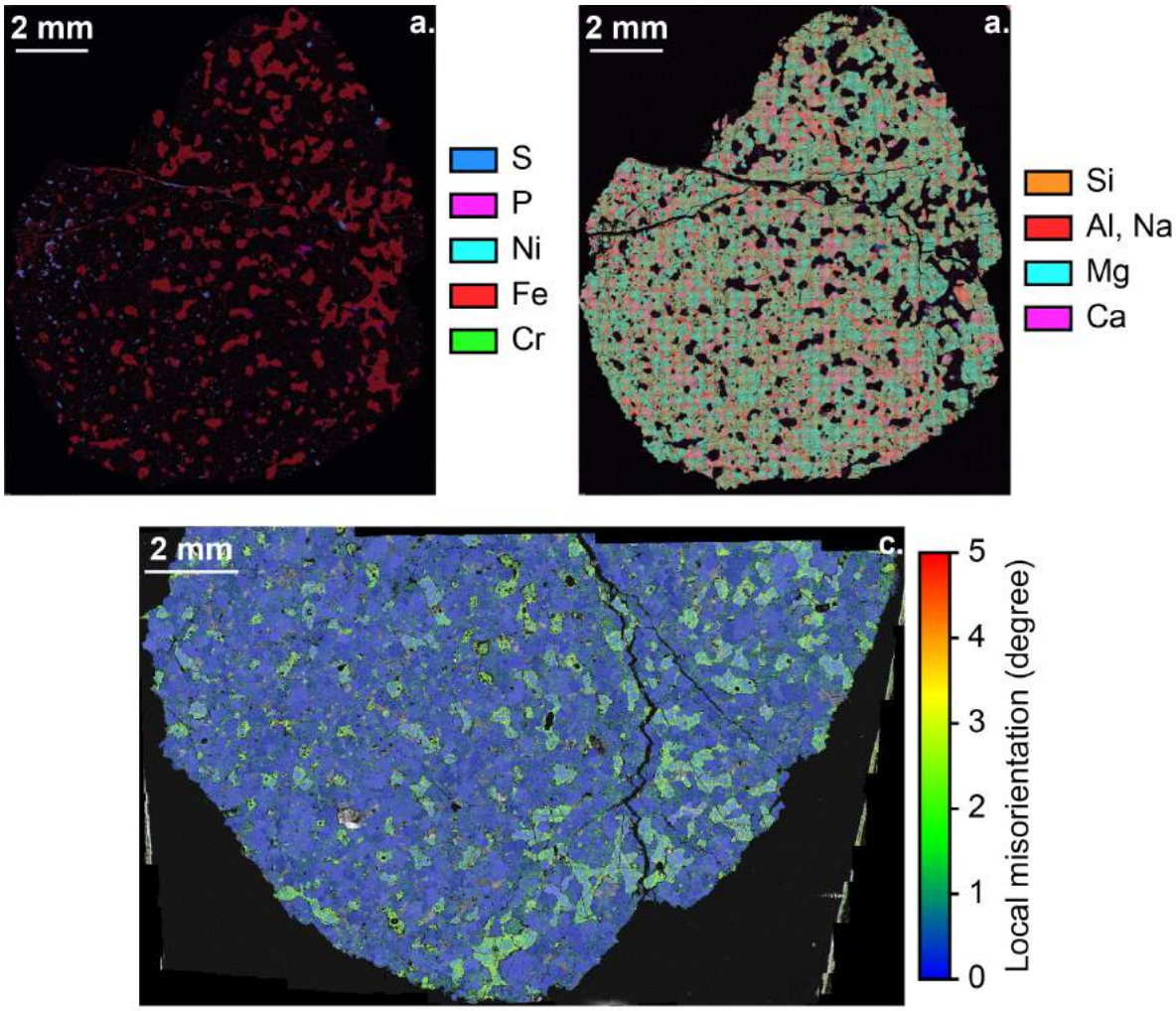

Figure 6.9 – (a.) Fe-Ni-Cr-P-S-Cr EDS map, (b.) Si-Al-Na-Mg-Ca EDS map and (c.) local misorientation map of GRA 95209. The local misoriention plots only the phases with the best EBSD signal, i.e. olivine, orthopyroxene and kamacite-taenite.

6.3.1.4 Modal compositions

The EBSD identification of the mineral phases is not used to determine the modal composition of the samples as clinopyroxene, feldspar and troilite showed a bad signal, with only a partial detection of the grains. Hence, maps of the different elements constituting the silicates were produced and then treated using ImageJ (Eliceiri et al., 2012; Schindelin et al., 2012) to determine the phase proportions. Elemental maps were produced from the EDS large-scale mapping. The following elements were detected: Si, Mg, Ca, Fe, Ni, P, Cr, S, Al and Na. Then, the different maps were converted into 8-bit grayscale images and a smooth filter was applied to decrease the grayscale level of isolated pixels. A simple thresholding method was applied to select the element of interest on the different sections. Thanks to the smoothing filter, isolated pixels corresponding to the background were neglected when applying the threshold.

Table 6.2 – Summary of the petrological observation on the different sections. Mineral abbreviations stand for: Cpx = clinopyroxenes, Flp = Feldspar, Ol = Olivine and Opx = orthopyroxene. Phase loss or gain are referred to as "n.d." if the depletion or enrichment was not observed qualitatively.

Winonaites					
	Chondrules	Irregular shapes	Rounded shapes	Phase loss	Phase gain
Dhofar 1222	Yes	Metal	Silicate	n.d.	n.d.
NWA 725	Yes	Metal	Silicate	n.d.	n.d.
Acapulcoites					
	Chondrules	Irregular shapes	Rounded shapes	Phase loss	Phase gain
A 881902	Yes	Metal, Cpx and Flp	Ol and Opx	n.d.	Troilite
Acapulco	No	Metal, Cpx and Flp	Ol and Opx	n.d.	n.d.
Dhofar 125	No	Metal	Silicate	n.d.	n.d.
MET 01198	No	Metal, Cpx and Flp	Ol and Opx	n.d.	n.d.
Monument Draw	No	Metal, Cpx and Flp	Ol and Opx	n.d.	Metal
Lodranites					
	Chondrules	Irregular shapes	Rounded shapes	Phase loss	Phase gain
GRA 95209	No	Metal, Cpx and Flp	Ol and Opx	Troilite	Fe-Ni, Cpx and Flp
Lodran	No	Metal	Ol and Opx	Cpx and Flp	n.d.

Table 6.3 – Modal compositions of the samples (in vol%).

Winonaites								
	Olivine	Opx[1]	Cpx[2]	Feldspar	Chromite	Whitlockite	Troilite	Fe-Ni
Dhofar 1222	12.6	46.0	3.8	10.5	0.7	0.8	10.7	14.8
NWA 725	14.2	43.6	2.8	10.9	0.8	1.1	9.1	17.5
Acapulcoites								
	Olivine	Opx[1]	Cpx[2]	Feldspar	Chromite	Whitlockite	Troilite	Fe-Ni
A 881902	21.8	34.7	1.9	11.3	0.5	1.4	18.5	9.8
Acapulco	31.6	37.8	3.0	11.9	0.9	1.6	7.1	5.9
Dhofar 125	30.5	35.3	3.7	11.3	0.6	1.0	7.6	10.0
MET 01198	25.6	42.8	0.9	6.6	2.4	2.7	4.6	14.6
Monument Draw	27.8	31.8	3.9	10.0	1.0	1.7	8.0	15.9
Lodranites								
	Olivine	Opx[1]	Cpx[2]	Feldspar	Chromite	Whitlockite	Troilite	Fe-Ni
GRA 95209	30.0	28.7	8.0	14.2	0.9	1.0	3.2	14.0
Lodran	42.9	34.7	0.1	None	1.4	1.6	9.6	9.7

[1]Opx is for orthopyroxene.
[2]Cpx is for clinopyroxene.

To determine the relative proportions of the different phases, aluminum was considered to be only hosted within feldspar. Indeed, the aluminum content in chromite is so low in comparison to that of feldspar that this former phase corresponded to the background level, especially after applying the smooth filter. Then, all chromium is considered as hosted in chromite and all phosphorous in whitlockite (the formation of schreibersite is neglected although detected in extremely small amounts with the EPMA). Both whitlockite and clinopyroxene host calcium. The phosphate surface proportion was thus substracted from that of calcium to account for

this effect, and the resulting surface is attributed to clinopyroxene. A similar procedure is used to determine the proportion of kamacite-taenite and troilite: all sulfur is hosted in troilite and the surface fraction of kamacite-taenite is obtained by substracting the sulfur proportion from that of iron. Here also, iron is so concentrated in kamacite-taenite and troilite that the silicates contribution is negligible. Finally, the case of olivine and orthopyroxene is slightly more complicated as both phases host the same elements but in different relative proportions. To determine their surface fraction, the magnesium map was considered. This element is also hosted in clinopyroxene, so this fraction was substracted from the magnesium surface fraction to only have the olivine and orthopyroxene. Then, as these two latter phases are the silicates with the best EBSD signal, the relative proportions of these two phases (olivine / (olivine + orthopyroxene), and orthopyroxene / (olivine + orthopyroxene)) obtained with this technique were used to determine their relative amount. Results obtained following this procedure are shown in Table 6.3. Surface and volume proportions were assumed to be identical. Data from the present study are in agreement with the data compilation of Keil and McCoy (2018).

The winonaites Dhofar 1222 and NWA 725 have similar modal compositions for the silicates. However, their metallic subsystems show more differences, with Dhofar 1222 exhibiting a larger proportion of troilite in the iron-sulfide subsystem (troilite / (troilite + kamacite-taenite) = 42%) than NWA 725 (troilite / (troilite + kamacite-taenite) = 34%). Overall, these samples are characterized by a large amount of orthopyroxenes in comparison to olivines and large contents of metallic phases (≈ 25 vol.%)

Acapulcoites show variations in the different phase proportions. Indeed, olivine content spans a range from 21.8 vol.% (A 881902) to 30.5 − 31.6 vol.% (Dhofar 125 and Acapulco respectively). Orthopyroxene contents are always larger than those of olivine, with values ranging from 31.8 vol.% (Monument Draw) to 42.8 vol.% (MET 01198). Overall, clinopyroxene contents are similar, from ≈2 to ≈4 vol.%, with MET 01198 being an outlier hosting only 0.9 vol.% of this phase. Similar features are observed for feldspar, with the same odd behavior for MET 01198. This artifact may be due to the small size of MET 01198 and small heterogeneities, at the millimeter scale. However, such a depletion in the low-melting temperature phases may also indicate a more evolved stage of the meteorite, with a larger degree of melting and more efficient silicate melt extraction. The different sections show similar amounts of chromite and whitlockite, except for MET 01198, which may be due to the reasons mentioned previously. No clear systematics seem to arise from the amount of the metallic phases. The total amount of metallic phases varies between ≈ 10 vol.% (Acapulco) to ≈ 29 vol.% (A 881902). Some sections host more troilite than kamacite-taenite (A 881902 and Acapulco), while the other ones host more kamacite-taenite than troilite. These features may indicate a depletion or enrichment in iron-sulfur melts with respect to a H chondrite precursor (3 vol% of troilite and 7 vol% of kamacite taenite from Guignard and Toplis (2015)), and hence different differentiation degrees.

In turn, lodranites also show large variations in the relative amounts of the different phases. Lodran shows a higher content of both olivine and orthopyroxene than GRA 95209 which shows similar volume proportions for these two phases. However the quantities of low-melting temperature phases, clinopyroxene and feldspar, are drastically different between the two sections: Lodran is characterized by the absence of feldspar and a strong depletion in clinopyroxene (0.1 vol.% left), while GRA 95209 still hosts 8 vol.% of clinopyroxene and 14

vol.% of feldspar. This difference emphasizes the greater differentiation degree of Lodran with respect to the silicate subsystem: a silicate melt bearing all the clinopyroxenes and feldspars was extracted. Chromite and whitlockite show similar contents among lodranites. However, the metallic subsystem differs drastically. Indeed, Lodran show similar amounts of troilite and kamacite-taenite, while GRA 95209 shows a kamacite-taenite to troilite ratio of almost five, highlighting a strong depletion in a sulfur-bearing melt in comparison to a H chondrite precursor. The present section of Lodran does not show a strong depletion in sulfur bearing phases as reported in literature (e.g. Bild and Wasson, 1976), which may be due to local heterogeneities.

Besides differences among the different meteorite groups, there are also differences between them, indicating different thermal conditions. Winonaites show the most pristine textures, with the presence of chondrules, and are characterized by lower olivine and much larger orthopyroxene contents than both acapulcoites and lodranites (except for MET 01198 which has similar orthopyroxene proportions). Acapulcoites can be enriched in metallic phases, but show an overall equal amount of olivine and orthopyroxene. The transitional acapulcoite GRA 95209 shows a depletion in troilite but an enrichment in clinopyroxenes and feldspars. Lodranites show then a strong depletion in low melting temperature phases (clinopyroxenes and feldspars). In comparison to a H chondrite precursor material (3 vol% troilite and 7 vol% kamacite-taenite, Guignard and Toplis, 2015), sections with greater or equal troilite contents than those of kamacite-taenite are likely to have accumulated a sulfur-rich iron-sulfide melt (e.g. A881902). On the opposite, samples with less than 30 vol.% of troilite in the metallic subsystem have lost a sulfur-rich metallic melt component (e.g. GRA 95209).

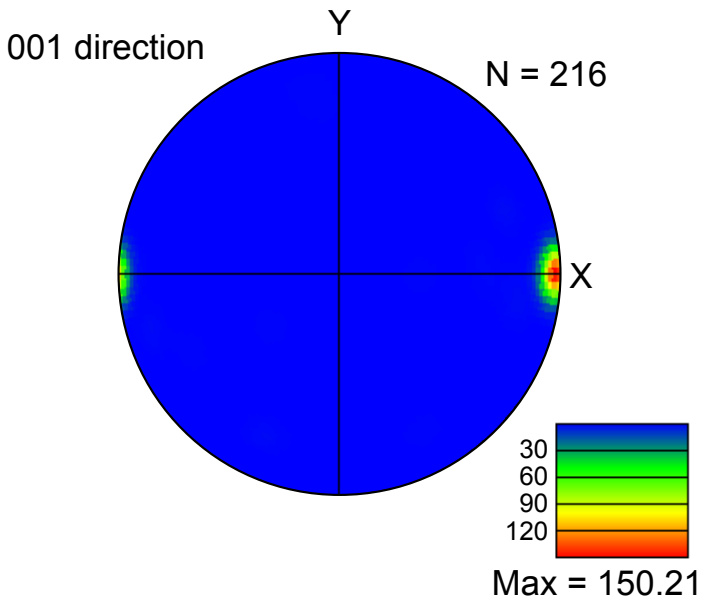

Figure 6.10 – Lattice preferred orientation of troilite grains in Lodran. Lower hemisphere and equa-area projection in the sample coordinate system. The color code correspond to the density of Multiples of Uniform Distribution (MUD). N is the number of grains measured. To give equal weights to the different grain, each grain was considered as a single point.

6.3.2 EBSD textures and grain sizes

EBSD maps were made on each section of this study. Textures are very similar from one section to another and show low deformation. Local misorientation is a good indicator of deformation, it compares the pixel to pixel orientation difference inside a single grain. Maps were realized for each different sample and show misorientation angles lower than 3° for both silicate and metallic phases (Figures 6.1-6.8c). Troilite or kamacite-taenite typically show slightly larger deformed textures than silicates, due to their lower viscosity. Indeed, larger misorientation angles ($\geq 5°$) are observed along rays due to polishing.

Orientations of the phases are randomly distributed, except for troilite grains in Lodran (Figure 6.10). Indeed, all troilite grains have the exact same orientation in this section, similarly to Bascou et al. (2008). One explanation for this phenomenon, due to the lack of evidence for deformation, is that all these grains constitute a single larger grain, which forms an interconnected network in three dimensions. Slicing effects are then responsible for these apparent populations of isolated grains. The formation of a percolative network is the first step to allow melts migration. Hence, in these samples, the network was formed but either did not segregate, or migration initiated but did not go to completion.

Table 6.4 – Mean grain sizes of the different sections. The mean sizes here do not correspond to the arithmetical means, but to the equivalent diameter of the mean surface area of the grains. Two standard errors ($\frac{2SD}{\sqrt{N}}$, with SD the standard deviation) are displayed in parentheses. N gives the number of grains detected.

	Olivine		Orthopyroxene		Kamacite-taenite	
	d_{mean} (µm)	N	d_{mean} (µm)	N	d_{mean} (µm)	N
A 881902	61.24 (1.41)	1733	68.37 (1.22)	2212	108.90 (11.29)	156
Acapulco	105.46 (2.05)	2578	113.05 (2.16)	2685	79.95 (3.96)	589
Dhofar 125	86.79 (1.14)	4928	71.79 (0.64)	8341	99.47 (7.05)	220
Dhofar 1222	56.46 (0.80)	4834	45.57 (0.20)	27147	80.95 (3.74)	828
GRA 95209	122.73 (2.91)	2811	106.37 (2.05)	3583	90.02 (2.56)	2585
Lodran	226.13 (8.62)	944	317.79 (21.16)	386	151.53 (8.33)	544
MET 01198	104.74 (8.44)	271	105.13 (6.26)	450	103.49 (13.83)	147
Monument Draw	60.80 (0.64)	9397	69.93 (0.83)	8148	75.47 (2.30)	1789
NWA 725	55.06 (0.63)	6607	44.78 (0.18)	30676	125.99 (4.74)	1179

The EBSD mapping also provides information on grain sizes of the minerals. Particular interest is given to olivine, orthopyroxene and metal as these phases were better detected than the others, hence measured grain sizes are more reliable. Mean grain sizes for each of the sections and above-mentioned phases are reported in Table 6.4. Here, the mean grain size corresponds to the mean value of the disk-equivalent diameter of the area determined for each grain. Based on these results for silicates, sections can be split into five categories. (1) Lodran clearly distinguishes from the other section with the largest silicate mean grain sizes: ≈ 230 µm for olivine. (2) The transitional acapulcoite GRA 95209 has lower grain sizes (≈ 120 µm for olivine), but larger ones than acapulcoites. (3) Then, the three acapulcoites Acapulco, Dhofar 125 and MET 01198 have similar grain sizes within errorbars ($\approx 90 - 100$ µm for olivine). (4) The rest of the acapulcoites, A 881902 (bearing residual chondrules) and Monument Draw, have mean grain sizes that are significantly lower (≈ 60 µm for olivine) and overlap within errorbars. (5) Finally, the winonaites Dhofar 1222 and NWA 725 have the lowest grain sizes (≈ 55 µm for olivine). As grain sizes are sensitive to the peak temperature

experienced and to the time spent at this temperature, these five categories are likely to be indicative of different thermal conditions and evolutions. These groups are also consistent with differences in their textures (Table 6.2) and modal compositions (Table 6.3). Mean grain sizes of kamacite-taenite do not show similar systematics to the silicate ones.

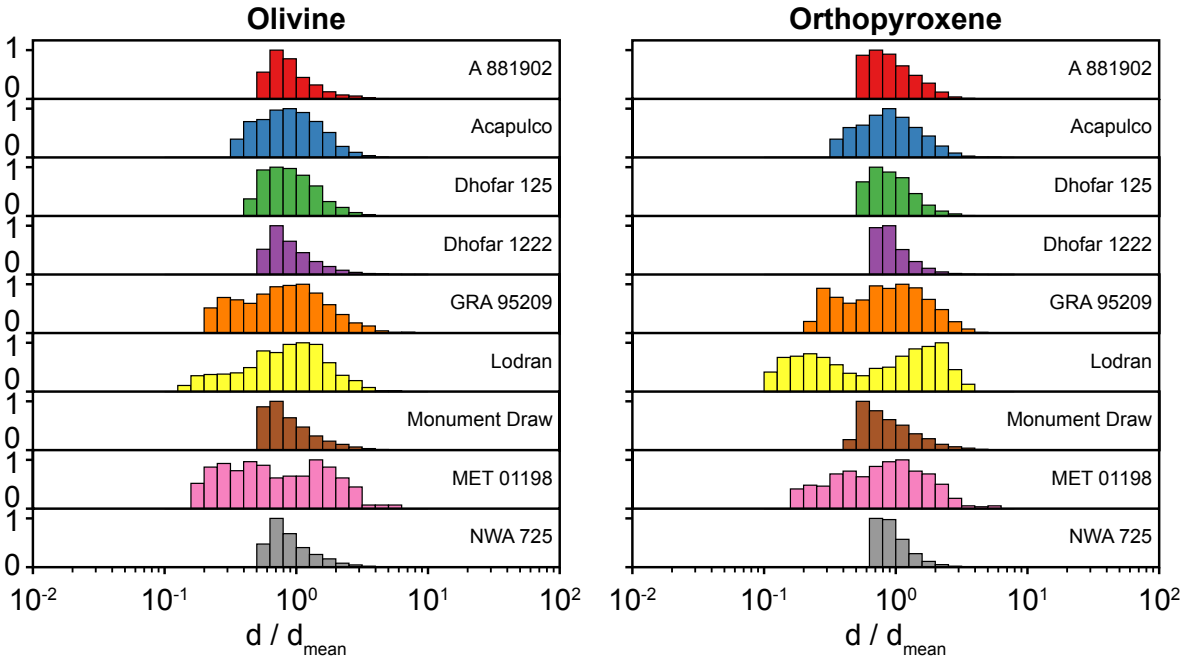

Figure 6.11 – Silicate grain size distributions normalized to the mean grain size. Heights of the distributions are normalized to the maximum height.

Grain size distributions normalized to the mean grain size for the different phases give information on the grain growth mechanisms, between normal or abnormal grain growth (Figures 6.11 and 6.12) and may help decipher the occurrence of igneous processes. Indeed, if the distributions have log-normal shapes (normal distribution in linear scale, but log-normal in log scale), then grain populations are the result of normal grain growth mechanisms. If not, other processes occurred to explain this variation, e.g. melting or crystallization. This representation also allows to neglect the effects of peak temperature and time spent at this peak, making comparison between the different distributions much easier.

Figure 6.11 shows the grain size distribution normalized to the mean size for the silicates (olivine and orthopyroxene). Overall, the distributions vary lateraly on the d / d_{mean} axis within two orders of magnitude (from 0.1 to 10) and have log-normal shapes. However, three samples show distributions that differ from this criteria: GRA 95209, Lodran and MET 01198, both for olivine and pyroxene. In more details, these sections seem to have bimodal distributions, indicating that grain growth did not follow normal mechanisms in these samples, in contrast to other samples. Figure 6.12 illustrates the same representation but for kamacite-taenite. Here, about a half of the samples (Acapulco, Dhofar 1222, GRA 95209, Monument Draw and MET 01198) have log-normal distributions, but they can spread over a much wider range on the d / d_{mean} axis. However, the other half (A 881902, Dhofar 125, Lodran and NWA 725) denotes, with the emergence of a bimodal distribution. It is of note that alteration processes may also influence these distributions, with the artificial

appearance of smaller grains, shifting the d / d_{mean} distributions toward lower values. Hence, results on kamacite-taenite for the most altered (Dhofar 125, Dhofar 1222 and NWA 725) have to be considered with caution.

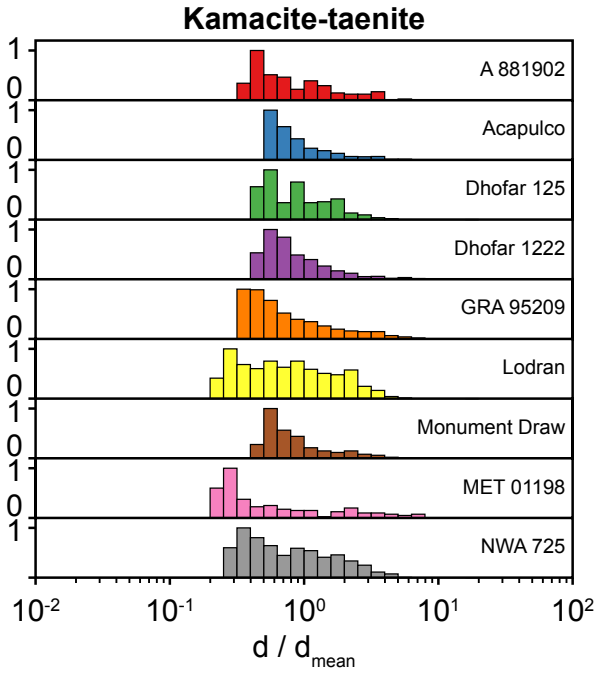

Figure 6.12 – Kamacite-taenite grain size distributions normalized to the mean grain size. Heights of the distributions are normalized to the maximum height.

Grain sizes distributions normalized to the mean size that differ from a log-normal shape are likely to indicate igneous processes that affected the different subsystems, both silicate and metallic. The lack of deformation textures in the different phases enhances this idea. Bimodal distribution can then arise from igneous processes such as melting, crystallization or mixing of different grain sizes populations.

6.4 Thermometry and calculation of oxygen fugacity

6.4.1 Phase and bulk compositions

Mineral compositions are displayed in Tables 6.5, 6.6 and 6.7, and in ternary diagrams for pyroxenes (Figure 6.14) and feldspars (Figure 6.15). For each section, compositions of olivine, orthopyroxene, clinopyroxene, feldspar, chromite, troilite, kamacite-taenite were measured with about 30 measurement points per phase, if possible. Chromite is a typical exception to this rule, as grains are scarce, repeated measurement on the same grain was avoided not to give large statistical weights to large grains. Clinopyroxenes in Lodran are the only other exception, as they were found as relict crystals included within olivine or orthopyroxene. Composition profiles were also measured, if possible, to investigate the presence of zoning.

Regarding the silicates, Lodran is the only section displaying zoning within the olivine grains (Figure 6.13). Indeed, the border of the olivines is more MgO-rich than the core by about 5 wt%. Bild and Wasson (1976) attributed this feature to a possible reduction event, leading to iron exsolution from the olivine. Such zoning is not observed in orthopyroxene due to lower Mg-Fe interdiffusion coefficients. In all the other sections all composition profiles are extremely flat, indicating a global chemical equilibrium. Due to the larger grain sizes of Lodran, it is possible that such reduction event affected only the smaller grains, while time and temperature did not allow to entirely reduce the larger ones. Hence, only local chemical equilibrium seems then to have been reached.

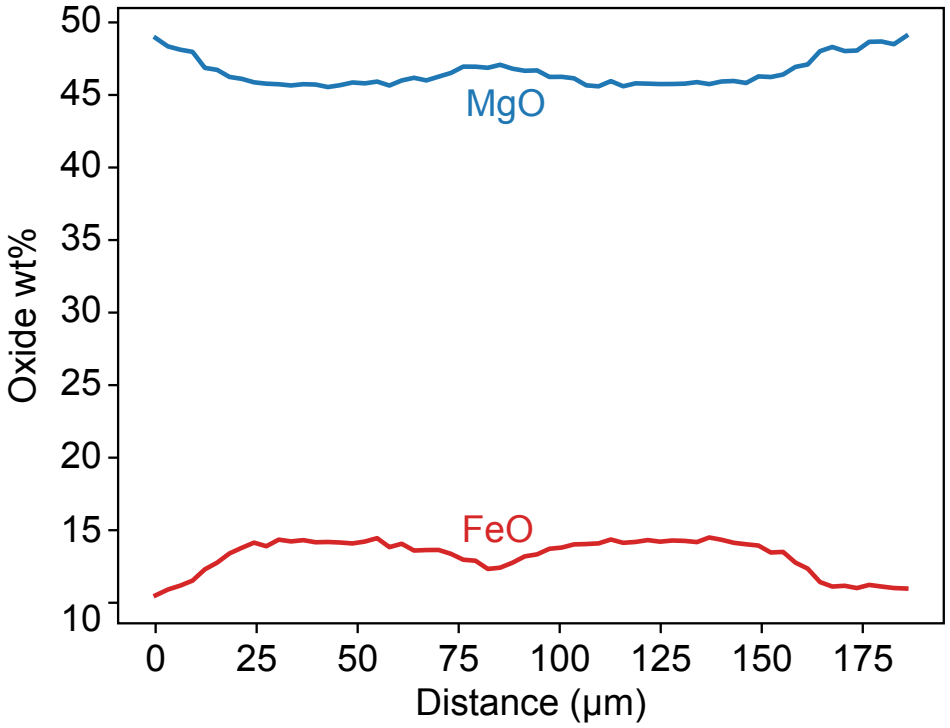

Figure 6.13 – FeO and MgO composition profile within an olivine of Lodran. Compositions are reported in oxide wt%.

In turn, kamacite-taenite crystals may show Fe-Ni zonings, with variations in Ni content that can reach up to 20 wt% (Table 6.7). However, no well defined Widmanstatten patterns seem to be formed, indicating a relatively fast cooling rate (more than a few tens of kelvins per million year, Bild and Wasson, 1976; Palme et al., 1981). Some sections show kamacite-taenite grains with Fe-Ni compositions that do not vary from a grain to another (Dhofar 1222, GRA 95209, MET 01198 and NWA 725) and similar compositions between the samples.

Olivine compositions in fayalite can span a large range between the different sections, from 6.27 (NWA 725) to 12.28 mol% (Lodran). Most sections exhibit extremely narrow errorbars (2 SD $<$ 1 mol%, Table 6.5), but not Lodran, Monument Draw and GRA 95209 (2 SD $>$ 1.5 mol%, Table 6.5). No zoning was observed in either of Monument Draw nor GRA 95209, indicating a variability of olivine composition within the section. These large error bars can be either explained by the global chemical equilibrium that is not reached, or by igneous processes that caused fractionate melting and / or crystallization of the phases. Monument

Draw do not show evidence of large scale silicate partial melting, but a significant fraction of metallic phases seem to have been molten and mobile. It is possible that the silicates were not able to equilibrate with these metallic intrusions. The variations observed in Lodran may be due to the olivine zoning and sectioning effects. GRA 95209 likely shows similar features.

Figures 6.14 and 6.15 show ternary diagrams in which are plotted the different endmembers for the pyroxenes and feldspars, respectively. All these silicate phases have identical compositions within error bars, with the exception of the few clinopyroxenes in Lodran which are slightly more Fe-rich. However, this observation may also be biased due to the low amount of measurements on this phase.

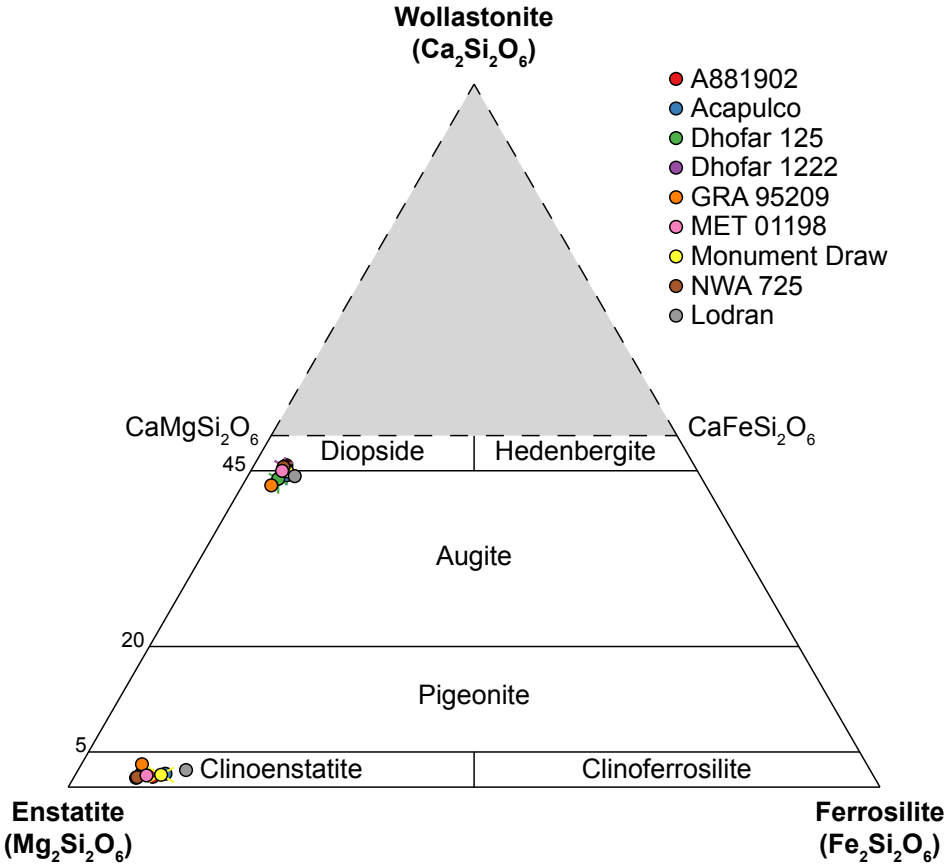

Figure 6.14 – Wollastonite ($Ca_2Si_2O_6$) - Ferrosilite ($Fe_2Si_2O_6$ - Enstatite ($Mg_2Si_2O_6$) ternary diagram with the mean compositions of ortho- and clinopyroxenes reported. Error bars represent two standard deviation with respect to each pure endmember.

Bulk compositions (Table 6.8) were calculated from modal (Table 6.3) and phase compositions (Tables 6.5, 6.6 and 6.7) of the samples. Results are in agreement with literature data (Keil and McCoy, 2018, and references therein). Variations in the major oxides (SiO_2, MgO and FeO) are correlated with variations in modal proportions. Due to the loss of clinopyroxene and feldspar, Lodran is highly depleted in compatible elements (Na, K, Ca and Al). Acapulco and Lodran have greater FeO contents than the other samples due to their lower olivine and orthopyroxene Mg#. Winonaites (Dhofar 1222 and NWA 725) have bulk compositions similar to that of A 881902 and Monument Draw, except for their FeO contents.

Table 6.5 – Olivine and chromite compositions measured in this study (in wt%). Two standard deviations are displayed in parentheses. N gives the number of measurements.

Olivine									
	A 881902	Acapulco	Dhofar 125	Dhofar 1222	GRA 95209	Lodran	MET 01198	Monument Draw	NWA 725
SiO_2	41.20 (0.41)	40.76 (0.43)	41.29 (0.33)	41.72 (0.50)	41.44 (0.88)	40.66 (0.78)	41.26 (0.77)	40.92 (0.93)	41.83 (0.45)
MnO	0.48 (0.08)	0.59 (0.08)	0.50 (0.07)	0.49 (0.06)	0.51 (0.07)	0.51 (0.07)	0.48 (0.07)	0.51 (0.08)	0.50 (0.05)
FeO	8.98 (0.37)	11.20 (0.23)	8.57 (0.36)	6.48 (0.62)	7.48 (1.46)	11.82 (3.10)	8.68 (0.68)	9.63 (1.79)	6.19 (0.44)
MgO	49.80 (0.51)	47.69 (0.51)	49.95 (0.42)	51.58 (0.88)	50.85 (1.33)	47.44 (2.64)	49.80 (1.01)	49.34 (0.89)	51.92 (0.68)
Total	100.46	100.26	100.27	100.28	100.28	100.43	100.22	100.40	100.44
Fo[a]	90.82 (0.39)	88.36 (0.20)	91.21 (0.36)	93.42 (0.34)	92.37 (1.57)	87.72 (3.41)	91.10 (0.74)	90.14 (1.77)	93.73 (0.45)
Fa[b]	9.18 (0.39)	11.64 (0.20)	8.79 (0.36)	6.58 (0.34)	7.63 (1.57)	12.28 (3.41)	8.90 (0.74)	9.86 (1.77)	6.27 (0.45)
N	37	31	34	31	33	49	35	32	32

Chromite									
	A 881902	Acapulco	Dhofar 125	Dhofar 1222	GRA 95209	Lodran	MET 01198	Monument Draw	NWA 725
Al_2O_3	5.62 (0.54)	5.88 (0.30)	6.45 (0.34)	5.20 (1.89)	3.97 (1.70)	6.08 (0.16)	6.62 (0.11)	6.18 (0.99)	5.39 (1.77)
MnO	1.73 (0.29)	1.19 (0.26)	1.21 (0.26)	2.47 (0.59)	1.38 (0.59)	1.05 (0.20)	1.28 (0.24)	1.45 (0.41)	2.26 (0.64)
FeO	19.95 (0.29)	20.35 (0.46)	21.16 (1.78)	16.31 (1.00)	26.81 (1.08)	18.16 (1.25)	17.89 (0.57)	20.02 (0.91)	16.24 (0.63)
MgO	6.98 (0.37)	7.02 (0.54)	5.09 (1.22)	9.12 (1.01)	1.35 (0.94)	8.43 (0.38)	8.51 (0.40)	6.90 (0.79)	9.36 (0.84)
Cr_2O_3	62.84 (0.65)	62.12 (0.51)	59.93 (1.06)	64.56 (2.24)	61.86 (1.75)	62.78 (1.39)	62.71 (0.80)	61.87 (1.33)	63.70 (2.18)
TiO_2	1.11 (0.21)	1.21 (0.15)	1.08 (0.06)	0.86 (0.32)	1.03 (0.14)	1.20 (0.29)	1.08 (0.06)	1.13 (0.21)	0.89 (0.18)
ZnO	0.70 (0.19)	0.92 (0.16)	3.22 (0.20)	n.d.	2.76 (0.25)	1.19 (0.41)	1.13 (0.24)	1.05 (0.36)	n.d.
V_2O_3	0.56 (0.13)	0.59 (0.10)	0.47 (0.07)	0.53 (0.11)	0.63 (0.17)	0.67 (0.07)	0.58 (0.09)	0.67 (0.16)	0.52 (0.12)
Total	99.57	99.28	98.60	99.07		99.55		99.28	98.40
N	10	17	18	17	10	10	8	13	29

[a] Fraction of Mg_2SiO_4 in mole fraction.
[b] Fraction of Fe_2SiO_4 in mole fraction.

Table 6.6 – Orthopyroxene and Clinopyroxene compositions measured in this study (in wt%). 2-standard deviations are displayed in parentheses. N gives the number of measurements.

Orthopyroxene

	A 881902	Acapulco	Dhofar 125	Dhofar 1222	GRA 95209	Lodran	MET 01198	Monument Draw	NWA 725
Al_2O_3	0.28 (0.07)	0.30 (0.06)	0.36 (0.03)	0.24 (0.07)	0.37 (0.06)	0.40 (0.81)	0.32 (0.07)	0.27 (0.05)	0.28 (0.43)
SiO_2	57.59 (0.44)	57.22 (0.59)	57.84 (0.54)	58.28 (0.54)	57.73 (0.71)	56.72 (0.02)	57.74 (0.67)	57.53 (2.00)	58.38 (0.62)
CaO	0.78 (0.29)	1.01 (0.33)	1.02 (0.18)	0.71 (0.28)	1.71 (0.27)	1.27 (0.06)	0.89 (0.30)	0.94 (0.27)	0.76 (0.28)
MnO	0.51 (0.07)	0.64 (0.09)	0.56 (0.07)	0.57 (0.09)	0.56 (0.07)	0.53 (0.24)	0.55 (0.08)	0.56 (0.09)	0.57 (0.06)
FeO	6.62 (0.40)	7.44 (0.31)	5.49 (0.29)	5.29 (0.45)	5.04 (0.30)	8.94 (0.53)	6.02 (0.61)	7.23 (2.42)	5.35 (0.56)
MgO	34.13 (0.46)	32.97 (0.39)	34.47 (0.44)	35.09 (0.77)	33.82 (0.56)	31.78 (0.05)	34.28 (0.62)	33.63 (1.16)	35.02 (0.59)
TiO_2	0.17 (0.04)	0.18 (0.03)	0.19 (0.03)	0.13 (0.06)	0.18 (0.04)	0.20 (0.12)	0.19 (0.05)	0.17 (0.03)	0.14 (0.04)
Cr_2O_3	0.23 (0.07)	0.30 (0.06)	0.45 (0.11)	0.24 (0.07)	0.81 (0.16)	0.38 (0.05)	1.67 (0.12)	0.26 (0.07)	0.25 (0.07)
Total	100.31	100.06	100.36	100.56	100.23	100.23	98.95	100.59	100.75
Wo[a]	1.47 (0.54)	1.91 (0.63)	1.91 (0.34)	1.33 (0.53)	3.25 (0.53)	2.43 (0.96)	1.66 (0.57)	1.76 (0.51)	1.41 (0.53)
Fs[b]	9.67 (0.54)	11.02 (0.42)	8.05 (0.37)	7.70 (0.69)	7.46 (0.42)	13.30 (0.26)	8.81 (0.83)	10.56 (3.37)	7.78 (0.81)
En[c]	88.86 (0.95)	87.07 (0.69)	90.04 (0.43)	90.97 (1.14)	89.29 (0.64)	84.27 (0.94)	89.52 (1.01)	87.68 (3.45)	90.80 (1.15)
N	32	32	32	31	24	33	42	32	31

Clinopyroxene

	A 881902	Acapulco	Dhofar 125	Dhofar 1222	GRA 95209	Lodran[d]	MET 01198	Monument Draw	NWA 725
Na_2O	0.66 (0.10)	0.72 (0.09)	0.79 (0.11)	0.70 (0.09)	0.86 (0.12)	0.66 (0.03)	0.79 (0.15)	0.68 (0.08)	0.71 (0.07)
Al_2O_3	0.72 (0.16)	0.78 (0.20)	0.89 (0.18)	0.66 (0.08)	0.96 (0.13)	0.86 (0.07)	0.84 (0.28)	0.70 (0.07)	0.66 (0.06)
SiO_2	53.87 (1.07)	54.43 (0.64)	54.42 (0.74)	54.31 (1.81)	54.49 (1.15)	53.95 (0.21)	54.53 (0.71)	54.48 (0.34)	54.68 (0.94)
CaO	22.17 (0.59)	21.28 (1.13)	21.08 (1.64)	22.07 (1.18)	20.45 (0.50)	21.39 (0.44)	21.57 (0.92)	21.79 (0.81)	22.16 (0.69)
MnO	0.24 (0.07)	0.34 (0.08)	0.30 (0.09)	0.26 (0.07)	0.30 (0.07)	0.26 (0.01)	0.30 (0.04)	0.28 (0.06)	0.27 (0.05)
FeO	2.47 (0.43)	2.88 (0.43)	2.43 (1.06)	2.43 (1.27)	2.17 (0.36)	3.58 (0.07)	2.37 (0.25)	2.83 (0.41)	2.34 (1.21)
MgO	17.48 (0.44)	17.58 (0.62)	18.04 (0.93)	17.59 (1.04)	18.33 (0.66)	17.37 (0.03)	17.63 (0.38)	17.63 (0.25)	17.73 (0.26)
TiO_2	0.61 (0.08)	0.48 (0.06)	0.59 (0.09)	0.50 (0.07)	0.58 (0.06)	0.47 (0.04)	0.57 (0.09)	0.54 (0.08)	0.52 (0.06)
Cr_2O_3	1.09 (0.11)	1.35 (0.24)	1.51 (0.21)	1.18 (0.12)	1.67 (0.12)	1.26 (0.09)	1.49 (0.46)	1.21 (0.13)	1.20 (0.12)
Total	99.32	99.84	100.06	99.70	98.95	99.79	99.31	100.13	100.26
Wo	45.81 (1.04)	44.34 (2.18)	43.85 (3.43)	45.57 (2.13)	42.92 (0.90)	44.23 (1.08)	44.98 (0.97)	44.90 (1.31)	45.54 (1.40)
Fs	3.98 (0.69)	4.69 (0.68)	3.94 (1.68)	3.91 (2.08)	3.55 (0.58)	5.78 (0.23)	3.86 (0.45)	4.55 (0.68)	3.76 (1.91)
En	50.22 (0.71)	50.97 (1.60)	52.21 (2.45)	50.52 (2.76)	53.52 (0.86)	49.98 (0.98)	51.16 (0.52)	50.54 (0.75)	50.70 (1.03)
N	33	30	32	30	22	3	4	32	31

[a] Wo = $Ca_2Si_2O_6$ in mole fraction.
[b] Fs = $Fe_2Si_2O_6$ in mole fraction.
[c] En = $Mg_2Si_2O_6$ in mole fraction.
[d] The clinopyroxenes analyzed in Lodran were found as inclusions within olivine and orthopyroxene large crystals.

Table 6.7 – Feldspar, troilite and kamacite-taenite (Fe-Ni alloy) compositions measured in this study (in wt%). 2-standard deviations are displayed in parentheses. N gives the number of measurements.

Feldspar									
	A 881902	Acapulco	Dhofar 125	Dhofar 1222	GRA 95209	Lodran	MET 01198	Monument Draw	NWA 725
Na_2O	9.50 (0.24)	9.52 (0.23)	9.79 (0.30)	9.44 (1.24)	10.12 (0.50)	-	9.91 (0.49)	9.74 (0.36)	9.67 (0.34)
Al_2O_3	22.07 (0.44)	22.06 (0.36)	22.01 (0.44)	21.06 (1.55)	22.34 (0.87)	-	22.32 (0.75)	21.87 (0.43)	21.50 (0.46)
SiO_2	63.73 (1.59)	64.39 (0.72)	64.48 (1.16)	64.97 (2.22)	64.00 (1.92)	-	64.40 (1.68)	64.29 (1.33)	65.09 (1.45)
K_2O	0.56 (0.13)	0.67 (0.14)	0.40 (0.11)	1.06 (0.30)	0.30 (0.12)	-	0.57 (0.12)	0.47 (0.15)	0.94 (0.25)
CaO	3.40 (0.20)	3.32 (0.23)	3.31 (0.14)	2.80 (1.03)	3.68 (0.85)	-	3.57 (0.22)	3.12 (0.27)	2.67 (0.17)
FeO	0.56 (0.67)	0.19 (0.32)	0.61 (1.17)	0.67 (1.96)	0.45 (1.47)	-	0.40 (1.11)	0.72 (1.33)	0.59 (0.95)
Total	99.82	100.15	100.60	100.00	100.90	-	101.17	100.20	100.45
Or[a]	3.15 (0.71)	3.73 (0.77)	2.19 (0.60)	5.98 (1.72)	1.60 (0.61)	-	3.06 (0.67)	2.61 (0.86)	5.24 (1.38)
An[b]	15.99 (0.89)	15.57 (1.11)	15.40 (0.62)	13.32 (5.69)	16.48 (3.84)	-	16.10 (0.92)	14.64 (1.22)	12.54 (0.65)
Ab[c]	80.86 (1.21)	80.71 (1.17)	82.41 (0.79)	80.70 (6.11)	81.92 (3.40)	-	80.84 (1.01)	82.75 (1.57)	82.22 (1.38)
N	37	35	32	32	40	-	41	29	32

Troilite									
	A 881902	Acapulco	Dhofar 125	Dhofar 1222	GRA 95209	Lodran	MET 01198	Monument Draw	NWA 725
S	36.74 (0.40)	36.74 (0.27)	36.52 (0.24)	36.51 (1.46)	n.m.	36.73 (0.31)	n.m.	36.75 (0.32)	36.88 (0.90)
Fe	64.36 (0.45)	62.81 (0.44)	64.09 (0.45)	64.09 (0.45)	n.m.	62.23 (0.49)	n.m.	62.85 (0.40)	62.24 (2.01)
Total	101.10	99.55	100.61	100.60	-	98.96	-	99.60	99.12
N	33	34	32	32	-	35	-	34	32

Fe-Ni alloy									
	A 881902	Acapulco	Dhofar 125	Dhofar 1222	GRA 95209	Lodran	MET 01198	Monument Draw	NWA 725
Fe	85.19 (15.72)	88.80 (4.36)	91.57 (3.75)	92.23 (0.42)	92.72 (1.27)	88.20 (24.01)	91.88 (1.04)	91.08 (5.00)	92.13 (0.38)
Ni	13.90 (15.90)	10.18 (4.54)	7.82 (3.83)	6.99 (0.13)	6.27 (0.43)	9.83 (17.86)	6.86 (0.22)	8.03 (4.99)	7.00 (0.13)
Total	99.09	98.98	99.39	99.22	98.99	98.03	98.74	99.11	99.13
Fe_{max}	93.37	92.87	92.93	93.03	94.85	92.49	93.20	93.35	93.03
Fe_{min}	69.84	76.91	70.77	91.37	91.94	80.93	90.89	84.32	91.44
Ni_{max}	29.01	25.1	29.16	7.27	6.50	17.90	7.12	14.32	7.26
Ni_{min}	6.51	5.38	6.85	6.68	5.21	7.00	6.54	6.33	6.7
N	33	34	33	33	35	35	37	31	35

[a] Or = $KAlSi_3O_8$ in mole fraction.
[b] An = $CaAl_2Si_2O_8$ in mole fraction.
[c] Or = $NaAlSi_3O_8$ in mole fraction.

Table 6.8 – Bulk composition (in wt.%) of the sections calculated from the modal and phases compositions.

	A 881902	Acapulco	Dhofar 125	Dhofar 1222	GRA 95209	Lodran	MET 01198	Monument Draw	NWA 725
Na_2O	0.76	0.88	0.82	0.69	1.06	<0.01	0.45	0.67	0.71
Al_2O_3	1.87	2.20	1.97	1.64	2.40	0.21	1.32	1.62	1.69
SiO_2	30.19	39.27	35.65	32.10	34.55	31.81	32.64	30.14	30.65
K_2O	0.04	0.06	0.03	0.07	0.03	-	0.03	0.03	0.07
CaO	0.86	1.27	1.28	1.17	2.20	0.39	0.64	1.17	0.97
MnO	0.25	0.42	0.32	0.29	0.30	0.37	0.34	0.29	0.28
FeO	3.81	6.26	4.28	2.89	3.63	7.59	4.57	4.42	2.78
MgO	19.48	26.16	24.52	18.92	22.46	27.01	23.30	20.57	18.41
TiO_2	0.07	0.09	0.08	0.07	0.10	0.08	0.10	0.07	0.07
Cr_2O_3	0.52	0.94	0.68	0.69	1.02	1.24	1.95	0.81	0.68
NiO	0.02	0.01	0.02	0.02	0.01	0.01	0.02	0.02	0.02
ZnO	< 0.01	0.01	0.03	< 0.01	0.03	0.02	0.03	0.01	< 0.01
V_2O_3	< 0.01	0.01	< 0.01	< 0.01	0.01	0.01	0.02	0.01	< 0.01
Fe	31.23	17.65	25.25	34.90	28.97	25.00	30.57	34.27	37.53
Ni	2.77	1.36	1.65	2.04	1.79	1.98	2.03	2.51	2.37
S	8.12	3.40	3.41	4.51	1.43	4.29	1.99	3.37	3.77

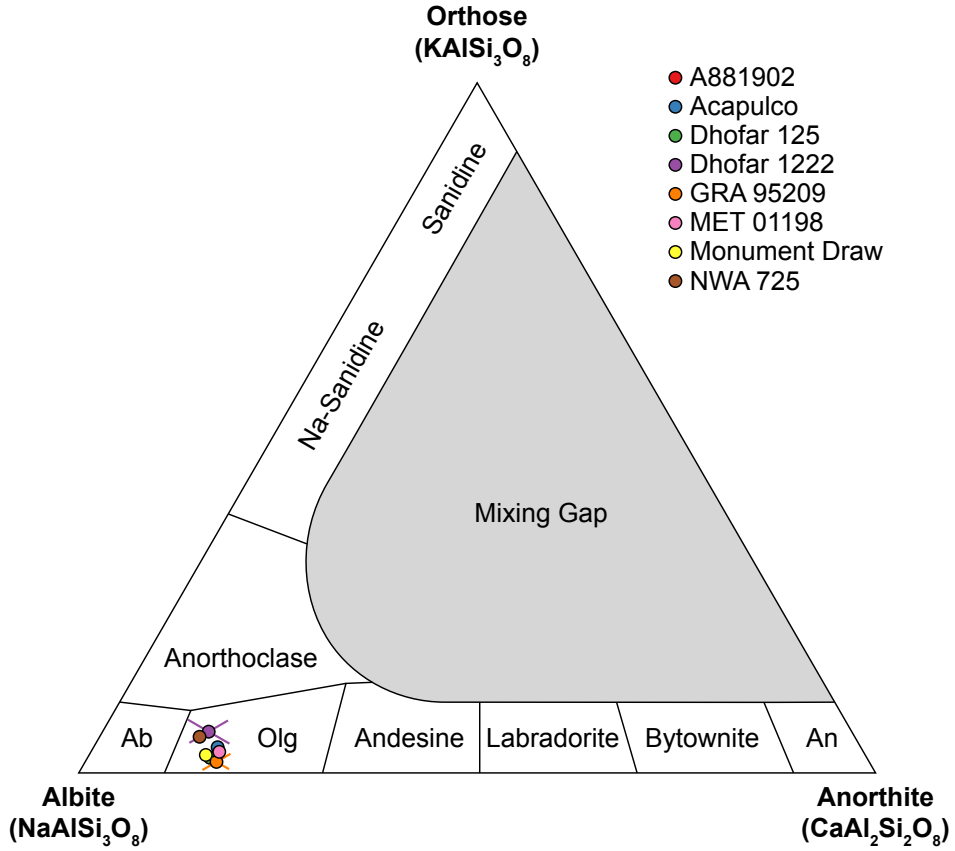

Figure 6.15 – Orthose ($KAlSi_3O_8$) - Anorthite ($CaAl_2Si_2O_8$) - Albite ($NaAlSi_3O_8$) ternary diagram with the mean compositions of feldspars reported. Error bars represent two standard deviation with respect to each pure endmember. Ab stands for Albite, Olg for Oligoclase and An for Anorthite.

6.4.2 Thermodynamic modeling

From the phase compositions, thermodynamics can be used as a tool to understand the conditions of the last equilibration between phases. Two thermometers (olivine-chromite and two-pyroxene) and two equilibria (quartz-iron-fayalite and quartz-iron-ferrosilite) are used, following the methodology of Benedix et al. (2005); Gardner-Vandy et al. (2012) and are described in the following.

6.4.2.1 Closure temperature

The closure temperature is the temperature at which the system no longer exchanges elements between phases. From a physical point of view, this temperature marks a the point in time when the diffusion coefficients of elements become so low that the system cannot evolve anymore over cooling time-scales. Chemical equilibrium has to be assumed to calculate these closure temperatures. Two closure temperatures were calculated, following the two-pyroxene and the olivine-chromite mineral thermometers. Results are displayed in Table 6.9.

The olivine-chromite closure temperature was determined from the MELTS olivine-spinel-orthopyroxene geothermometer-oxybarometer (Sack and Ghiorso, 1989, 1991, 1994a,b,c; Ghiorso and Sack, 1991). Input compositions are the mean ones measured with EPMA and input pressure is set to 1 bar, due to the low pressure in early-accreted small bodies (see Chapter 1). The closure temperature returned is based on Fe^{2+}/Mg exchanges between olivine and chromite. However, the result may be biased for the present samples, as it is difficult to have good analytical data on chromian spinels (M. Ghiorso, personnal communication). Lodran shows a Mg-Fe zoning in olivines. Thus closure temperature was calculated on contacting olivine - chromite pairs, with the care of measuring the composition along the grain boundary to ensure that local equilibrium is reached.

The two-pyroxene geothermometer was calibrated by Kretz (1982) based on transfer reactions between Ca-Mg-Fe in pyroxenes. This parametrization allows to determine the slope of the clinopyroxene solvus i.e. the temperature at which the clino- and orthopyroxenes become unmixed. The slope of the solvus surface follows (Kretz, 1982):

$$> 1353\,\mathrm{K}: \quad T = \frac{1000}{0.468 + 0.246 X^{\mathrm{Cpx}} - 0.123 \ln\left(1 - 2\,[\mathrm{Ca}]\right)} \tag{6.1}$$

$$< 1353\,\mathrm{K}: \quad T = \frac{1000}{0.054 + 0.608 X^{\mathrm{Cpx}} - 0.304 \ln\left(1 - 2\,[\mathrm{Ca}]\right)}\,, \tag{6.2}$$

where T is the temperature (in K), X^{Cpx} is the $Fe^{2+}/(Mg + Fe^{2+})$ ratio of clinopyroxenes (Cpx) and [Ca] the $Ca/(Ca + Mg + Fe^{2+})$ ratio of clinopyroxenes. The parameters X^{Cpx} and [Ca] are calculated from the compositions measured by EPMA (Table 6.6). Temperature is calculated with both equations, the one which falls into the right interval is then selected.

6.4.2.2 Oxygen fugacity

From the closure temperatures determined above, oxygen fugacity can be determined based on the FeO composition of olivine and pyroxene (Table 6.9). To do so, two equilibria can be used: QIFa (Quartz - Iron - Fayalite) and QIFs (Quartz - Iron - Ferrosilite) for which the relation between mineral composition and oxygen fugacity f_{O_2} are given by Gardner-Vandy et al. (2012):

$$2\,\mathrm{Fe} + \mathrm{SiO_2} + \mathrm{O_{2(g)}} = \mathrm{Fe_2SiO_4} \tag{6.3}$$

$$2\,\mathrm{SiO_2} + 2\,\mathrm{Fe} + \mathrm{O_{2(g)}} = \mathrm{Fe_2Si_2O_6}\,, \tag{6.4}$$

with Fe_2SiO_4 the fayalite and $Fe_2Si_2O_6$ the ferrosilite. The equilibrium constant K of each reaction links the closure temperature determined above to the oxygen fugacity:

$$\log K_{\mathrm{QIFa}} = \log\left(\frac{a_{\mathrm{Fa}}}{a_{\mathrm{Fe}}^2\, a_{\mathrm{SiO_2}}\, f_{\mathrm{O_2}}}\right) = \frac{29592}{T} - 7.61 \tag{6.5}$$

$$\log K_{\mathrm{QIFs}} = \log\left(\frac{a_{\mathrm{Fs}}}{a_{\mathrm{Fe}}^2\, a_{\mathrm{SiO_2}}^2\, f_{\mathrm{O_2}}}\right) = \frac{29634}{T} - 7.60\,, \tag{6.6}$$

with a the activity coefficients of the different phases. The previous equations are valid within the temperature interval $773\,\mathrm{K} \leq T \leq 1373\,\mathrm{K}$.

Activity coefficients of fayalite a_{Fa} and ferrosilite a_{Fs} were calculated using the MELTS supplemental calculator (Ghiorso and Sack, 1995) from the measured compositions (FeO - MgO - CaO - SiO_2). Similarly to Benedix et al. (2005) and based on the experimental work of Larimer (1968), the activity coefficient of quartz a_{SiO_2} was set to 0.9. Finally, the activity coefficient of iron a_{Fe} is determined from the mean Fe-Ni composition of kamacite-taenite crystals and assuming an ideal solid solution.

6.4.2.3 Results

Results of the calculated closure temperatures are shown in Table 6.9. Two-pyroxene closure temperatures range from 1175.6 (for A 881902) to 1381.7 K (for GRA 95209). Overall, lodranites have higher closure temperatures ($\approx$ 1300 K) but are in the range of acapulcoites (1175 to 1350 K). Based on precision and accuracy errors on the parametrization of Kretz (1982) and on compositional variability in the ortho- and clinopyroxenes of the sections (Table 6.6), uncertaintes on these closure temperatures are estimated to be around $\approx$ 100 K. These values are in the range of the closure temperatures calculated by Zipfel et al. (1995) for Acapulco (1263 $\pm$ 30 K). In turn, olivine-chromite closure temperatures range from 677.7 (for GRA 95209) to 1230.8 K (for Lodran). This geothermometer is particularly affected by small changes in olivine and chromite compositions, which may explain the discrepancy within Lodran mineral pairs and the extremely low temperature calculated for GRA 95209.

In turn, oxygen fugacities were calculated from equations 6.5 and 6.6, using the closure temperatures determined above and the activity of each component calculated from the composition of the phases. Calculated values are expressed as a function of the deviation from the Iron-Wustite (Fe-FeO, noted as IW) buffer in log units. Temperature - f_{O_2} relation along the IW buffer was taken from O'Neill and Pownceby (1993). QIFs oxygen fugacity values range from ΔIW = -2.0 to ΔIW = -2.6 and QIFa f_{O_2} range from ΔIW = -1.9 to ΔIW = -3.0, indicating small variations. These values are in agreement with the igneous processes commonly assumed for these objects. Indeed, acapulcoites and lodranites are thought to have experienced maximum temperatures of 1373 and 1473 K respectively (Bild and Wasson, 1976; Palme et al., 1981; McCoy et al., 1996). Hence, closure temperatures obtained are expected to be lower than these values. The oxygen fugacities indicate a slightly more reduced material than H ordinary chondrites (ΔIW = -1 Brett and Sato, 1984) but are in the range of those obtained for winonaites and silicate-bearing IAB irons (ΔIW from -2.3 to -3.2 Benedix et al., 2005)

6.5 Formation conditions of primitive achondrites

All data acquired in this study provide information on different steps of evolution of these meteorites. The wetting textures of certain phases indicate that at least some partial melting occurred. This feature is enhanced by the presence of large patches of feldspar and clinopyroxene that may enclose refractory minerals (e.g. olivine and orthopyroxene). In turn, iron-rich phases also show wetting textures, which is unlikely to be at equilibrium given the interfacial energy balance of this system (Chapters 3 and 4). The depletion or enrichment in

Table 6.9 – Closure temperature and oxygen fugacity ($\log(fO_2)$) calculated for different thermodynamic equilibria. Values calculated for each olivine-chromite (Ol-Chr) mineral pair in Lodran are displayed. ΔIW corresponds to the distance to the Iron-Wustite buffer, in log units. QIFs and QIFa stand for Quartz-Iron-Ferrosilite (equilibrium 6.4) and Quartz-Iron-Fayalite (equilibrium 6.3 respectively. ΔT indicates the temperature difference between the two-pyroxene and the olivine-chromite geothermometers.

	Two-Pyroxene[a] Temperature (K)	QIFs[b] $\log(fO_2)$	ΔIW	Olivine-Chromite[c] Temperature (K)	QIFa[b] $\log(fO_2)$	ΔIW
A 881902	1175.7	−19.0	−2.3	999.4	−23.1	−2.3
Acapulco	1302.5	−16.6	−2.2	1095.6	−20.4	−2.0
Dhofar 125	1363.4	−15.7	−2.3	918.8	−25.6	−2.4
Dhofar 1222	1198.3	−18.8	−2.6	950.8	−24.8	−2.6
GRA 95209	1381.7	−15.5	−2.3	677.7	−36.9	−3.0
Lodran (Ol-Chr 1)	1292.1	−16.5	−2.0	1230.8	−17.5	−1.9
Lodran (Ol-Chr 2)	1292.1	−16.5	−2.0	1115.9	−20.1	−2.1
Lodran (Ol-Chr 3)	1292.1	−16.5	−2.0	1139.6	−19.5	−2.0
Lodran (Ol-Chr 4)	1292.1	−16.5	−2.0	958.4	−24.5	−2.5
Lodran (Ol-Chr 5)	1292.1	−16.5	−2.0	1012.1	−22.8	−2.4
Lodran (Ol-Chr 6)	1292.1	−16.5	−2.0	1012.6	−22.8	−2.3
Lodran (Ol-Chr 7)	1292.1	−16.5	−2.0	1069.6	−21.2	−2.2
Lodran (Ol-Chr 8)	1292.1	−16.5	−2.0	1114.3	−20.1	−2.1
Lodran (mean)	1292.1	−16.5	−2.0	1081.7	−21.1	−2.2
MET 01198	1351.1	−15.9	−2.2	1050.0	−21.7	−2.2
Monument Draw	1252.2	−17.4	−2.2	1021.0	−22.4	−2.2
NWA 725	1203.5	−18.6	−2.5	942.4	−25.1	−2.6

some low-melting temperature phases (e.g. feldspar, clinopyroxene or troilite) and elements carried by these phases (e.g. Na, K, Ca and Al) also argue in favor of partial melting of the precursor material, but also indicates a migration of these phases. The composition of the compounds lost or accumulated may be indicative of the melting temperature. However, one should keep in mind that a given region does not simply lose a phase through a percolative network, it may also receive melts from the surrounding areas. Grain sizes may also be a strong indicator of peak temperatures and time spent at high temperature provided that the distributions are not perturbed by deformation processes. Finally, the closure temperature of some geothermometers and oxygen fugacities indicate the conditions recorded during the cooling of the parent body. These different points are detailed in the following.

6.5.1 Cooling history of acapulcoites and lodranites on the basis of thermodynamics and textures

6.5.1.1 Interpretation of olivine-chromite closure temperature

Within each sample, the two-pyroxene geothermometer indicates greater closure temperatures than the olivine one. This feature is relevant given that the Ca-transfer between pyroxenes should close at higher temperatures than the Fe-Mg exchange between olivine and chromite. GRA 95209 distinguishes itself from the other samples as it displays the lowest olivine-chromite closure temperature (677.7 K) with a huge gap of ≈ 250 K between the rest of the other samples. At the scale of the section, FeO - MgO compositions in olivine are homogeneous with 2SD on the order of 1 wt% (Table 6.5). However, chromite grains are scarce, extremely small and show compositions that largely deviates from the other samples (Table 6.5) with large variations in the Cr_2O_3 - Al_2O_3 and FeO - MgO compositions with

respect to other samples. These features most likely result in this huge gap from the rest of the samples.

Samples with similar textural features are expected to have undergone similar thermal histories. Hence, the temperature difference between the two geothermometers ΔT could be expected to be identical between the different samples. Results in Table 6.9 indicate that they are not; among the different sections, values of ΔT range from $\approx$ 60 K for Lodran (olivine-chromite mineral pair 1) to $\approx$ 700 K for GRA 95209. Besides, at the scale of a single sample, there can also be large variations. For instance, Lodran shows ΔT varying from $\approx$ 60 K to $\approx$ 330 K. Following a similar line of idea than Benedix et al. (2005), the non-correlation between the two-pyroxene and the olivine-chromite thermometers may be explained in two different ways. The first one is that these different meteorites do not originate from the same parent body but sample similar reservoir (due to their similar oxygen isotopic compositions Greenwood et al., 2017), while the second is that heating and / or cooling was localized, explaining the discrepancy between the different samples. The winonaites Dhofar 1222 and NWA 725 originate from a different parent body than the acapulcoites and lodranites due to their different oxygen isotopes signature (Greenwood et al., 2012). This feature is relevant with their lower closure temperatures and oxygen fugacities (in term of deviation from the IW buffer) from the other acapulcoites-lodranites. Textural arguments (e.g. silicate grain sizes, presence of relict chondrules and alteration) also point toward materials that are extremely similar. Both samples seem then to have undergone similar thermal evolutions. Regarding acapulcoites and lodranites, it is not possible to argue in favor of a given scenario or another.

Noteworthy, the olivine-chromite geothermometer is highly sensitive to the FeO-MgO content of the olivine, which may cause these large variations of ΔT. Large discrepancies exist in term of oxides composition within the samples of this survey. Indeed, the FeO content of the olivine varies from $\approx$ 12 wt% for Lodran to $\approx$ 6 wt% for the winonaites. At the scale of a single sample, e.g. in the contacting olivine pairs of Lodran, variations in the FeO content are on the same order of magnitude. Hence, this high sensitivity of the olivine-chromite geothermometer makes the exploitation of the ΔT inconclusive between the different scenarios. Isotopic data would be required to determine if these samples originate from a single parent body which is affected by small-scale heterogeneities or if they originate from different parent bodies.

Calculated oxygen fugacities also show some discrepancies but on a much smaller scale. Here the variation amplitude of ΔIW is only of half an order of magnitude for the QIFs equilibrium, while it is of one order of magnitude for the QIFa one. These differences are likely to be explained by the wider range of variation obtained for the olivine-chromite closure temperatures. Once again, GRA 95209 distinguishes itself with a high ΔIW value of -3.0 log units. The gap between this oxygen fugacity and the rest of the population is most likely explained by its extremely low olivine-chromite temperature. Within Lodran, distances to the IW buffer also vary by half an order of magnitude and may be explained by the large differences in the olivine-chromite closure temperatures.

6.5.1.2 Closure temperature - oxygen fugacity relation

Figure 6.16 shows the evolution of the deviation to the IW buffer as a function of the closure temperature calculated for the two geothermometers. Overall, for each sample, the oxygen fugacities determined with the two equilibria are extremely close (less than 0.2 log units), except for GRA 95209 and Lodran (more than 0.5 log units). This feature on GRA 95209 can be explained by the chromite composition that largely differs from the other sections. If the olivine-chromite closure temperature would have been found at 950 K (similar to other acapulcoites), the oxygen fugacity would have been found at $\Delta IW = -2.5$, much closer to the value obtained pyroxene equilibrium. The case of Lodran is more complicated. Bild and Wasson (1976) proposed that the FeO-MgO zoning in olivines have been caused by a late reducing event. As pyroxenes have Fe-Mg interdiffusion coefficients that are much lower than in olivine, the QIFs equilibrium would have recorded the conditions before reduction, while the QIFa one would have recorded the conditions after the event. Due to this difference in Fe - Mg interdiffusion coefficients between olivine and pyroxenes, the QIFs equilibrium closes at higher temperatures than the QIFa. However, there is a large spread within the values given by the QIFa equilibrium, which may be due to different olivine grain sizes: they were not all affected in the same manner by the reduction event.

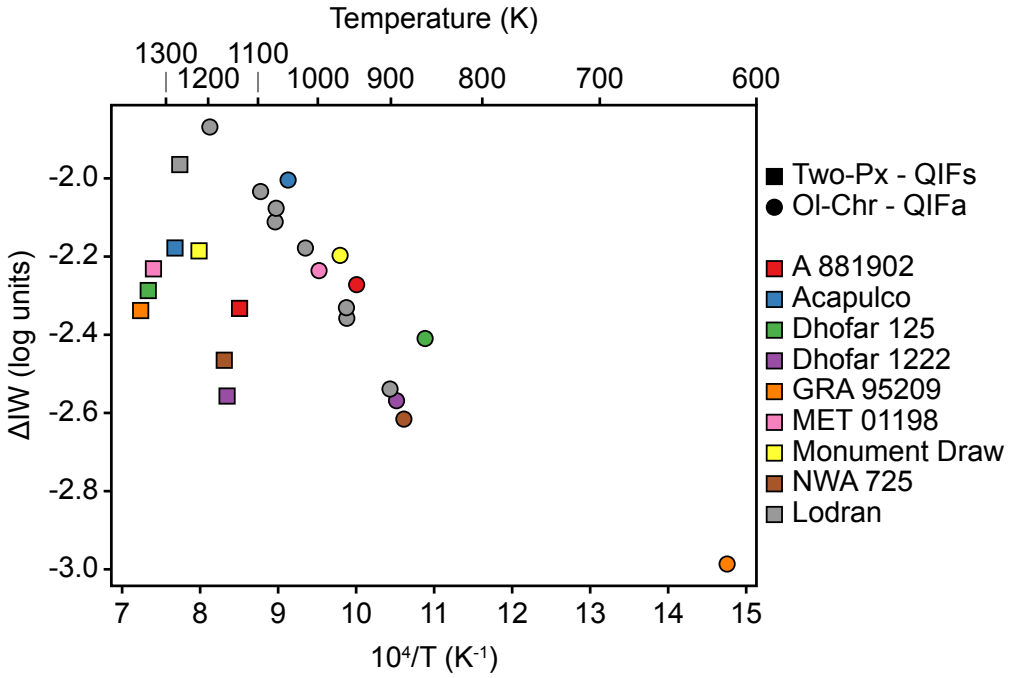

Figure 6.16 – Oxygen fugacity (expressed as deviation from the IW buffer in log units) as a function of the closure temperature calculated. Squares correspond to the pyroxene equilibrium while circles correspond to the olivine equilibrium.

The oxygen fugacities as a function of closure temperatures show that values determined for the olivine-chromite geothermometer and the QIFa oxymeter seem to be aligned, while that for pyroxenes do not seem correlated. The study of Benedix et al. (2005) shows similar features for winonaites and silicate inclusions in IAB irons, for both geothermometers an oxybarometers, and invoked that these samples followed an unknown buffer with a different

slope than that of IW. Such evolution along a similar buffer may be an argument in favor of a common parent body for the acapulcoites and lodranites of this study.

Closure temperatures should not be considered as peak temperatures, they provide information on temperatures experienced during the cooling. For most samples, two-pyroxene closure temperatures are higher or close to the eutectics of both silicate and iron-sulfur subsystems, which is consistent with a low degree of partial melting.

6.5.2 Grain sizes in the framework of silicate melt extraction

6.5.2.1 Comparison with literature data

Grain sizes found here are significantly lower than what is usually reported in the literature. Indeed, typical values of silicate grain sizes for acapulcoites are on the order of 150-230 µm (Palme et al., 1981; Keil and McCoy, 2018), while here they span a range from 60 to 110 µm. In turn, literature data report silicate grain sizes in lodranites on the order of 500-700 µm (Bild and Wasson, 1976; Keil and McCoy, 2018), but they are found here to be on the order of 120-320 µm. These differences may rise from the different techniques used to determine the grain sizes, however such a huge discrepancy remains odd.

6.5.2.2 Grain sizes as a sensor for igneous processes

The meteorite sections of this study do not show any signs of deformation, making grain sizes a good marker of igneous processes that may have occurred. Mean grain sizes (Table 6.4) define five different populations of meteorites: (1) Lodran ($d_{mean} \approx 220$ µm), (2) GRA 95209 ($d_{mean} \approx 120$ µm) (3) Acapulco, Dhofar 125 and MET 01198 ($d_{mean} \approx 90 - 100$ µm) and (4) A 881902 and Monument Draw ($d_{mean} \approx 60$ µm) (5) Dhofar 1222 and NWA 725 ($d_{mean} \approx 55$ µm). Lodran is obviously one end-member as it is a lodranite, it should have experience higher temperatures, enhancing grain growth. However, GRA 95209 is also classified as a lodranite but is found to have grain sizes similar to some acapulcoites (Acapulco and MET 01198). In detail, GRA 95209 can be classified as a transitional acapulcoite following the refined classification of Patzer et al. (2004). This category is defined by a loss of iron-sulfur melt and a small loss of silicate melt, with textures that are then less evolved than lodranites. MET 01198 could also be classified as a transitional acapulcoite as this section shows textures with relatively more kamacite-taenite than troilite and the formation of large patches of feldspar which may indicate mobility of silicate melt. But the enrichment in these phases is not as significant as for GRA 95209, thus MET 01198 is not likely to be classified as a transitional acapulcoite. However, Acapulco and Dhofar 125 differ from these sections, as they do not show evidence for the loss of a sulfur-rich or a silicate melt. Nevertheless, the formation of large patches of clinopyroxenes and feldspars in both meteorites may also indicate the onset of silicate melt mobility. These sections would then match the typical acapulcoites as defined by Patzer et al. (2004). Meteorites with lower grain sizes, show less evolved textures, which would correspond to a primitive acapulcoite state (Patzer et al., 2004), i.e. a material that barely lost its chondritic texture and may still host relict chondrules. A 881902 and

Monument show evidence for a sulfur-rich metallic melt mobilization, which is expressed by an increase in troilite and kamacite-taenite proportions. A more refined way to classify them would be to define a more evolved sulfur-enriched primitive acapulcoite class. On the basis of textural arguments, the winonaites Dhofar 1222 and NWA 725 are similar to the primitive acapulcoite category. However the textural definition of this class indicates a material that would extremely similar to thermally metamorphosed H chondrites, indicating a continuum between chondrites and more evolved partially differentiated primitive achondrites.

Bimodal populations observed for the silicates on the d / d_{mean} distributions (Figure 6.11) of GRA 95209, Lodran and MET 01198 can be explained by partial melting and subsequent recrystallization. Indeed, these sections are among the most evolved. However, this feature on the section of MET 01198 may be biased due to its small surface area and poor statistics. Lodran and GRA 95209 should display a significant melting of their silicate and metallic subsystems. Textural arguments indicate that these two sections underwent silicate melt mobilization that went to its extraction (Lodran) or not (GRA 95209); the iron-sulfide subsystem is also affected (e.g. GRA 95209). The bimodal distributions of the silicates indicate that there are two populations of grains that did not evolve in similar conditions. If a silicate melt was present and crystallized, it is likely that it formed small grains which may not have been able to grow any further due to the cooling of the material. This effect may have been enhanced by the presence of the silicate melt itself. Indeed, in the presence of silicate melt, the silicate solid residues have grain growth rates that are drastically increased (e.g. Faul and Scott, 2006). Kamacite-taenite also show distributions that do not follow unimodal log-normal shapes. This can be due to alteration processes that affected metallic grains and left only the core as a pure FeNi phase (e.g. in the case of NWA 725) or the melting and migration of a sulfur-rich melt altered the grain size distribution (e.g. Lodran). In any cases, comparison between textural properties and grain size distributions allow to highlight igneous or alteration processes.

6.5.2.3 Timescales for grain growth

Normal grain growth is a thermally activated process that is commonly described by:

$$d^n - d_0^n = k_0 \exp\left(-\frac{Q}{RT}\right) t\,, \tag{6.7}$$

with d the mean grain size (in µm) at a given time t (in s), d_0 the initial grain size (in µm, taken as 1 µm in the remainder), n the grain growth exponent, k_0 an integration constant, Q the activation energy (in J.mol^{-1}), R the ideal gas constant (in J.mol^{-1}.K^{-1}) and T the temperature (in K).

Due to the exponential dependence on temperature, this law indicates that once temperature decreases, further grain growth will be negligible in comparison to the grain sizes reached during the peak temperature. Hence, most likely, grain sizes recorded a mixture of peak temperature and time spent at this peak, allowing to compare the grain sizes of this study to thermal evolution models of the acapulcoites and lodranites parent-body (e.g. Golabek et al., 2014; Neumann et al., 2018). Closure temperatures determined earlier (Table 6.9) likely underestimate the peak temperatures experienced by the samples, a different estimate is given

from the textural observations in Table 6.10 and is used to calculate the timescales for grain growth. Noteworthy, as this equation considers a constant temperature, the heating before this plateau is neglected. Models show that grains grow during this temperature increase (e.g. Guignard et al., 2016), thus the time necessary for grain growth may be overestimated.

Table 6.10 – Peak temperature estimates from the analysis of textures.

	Peak temperature (K)	Reason
A 881902	1323	Small grain sizes and possible evidence silicate partial melting
Acapulco	1373	Wetting textures of clinopyroxene and feldspar
Dhofar 125	1373	Wetting textures of clinopyroxene and feldspar
Dhofar 1222	1261	Small grain sizes and relict chondrules
GRA 95209	1423	Evidence for mobilization of clinopyroxene and feldspar
Lodran	1473	Complete melting and loss of clinopyroxene and feldspar
MET 01198	1373	Wetting textures of clinopyroxene and feldspar
Monument Draw	1323	Small grain sizes and possible evidence silicate partial melting
NWA 725	1261	Small grain sizes and relict chondrules

Silicates and metal are likely to have grown under the same conditions in these samples. Hence the time necessary for grain growth should be similar for both phases, i.e. the time necessary to reach the measured grain size of olivine as a function of that required for kamacite-taenite grains should fall on a 1:1 line. Such plot is shown on Figure 6.17 for the the different sections. Peak temperature were taken from Table 6.10 and an initial grain size of 1 µm was assumed. Different grain growth laws are used depending on the textural characteristics of the sections. Indeed, A 881902, Dhofar 1222, Monument Draw and NWA 725 show no evidence for silicate partial melting, thus the grain growth laws of Guignard et al. (2012, 2016) in a dry system were used for both olivine and kamacite-taenite. These laws correspond to Zener pinning grain growth mechanisms, i.e. hindered growth rates due to simultaneous grain growth in a polyphased aggregate. Such effects depend on the relative phase proportions, which are taken from Table 6.3. In turn, other sections show evidence for partial melting, hence the grain growth laws in presence of a silicate of Guignard (2011) and Guignard et al. (in prep.) were used.

Results indicate that the poorly evolved sections of primitive acapulcoites (A 881902 and Monument Draw) and winonaites (Dhofar 1222 and NWA 725) have grain sizes that are relevant with a dry grain growth mechanism, as both calculated time for grain growth are similar and on the order of $\approx 10^7$ Myr. However, it is not excluded that A 881902 and Monument Draw may have experienced low degree of silicate partial melting. In this case, results are not relevant for A 881902 and Monument Draw, and the more evolved sections of Acapulco, Dhofar 125, GRA 95209, Lodran, MET 01198 as the grain growth laws indicate a much shorter time to reach the olivine grain sizes than to reach that of kamacite-taenite, by about 2 orders of magnitude. The growth rate for olivine seems to be overestimated in comparison to that for kamacite-taenite rather than the opposite. Indeed, an exposure to the peak temperature of only 10^3 to 10^4 yr seem to be too short by contrast to a typical cooling thermal history. Shocks would have to be invoked to justify such short timescales, but the phases do not show evidence for such processes. Besides, metal is most likely a follow-up phase with its own grain growth mechanism (Guignard et al., 2012, 2016). Hence, Zener pinning between the different silicate phases likely occurred to hinder their grain growth. Experiments

of coupled grain growth between different silicate phases (e.g. forsterite - enstatite or forsterite - diopside) show that for the same run duration, final grain sizes can vary within ten orders of magnitude depending on the relative proportions of each phase (Ohuchi and Nakamura, 2007; Hiraga et al., 2010; Tasaka and Hiraga, 2013). Although silicate melt is present, Zener pinning remains the most likely grain growth mechanism for silicates, as in Al-rich silicate melts, grain growth occurs by grain boundary migration and thus depends on the relative proportions of the different phases (Guignard, 2011, Guignard et al. in prep.). Zener pinning is a thermally activated process, thus extrapolation of this process to low temperatures is quite uncertain (Ohuchi and Nakamura, 2007; Hiraga et al., 2010; Tasaka and Hiraga, 2013). It is likely not activated for the winonaites nor for the S-enriched primitive acapulcoites, making the consideration of a simplified silicate system valid. Such mechanism would then increase the time for olivine to reach its measured grain size, yielding values of about 10^5 to 10^6 yr which seem more relevant with a thermal history. This exercise shows that simplified systems fail to model the grain growth of different phases at relatively high temperature ($\geq$ 1373 K). Additional experimental work on three-phase systems would be required to understand the exact dynamics of grain growth in systems close to natural samples undergoing differentiation, and to determine the exact contribution of each different mechanisms.

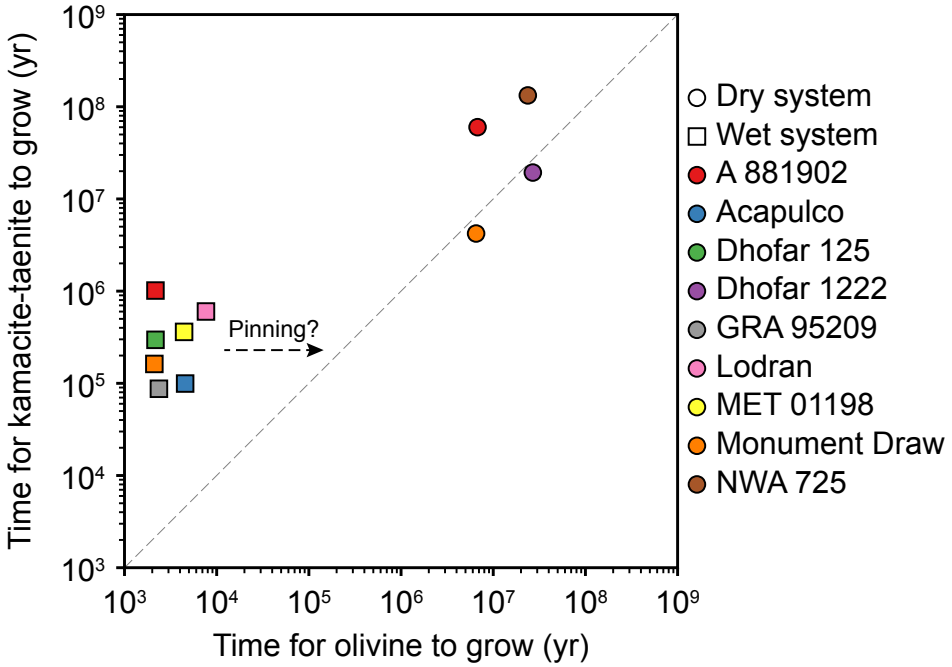

Figure 6.17 – Plot showing the time necessary to reach the measured grain sizes of olivine as a function of that required for kamacite-taenite grains for the different sections. Circles indicate grain growth laws of Guignard et al. (2012, 2016) in a dry system. Squares indicate grain growth laws of Guignard (2011) in a system bearing silicate melt. The colors correspond to the different sections of this survey. The dashed grey line has a slope of one. If metal and silicate grew in similar conditions, which is likely to be the case, natural samples should fall on this line. Deviation to this line seem to indicate Zener pinning growth mechanisms.

Winonaites that do not show signs of silicate partial melting require $\approx$ 10 Myr to reach the measured grain sizes. In this case these samples are likely buried deep inside their parent body in order to have such large exposure times at their peak temperatures. It is not clear on the basis of textural arguments whether the sections of A 881902 and Monument Draw

experienced partial melting or not. Considering one case or another, the time required to grow olivine and kamacite-taenite vary drastically, from values similar to the winonaites to 0.1-1 Myr. These samples may then originate from different parent bodies. Indeed, as for the winonaites, such large times at high temperature are rather indicative of a deep origin. On the contrary, if the samples experienced silicate partial melting, then they rather come from a shallow depth of their parent body. Similarly, the other sections of acapulcoites and lodranites may sample the innermost region of their parent body. Such shallow origin due to the presence of silicate melt is compatible with the differentiation models of Golabek et al. (2014) and Neumann et al. (2018).

6.5.2.4 Mobility of silicate and iron-sulfide melts

The question is then, what are the timescales required to extract the silicate and iron-sulfide melts and freeze the grain sizes. Following the theoretical formalism shown in section 1.4.2.2, it is possible to constrain the timescale of extraction of a melt from the knowledge of grain sizes, radius of the body and viscosities of both the silicate matrix and the melt (either silicate or iron-sulfide) and to compare this time with the cooling timescale. Using the results of the numerical simulations of Golabek et al. (2014) and Neumann et al. (2018), the radius of the planetesimal was considered to range between 60 and 260 km. Then, following the grain sizes measured in this study and those reported in literature, the timescale of melt migration can be determined. It is of note that the calculation of the migration timescale assumes the formation of an interconnected network and does not consider surface tensions.

Figure 6.18 shows that for the winonaites Dhofar 1222 and NWA 725, and the acapulcoites A 881902 and Monument Draw, the silicate melt has a migration timescale on the order of 100 Myr, which is much larger than the time spent above the silicate solidus as shown by mean grain sizes. However, if there were an iron-sulfide melt, it may have been able to migrate over small timescales (0.1 to 1 Myr), provided that it formed an interconnected network. This may have been the case for A 881902 and Monument Draw which show a mobilization of the iron-sulfur phases while the silicates have small grain sizes. Most acapulcoites of this study also show long silicate melt migration timescales $\approx$ 10 Myr, which is much larger than the time spent above the silicate eutectic temperature (e.g. Neumann et al., 2018). Here also, a mobilization of the metallic phases is likely, as the migration timescales of iron-sulfide melts are lower than 1 Myr, explaining the discrepancy in the troilite to metallic phases ratio of acapulcoites. Increasing grain sizes from $\approx$ 100 µm does not change the migration timescale of metallic phases, it remains lower than 1 Myr. Indeed, the migration mechanism is mostly driven by the matrix compaction and does not depend on grain size anymore. Hence, if the iron-sulfur metallic melt is able to form an interconnected network, its extraction is unavoidable. Larger grain sizes still affect the timescale for silicate melt migration. In the case of Lodran (this study) or grain sizes reported in the literature for acapulcoites ($\approx$ 220 µm), silicate melt migration timescales are slightly lower than 10 Myr. Hence, partial silicate melt migration can be expected. Mean grain sizes on the order of 500 µm, as reported for Lodran in the literature, show a very efficient silicate melt migration, on timescales of $\approx$ 1 Myr. In this case, both silicate and iron-sulfur melts are expected to segregate, leaving a refractory residue, which is likely to match the mineralogy of Lodran. This efficient melt removal also argues in favor of a freezing of the silicate grain sizes.

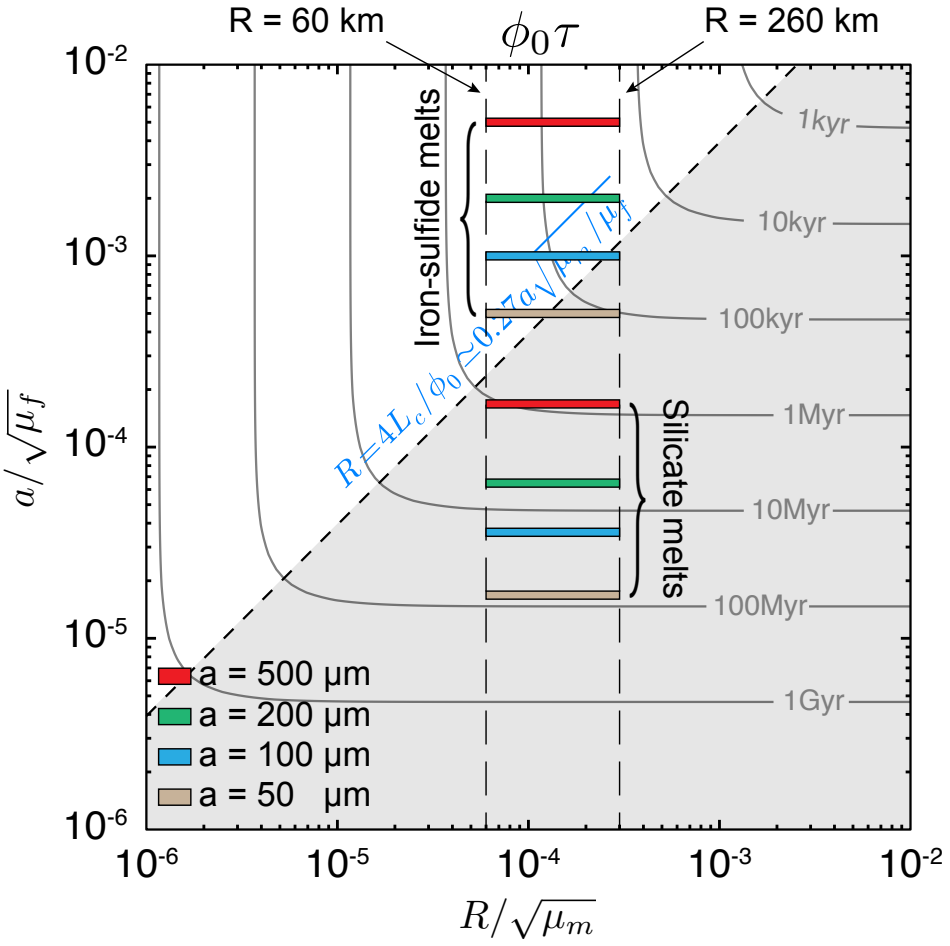

Figure 6.18 – Timescale of melt migration as a function of the $a/\sqrt{\mu_f}$ and $R/\sqrt{\mu_m}$ ratios, which correspond to the Darcy and the compaction timescales respectively. Acapculoite-lodranite parent body is thought to have a radius ranging from 60 (Golabek et al., 2014) to 260 km (Neumann et al., 2018). The different grain sizes determined in the acapulcoite-lodranite-winonaite samples of this study are represented. 50 µ corresponds to the mean winonaites and the A 881902 and Monument Draw acapulcoites. 100 µm corresponds to the mean grain size of most acapulcoites and GRA 95209. 200 µm corresponds to the mean grain size of Lodran or to that of acapulcoites reported in literature (e.g. Keil and McCoy, 2018, and references therein). Finally, 500 µm corresponds to the mean grain size of lodranites as reported by Keil and McCoy (2018, and references therein). Viscosity of the silicate melt is taken to be 10 Pa.s (Dingwell et al., 2004), while that of the silicate matrix is 10^{18} Pa.s (Hirth and Kohlstedt, 2003). Viscosity of iron-sulfur melts is taken to 10^{-2} Pa.s (Dobson et al., 2000).

6.5.3 Reassessment of the winonaite - acapulcoite - lodranite classification

Based on modal compositions of the different sections, grain sizes and textural arguments, a reassessment of winonaite - acapulcoite - lodranite classification can be proposed (Figure 6.19), emphasizing the igneous processes undergone by the different categories. Winonaites are the least evolved samples of this survey. Textures of Dhofar 1222 and Monument Draw indicate that the Fe-FeS eutectic temperature may have been reached in these samples but not that of the silicates. The long time required to grow silicate and metallic phases (≈ 10 Myr) at low temperature (≈ 1261 K) in a dry system most likely indicates a deep origin of these

samples (Figure 6.19a). Due to the high mobility of metallic melts, the winonaite forming region is likely to surround a sulfur-depleted region once the Fe-FeS eutectic temperature is exceeded. This would require the existence of a deeper sulfur-enriched region, which stored to sulfur-rich metallic melts from the above regions. A sulfur-rich metallic core may also exist at the center of such body, as suggested by the model of Zeng et al. (2019). If A 881902 and Monument did not reach the silicate eutectic temperature, these samples may be originated from the sulfur-enriched region of a similar but different planetesimal. The low temperatures of this model indicate that the thermal history is quite similar to that of the H chondrites, indicating a late accretion and a small radius (2 Myr after CAIs and no larger than 130 km, Monnereau et al., 2013). Due to the low temperature of the inner parts of this material, a significant chondritic crust is expected. The classification of winonaites as primitive achondrites is odd as this material is not so different from a chondritic one due to the presence of relict chondrules. Indeed, H-type chondrites and mostly H6 and H7 types have similar textures and grain sizes (Tait et al., 2014; Guignard and Toplis, 2015) to winonaites. This category should then be considered as a thermally metamorphosed chondrite.

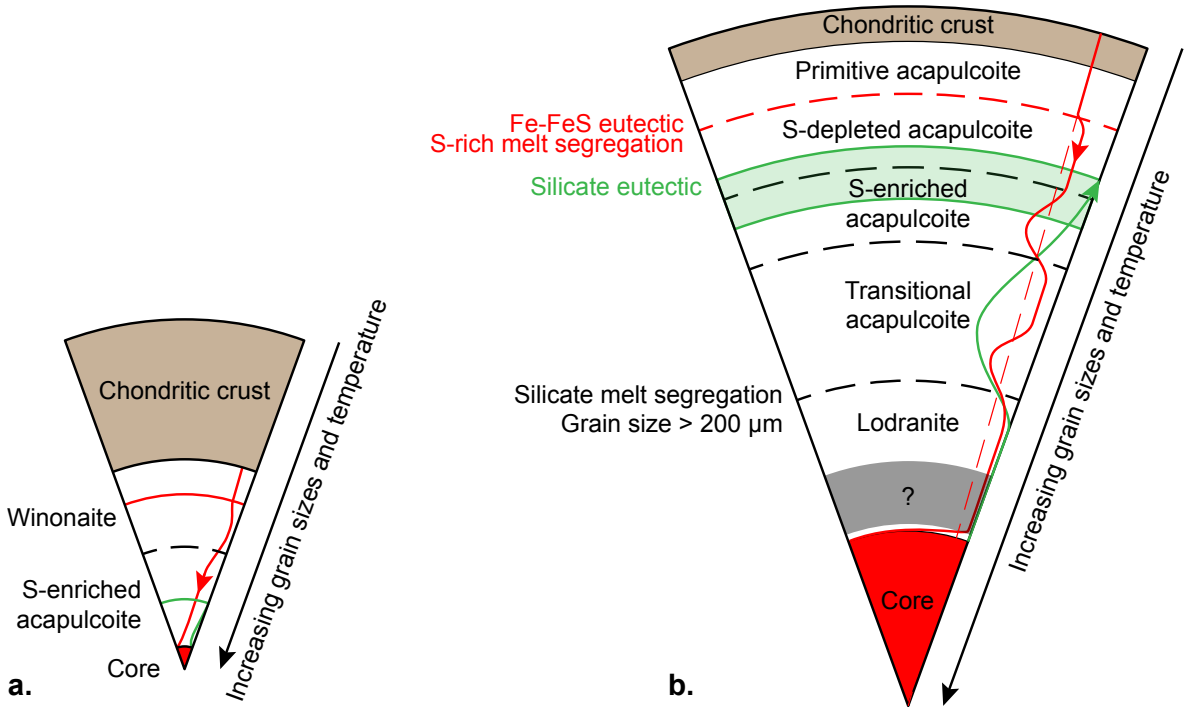

Figure 6.19 – Scheme showing the evolution of a parent body to form winonaites, acapulcoites and lodranites, based on the textural arguments described in this Chapter. Dashed lines correspond to boundaries between the different categories of primitive achondrites. The red line indicates the Fe-FeS eutectic; due to the low viscosity of metallic melts, they are expected to migrate over short timescales provided that they form an interconnected network. The green line indicates the silicate eutectic; efficient segregation of the silicate melts is not possible until large grain sizes are reached ($\approx$ 200 µm). Red and green arrows indicate the absolute proportions and the migration of sulfur-rich and silicate melts, respectively. (a.) Scenario giving a deep origin of winonaites and possibly sulfur-enriched acapulcoites. For the sake of simplicity, both categories were represented on the same parent body, but they are not due to their different oxygen isotopic composition (Greenwood et al., 2012, 2017) and their different oxygen fugacities (Table 6.9). (b.) Scenario giving a shallow origin of acapulcoites, similarly to the models of Golabek et al. (2014) and Neumann et al. (2018). The grey shaded area indicates part of the body which may be more evolved than lodranites, its thickness is likely to be large following the model of Neumann et al. (2018).Schemes are not to scale.

If A 881902 and Monument Draw experienced partial silicate melting, then the time spent at their peak temperature most likely indicates a shallow origin (Figure 6.19b). In such scenario, the temperature gradient due to a conductive profile indicates the presence of a chondritic outer crust. This idea is emphasized by the recent reassessment of the poorly metamorphosed H4 chondrite GRV 020043 to the acapulcoite clan based on textural and compositional arguments (McCoy et al., 2019). The sulfur-enriched nature of A 881902 and Monument Draw is indicative of a sulfur-depleted region overlying the sulfur-enriched area from which these samples originate. Such S-depleted region is not sampled in the present study. Based on textural arguments, it is not possible to determine the exact position of the silicate eutectic temperature. Hence, it could be place in the S-depleted or S-enriched regions (green shaded area, Figure 6.19). The other acapulcoites (Acapulco, Dhofar 125, MET 01198) show evidence for partial melting and a possible enrichment in sulfur. These samples seem to sample a deeper part of the S-enriched reservoir, explaining a higher peak temperature and the larger grain sizes. However, grain sizes remain low enough to allow an inefficient silicate melt migration, allowing the formation of patches of clinopyroxenes and feldspars that wet the surrounding silicates. Such sulfur-rich metallic melts can be stored and persist in these shallow regions throughout time due to the presence of compaction waves, as predicted by numerical simulations (e.g. Šrámek et al., 2012; Mizzon, 2015). Such features are also likely to be present in deeper regions, creating an succession of S-depleted and S-enriched regions. Within this alternance could be found a "transitional acapulcoite" material similar to GRA 95209 with a significant degree of partial melting, grain sizes of about 120 µm, and a strong depletion in sulfur-rich metallic melt. This region may be significantly enriched in low-melting temperature phases (e.g. clinopyroxenes and feldspars) as it should store the silicate melt extracted from deeper regions. Indeed, Lodran is expected to have experienced greater peak temperatures that allowed an efficient grain growth until an efficient silicate melt extraction is favored (silicate grain size $\geq$ 200 µm). This extraction event freezes the grain sizes. Due to the density gradient, the silicate melt went to shallower regions until grain sizes did not allow it to go further and creating these accumulation regions of transitional acapulcoites. The lodranite forming region is expected to be depleted in both silicate and metallic melts.

The numerical models of Neumann et al. (2018) indicates that the lodranite forming region is relatively shallow and overlay a material with a greater degree of silicate melting, that could have gone up to a magma ocean stage. The low timescales for olivine and kamacite-taenite grain to grow to their measured grain sizes argue in favor on such shallow origin. Indeed, the shallower regions have much lower cooling timescales than deeper ones. The removal of silicate melts in Lodran froze the grain sizes; it cannot be ruled out that Lodran experienced a much larger peak temperature than what is inferred from Figure 6.17. A deep origin of lodranites would then be also possible.

6.5.4 Precursor material for primitive achondrites and evolution pattern

Although H chondrites have oxygen isotopic compositions that differ from the acapulcoites-lodranites (Greenwood et al., 2017), their bulk compositions are very similar. Hence, these primitive achondrites are often assumed to originate from a H chondrite-like material (Palme et al., 1981). However, H chondrites have oxygen fugacities along $\Delta\text{IW} = -1$ (Brett and

Sato, 1984), while acapulcoites-lodranites range along $\Delta IW = -2$ and the winonaites along $\Delta IW = -2.5$. These different oxygen fugacities are responsible for the apparent modal composition: H chondrites have a olivine / (olivine + orthopyroxene) ratio higher than 50 vol.% while acapulcoites have equal amounts of these phases and winonaites have a strong disproportion, with much more orthopyroxene than olivine (Table 6.3).

In order to determine the effect of reducing conditions on a H chondrite material, thermodynamic calculations were conducted using the *Rhyolite MELTS* calculator (Asimow and Ghiorso, 1998; Ghiorso and Gualda, 2015; Ghiorso and Sack, 1995; Gualda et al., 2012). The H chondrite composition is taken from Wasson and Kallemeyn (1988) (Table 2.2), with the FeO content of silicates calculated from the FeO / (FeO + MgO) reported. Temperature is varied between 900 and 2000 °C and pressure is set to 1 bar. Three calculations were run with varying offsets from the FMQ buffer, which can only be integers: $\Delta FMQ = -5$ ($\Delta IW = -1.5$ at 1373 - 1573 K), $\Delta FMQ = -6$ ($\Delta IW = -2.5$ at 1373 - 1573 K) and $\Delta FMQ = -7$ ($\Delta IW = -3.5$ at 1373 - 1573 K). Data of interest here are the olivine Mg# (MgO / (MgO + FeO) in mol.%) and the relative olivine - pyroxene volume proportion (olivine / (olivine + pyroxene) in vol.%), as these results can directly be compared to the natural samples (Tables 6.3 and 6.5) and correspond to the majority of the silicates. Temperatures used to plot the samples correspond to the estimated peak temperatures of Table 6.10. Error bars of ±100 K were arbitrarily added to these values.

Evolution of the olivine Mg# and of the olivine - pyroxene relative proportions as a function of the different oxygen fugacities ($\Delta FMQ = -5$, $\Delta FMQ = -6$, $\Delta FMQ = -7$) are represented in Figure 6.20a and 6.20b respectively. As expected, the olivine Mg# increases for more reducing conditions, but also along with temperature, as magnesium is more refractory than iron. In turn, the relative proportion of olivine decreases with more reducing conditions: the decrease of the bulk FeO content favors the formation of orthopyroxene ((Mg,Fe) / Si ratio of 1 instead of 2 for the olivine), but the relative proportion of olivine increases with temperature as this mineral is more refractory. Results shown here do not consider the metallic subsystem, nor the loss of a low melting temperature silicate melt, interest being concentrated on the refractory olivines and orthopyroxenes. Acapulcoites and lodranites are plotted at an intermediate oxygen fugacity between $\Delta FMQ = -5$ and $\Delta FMQ = -6$ for both their Mg# and relative olivine proportion (Figures 6.20a and 6.20b, respectively) within errorbars, which is in agreement with the oxygen fugacities determined with the QIFs and QIFa equilibria of $\Delta IW = -2$ (Table 6.9).

However winonaites show a different behavior. Indeed, their olivine Mg# indicate that their oxygen fugacity is intermediate between $\Delta IW = -2.5$ and $\Delta IW = -3.5$ (Figure 6.20a), while their olivine relative contents indicate an oxygen fugacity lower than $\Delta IW = -3.5$ (Figure 6.20b). A misevaluation of the peak temperature experienced by these objects cannot explain this discrepancy (Figure 6.20b). Most likely, H chondrites are not the precursor material of winonaites, a material with a lower Mg / Si ratio could be a better match and may correspond to L, LL or even to enstatite chondrites (Wasson and Kallemeyn, 1988, data from Table 1).

Overall, modal compositions and forsterite - fayalite content of acapulcoites-lodranites are in agreement with a reduced H chondrite precursor material. In this case, these objects originate from a reservoir with a similar bulk composition than H chondrites but different

oxygen fugacities. Hence, acapulcoites and lodranites have no reason to have oxygen isotopic signatures similar to H chondrites. However, results for winonaites are not consistent with the model developed here. Thus, these objects likely sample a pristine reservoir with an even lower oxygen fugacity and a different bulk composition than H chondrites, with a lower Mg / Si ratio. Under these conditions, winonaites have also no reason to have an oxygen isotopic signature similar to acapulcoites, lodranites or H chondrites.

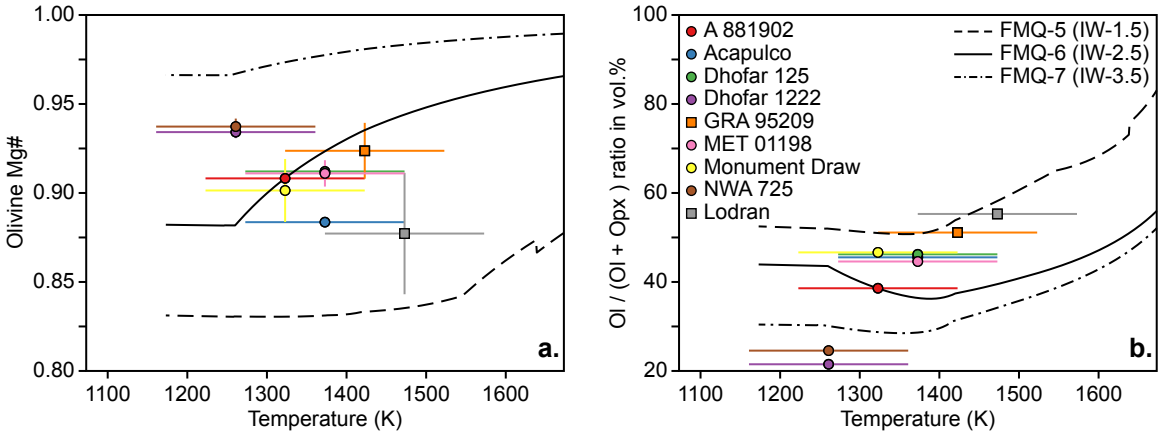

Figure 6.20 – (a.) Olivine Mg# as a function of temperature and (b.) relative olivine volume fraction (olivine / (olivine + orthopyroxene) ratio) as a function of temperature, both for different oxygen fugacity conditions: ΔFMQ = −5 (ΔIW = −1.5) in dashed line, ΔFMQ = −6 (ΔIW = −2.) in full line and ΔFMQ = −7 (ΔIW = −3.5) in dashed-dotted line. Color dots correspond to the acapulcoites and color squares to the lodranites. Vertical errorbars for the Mg# correspond to the 2SD from Table 6.5 and horizontal ones are estimated to be ±100 °C.

6.6 Conclusion

I conducted a petrological survey on nine samples of primitive achondrites: five acapulcoites with different degrees of thermal evolution, two lodranites (with one, GRA 95209, reevaluated as a transitional acapulcoite Patzer et al., 2004) and two sections reevaluated as winonaites (on the basis of their oxygen isotopic compositions Greenwood et al., 2012). All sections were characterized using SEM-EDS, SEM-EBSD and EPMA. On the basis of petrological and compositional arguments, different groups of meteorites can be determined. All the different arguments point toward the same subgroups. From the least to the most evolved: (1) the winonaites Dhofar 1222 and NWA 725, (2) the primitive acapulcoites A 881902 and Monument Draw and finally, (3) the acapulcoites Acapulco, Dhofar 125 and MET 01198, (4) the transitional acapulcoites GRA 95209, and finally (5) the lodranite Lodran.

Subgroup (1) corresponds to meteorites that poorly heated, not even to the Fe-FeS eutectic temperature. Crossing this eutectic temperature (subgroup 2), the sulfur-rich melts are able to migrate although the grain sizes remain low (e.g. A 881902 and Monument Draw). If the peak temperature was more important (subgroup 3), grain sizes reached larger values and part of the silicates were molten (feldspar and clinopyroxene). However, they still were too small to allow efficient silicate melt extraction. A slight mobilization may have occurred, forming large pools which maintained their wetting textures with the other silicates upon

cooling. Further heating (subgroup 4) shows a slight migration of the silicate melts with an enrichment in feldspars and clinopyroxenes, but it remains relatively inefficient. Finally, the last subgroup (5) experienced higher temperatures, enhancing drastically grain growth mechanisms until the silicate melt is efficiently extracted. This caused the complete loss of feldspars and clinopyroxenes, but also froze the grain size as grain growth is much more efficient in the presence of silicate melt.

Based on their bulk compositions, these samples are usually thought to originate from a material similar to the H chondrites but with a different oxygen isotopic signature. To assess the precursor material of acapulcoites-lodranites and of winonaites, the evolution of a H-like chondritic material was modeled upon increasing temperature for different oxygen fugacities. Results show that the acapulcoites-lodranites olivine Mg# and olivine to orthopyroxene modal compositions are in agreement with a reduced H chondrite material, to oxygen fugacities conditions of $\Delta\text{IW} = -2$. However, results for winonaites are not consistent with a H chondrite precursor material. Based on the modal proportions, a precursor material with a lower Mg / Si ratio than H chondrites is more likely. Overall, this thermodynamic calculation confirms that acapulcoites-lodranites originate from a reservoir with a bulk composition similar to that of H chondrites, but with a lower oxygen fugacity. In turn, winonaites sample a different reservoir, with an even lower oxygen fugacity $\Delta\text{IW} = -2.5$ to -3 and a bulk composition with a lower Mg / Si ratio, perhaps close to that of L, LL or even enstatite chondrites. These meteorites have no reason to have similar oxygen isotopic signatures.

Chapter 7

Conclusions et perspectives

Conclusion — Cette thèse vise à apporter des contraintes sur les processus physiques de différenciation métal-silicate dans les petits corps du Système Solaire, leurs échelles de temps et leur efficacité. Pour cela, un système expérimental à trois phases, constitué d'olivine, de silicate fondu et de nickel, a été mis au point et constitue un analogue d'échantillons naturels en cours de différenciation. Trois montages expérimentaux différents ont été utilisés pour déterminer les géométries d'équilibre de la phase métallique aux échelles microscopiques et macroscopiques. Tout d'abord, des expériences dans des fours à haute température (AF) à atmosphère contrôlée ont été menées pour déterminer la géométrie d'équilibre à la micro-échelle, à travers des mesures répétées d'angles dièdres et en déterminant les énergies d'interfaces. Ensuite, des expériences en piston-cylindre (PC) ont été effectuées pour éliminer la porosité retrouvée dans les échantillons des expériences AF et pour déterminer le seuil d'interconnectivité du métal. Des expériences complémentaires en presse Paris-Edimbourg (PE) ont été réalisées au synchrotron SOLEIL. L'atteinte de l'équilibre textural et la distribution macroscopique du métal suivant les proportions relatives de chaque phase ont également été étudiées sur la base de mesures de microtomographie 3D à rayons X, *ex-situ* pour les expériences piston-cylindre et *in-situ* pour les expériences en presse Paris-Édimbourg sous rayonnement synchrotron (PSICHE beamline, SOLEIL synchrotron).

Les échantillons des expériences AF ont été étudiés à l'aide de microsonde électronique et d'imagerie MEB pour caractériser les géométries d'équilibre à l'échelle microscopique du système à trois phases. Des mesures répétées d'angles dièdres à différents grossissements indiquent que des résolutions élevées sont nécessaires pour caractériser précisément les textures microscopiques. Dans ces conditions, l'angle dièdre moyen du silicate fondu est relativement faible ($\approx 25°$) alors que celui du nickel est presque tangent ($\approx 176°$). Tous les échantillons se placent dans le même régime d'énergies d'interfaces, quel que soit le grossissement. L'énergie d'interface la plus élevée est celle entre le nickel et l'olivine, tandis que la plus faible est celle entre l'olivine et le liquide silicaté. Globalement, le nickel possède une énergie d'interface élevée avec les silicates, ce qui empêche à son interconnexion et indique un seuil d'interconnectivité élevé. Une observation particulière des échantillons ayant peu de métal et beaucoup de liquide silicaté a été le regroupement des grains de nickel solide sur des échelles de temps très courtes. Les bulles de gaz piégées dans ces échantillons ont certainement agité le milieu en essayant de s'échapper, favorisant la coalescence du nickel. Cet effet s'observe que le métal soit solide ou fondu, conduisant soit à chapelet de grains solides, soit à une grande sphère métal fondu.

Afin de déterminer les textures macroscopiques à l'équilibre du nickel en fonction des proportions relatives des différentes phases, tout en s'affranchissant des bulles de gaz, des expériences en piston-cylindre et en presse Paris-Édimbourg (PSICHE beamline, Synchrotron

SOLEIL) ont été menées. Les échantillons récupérés ont été analysés par microtomographie 3D à rayons X. La grande variété de textures obtenues en fonction des proportions initiales dépend de différents taux de maturation texturale. La fraction de cristaux, la proximité au seuil d'interconnexion et l'état du métal, solide ou fondu, affectent les échelles de temps sur lesquelles la minimisation des énergies d'interfaces a lieu. Les paramètres idéaux pour une équilibration rapide sont : de grandes quantités de liquide silicaté ($\geq$ 10 vol%) et une quantité de métal fondu bien en-dessous de son seuil d'interconnectivité. Les expériences en presse Paris-Édimbourg ont montré un autre effet, à savoir la formation forcée d'un réseau métallique interconnecté pendant la compression à froid lors de la mise en place de l'expérience. En effet, le nickel est la phase "molle" par rapport aux silicates solide, il s'étale le long des joints des grains lors de la compression. Ces résultats indiquent que ce réseau est instable et se brise pendant l'expérience à condition que le taux de maturation texturale soit suffisant. En faisant varier le taux de maturation texturale pendant l'expérience, il est possible de déterminer la stabilité d'un réseau métallique, indiquant un seuil d'interconnectivité du nickel métal entre 20 et 25 vol%, à l'équilibre.

À partir du seuil d'interconnectivité élevé pour un métal pur et de la dépendance du seuil d'interconnectivité du liquide métallique en fonction de sa teneur en soufre, un modèle a été construit pour expliquer la formation des acapulcoites et des lodranites. Lors de la fusion progressive d'un planétésimal, la teneur en soufre du liquide métallique évolue. Comme la dépendance exacte entre seuil d'interconnectivité d'un liquide métallique et sa teneur en soufre est peu contrainte, plusieurs fonctions de seuil hypothétiques ont été étudiées. Les courbes de fusion des sous-systèmes silicatés et métalliques ont été calculées à l'aide du calculateur thermodynamique *Rhyolite MELT* et des données bibliographiques. Les processus de fusion à l'équilibre ne permettent pas au liquide métallique d'atteindre son seuil d'interconnectivité. Des processus de fusion fractionnée sont donc nécessaires. Seulement deux fonctions de seuil avec des formes similaires à des fonctions inverses permettent l'extraction du liquide métallique riche en soufre avec des degrés de fusion et d'extraction des silicates qui sont pertinents avec les lodranites. Des données expérimentales semblent confirmer ces tendances. De plus, ces extractions de liquides métalliques riches en soufre ont lieu avant la fusion complète du sous-système métallique, ce qui permet d'avoir un fractionnement en composition de la teneur en soufre et fournit une explication aux variations de composition en cet élément dans les différentes sections d'acapulcoites et de lodranites.

La coalescence des particules de métal a probablement lieu dans les océans de magma en convection. L'étude des paramètres à l'équilibre des océans de magma dans les petits corps indique qu'ils sont loin d'être entièrement fondus. La fraction de résidu silicaté dépend principalement du seuil rhéologique et, dans une moindre mesure, de la date d'accrétion et du rayon du planétesimal. Les données de la littérature indiquent un seuil rhéologique d'à peu près 0.5 pour des conditions semblables à celles des océans de magma, réduisant drastiquement les vitesses de sédimentation des particules métalliques et empêchant la différenciation par ce processus. La percolation d'un réseau métallique interconnecté est donc le processus principal de différenciation. Lorsque la source de chaleur s'épuise, les aggrégats de silicates solides et de gouttelettes métalliques sédimentent au fond de l'océan magma. La compaction permet d'extraire efficacement le liquide silicaté, ce qui permet l'interconnection et la percolation du liquide métallique. À cause de la pression liée à la hauteur de colonne de silicates solides, la partie la plus profonde de cette colonne est forcée de baigner dans un liquide métallique. Les

simulations thermodynamiques montrent qu'avec un degré de fusion de 50 vol%, l'olivine est la seule phase silicatée restante et a un Mg# égal à celui des pallasites. Ces caractéristiques suggèrent une origine magmatique pour ces météorites.

Cette thèse s'est aussi intéressée à l'étude pétrologique de neuf sections d'achondrites primitives : cinq acapulcoites, deux lodranites et deux winonaites, à l'aide d'analyses de microsonde électronique et de cartographies SEM-EDS, SEM-EBSD et EPMA. Différentes catégories d'échantillons ont pu être définies sur la base de leurs compositions modales, des tailles de grains et des fugacités d'oxygène. Ces échantillons sont restés partiellement différenciés à cause d'expositions à des températures maximales faibles n'ayant pas permis de larges taux de fusion ou des tailles de grains suffisamment grandes pour extraire efficacement les liquides silicatés. Cependant, en raison de viscosités plus faibles, les échelles de temps de migration des liquides métalliques sont beaucoup plus courts que ceux des liquides silicatés, à condition qu'ils forment des réseaux interconnectés. Dans ces conditions, des échantillons peuvent avoir été sujets à une perte ou un gain précoce de liquides métalliques riches en soufre alors que la température de solidus des silicates n'était pas encore atteinte. Des températures plus élevées et de plus grandes tailles de grains favorisent la migration et la séparation efficaces des deux liquides immiscibles. Le cas de l'échantillon de Lodran étudié ici reste particulier, car une fraction significative des liquides sulfurés ne s'est pas échappée, contrairement aux liquides silicatés. Des simulations thermodynamiques indiquent que les acapulcoites et les lodranites peuvent provenir d'un matériel précurseur avec une composition en éléments majeurs similaire aux chondrites de type H, mais échantillonent un réservoir différent avec des fugacités d'oxygène plus faibles. Des modèles similaires pour les winonaites indiquent que leur matériel précurseur a une composition en éléments majeurs différente des chondrites de type H, notamment avec un rapport Mg/Si plus élevé, mais aussi un environnement encore plus réducteur.

Perspectives — Dans le cadre de cette thèse, j'ai montré que la percolation d'un réseau interconnecté de liquide métallique est le processus majeur de la différenciation métal-silicates dans les petits corps accrétés tôt dans l'historie du Système Solaire, mais aussi dans le cadre de la formation des achondrites primitives et des achondrites totalement différenciées. La dépendence du seuil d'interconnectivité du liquide métallique en fonction de sa teneur en soufre est l'un des paramètres principaux qui contrôlent les conditions de l'interconnexion. Cette relation et les seuils d'interconnectivité restent encore peu contraints, avec de gros désaccords dans les valeurs reportées dans la littérature : de 3 à 17.5 vol%. Ces différences sont certainement dues à différent taux de maturations texturales, donnant lieu à des réseaux méta-stables. Ainsi, une part du travail futur à mener pour compléter notre compréhension globale des processus de différenciation métal-silicates serait de préciser cette tendance, en prenant soin d'atteindre l'équilibre textural. Une façon de procéder serait d'ajouter environ 10 vol% de liquide silicaté, ce qui augmenterait drastiquement le taux de maturation texturale. Ensuite, des analyses de conductivité électrique et de microtomographie 3D à rayons X devraient être menées pour déterminer le seuil d'interconnectivité, pour différentes teneurs en soufre. Selon les résultats, le nombre d'évènements d'extraction de liquide métallique peut être déterminé, mais cela permettra aussi de déterminer si la différenciation des achondrites primitives s'est faite par la formation de réseaux stables ou méta-stables. En effet, si un seuil d'interconnectivité élevé est trouvé (environ 17-18 vol%), alors la formation d'un réseau stable

nécessiterait l'extraction de plus de 40 vol% des silicates, ce qui est bien plus que ce montrent les lodranites. Des processus hors équilibre devront donc être invoqués.

Les phases métalliques dans certaines achondrites primitives ne montrent pas l'atteinte de l'équilibre textural, de part leur formes irrégulières et non de sphères comme attendu par leurs énergies d'interfaces. Je propose que leurs formes ont été acquises lors de l'extraction de liquide silicaté, ce qui a causé la compaction de la matrice. Comme les phases métalliques sont "molles" en comparaison aux silicates, elles auraient alors pris la forme des espaces disponibles, même si ce n'est pas énergétiquement favorable. Afin de mimer ces effets et de vérifier cette hypothèse, des expériences de déformation pourraient être menées. L'analyse 2D ou 3D des échantillons permettrait de déterminer le stress nécessaire pour vaincre les énergies d'interface et pour forcer les phases métalliques à adopter leurs formes irrégulières. De telles expériences pourraient aussi être utilisées pour étudier la formation et la méta-stabilité des réseaux, en déterminant le jeu conjoint des énergies d'interface et du stress. Des expériences en séries-temporelles après l'acquisition de telles formes irrégulières permettraient de déterminer les échelles de temps nécessaires à la maturation texturale dans différentes conditions (en présence ou non de liquide silicaté, selon les tailles de grains, etc ...) et de déterminer dans quelles conditions de telles textures hors équilibre peuvent être préservées.

Les simulations numériques indiquent qu'une petite fraction d'un réseau percolant reste piégée lors de son extraction. La présence ou l'absence de cette fraction piégée est extrêmement importante lors de la différenciation, car elle permet dé ménager un réservoir de soufre, ce qui diminue le seuil d'interconnectivité du liquide métallique, mais réduit aussi la température de liquidus du sous-système métallique. De plus, la présence ou l'absence de cette fraction a des conséquences importantes sur les bilans géochimiques des éléments modérément et fortement sidérophiles. Une distribution différente de ces éléments peut affecter le chronomètre ^{182}Hf-^{182}W et modifier les âges modèles de nombreux échantillons. Cet effet de piégeage d'une fraction du réseau percolant pourrait être vérifié expérimentalement avec des expériences centrifuges. Cependant, un déséquilibre semble être nécessaire dès le début de l'expérience pour le mettre en évidence. Un assemblage avec un échantillon en deux compartiments communiquants peut être utilisé : un premier avec des silicates partiellement fondus et un réseau métallique stable, et un second sans métal. Les deux compartiments doivent contenir du liquide silicaté pour favoriser la migration du réseau métallique. Ainsi, lorsque le réseau se déplace d'un compartiment à l'autre, il est possible de vérifier si une partie du réseau est laissée en arrière ou non.

Certains échantillons naturels se sont montrés particulièrement hétérogènes dans la distribution spatiale de leurs phases métalliques. Des mesures de microtomographie 3D à rayons X sur les masses principales d'achondrites primitives mettraient en évidence ces hétérogénéités et permettraient de comprendre les variations locales de teneurs en phases métalliques. La formation de chenaux de métaux peut être mise en évidence à travers tout un échantillon. Une meilleure détermination des matériaux précurseurs des achondrite primitives permettraient d'affiner l'histoire de l'évolution de ces corps, en suivant plus précisément les fractions extraites ou enrichies en certaines phases. L'étude de plus d'échantillons d'achondrites primitives est aussi un aspect à ne pas négliger, afin de mieux comprendre leur formation et les processus de différenciation. Les données pétrologiques et géochimiques sur ces échantillons sont rares. Il serait intéressant d'en acquérir plus, sur plus d'échantillons, pour compléter notre savoir

sur leur évolution, notamment avec des données chronologiques plus précises (e.g. ^{182}Hf-^{182}W ou ^{26}Al-^{26}Mg), des données sur les quantités initiales en sources de chaleur, ou encore, des données supplémentaires sur les terres-rares afin d'obtenir des contraintes précises sur les processus ignés à l'œuvre. En associant ces données avec les températures de fermeture des différents chronomètres, des données pétrologiques, des simulations thermodynamiques et des modèles de différenciation, il serait possible de reconstruire les histoires d'évolutions thermique et de différenciation des achondrites primitives partiellement différenciées, mais aussi des achondrites totalement différenciées.

Chapter 8

Conclusions and future prospects

Conclusion — This PhD aimed at shedding light on the physical processes of metal-silicate differentiation in early accreted small bodies, their timescales and efficiency. To do so, a three-phase experimental system relevant to natural samples undergoing differentiation was constructed, consisting of olivine, silicate melt and nickel. Three different experimental set ups were used to determine the equilibrium geometries of the metallic phase on both micro- and macro-scales. First, controlled atmosphere high temperature furnace (AF) experiments were conducted to determine the small-scale equilibrium geometry by measuring dihedral angles and determining interfacial energies. Then, piston-cylinder (PC) experiments were performed to eliminate the porosity found in samples recovered from AF experiments and to determine the interconnection threshold of the metal. Complementary experiments with a Paris-Edinburgh press (PE) were carried out at the SOLEIL synchrotron facility. The attainment of textural equilibrium following the relative proportions of each phase was also investigated based on 3D X-ray microtomography measurements, *ex-situ* for piston-cylinder experiments and *in-situ* for Paris-Edinburgh press under synchrotron radiation (PSICHE beamline, SOLEIL synchrotron).

Recovered samples from AF experiments were studied using EPMA and SEM imaging to characterize the microscale equilibrium geometries of the three-phase system. Repeated dihedral angle measurements at different magnifications indicate that high resolutions are necessary to characterize the microscale textures accurately. At these conditions, the mean dihedral angle of the silicate melt is relatively low ($\approx 25°$) while that of the nickel is almost tangent ($\approx 176°$). All samples plot within the same energy regime, no matter the magnification. The highest interfacial energy is that between nickel and olivine while the lowest is that between olivine and silicate melt. Overall, nickel has a high interfacial energy with silicates, which is likely to hinder its interconnectivity and to lead to a high interconnection threshold. An odd observation on these samples was the grouping together of solid nickel grains on short timescales for experiments with low nickel contents and high fractions of silicate melt. Gas bubbles trying to escape the samples most likely agitated the medium, favoring nickel coalescence. This effect is observed whether the metal is solid or molten, leading to an irregular elongated cluster for solid nickel or a large sphere for molten nickel.

To determine the macroscale equilibrium textures of nickel when varying the relative contents of each phase and getting rid of gas bubbles, piston-cylinder and Paris-Edinburgh press (PSICHE beamline, Synchrotron SOLEIL) experiments were conducted. Recovered samples were analyzed with computed 3D X-ray microtomography. The variety of textures observed as a function of the initial phase proportions indicates different textural maturation rates. The crystal fraction, proximity to the interconnection threshold and state of the metal - solid or molten - affect the timescales of the minimization of interfacial energies. Equilibration

is fast for large amounts of silicate melt ($\geq$ 10 vol%) and molten metal in much lower amounts than its interconnection threshold. Paris-Edinburgh press experiments showed another effect which is the forced interconnection of the nickel during the cold compression at the beginning of the experiment. Indeed, nickel being "soft" in comparison to the solid olivine and the silicate glass, it will spread along grain boundaries during compression. These experiments showed that this forced network is disrupted during experiment if the textural maturation rate is high enough. Assessing the stability of interconnected networks while varying these parameters indicated an equilibrium interconnection threshold of pure nickel between 20 and 25 vol%.

Based on the dependence of the interconnection threshold on the sulfur content of the metallic melt and the high interconnection threshold for pure metal, a model was derived to explain the formation of acapulcoites and lodranites. Upon progressive melting of a planetesimal, the sulfur content of the iron-sulfide melt evolves. However, as the exact dependence of the interconnection threshold on the sulfur content of the metallic melt is not known, several hypothetical threshold functions were investigated. Melting of both silicate and metallic subsystems were calculated using the *Rhyolite MELT* thermodynamic calculator and literature data. These calculations indicate that equilibrium melting of the silicates does not allow the iron-sulfur melt to reach its interconnection threshold. Therefore a fractional melting process is necessary. Only two threshold functions, with shapes similar to inverse functions, allowed iron-sulfide melt extraction to take place, with silicate melt removal degrees comparable to those inferred for lodranites. Experimental data seem to support such trends. In addition, removal of the sulfur-rich melt occurred before complete melting of the metallic subsystem, allowing fractionation of the sulfur content and providing a good explanation for the compositional variation in this element throughout the different sections of acapulcoites and lodranites.

Coalescence effects of metal particles are likely to occur within convecting magma oceans. Investigating the equilibrium parameters of magma oceans indicated that they are far from being entirely molten. The fraction of remaining solid silicates depends on the maximum packing fraction and to a lesser extent on the accretion date and radius of the planetesimal. Literature data indicate a low maximum packing fraction of about 0.5 for conditions similar to magma oceans, hindering sinking and preventing the segregation of metallic droplets by settling. In this case, differentiation is driven by the percolation of an interconnected iron-sulfide network. When the heat source is exhausted, i.e. ^{26}Al, the remaining solid silicates aggregated with metallic blobs will settle to the bottom of the magma ocean. Compaction will efficiently extract the silicate melt, allowing the iron-sulfide melt to form an interconnected network and to percolate. Due to the pressure of the overlying column of solid silicates, the deepest part of this column is forced to be bathed within molten iron-sulfide. Thermodynamic simulations show that with a 50 vol% melting degree, olivine is the only silicate phase left and has a Mg# matching that of pallasites. These features suggest a magmatic origin for these meteorites.

This PhD also focused on the petrological analysis of nine thick sections of primitive achondrites: five acapulcoites, two lodranites and two winonaites, using SEM-EDS, SEM-EBSD and EPMA electronic analyses. Different categories of samples could be defined based on their modal compositions, grain sizes and oxygen fugacities. The partially differentiated

state of these samples is caused by low to moderate peak temperatures and small to large grain sizes. Low temperatures do not allow efficient silicate grain growth, hindering the timescales of melt migration. However, due to lower viscosities, timescales for metallic melt migration are much lower than that for silicate melts, once interconnected. In these conditions, samples may have been subject to an early loss or gain of sulfur-rich melt while the silicates were below or slightly above their solidus. Higher temperatures and larger grain sizes promote the efficient migration and separation of both melts. The case of the Lodran sample studied here remains puzzling, as a significant fraction of sulfur-rich melt did not escape, while the silicate efficiently did. Thermodynamic simulations indicates that acapulcoites and lodranites may originate from a material with a H chondrite-like bulk composition but derived from a different reservoir with more reducing conditions. Similar models for winonaites indicate different precursor material, with a different Mg/Si ratio and even more reducing conditions.

Future prospects — In the framework of these studies, I highlighted the importance of the percolation of an interconnected iron-sulfide melt as the principal differentiation mechanism in early accreted small bodies and for the formation of both partially and fully differentiated achondrites. The dependence of the interconnection threshold on the sulfur content of the metallic melt is one of the main parameters controlling the conditions for interconnection. This relation and interconnection thresholds remain poorly constrained with a strong disagreement in literature data for similar compositions: from 3 to 17.5 vol%. These discrepancies likely arise from different textural maturation rates and the existence of unstable networks. Hence, a part of a future work to complete the global understanding of differentiation processes would be to refine this trend, taking care to reach textural equilibrium. A way to do so is to add about 10 vol% of silicate melt, which drastically increases the textural maturation rate. Then, both conductivity measurements and 3D X-ray microtomography should be conducted at different iron-sulfur compositions to determine the interconnectivity of the metallic melt. Depending on the results, the number of extraction events of the metallic melt can be determined, but it can also be inferred if the differentiation of primitive achondrites requires the formation of an equilibrium or a disequilibrium network. Indeed, if a high interconnection threshold ($\approx 17-18$ vol%) is confirmed, then the formation of an equilibrium network only occurs with the removal of more than 40 vol% of the silicates, in contradiction with the formation of lodranites. Disequilibrium processes may thus have to be invoked.

Metallic phases in some primitive achondrites do not seem to have reached textural equilibrium, due to the formation of irregular patches and not spheres as would be expected from interfacial energies. I proposed that their shapes were acquired due to the extraction of a silicate melt causing the compaction of the matrix. As metallic phases are "soft", they occupy the space available, even if it is not energetically favorable. To mimic this effect and check this hypothesis, deformation experiments would be interesting to conduct. 2D or 3D analysis of the recovered samples would allow to determine the stress necessary to overcome interfacial energies and to force the metallic phases into their irregular shapes. Such experiments can also be used to investigate the formation and meta-stability of unstable networks, by determining the exact interplay of interfacial energies and stress. Time-series experiments after the acquisition of these shapes would allow to study the time-scale of textural maturation in different conditions (in presence or absence of silicate melt, with varying grain sizes, etc...) and determining under which conditions such disequilibrium textures can be preserved.

Numerical simulations indicated that there is small fraction of a network that remains trapped upon its extraction. The presence or absence of this trapped fraction is extremely important during differentiation, as it allows to have some sulfur left which decreases the interconnection threshold of the metallic melt and the melting liquidus of the metallic subsystem. In addition, it has large consequences on geochemical budgets for moderately to highly siderophile elements. Different distribution of these elements may affect the ^{182}Hf-^{182}W chronometer and change the model ages for many samples. This trapping threshold could be experimentally checked with centrifuge-assisted experiments. However, a disequilibrium at the beginning of the experiment may be necessary to highlight this effect in a sample. A set up with two open compartments could be used: a first one with solid and molten silicates and a stable metallic network, and a second one without any metal. Both compartments have to bear silicate melt to enhance the migration of the metallic network. Hence, while the network travels from a compartment to another, it can be checked if a fraction of the network is left behind or not.

Some samples have been proved to be highly heterogeneous in terms of the spatial distribution of metallic phases. 3D X-ray microtomography measurements carried out on the principal masses of some samples of primitive achondrites would help unravel these heterogeneities and understand small-scale variations in metallic phase contents. The formation of channels of metal may be highlighted through the whole sample. A better determination of their precursor material would also improve the quality of the models and allow to track precisely the loss or enrichment in different mineral phases. The study of more samples of primitive achondrites is also an aspect which should not be neglected in order to understand their formation and the differentiation processes. To the best of my knowledge, few studies report petrological or geochemical analyses of these samples. More work should be done to complete the evolutionary picture of these samples, with precise chronological analyses (e.g. ^{182}Hf-^{182}W or ^{26}Al-^{26}Mg), quantification of the initial amounts of heat sources and additional data on rare earth elements to have constraints on igneous processes. Combining these data with the closure temperatures of the different chronometers, with petrological data, thermodynamic simulations and differentiation models, the whole thermal evolution and history of partially differentiated primitive achondrites and entirely differentiate achondrites could be reconstructed.

Appendix A

Appendix — Chapter 3

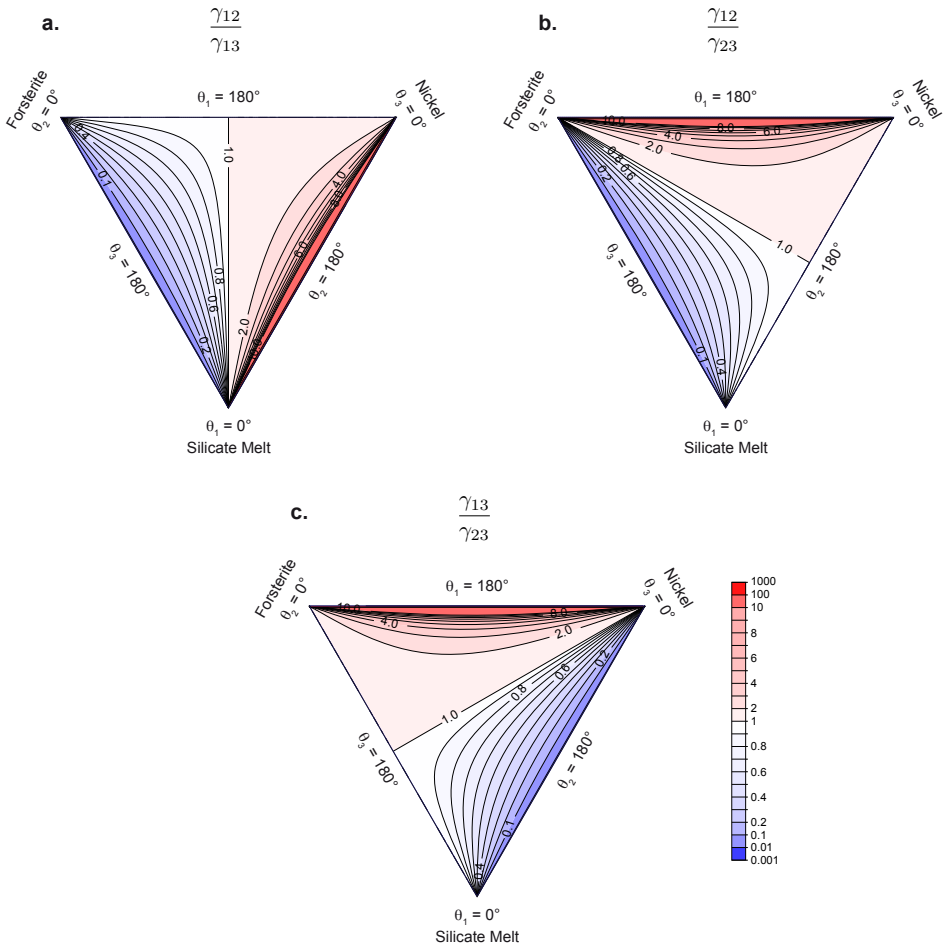

Figure A.1 – From equations 3.2 and 3.3 in the main text (chapter 3), the value of each interfacial energy ratio can be calculated for each triplet of dihedral angles. In each diagram, the straight-line represents an interfacial energy ratio equal to 1, other curved lines representing the isovalues for different ratios. Most of the dihedral angle values map variations of interfacial energy ratios over two orders of magnitude, from 0.1 to 10. Close to the iso-line of 1, the ratio of interfacial energies barely varies. However approaching each apex and edge of the ternary diagram (with the exception of the edge orthogonal to the 1:1 line), curves of constant energy ratio are increasingly closely spaced, requiring very precise measurements of dihedral angles to determine interfacial energy ratios accurately.

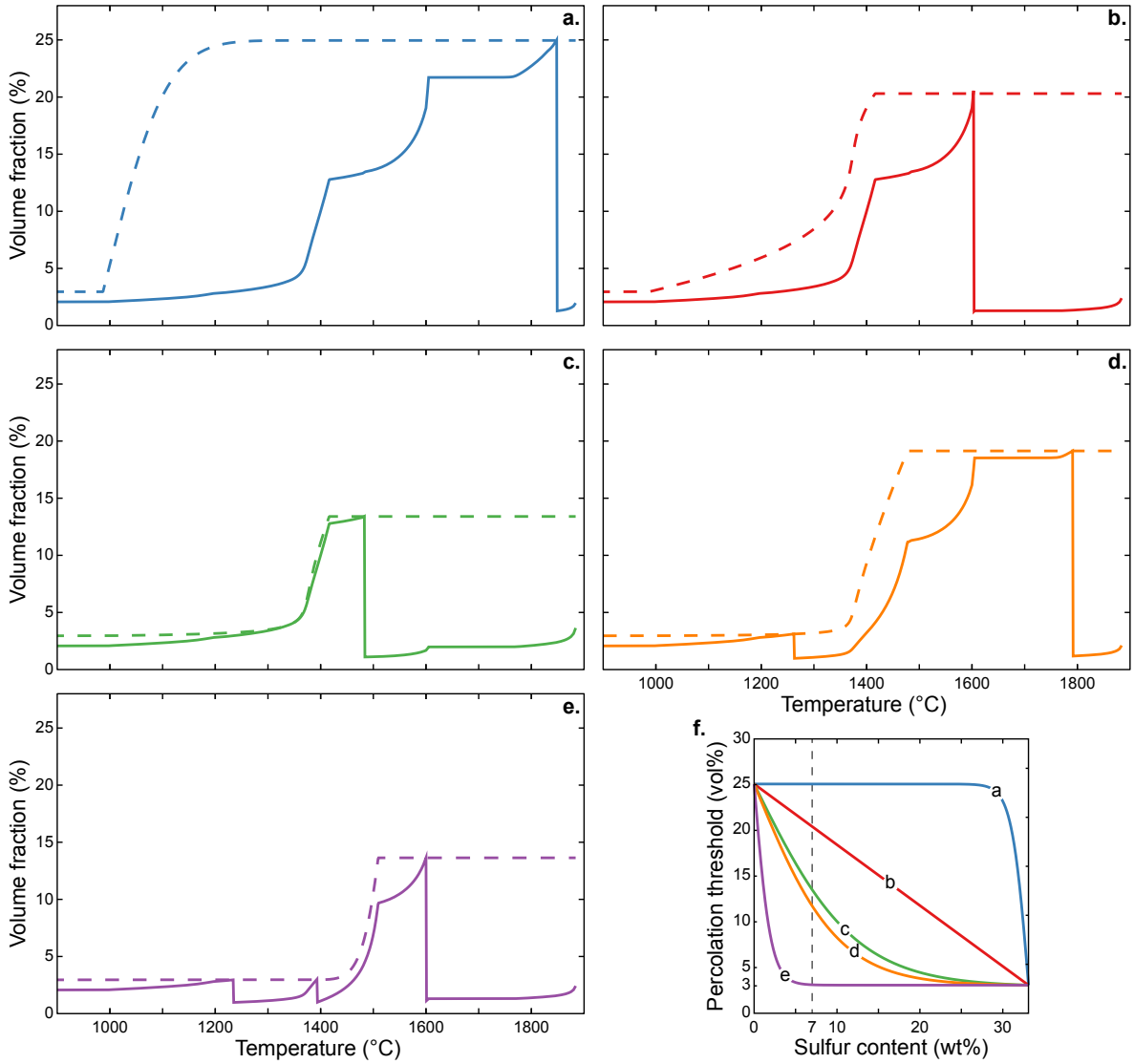

Figure A.2 – Evolution of the percolation threshold function (dashed line) and of the associated sulfide melt content (full line) as a function of temperature. Figures (a), (b), (c), (d) and (e) correspond to different threshold functions as defined on figure (f). Each time the sulfide melt curve crosses tha of the interconnection threshold, i.e. when its content is greater than the interconnection threshold, the sulfide is extracted and only a trapped fraction - set to 1 vol.% (see chapter 3 for more details) - is left.

Bibliography

Abdullaev, R. N., Y. M. Kozlovskii, R. A. Khairulin, and S. V. Stankus
2015. Density and Thermal Expansion of High Purity Nickel over the Temperature Range from 150 K to 2030 K. *International Journal of Thermophysics*, 36(4):603–619.

Ahrens, J., B. Gevici, and C. Law
2005. ParaView: An End-User Tool for Large-Data Visualization. In *Visualization Handbook*, volume 836, Pp. 717–731. Elsevier.

Amelin, Y. and A. Krot
2007. Pb isotopic age of the Allende chondrules. *Meteoritics and Planetary Science*, 42(7-8):1321–1335.

Amelin, Y., A. N. Krot, I. D. Hutcheon, and A. a. Ulyanov
2002. Lead Isotopic Ages of Chondrules and Calcium-Aluminum-Rich Inclusions. *Science*, 297(5587):1678–1683.

Asimow, P. D. and M. S. Ghiorso
1998. Algorithmic modifications extending MELTS to calculate subsolidus phase relations. *American Mineralogist*, 83(9-10):1127–1132.

Ayachit, U.
2019. *The ParaView Guide*. Kitware Inc.

Bagdassarov, N., G. J. Golabek, G. Solferino, and M. W. Schmidt
2009a. Constraints on the Fe-S melt connectivity in mantle silicates from electrical impedance measurements. *Physics of the Earth and Planetary Interiors*, 177(3-4):139–146.

Bagdassarov, N., G. Solferino, G. Golabek, and M. Schmidt
2009b. Centrifuge assisted percolation of Fe–S melts in partially molten peridotite: Time constraints for planetary core formation. *Earth and Planetary Science Letters*, 288(1-2):84–95.

Ballhaus, C. and D. J. Ellis
1996. Mobility of core melts during Earth's accretion. *Earth and Planetary Science Letters*, 143(1-4):137–145.

Bascou, J., E. Dobrica, C. Maurice, B. N. Moine, and M. J. Toplis
2008. Texture analysis in Acapulco and Lodran achondrites. *LPSC 39th*.

Benedix, G., T. McCoy, K. Keil, D. Bogard, and D. Garrison
1998. A petrologic and isotopic study of winonaites: evidence for early partial melting, brecciation, and metamorphism. *Geochimica et Cosmochimica Acta*, 62(14):2535–2553.

Benedix, G. K., D. S. Lauretta, and T. J. McCoy
2005. Thermodynamic constraints on the formation conditions of winonaites and silicate-bearing IAB irons. *Geochimica et Cosmochimica Acta*, 69(21):5123–5131.

Bild, R. W. and J. T. Wasson
1976. The Lodran meteorite and its relationship to the ureilites. *Mineralogical Magazine*, 40(315):721–735.

Boesenberg, J. S., A. M. Davis, M. Prinz, M. K. Weisberg, R. N. Clayton, and T. K. Mayeda
2000. The pyroxene pallasites, Vermillion and Yamato 8451: Not quite a couple. *Meteoritics & Planetary Science*, 35(4):757–769.

Boesenberg, J. S., J. S. Delaney, and R. H. Hewins
2012. A petrological and chemical reexamination of Main Group pallasite formation. *Geochimica et Cosmochimica Acta*, 89:134–158.

Borisov, A. A.
2006. Experimental study of the effect of SiO2 on Ni solubility in silicate melts. *Petrology*, 14(6):530–539.

Boss, A. and J. Goswami
2006. Presolar cloud collapse and the formation and early evolution of the solar nebula. In *Meteorites and the Early Solar System II*, Pp. 171–186. University of Arizona Press.

Bouhifd, M. A., D. Andrault, G. Fiquet, and P. Richet
1996. Thermal expansion of forsterite up to the melting point.

Boulard, E., A. King, N. Guignot, J.-P. Deslandes, Y. Le Godec, J.-P. Perrillat, A. Clark, G. Morard, and J.-P. Itié
2018. High-speed tomography under extreme conditions at the PSICHE beamline of the SOLEIL Synchrotron. *Journal of Synchrotron Radiation*, 25(3):818–825.

Bouvier, A. and M. Wadhwa
2010. The age of the Solar System redefined by the oldest Pb-b age of a meteoritic inclusion. *Nature Geoscience*, 3(9):637–641.

Brett, R. and M. Sato
1984. Intrinsic oxygen fugacity measurements on seven chondrites, a pallasite, and a tektite and the redox state of meteorite parent bodies. *Geochimica et Cosmochimica Acta*, 48(1):111–120.

Britt, D. T. and S. J. Consolmagno
2003. Stony meteorite porosities and densities: A review of the data through 2001. *Meteoritics and Planetary Science*, 38(8):1161–1180.

Bryson, J. F. J., C. I. O. Nichols, J. Herrero-Albillos, F. Kronast, T. Kasama, H. Alimadadi, G. van der Laan, F. Nimmo, and R. J. Harrison
2015. Long-lived magnetism from solidification-driven convection on the pallasite parent body. *Nature*, 517(7535):472–475.

Budde, G., T. S. Kruijer, M. Fischer-gödde, A. J. Irving, and T. Kleine
2015. Planetesimal differentiation revealed by the Hf – W systematics of ureilites. *Earth and Planetary Science Letters*, 430:316–325.

Bulau, J. R., H. S. Waff, and J. A. Tyburczy
1979. Mechanical and thermodynamic constraints on fluid distribution in partial melts. *Journal of Geophysical Research: Solid Earth*, 84(B11):6102–6108.

Buono, A. S. and D. Walker
2011. The Fe-rich liquidus in the Fe–FeS system from 1bar to 10GPa. *Geochimica et Cosmochimica Acta*, 75(8):2072–2087.

Buseck, P. R.
1977. Pallasite meteorites—mineralogy, petrology and geochemistry. *Geochimica et Cosmochimica Acta*, 41(6):711–740.

Caricchi, L., L. Burlini, P. Ulmer, T. Gerya, M. Vassalli, and P. Papale
2007. Non-Newtonian rheology of crystal-bearing magmas and implications for magma ascent dynamics. *Earth and Planetary Science Letters*, 264(3-4):402–419.

Cerantola, V., N. P. Walte, and D. C. Rubie
2015. Deformation of a crystalline olivine aggregate containing two immiscible liquids: Implications for early core-mantle differentiation. *Earth and Planetary Science Letters*, 417:67–77.

Chabot, N. L. and H. Haack
2006. Evolution of Asteroidal Cores. In *Meteorites and the Early Solar System II*, Pp. 747–771. University of Arizona Press.

Chambers, J.
2006. Meteoritic Diversity and Planetesimal Formation. In *Meteorites and the Early Solar System II*, Pp. 487–497. University of Arizona Press.

Champallier, R., M. Bystricky, and L. Arbaret
2008. Experimental investigation of magma rheology at 300 MPa: From pure hydrous melt to 76 vol.% of crystals. *Earth and Planetary Science Letters*, 267(3-4):571–583.

Chandrasekhar, S.
1961. *Hydrodynamic and Hydromagnetic Stability*, International series of monographs on physics. Clarendon Press.

Chung, H. Y. and J. E. Mungall
2009. Physical constraints on the migration of immiscible fluids through partially molten silicates, with special reference to magmatic sulfide ores. *Earth and Planetary Science Letters*, 286(1-2):14–22.

Ciesla, F. and S. Charnley
2006. The Physics and Chemistry of Nebular Evolution. In *Meteorites and the Early Solar System II*, Pp. 209–230. University of Arizona Press.

Cmíral, M., J. D. F. Gerald, U. H. Faul, and D. H. Green
1998. A close look at dihedral angles and melt geometry in olivine-basalt aggregates: a TEM study. *Contributions to Mineralogy and Petrology*, 130(3-4):336–345.

Connolly, H. C. and R. H. Jones
2016. Chondrules: The canonical and noncanonical views. *Journal of Geophysical Research: Planets*, 121(10):1885–1899.

Cooper, R. F. and D. L. Kohlstedt
1982. Interfacial Energies in the Olivine-Basalt System. In *High-Pressure Research in Geophysics*, number Advances in Earth and Planetary Sciences, 12, Pp. 217–228. Dordrecht: Springer Netherlands.

Costa, A., L. Caricchi, and N. Bagdassarov
2009. A model for the rheology of particle-bearing suspensions and partially molten rocks. *Geochemistry, Geophysics, Geosystems*, 10(3):1–13.

Crichton, W. and M. Mezouar
2002. Noninvasive pressure and temperature estimation in large-volume apparatus by equation-of-state cross-calibration. *High Temperatures-High Pressures*, 34(2):235–242.

Cuzzi, J. N. and S. J. Weidenschilling
2006. Particle-Gas Dynamics and Primary Accretion. In *Meteorites and the Early Solar System II*, Pp. 353–381. University of Arizona Press.

Davis, A. M. and F. M. Richter
2013. *Condensation and Evaporation of Solar System Materials*, volume 1, 2 edition. Elsevier Ltd.

Demeo, F. E. and B. Carry
2014. Solar System evolution from compositional mapping of the asteroid belt. *Nature*, 505(7485):629–634.

Dingwell, D., P. Courtial, D. Giordano, and A. Nichols
2004. Viscosity of peridotite liquid. *Earth and Planetary Science Letters*, 226(1-2):127–138.

Dingwell, D., H. O'Neill, W. Ertel, and B. Spettel
1994. The solubility and oxidation state of nickel in silicate melt at low oxygen fugacities: Results using a mechanically assisted equilibration technique. *Geochimica et Cosmochimica Acta*, 58(8):1967–1974.

Dobson, D. P., W. A. Crichton, L. Vo{\u c}adlo, A. P. Jones, Y. Wang, T. Uchida, M. Rivers, S. Sutton, and J. P. Brodholt
2000. In situ measurement of viscosity of liquids in the Fe-FeS system at high pressures and temperatures. *American Mineralogist*, 85(11-12):1838–1842.

Eliceiri, K., C. A. Schneider, W. S. Rasband, and K. W. Eliceiri
2012. NIH Image to ImageJ : 25 years of image analysis. *Nature Methods*, 9(7):671–675.

Faroughi, S. A. and C. Huber
2015. Unifying the relative hindered velocity in suspensions and emulsions of nondeformable particles. *Geophysical Research Letters*, 42(1):53–59.

Faul, U. H.
2000. *Constraints on the Melt Distribution in Anisotropic Polycrystalline Aggregates Undergoing Grain Growth*, Pp. 67–92. Dordrecht: Springer Netherlands.

Faul, U. H. and D. Scott
2006. Grain growth in partially molten olivine aggregates. *Contributions to Mineralogy and Petrology*, 151(1):101–111.

Floss, C.
2000. Complexities on the acapulcoite-lodranite parent body: Evidence for trace element distributions in silicate minerals. *Meteoritics & Planetary Science*, 35:1073–1085.

Gaetani, G. A. and T. L. Grove
1999. Wetting of mantle olivine by sulfide melt: implications for Re/Os ratios in mantle peridotite and late-stage core formation. *Earth and Planetary Science Letters*, 169(1-2):147–163.

Garapić, G., U. H. Faul, and E. Brisson
2013. High-resolution imaging of the melt distribution in partially molten upper mantle rocks: evidence for wetted two-grain boundaries. *Geochemistry, Geophysics, Geosystems*, 14(3):556–566.

Gardner-Vandy, K. G., D. S. Lauretta, R. C. Greenwood, T. J. McCoy, M. Killgore, and I. A. Franchi
2012. The Tafassasset primitive achondrite: Insights into initial stages of planetary differentiation. *Geochimica et Cosmochimica Acta*, 85:142–159.

Ghanbarzadeh, S., M. A. Hesse, and M. Prodanović
2017. Percolative core formation in planetesimals enabled by hysteresis in metal connectivity. *Proceedings of the National Academy of Sciences*, 114(51):13406–13411.

Ghiorso, M. and R. Sack
1991. An internally consistent model for the thermodynamic properties of Fe-Mg -oxides. *Contributions to Mineralogy and Petrology*, 204:474–505.

Ghiorso, M. S. and G. A. R. Gualda
2015. An H2O–CO2 mixed fluid saturation model compatible with rhyolite-MELTS. *Contributions to Mineralogy and Petrology*, 169(6):53.

Ghiorso, M. S. and R. O. Sack
1995. Chemical mass transfer in magmatic processes IV. A revised and internally consistent thermodynamic model for the interpolation and extrapolation of liquid-solid equilibria in magmatic systems at elevated temperatures and pressures. *Contributions to Mineralogy and Petrology*, 119(2-3):197–212.

Golabek, G. J., B. Bourdon, and T. V. Gerya
2014. Numerical models of the thermomechanical evolution of planetesimals : Application to the acapulcoite-lodranite parent body. *Meteoritics & Planetary Science*, 1099(6):1083–1099.

Goldstein, J. I., E. R. Scott, and N. L. Chabot
2009. Iron meteorites: Crystallization, thermal history, parent bodies, and origin. *Chemie der Erde*, 69(4):293–325.

Gomes, R., H. F. Levison, K. Tsiganis, and A. Morbidelli
2005. Origin of the cataclysmic Late Heavy Bombardment period of the terrestrial planets. *Nature*, 435(7041):466–469.

Greenwood, R. C., J.-A. Barrat, A. Yamaguchi, I. A. Franchi, E. R. Scott, W. F. Bottke, and J. M. Gibson
2014. The oxygen isotope composition of diogenites: Evidence for early global melting on a single, compositionally diverse, HED parent body. *Earth and Planetary Science Letters*, 390:165–174.

Greenwood, R. C., T. H. Burbine, M. F. Miller, and I. A. Franchi
2017. Melting and differentiation of early-formed asteroids: The perspective from high precision oxygen isotope studies. *Chemie der Erde - Geochemistry*, 77(1):1–43.

Greenwood, R. C., I. A. Franchi, J. M. Gibson, and G. K. Benedix
2012. Oxygen isotope variation in primitive achondrites: The influence of primordial, asteroidal and terrestrial processes. *Geochimica et Cosmochimica Acta*, 94:146–163.

Gualda, G. A. R., M. S. Ghiorso, R. V. Lemons, and T. L. Carley
2012. Rhyolite-MELTS: a Modified Calibration of MELTS Optimized for Silica-rich, Fluid-bearing Magmatic Systems. *Journal of Petrology*, 53(5):875–890.

Guignard, J.
2011. *Caractérisation texturale des assemblages Métal-Silicate lors de la différenciation des planétésimaux : Etude de météorites & Approche expérimentale.* Thesis, Université Toulouse III Paul Sabatier.

Guignard, J., M. Bystricky, and F. Béjina
2011. Dense fine-grained aggregates prepared by spark plasma sintering (SPS), an original technique in experimental petrology. *European Journal of Mineralogy*, 23(3):323–331.

Guignard, J., M. Bystricky, and M. J. Toplis
2012. Grain growth in forsterite-nickel mixtures: Analogues of small parent bodies during early accretion. *Physics of the Earth and Planetary Interiors*, 204-205:37–51.

Guignard, J. and M. Toplis
2015. Textural properties of iron-rich phases in H ordinary chondrites and quantitative links to the degree of thermal metamorphism. *Geochimica et Cosmochimica Acta*, 149:46–63.

Guignard, J., M. J. Toplis, M. Bystricky, and M. Monnereau
2016. Temperature dependent grain growth of forsterite-nickel mixtures: Implications for grain growth in two-phase systems and applications to the H-chondrite parent body. *Earth and Planetary Science Letters*, 443:20–31.

Haisch, Jr., K. E., E. A. Lada, and C. J. Lada
2001. Disk Frequencies and Lifetimes in Young Clusters. *The Astrophysical Journal*, 553(2):L153–L156.

Hevey, P. J. and I. S. Sanders
2006. A model for planetesimal meltdown by 26 Al and its implications for meteorite parent bodies. *Meteoritics & Planetary Science*, 41(1):95–106.

Hiraga, T., C. Tachibana, N. Ohashi, and S. Sano
2010. Grain growth systematics for forsterite ± enstatite aggregates: Effect of lithology on grain size in the upper mantle. *Earth and Planetary Science Letters*, 291(1-4):10–20.

Hirth, G. and D. Kohlstedt
2003. Rheology of the upper mantle and the mantle wedge: A view from the experimentalists. In *Geophysical Monograph Series*, volume 138, Pp. 83–105.

Höink, T., J. Schmalzl, and U. Hansen
2005. Formation of compositional structures by sedimentation in vigorous convection. *Physics of the Earth and Planetary Interiors*, 153(1-3):11–20.

Holzheid, A., M. D. Schmitz, and T. L. Grove
2000. Textural equilibria of iron sulfide liquids in partly molten silicate aggregates and their relevance to core formation scenarios. *Journal of Geophysical Research: Solid Earth*, 105(B6):13555–13567.

Homma, Y., T. Iizuka, and A. Ishikawa
2019. Hf-W dating of main-group pallasites. *Goldschmidt2019 Abstract*.

Humenik Jr., M. and W. D. Kingery
1954. Metal-Ceramic Interactions: III, Surface Tension and Wettability of Metal-Ceramic Systems. *Journal of the American Ceramic Society*, 37(1):18–23.

Ichikawa, H., S. Labrosse, and K. Kurita
2010. Direct numerical simulation of an iron rain in the magma ocean. *Journal of Geophysical Research*, 115(B1):1–12.

Jung, E.-J., W. Kim, I. Sohn, and D.-J. Min
2010. A study on the interfacial tension between solid iron and CaO–SiO2–MO system. *Journal of Materials Science*, 45(8):2023–2029.

Jung, H. and H. S. Waff
1998. Olivine crystallographic control and anisotropic melt distribution in ultramafic partial melts. *Geophysical Research Letters*, 25(15):2901–2904.

Jurewicz, S. R. and A. J. G. Jurewicz
1986. Distribution of apparent angles on random sections with emphasis on dihedral angle measurements. *Journal of Geophysical Research*, 91(B9):9277.

Jurewicz, S. R. and E. Watson
1985. The distribution of partial melt in a granitic system: The application of liquid phase sintering theory. *Geochimica et Cosmochimica Acta*, 49(5):1109–1121.

Keil, K. and T. J. McCoy
2018. Acapulcoite-lodranite meteorites: Ultramafic asteroidal partial melt residues. *Geochemistry*, 78(2):153–203.

Ketcham, R. A.
2005. Computational methods for quantitative analysis of three-dimensional features in geological specimens. *Geosphere*, 1(1):32.

King, A., P. Schofield, K. Howard, and S. Russell
2015. Modal mineralogy of CI and CI-like chondrites by X-ray diffraction. *Geochimica et Cosmochimica Acta*, 165:148–160.

Kivelson, M. G., K. K. Khurana, C. T. Russell, R. J. Walker, J. Warnecke, F. V. Coroniti, C. Polanskey, D. J. Southwood, and G. Schubert
1996. Discovery of Ganymede's magnetic field by the Galileo spacecraft. *Nature*, 384(6609):537–541.

Kraichnan, R. H.
1962. Turbulent Thermal Convection at Arbitrary Prandtl Number. *Physics of Fluids*, 5(11):1374.

Kretz, R.
1982. Transfer and exchange equilibria in a portion of the pyroxene quadrilateral as deduced from natural and experimental data. *Geochimica et Cosmochimica Acta*, 46(3):411–421.

Kruijer, T. S., M. Touboul, M. Fischer-Godde, K. R. Bermingham, R. J. Walker, and T. Kleine
2014. Protracted core formation and rapid accretion of protoplanets. *Science*, 344(6188):1150–1154.

Laporte, D. and A. Provost
2000. The Grain-Scale Distribution of Silicate, Carbonate and Metallosulfide Partial Melts: a Review of Theory and Experiments. In *Physics and Chemistry of Partially Molten Rocks*, N. Bagdassarov, D. Laporte, and A. B. Thompson, eds., number 11, Pp. 93–140. Springer Netherlands.

Larimer, J. W.
1968. Experimental studies on the system Fe-MgO-SiO2-O2 and their bearing on the petrology of chondritic meteorites. *Geochimica et Cosmochimica Acta*, 32(11):1187–1207.

Lavorel, G. and M. Le Bars
2009. Sedimentation of particles in a vigorously convecting fluid. *Physical Review E*, 80(4):046324.

Le Godec, Y., D. Martinez-Garcia, M. Mezouar, G. Syfosse, J.-P. Itié, and J.-M. Besson
2000. Thermoelastic behaviour of hexagonal graphite-like boron nitride. *High Pressure Research*, 17(1):35–46.

Liao, Y. and D. Lucas
2010. A literature review on mechanisms and models for the coalescence process of fluid particles. *Chemical Engineering Science*, 65(10):2851–2864.

Lichtenberg, T., T. Keller, R. F. Katz, G. J. Golabek, and T. V. Gerya
2019. Magma ascent in planetesimals: Control by grain size. *Earth and Planetary Science Letters*, 507:154–165.

Markowski, A., G. Quitté, A. Halliday, and T. Kleine
2006. Tungsten isotopic compositions of iron meteorites: Chronological constraints vs. cosmogenic effects. *Earth and Planetary Science Letters*, 242(1-2):1–15.

Marsh, B. D.
1981. On the crystallinity, probability of occurrence, and rheology of lava and magma. *Contributions to Mineralogy and Petrology*, 78(1):85–98.

Matzen, A. K., M. B. Baker, J. R. Beckett, B. J. Wood, and E. M. Stolper
2017. The effect of liquid composition on the partitioning of Ni between olivine and silicate melt. *Contributions to Mineralogy and Petrology*, 172(1):3.

Maurel, C., B. P. Weiss, and J. F. Bryson
2019. Meteorite cloudy zone formation as a quantitative indicator of paleomagnetic field intensities and cooling rates on planetesimals. *Earth and Planetary Science Letters*, 513:166–175.

Mayor, M. and D. Queloz
1995. A Jupiter-mass companion to a solar-type star. *Nature*, 378(6555):355–359.

McCoy, T., K. Keil, R. Clayton, T. Mayeda, D. Bogard, D. Garrison, G. Huss, I. Hutcheon, and R. Wieler
1996. A petrologic, chemical, and isotopic study of Monument Draw and comparison with other acapulcoites: Evidence for formation by incipient partial melting. *Geochimica et Cosmochimica Acta*, 60(14):2681–2708.

McCoy, T., K. Keil, R. Clayton, T. Mayeda, D. Bogard, D. Garrison, and R. Wieler
1997. A petrologic and isotopic study of lodranites: Evidence for early formation as partial melt residues from heterogeneous precursors. *Geochimica et Cosmochimica Acta*, 61(3):623–637.

McCoy, T. J., C. M. Corrigan, T. L. Dickinson, G. K. Benedix, D. L. Schrader, and J. Davidson
2019. Grove Mountains (GRV) 020043: Insights into acapulcoite-lodranite genesis from the most primitive member. *Geochemistry*.

McKibbin, S., T. Ireland, P. Holden, H. O'Neill, and G. Mallmann
2016. Rapid cooling of planetesimal core-mantle reaction zones from Mn-Cr isotopes in pallasites. *Geochemical Perspectives Letters*, Pp. 68–77.

McSween, H. Y., D. W. Mittlefehldt, A. W. Beck, R. G. Mayne, and T. J. McCoy
2011. HED Meteorites and Their Relationship to the Geology of Vesta and the Dawn Mission. *Space Science Reviews*, 163(1-4):141–174.

Minarik, W. G., F. J. Ryerson, and E. B. Watson
1996. Textural Entrapment of Core-Forming Melts. *Science*, 272(5261):530–533.

Mirone, A., E. Brun, E. Gouillart, P. Tafforeau, and J. Kieffer
2014. The PyHST2 hybrid distributed code for high speed tomographic reconstruction with iterative reconstruction and a priori knowledge capabilities. *Nuclear Instruments and Methods in Physics Research, Section B: Beam Interactions with Materials and Atoms*, 324:41–48.

Mittlefehldt, D. W., M. M. Lindstrom, D. D. Bogard, D. H. Garrison, and S. W. Field
1996. Acapulco- and Lodran-like achondrites: Petrology, geochemistry, chronology, and origin. *Geochimica et Cosmochimica Acta*, 60(5):867–881.

Mizzon, H.
2015. *The magmatic crust of Vesta*. Thesis, Université Toulouse III Paul Sabatier.

Monnereau, M., M. J. Toplis, D. Baratoux, and J. Guignard
2013. Thermal history of the H-chondrite parent body: Implications for metamorphic grade and accretionary time-scales. *Geochimica et Cosmochimica Acta*, 119:302–321.

Morbidelli, A., H. F. Levison, K. Tsiganis, and R. Gomes
2005. Chaotic capture of Jupiter's Trojan asteroids in the early Solar System. *Nature*, 435(7041):462–465.

Morse, S. A.
1980. *Basalts and phase diagrams: an introduction to the quantitative use of phase diagrams in igneous petrology*. New York: Springer-Verlag.

Moskovitz, N. and E. Gaidos
2011. Differentiation of planetesimals and the thermal consequences of melt migration. *Meteoritics and Planetary Science*, 46(6):903–918.

Murr, L. E.
1975. *Interfacial phenomena in metals and alloys*. Addison-Wesley Pub. Co., Advanced Book Program.

Néri, A., J. Guignard, M. Monnereau, M. Toplis, and G. Quitté
2019. Metal segregation in planetesimals: Constraints from experimentally determined interfacial energies. *Earth and Planetary Science Letters*, 518:40–52.

Neumann, W., D. Breuer, and T. Spohn
2012. Differentiation and core formation in accreting planetesimals. *a&a*, 543.

Neumann, W., S. Henke, D. Breuer, H.-P. Gail, W. H. Schwarz, M. Trieloff, J. Hopp, and T. Spohn
2018. Modeling the evolution of the parent body of acapulcoites and lodranites: A case study for partially differentiated asteroids. *Icarus*, 311:146–169.

Nichols, C. I., J. F. Bryson, J. Herrero-Albillos, F. Kronast, F. Nimmo, and R. J. Harrison
2016. Pallasite paleomagnetism: Quiescence of a core dynamo. *Earth and Planetary Science Letters*, 441:103–112.

Nichols Jr, R. H.
2006. Chronological Constraints on Planetesimal Accretion. In *Meteorites and the Early Solar System II*, Pp. 463–472. University of Arizona Press.

Ohuchi, T. and M. Nakamura
2007. Grain growth in the system forsterite–diopside–water. *Physics of the Earth and Planetary Interiors*, 161(3-4):281–304.

O'Neill, H. S. C. and M. I. Pownceby
1993. Thermodynamic data from redox reactions at high temperatures. I. An experimental and theoretical assessment of the electrochemical method using stabilized zirconia electrolytes, with revised values for the Fe-"FeO", Co-CoO, Ni-NiO and Cu-Cu2O oxygen buffe. *Contributions to Mineralogy and Petrology*, 114(3):296–314.

Paganin, D., S. C. Mayo, T. E. Gureyev, P. R. Miller, and S. W. Wilkins
2002. Simultaneous phase and amplitude extraction from a single defocused image of a homogeneous object. *Journal of Microscopy*, 206(1):33–40.

Palme, H., L. Schultz, B. Spettel, H. Weber, H. Wänke, M. Michel-Levy, and J. Lorin
1981. The Acapulco meteorite: Chemistry, mineralogy and irradiation effects. *Geochimica et Cosmochimica Acta*, 45(5):727–752.

Papike, J., M. Spilde, G. Fowler, G. Layne, and C. Shearer
1995. The Lodran primitive achondrite: petrogenetic insights from electron and ion microprobe analysis of olivine and orthopyroxene. *Geochimica et Cosmochimica Acta*, 59(14):3061–3070.

Patzer, A., D. H. Hill, and W. V. Boynton
2004. Evolution and classification of acapulcoites and lodranites from a chemical point of view. *Meteoritics & Planetary Science*, 39(1):61–85.

Petry, C., S. Chakraborty, and H. Palme
2004. Experimental determination of Ni diffusion coefficients in olivine and their dependence on temperature, composition, oxygen fugacity, and crystallographic orientation. *Geochimica et Cosmochimica Acta*, 68(20):4179–4188.

Presnall, D. C., S. A. Dixon, J. R. Dixon, T. H. O'Donnell, N. L. Brenner, R. L. Schrock, and D. W. Dycus
1978. Liquidus phase relations on the join diopside-forsterite-anorthite from 1 atm to 20 kbar: Their bearing on the generation and crystallization of basaltic magma. *Contributions to Mineralogy and Petrology*, 66(2):203–220.

Quitté, G., A. Markowski, C. Latkoczy, A. Gabriel, and A. Pack
2010. Iron-60 heterogeneity and incomplete isotope mixing in the early solar system. *The Astrophysical Journal*, 720(2):1215–1224.

Righter, K.
2002. Does the Moon Have a Metallic Core? Constraints from Giant Impact Modeling and Siderophile Elements. *Icarus*, 158(1):1–13.

Roberts, J. J., J. H. Kinney, J. Siebert, and F. J. Ryerson
2007. Fe-Ni-S melt permeability in olivine: Implications for planetary core formation. *Geophysical Research Letters*, 34(14):L14306.

Roscoe, R.
1952. The viscosity of suspensions of rigid spheres. *British Journal of Applied Physics*, 3(8):267–269.

Rose, L. A. and J. M. Brenan
2001. Wetting Properties of Fe-Ni-Co-Cu-O-S Melts against Olivine: Implications for Sulfide Melt Mobility. *Economic Geology*, 96(1):145–157.

Rubie, D. C.
2015. *Formation of the Earth ' s Core*. Elsevier B.V.

Russell, S., L. Hartmann, and J. Cuzzi
2006. Timescales of the solar protoplanetary disk. In *Meteorites and the Early Solar System II*, Pp. 233–251. University of Arizona Press.

Sack, R. O. and M. S. Ghiorso
1989. Importance of considerations of mixing properties in establishing an internally consistent thermodynamic database: thermochemistry of minerals in the system Mg2SiO4-Fe2SiO4-SiO2. *Contributions to Mineralogy and Petrology*, 102(1):41–68.

Sack, R. O. and M. S. Ghiorso
1991. Chromian spinels as petrogenetic indicators: thermodynamics and petrological applications. *American Mineralogist*, 76(5-6):827–847.

Sack, R. O. and M. S. Ghiorso
1994a. Thermodynamics of multicomponent pyroxenes: I. Formulation of a general model. *Contributions to Mineralogy and Petrology*, 116(3):277–286.

Sack, R. O. and M. S. Ghiorso
1994b. Thermodynamics of multicomponent pyroxenes: II. Phase relations in the quadrilateral. *Contributions to Mineralogy and Petrology*, 116(3):287–300.

Sack, R. O. and M. S. Ghiorso
1994c. Thermodynamics of multicomponent pyroxenes: III. Calibration of Fe2+(Mg)-1, TiAl2(MgSi2)-1, TiFe 2 3+ (MgSi2)-1, AlFe3+(MgSi)-1, NaAl(CaMg)-1, Al2(MgSi)-1 and Ca(Mg)-1 exchange reactions between pyroxenes and silicate melts. *Contributions to Mineralogy and Petrology*, 118(3):271–296.

Schindelin, J., I. Arganda-Carreras, E. Frise, V. Kaynig, M. Longair, T. Pietzsch, S. Preibisch, C. Rueden, S. Saalfeld, B. Schmid, J.-Y. Tinevez, D. J. White, V. Hartenstein, K. Eliceiri, P. Tomancak, and A. Cardona
2012. Fiji: an open-source platform for biological-image analysis. *Nature Methods*, 9(7):676–682.

Scott, T. and D. L. Kohlstedt
2006. The effect of large melt fraction on the deformation behavior of peridotite. *Earth and Planetary Science Letters*, 246(3-4):177–187.

Shannon, M. C. and C. B. Agee
1996. High pressure constraints on percolative core formation. *Geophysical Research Letters*, 23(20):2717–2720.

Smith, C. S.
1964. Some elementary principles of polycrystalline microstructure. *Metallurgical Reviews*, 9(1):1–48.

Solferino, G. F. and G. J. Golabek
2018. Olivine grain growth in partially molten Fe–Ni–S: A proxy for the genesis of pallasite meteorites. *Earth and Planetary Science Letters*, 504:38–52.

Solomatov, V.
2015. *Magma Oceans and Primordial Mantle Differentiation*, volume 9. Elsevier B.V.

Solomatov, V. S., P. Olson, and D. J. Stevenson
1993. Entrainment from a bed of particles by thermal convection. *Earth and Planetary Science Letters*, 120(3-4):387–393.

Šrámek, O., L. Milelli, Y. Ricard, and S. Labrosse
2012. Thermal evolution and differentiation of planetesimals and planetary embryos. *Icarus*, 217(1):339–354.

Strong, H. M. and F. P. Bundy
1959. Fusion Curves of Four Group VIII Metals to 100 000 Atmospheres. *Physical Review*, 115(2):278–284.

Sugiura, N. and W. Fujiya
2014. Correlated accretion ages and ϵ 54 Cr of meteorite parent bodies and the evolution of the solar nebula. *Meteoritics and Planetary Science*, 49(5):772–787.

Swedenborg, E.
1734. *Opera Philosophica et Mineralia*.

Sweeney, S. M. and C. L. Martin
2003. Pore size distributions calculated from 3-D images of DEM-simulated powder compacts. *Acta Materialia*, 51(12):3635–3649.

Tait, A. W., A. G. Tomkins, B. M. Godel, S. A. Wilson, and P. Hasalova
2014. Investigation of the H7 ordinary chondrite, Watson 012: Implications for recognition and classification of Type 7 meteorites. *Geochimica et Cosmochimica Acta*, 134:175–196.

Takahashi, E.
1983. Melting of a Yamato L3 chondrite (Y-74191) up to 30 kbar. *Memoirs of National Institute of Polar Research. Special issue*, 30:168–180.

Tarduno, J. A., R. D. Cottrell, F. Nimmo, J. Hopkins, J. Voronov, A. Erickson, E. Blackman, E. R. D. Scott, and R. McKinley
2012. Evidence for a Dynamo in the Main Group Pallasite Parent Body. *Science*, 338(6109):939–942.

Tasaka, M. and T. Hiraga
2013. Influence of mineral fraction on the rheological properties of forsterite + enstatite during grain-size-sensitive creep: 1. Grain size and grain growth laws. *Journal of Geophysical Research: Solid Earth*, 118(8):3970–3990.

Taylor, G. J.
1992. Core formation in asteroids. *Journal of Geophysical Research*, 97(E9):14717.

Terasaki, H., D. J. Frost, D. C. Rubie, and F. Langenhorst
2005. The effect of oxygen and sulphur on the dihedral angle between Fe-O-S melt and silicate minerals at high pressure: Implications for Martian core formation. *Earth and Planetary Science Letters*, 232(3-4):379–392.

Terasaki, H., D. J. Frost, D. C. Rubie, and F. Langenhorst
2007. Interconnectivity of Fe-O-S liquid in polycrystalline silicate perovskite at lower mantle conditions. *Physics of the Earth and Planetary Interiors*, 161(3-4):170–176.

Terasaki, H., D. J. Frost, D. C. Rubie, and F. Langenhorst
2008. Percolative core formation in planetesimals. *Earth and Planetary Science Letters*, 273(1-2):132–137.

Touboul, M., T. Kleine, B. Bourdon, J. A. Van Orman, C. Maden, and J. Zipfel
2009. Hf–W thermochronometry: II. Accretion and thermal history of the acapulcoite–lodranite parent body. *Earth and Planetary Science Letters*, 284(1-2):168–178.

Trappitsch, R., P. Boehnke, T. Stephan, M. Telus, M. R. Savina, O. Pardo, A. M. Davis, N. Dauphas, M. J. Pellin, and G. R. Huss
2018. New Constraints on the Abundance of 60Fe in the Early Solar System. *The Astrophysical Journal*, 857(2):L15.

Tsiganis, K., R. Gomes, A. Morbidelli, and H. F. Levison
2005. Origin of the orbital architecture of the giant planets of the Solar System. *Nature*, 435(7041):459–461.

Uehara, M., J. Gattacceca, H. Leroux, D. Jacob, and C. J. van der Beek
2011. Magnetic microstructures of metal grains in equilibrated ordinary chondrites and implications for paleomagnetism of meteorites. *Earth and Planetary Science Letters*, 306(3-4):241–252.

Vigneresse, J. L., P. Barbey, and M. Cuney
1996. Rheological transitions during partial melting and crystallization with application to felsic magma segregation and transfer. *Journal of Petrology*, 37(6):1579–1600.

Vigneresse, J. L. and J. P. Burg
2004. Strain-rate-dependent rheology of partially molten rocks. *Geological Society, London, Special Publications*, 227(1):327–336.

Villeneuve, J., M. Chaussidon, and G. Libourel
2009. Evidence for 26Al Homogeneous Distribution in the Early Solar System from Chondrules Mg Isotopic Composition. *Meteoritics & Planetary Science*, 44(AUGUST):A212–A212.

Walker, D. and C. B. Agee
1988. Ureilite Compaction. *Meteoritics*, 23(1):81–91.

Walsh, K. J., A. Morbidelli, S. N. Raymond, D. P. O'Brien, and A. M. Mandell
2011. A low mass for Mars from Jupiter's early gas-driven migration. *Nature*, 475(7355):206–209.

Walsh, K. J., A. Morbidelli, S. N. Raymond, D. P. O'Brien, and A. M. Mandell
2012. Populating the asteroid belt from two parent source regions due to the migration of giant planets-"The Grand Tack". *Meteoritics and Planetary Science*, 47(12):1941–1947.

Walte, N. P., J. K. Becker, P. D. Bons, D. C. Rubie, and D. J. Frost
2007. Liquid-distribution and attainment of textural equilibrium in a partially-molten crystalline system with a high-dihedral-angle liquid phase. *Earth and Planetary Science Letters*, 262(3-4):517–532.

Walte, N. P., D. C. Rubie, P. D. Bons, and D. J. Frost
2011. Deformation of a crystalline aggregate with a small percentage of high-dihedral-angle liquid : Implications for core – mantle differentiation during planetary formation. *Earth and Planetary Science Letters*, 305(1-2):124–134.

Wanamaker, B. and D. Kohlstedt
1991. The effect of melt composition on the wetting angle between silicate melts and olivine. *Physics and Chemistry of Minerals*, 18(1):26–36.

Wasson, J. T. and G. W. Kallemeyn
1988. Compositions of Chondrites. *Philosophical Transactions of the Royal Society A: Mathematical, Physical and Engineering Sciences*, 325(1587):535–544.

Watson, H. C. and J. J. Roberts
2011. Connectivity of core forming melts: Experimental constraints from electrical conductivity and X-ray tomography. *Physics of the Earth and Planetary Interiors*, 186(3-4):172–182.

Weidenschilling, S. and J. Cuzzi
2006. Accretion Dynamics and Timescales: Relation to Chondrites. In *Meteorites and the Early Solar System II*, Pp. 473–485. University of Arizona Press.

Weisberg, M. K., T. J. McCoy, and A. N. Krot
2006. Systematics and Evaluation of Meteorite Classification. In *Meteorites and the early solar system II*, D. S. Lauretta and H. Y. McSween, eds., Pp. 19–52. University of Arizona Press.

Wray, P.
1976. The geometry of two-phase aggregates in which the shape of the second phase is determined by its dihedral angle. *Acta Metallurgica*, 24(2):125–135.

Yoshino, T., M. J. Walter, and T. Katsura
2003. Core formation in planetesimals triggered by permeable flow. *Nature*, 422(6928):154–157.

Zanda, B.
2004. Chondrules. *Earth and Planetary Science Letters*, 224(1-2):1–17.

Zeng, X., Y. Shang, S. Li, X. Li, S. Wang, and Y. Li
2019. The layered structure model for winonaite parent asteroid implicated by textural and mineralogical diversity. *Earth, Planets and Space*, 71(1):38.

Zha, C.-S., K. Mibe, W. A. Bassett, O. Tschauner, H.-K. Mao, and R. J. Hemley
2008. P-V-T equation of state of platinum to 80GPa and 1900K from internal resistive heating/x-ray diffraction measurements. *Journal of Applied Physics*, 103(5):054908.

Zipfel, J., H. Palme, A. Kennedy, and I. Hutcheon
1995. Chemical composition and origin of the Acapulco meteorite. *Geochimica et Cosmochimica Acta*, 59(17):3607–3627.

Résumé — De nombreux petits corps du système solaire ont connu la différenciation métal-silicate. Ce processus a provoqué la séparation du métal et du silicate, et peut avoir entraîné la formation d'un noyau métallique. Cette thèse porte sur la compréhension des processus physiques à l'origine de cette différenciation et de leurs conséquences sur les matériaux trouvés dans l'enregistrement météoritique. Afin de proposer des modèles les plus pertinents possibles, une approche conjointe expérimentale et de modélisation a été menée. Un système expérimental à trois phases a été conçu pour être représentatif d'échantillons naturels en cours de différenciation, et analysé à l'aide de techniques électroniques et de microtomographie 3D par rayons X. La différenciation métal-silicate se produit principalement par percolation d'un réseau métallique interconnecté. Cependant, une extraction importante des liquides silicatés est nécessaire pour permettre la formation d'un tel réseau. La différenciation est restée partielle dans les achondrites primitives à cause d'une accrétion tardive et des faibles tailles de grain des silicates, ce qui n'a pas permis une fusion complète des phases riches en fer ou encore une extraction efficace des produits de fusion. Les corps accrétés plus tôt qui ont connu un stade d'océan de magma sont sujets à une différenciation totale. Les modèles suggèrent qu'une fraction significative des silicates ne fond pas (correspondant au seuil rhéologique), empêchant les particules métalliques de sédimenter. A la fin de la phase d'océan de magma, la compaction et l'extraction efficace des produits de fusion favorisent la différenciation et la formation des météorites de fer, des achondrites et des pallasites.

Mots clés : Différenciation métal-silicates - planétésimaux - météorites - achondrites primitives - interconnectivité - pétrologie expérimentale - microtomographie 3D à rayons X - simulations thermodynamiques - modélisation

Abstract — Many early-accreted small bodies of the Solar System experienced metal-silicate differentiation. This process caused the metal and silicate to separate and may have led to the formation of a metallic core. This PhD focused on understanding the physical processes that drove this differentiation and their consequences on the materials found in the meteoritic record. In order to provide the most plausible models, a joint experimental and modeling approach was used. A three-phase experimental system was designed to be representative of natural samples undergoing differentiation and analyzed using computed 3D X-ray microtomography and electronic techniques. Metal-silicate differentiation mostly occurs though the percolation of an interconnected metallic network. However, significant extraction of the silicate melt is required to allow the formation of such a network. Differentiation remained partial in primitive achondrites due to late accretion and low silicate grain sizes that did not allow complete melting of the iron-rich phases or efficient melt extraction. Complete differentiation occurs for bodies accreted earlier that experienced a magma ocean stage. Models suggest that a significant fraction of the silicates does not melt (corresponding to the rheological threshold), preventing the metal particles from settling. At the end of the magma ocean phase, compaction and efficient extraction of the melts favors differentiation and the formation of achondrites (pallasites, stony and iron meteorites).

Keywords: Metal silicate differentiation - planetesimals - meteorites - primitive achondrites - interconnectivity - experimental petrology - 3D X-ray microtomography - thermodynamic simulations - modeling

Institut de Recherche en Astrophysique et Planétologie,
14 Avenue Edouard Belin, 31400 Toulouse